

THE MATERIALS PROCESSING, CONNECTIVITY, FLUX  
PINNING, AND CRITICAL CURRENT DENSITY OF Ag-CLAD  
 $(\text{Bi,Pb})_2\text{Sr}_2\text{Ca}_2\text{Cu}_3\text{O}_x$  SUPERCONDUCTING TAPES

by

Jeffrey A. Parrell

A dissertation submitted in partial fulfillment  
of the requirements for the degree of

Doctor of Philosophy  
(Materials Science)

at the

UNIVERSITY OF WISCONSIN - MADISON

1996

© Copyright by Jeffrey A. Parrell 1996  
All Rights Reserved

## Acknowledgments

I would like to thank the many people who have contributed to the work described in this dissertation. I am very grateful to my advisor, Professor David C. Larbalestier, for all of his help and guidance over the years. It is because of him and the strong supporting group he has built and maintained that I will always look back on my time at Wisconsin with fond memories. Many thanks to Bill Starch for maintaining the fabrication lab, and to Alex Squitieri for his help with the electronic equipment in the measurement labs. I also need to acknowledge several of the scientists in the group, including Xue Yu Cai, Tolya Polyanskii, and Milan Polak, as well as my fellow graduate students, including Alex Pashitski, Harry Edelman, and Rob Heussner, for many helpful discussions and collaborations. I was also fortunate to work with a number of bright undergraduates, including John Anderson, Jim Purins, and Kevin Eberman. Outside of the group at Wisconsin, I benefited from collaborations with Steve Dorris at Argonne National Laboratory, and Bart Riley at American Superconductor Corporation. Much of the work in this dissertation is really the result of the collective effort of all of the people recognized here, as well as many others both within and outside the Applied Superconductivity Center that I have not acknowledged by name. Many thanks to all of you.

THE MATERIALS PROCESSING, CONNECTIVITY, FLUX PINNING,  
AND CRITICAL CURRENT DENSITY OF Ag-CLAD  $(\text{Bi,Pb})_2\text{Sr}_2\text{Ca}_2\text{Cu}_3\text{O}_x$   
SUPERCONDUCTING TAPES

Jeffrey A. Parrell

Under the supervision of Professor David C. Larbalestier

At the University of Wisconsin-Madison

The critical current density ( $J_c$ ) of Ag-clad  $(\text{Bi,Pb})_2\text{Sr}_2\text{Ca}_2\text{Cu}_3\text{O}_x$  (2223) superconducting tapes is determined by a hierarchy of limiting mechanisms. Experiments described in this dissertation show that the  $J_c$  (77 K) of a 2223 tape can be determined first by any of several connectivity-limiting factors, and ultimately by the intragranular flux pinning strength. The 2223 phase is formed in tapes by a liquid-assisted reaction between precursor oxides. At the early stages of thermomechanical processing, a low volume fraction of the 2223 phase is the primary  $J_c$  limitation. As the phase purity is increased by further thermal treatment, the porosity within the core limits the intergranular connectivity and  $J_c$ . This porosity, which can be measured by microhardness, can be reduced by mechanically deforming the sample between heat treatments. However, deforming the sample when the 2223 phase purity is high, and is thus with little liquid-formation capacity, leaves residual microcracks throughout the tape. As shown by magneto-optical imaging, the connectivity at this stage of processing is limited mainly by microcracking.

Reducing the microcrack density can increase  $J_c$ , until the point where the connectivity is then determined by small quantities of residual liquid phase that wet the 2223 grains, inhibiting supercurrent transport. Slow cooling increases the intergranular connectivity by eliminating these liquid regions, crystallizing them into Pb-rich second phase particles. When this connectivity limit is removed,  $J_c$  (at 77 K) is limited by the intragranular flux pinning. Improvements in the irreversibility field, which were used in this dissertation as a measure of flux pinning strength of the tape, are then required to increase  $J_c$ . Slow cooling is also effective at increasing the irreversibility field, as determined by extended electric field-current density measurements and by the field of magnetization loop closure. This can be attributed to two effects: A reduction in anisotropy as the material is oxygenated during cooling, and by the introduction of flux pinning defects into the crystal structure by decomposition of the 2223 phase.

## Contents

<i>Abstract</i> _____	<i>ii</i>
<b>1. Introduction</b> _____	<b>1</b>
1.1 Motivation _____	2
1.2 Relevant details of superconductivity _____	4
1.3 Possible critical current density limitations in 2223 tapes _____	8
1.3.1 Why is flux pinning important in BSCCO-2223? _____	8
1.3.2 What about the intergranular connectivity? _____	10
1.4 Structure of this dissertation _____	11
<b>2. Fabrication of Ag-clad tapes</b> _____	<b>13</b>
2.1 Powder packing density and the Ag:Superconductor ratio _____	13
2.2 Aspects of billet design _____	16
2.3 Composite metalworking _____	19
2.3.1 Wire drawing _____	19
2.3.2 Rolling of wire into tape _____	23
2.4 Ag-Mg-Ni alloys _____	25
<b>3. Formation and stability of the 2223 phase</b> _____	<b>29</b>
3.1 Formation mechanism _____	30
3.1.1 The importance of Pb, liquid, and the overall cation composition _____	31
3.1.2 Nucleation and growth _____	33
3.1.3 Intercalation _____	37
3.2 Role of Ag and the Ag cladding _____	39

3.3 The stability of 2223 as a function of temperature and oxygen partial pressure	42
<b>4. Thermomechanical processing</b>	<b>46</b>
4.1 Heat treatments	47
4.2 Intermediate deformation steps	48
4.2.1 Mechanics of uniaxial pressing	49
4.2.2 Mechanics of cold rolling	52
4.2.3 Cracking behavior	55
<b>5. The relationship between microhardness, density, connectivity, and <math>J_c</math></b>	<b>59</b>
5.1 Introduction	59
5.2 Experimental Details	62
5.3 Results	64
5.4 Discussion	73
5.5 Summary	79
<b>6. The effect of sheath material and deformation method on the microhardness, connectivity, and <math>J_c</math></b>	<b>80</b>
6.1 Introduction	80
6.2 Experimental details	83
6.3 Results	85
6.4 Discussion	90
6.5 Summary	99
<b>7. Residual microcracks in processed tapes</b>	<b>100</b>
7.1 Introduction	100
7.2 Experimental details	103

7.3 Results_____	105
7.4 Discussion_____	111
7.5 Summary_____	114
<b>8. Control of the liquid phase and the healing of microcracks _____</b>	<b>115</b>
8.1 Controlled, reversible decomposition of 2223 tapes in oxygen atmospheres into pseudoprecursor phase mixtures_____	115
8.1.1 Introduction_____	115
8.1.2 Experimental details_____	121
8.1.3 Results _____	124
8.1.4 Discussion _____	134
8.1.5 Summary_____	139
8.2 Experiments designed to improve the CDR process_____	140
8.2.1 Decomposition in nitrogen _____	140
8.2.2 Testing of a minimal-decomposition hypothesis _____	151
8.2.3 DTA and XRD studies of the pseudoprecursor phase mixtures produced by 2223 decomposition in oxygen _____	158
8.2.4 Summary_____	164
<b>9. Effect of the cooling rate on the microstructure, <math>T_c</math>, and <math>J_c</math> of 2223 tapes _</b>	<b>167</b>
9.1 Introduction_____	167
9.2 Experimental details _____	169
9.2.1 One-powder tape processing _____	169
9.2.2 Two-powder tape processing_____	169
9.3 Results_____	171
9.3.1 Fully processed one-powder tape experiments _____	171
9.3.2 Two-powder tape experiments _____	175
9.4 Discussion_____	177

9.5 Summary _____	181
<b><i>10. Connectivity and flux pinning improvements in 2223 tapes produced by changes in the cooling rate</i></b> _____	<b>182</b>
10.1 Introduction _____	182
10.2 Experimental Procedure _____	185
10.3 Results _____	189
10.4 Discussion _____	200
10.4.1 Intragranular flux pinning _____	202
10.4.2 Intergranular connectivity _____	207
10.5 Summary _____	212
<b><i>11. Review and conclusions</i></b> _____	<b>214</b>
<b><i>12. References</i></b> _____	<b>223</b>

# 1. Introduction

Superconducting materials have long held the promise of many wonderful technological benefits. Most applications of superconductivity make use of the special ability of a superconductor to carry electric current without dissipation. While applications such as cross-country, levitating bullet trains are still somewhat out of reach, they grow closer each day. Indeed, superconductors have progressed out of the laboratory and into near-commodity, “real world” products such as magnetic resonance imaging systems. However, most present successful applications of superconductors utilize so-called “low temperature” materials such as alloys of niobium and titanium. The inconvenience, expense, and perhaps impracticality associated with the cooling of such materials below their critical temperature ( $T_c$ ), which is  $\sim 10$  K, has restricted their use to applications where performance outweighs the costs of expensive refrigeration.

The discovery of “high temperature” superconductivity in 1986 [1] resulted in the expansion of the study of superconductors from a handful of laboratories to hundreds of laboratories world wide. The discovery of superconductivity above 77 K (the boiling point

of liquid nitrogen) in compounds of Y-Ba-Cu-O [2] gave new hope for the economical and widespread application of superconductivity.

## **1.1 Motivation**

The early widespread excitement of 1987-1988 was soon tempered when it was realized that although single crystals of compounds such as Y-Ba-Cu-O had very high critical current densities and strong flux pinning, they were not useful in polycrystalline forms, such as wires or tapes. This was because supercurrent effectively cannot cross the boundaries between grains which are misaligned by more than  $\sim 10^\circ$ , making most of the grains in a random polycrystal “weakly linked” [3]. The discovery of the Bi-Sr-Ca-Cu-O (BSCCO) compounds in 1988 [4] made it possible to consider useful polycrystalline forms of high  $T_c$  material, as weak links seemed less of a problem in BSCCO.

There are three superconducting phases in the BSCCO system,  $\text{Bi}_2\text{Sr}_2\text{Cu}_1\text{O}_x$  (“2201”),  $\text{Bi}_2\text{Sr}_2\text{Ca}_1\text{Cu}_2\text{O}_x$  (“2212”) and  $\text{Bi}_2\text{Sr}_2\text{Ca}_2\text{Cu}_3\text{O}_x$  (“2223”). The three phases differ mainly by the number of Cu-O layers that rest between the Bi-O layers which cap the unit cell. Presently, the most promising of the BSCCO compounds for long length conductor manufacture is BSCCO-2223, which is the BSCCO phase with the highest  $T_c$ , at  $\sim 110$  K. These materials have micaceous crystal structures, and their grains can be highly aligned by careful thermomechanical processing.

Although 2223 can be made into useful conductor forms, its superconducting properties at 77 K are not as good as the Y-Ba-Cu-O compounds. As will be discussed in the following sections, the principal reason for this is that 2223 is more anisotropic than

YBCO-123. The almost two-dimensional character of the 2223 compound is responsible for poor flux pinning within the grains. However, at temperatures below  $\sim 30$  K, where flux pinning is strong, 2223 tapes can carry significant current densities in very high magnetic fields. Figure 1-1 plots the critical current density ( $J_c$ ) at 4.2 K, as a function of applied magnetic field for several different types of superconducting wires and tapes. Although conventional low  $T_c$  materials can carry significantly greater current densities at low magnetic fields, the BSCCO compounds can carry higher current densities at fields above  $\sim 8$  T. Thin films or single crystals of a number of other high  $T_c$  materials can carry even greater  $J_c$  values, but presently they cannot be economically made into long lengths of conductor. Although BSCCO-2212 typically has better properties than BSCCO-2223 at 4.2 K, its low  $T_c$  ( $\sim 80$  K) makes only the 2223 phase attractive for operation at liquid nitrogen temperatures.

The fact that 2223 can carry high current densities in high fields at low temperatures, and still significant currents at high temperatures, makes it a promising material to study. Improvements in the current carrying capacity at either or both high and low temperatures could make the use of 2223 tapes feasible for many applications. Broadly stated, the goal of this thesis was to understand the relationship between the tape processing parameters and the resultant  $J_c$  values, and to use this information in the processing/properties feedback loop so as to further increase the critical current density.

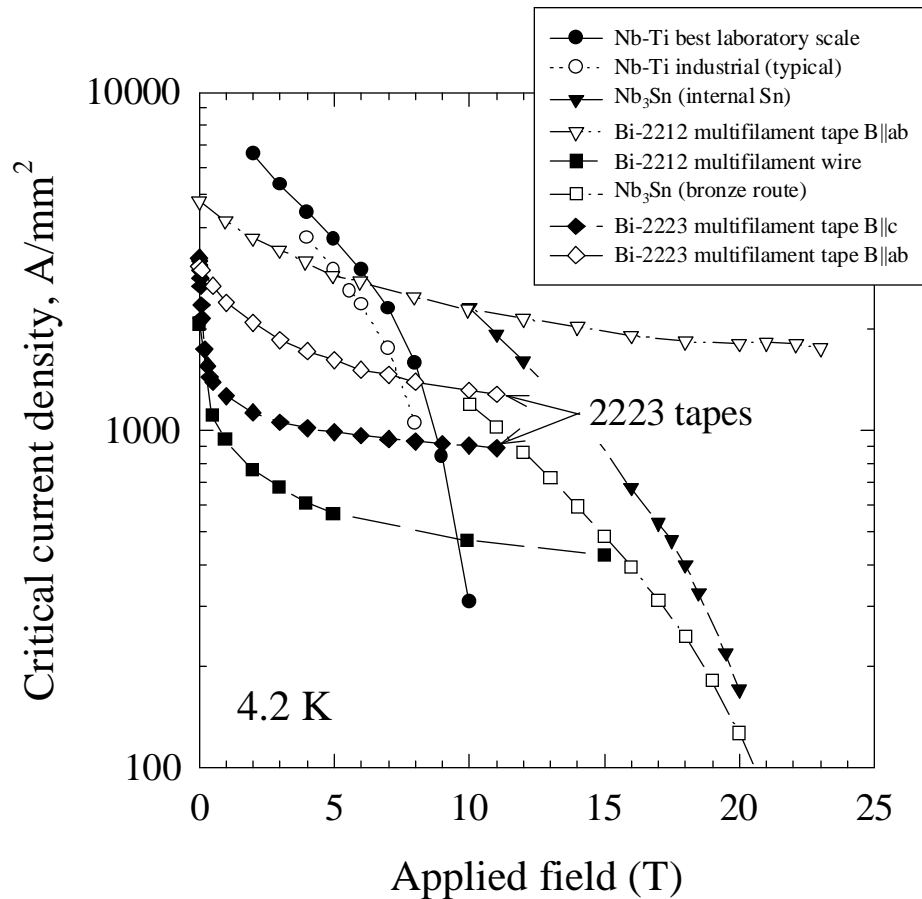


Figure 1-1.  $J_c$  (4.2 K) as a function of magnetic field for several types of industrially-produced superconducting composites. BSCCO conductors have higher  $J_c$  values than Nb-Ti or Nb<sub>3</sub>Sn conductors in high magnetic fields. Data from various sources compiled by P.J. Lee (University of Wisconsin).

## 1.2 Relevant details of superconductivity

The superconducting phase field is a volume bounded by three critical parameters, the critical current density  $J_c$ , the critical temperature  $T_c$ , and the critical magnetic field

strength  $H_c$  or flux density  $B_c$ . Within this volume, superconducting materials can carry an electric current with zero resistance (a “supercurrent”).

There are two basic classes of superconductors, known as Type I and Type II. Type I superconductors do not allow the penetration of magnetic flux into their interior, and carry a supercurrent only within a thin layer  $\lambda$ , the penetration depth, of their surface. Type I superconductors are only found as pure elements (e.g. Pb), although there are some elements (e.g. Nb) that are Type II superconductors. At a field known as the lower critical field  $B_{c1}$ , magnetic flux penetrates into the interior of Type II superconductors. The magnetic flux enters a Type II superconductor as *fluxoids* which consist of an integral number of a quantum known as the *fluxon*, which has a value of  $2.07 \times 10^{-15}$  Wb [5]. A Type II superconductor which contains some penetrated fluxons, but at a density less than the upper critical flux density  $B_{c2}$ , has regions in both the superconducting and normal states, and is said to be in the “mixed” state. Type II superconductors (like BSCCO-2223) are more useful from a technological point of view than Type I superconductors, because current is carried throughout the bulk, and because of their typically much greater upper critical field.

When transport current of density  $J$  is passed through a Type II conductor in the mixed state, there is an electromagnetic interaction between the electrons carrying the current and the fluxoids threading the superconductor. This Lorentz force  $F_L$  acts on each fluxoid at right angles to both the direction of the flux penetration and the transport current, and is given by [5]

$$\vec{F}_L = \vec{J} \times \vec{B}$$

A schematic of the situation described above is shown in Figure 1-2 for a slab (or tape) of Type II material. The fluxoids remain stationary, and the conductor continues to have true zero resistance, as long as there is present a pinning force at least equal to the Lorentz force  $F_L$  acting to move the fluxoids across the sample. This force resisting the fluxoid motion is known as the flux pinning force  $F_p$ , and arises because the lowest energy state for a superconductor in the mixed state is one where the fluxoids are contained within non-superconducting (normal) regions. Thus, non-superconducting phases, defects, or inclusions within the superconductor can act as flux pinning sites. As individual fluxoids repel one another, resulting in the formation (at least at low temperatures) of a regularly spaced fluxoid lattice, it is not necessary for each and every fluxoid in the lattice to be pinned for fluxoid motion to be inhibited in the sample; a small number of strong pins can effectively inhibit the movement of all fluxoids.

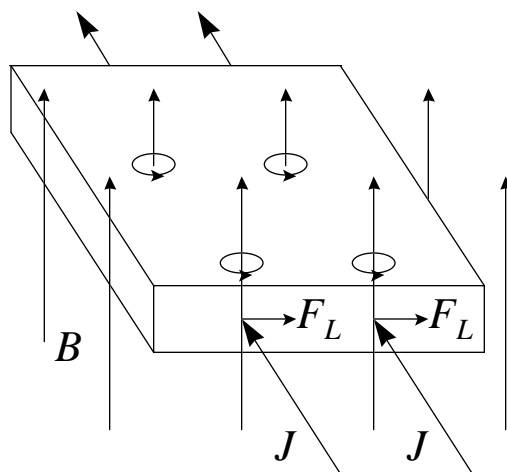


Figure 1-2. The interaction between the transport current density  $J$ , magnetic flux  $B$ , and Lorentz force  $F_L$  in a slab of Type II superconducting material in the mixed state. Supercurrent vortices ring the fluxoids. The fluxoids remain stationary as long as  $F_L$  is less than the flux pinning strength  $F_p$ .

When the Lorentz force acting on the fluxoids exceeds the pinning force, the fluxoids begin to move across the sample. The energy dissipated by the drag or viscous force opposing this motion is supplied by the transport current. Thus, when fluxoids are set into motion, the material becomes resistive (i.e. there is a voltage drop along the conductor), and is no longer truly without loss. This fluxoid motion is known as “flux flow”, and in conductors where  $J_c$  is limited by the flux pinning force, it is the source of the resistance observed at currents greater than the critical current [5].

### **1.3 Possible critical current density limitations in 2223 tapes**

The critical current density  $J_c$  (defined as the critical current  $I_c$  divided by the total cross section of superconductor  $A$ ) of a superconducting wire or tape can be limited by either intrinsic or extrinsic factors. Although the absolute upper limit is determined by the depairing current density, which is  $\sim 10^7$  A/cm<sup>2</sup> for 2223 at 77 K [6], the practical intrinsic  $J_c$  limitation of a conductor is determined by the flux pinning strength. Extrinsic limitations such as filament sausaging [7,8,9], porosity, cracks, or other inhomogeneities or defects can further reduce the  $I_c$  and therefore the  $J_c = I_c/A$  of a conductor.

While there can be a clear distinction between an intrinsically- (i.e. flux pinning) or extrinsically- (inhomogeneity) limited  $J_c$  for conventional low  $T_c$  superconductors like Nb-Ti, for high  $T_c$  2223 tapes it is not so obvious where to make this division. As it is essentially impossible to avoid defects like misaligned grains, second phase impurities, pores, and cracks in 2223 tapes, these could also be considered limitations intrinsic to BSCCO-2223. In reality, the  $J_c$  of 2223 tapes is controlled by a hierarchy of mechanisms [10], the determination of which has been a major part of this thesis work. In this section, the origins of the primary  $J_c$  limitations in 2223 tapes are discussed. Although detailed discussions and reviews of the literature are given later, the points are first briefly summarized here to set the stage for what follows.

#### **1.3.1 Why is flux pinning important in BSCCO-2223?**

As alluded to earlier, the motion of fluxoids plays a key role in determining the useful operating regime for high  $T_c$  superconductors. This is especially true at high

temperatures (e.g. 77 K), where it is more difficult to pin flux, as the thermal energy causes the fluxoid lattice to change from a “glassy” state to one where fluxoids can “creep” or “flow”, and the interaction between fluxoids is decreased [11]. Flux creep at high temperatures imposes a significant additional transition line within the superconducting phase field, known as the irreversibility field  $H^*$ , which is considerably lower than  $H_{c2}$ . Above the irreversibility field, the fluxoids move easily and reversibly with changes in field, and therefore the sample as a whole no longer exhibits zero resistance.

As discussed by Tinkham [12], the reason  $H^*$  is significantly lower than  $H_{c2}$  for BSCCO superconductors (although  $H^*$  is slightly lower than  $H_{c2}$  for low  $T_c$  conductors as well, the difference is often not detectable) is because of the great anisotropy of the penetration depth  $\lambda$  and coherence length  $\xi$  along the  $a$ - and  $b$ -directions of the crystal (i.e. in the Cu-O planes) and the  $c$ -direction. For BSCCO-2223, the anisotropy factor  $\gamma$ , defined as

$$\gamma = \frac{\lambda_c}{\lambda_{ab}} = \frac{\xi_{ab}}{\xi_c} = \frac{H_{c2} \parallel ab}{H_{c2} \parallel c},$$

is estimated to be  $\sim 20,000$  [12]. Assuming the material acts as a three dimensional superconductor (i.e. strong coupling between the individual superconducting layers, which is not necessarily a good approximation for BSCCO), the value of the irreversibility field  $H^*$  as a fraction of  $H_{c2}$  is approximately

$$\frac{H^*}{H_{c2}} \propto \frac{C \xi_{ab}^2}{T^2 \lambda_{ab}^4 \gamma^2},$$

where  $C$  is a constant and  $T$  is the temperature [12]. Thus, although some of the assumptions are not good for 2223, it can at least be seen from this expression that because of the high value of  $\gamma$ ,  $H^*$  will be significantly lower than  $H_{c2}$  for BSCCO, especially at high temperatures. It is for this reason that  $H^*$  can play an important in determining the  $J_c$  of 2223 tapes at 77 K.

### 1.3.2 What about the intergranular connectivity?

The above discussion notwithstanding, flux pinning may not be the primary  $J_c$  limitation in 2223 tapes, even at 77 K, and especially for low values of applied magnetic field. As will be shown later, BSCCO-2223 tapes typically have  $H^*$  ( $\parallel c$ ) values greater than 0.1 T. At fields well below this, e.g. zero field (in this thesis the expression “zero field” will be understood to mean zero applied field, and includes any self field generated by the sample),  $J_c$  may well be limited by the connections between the grains. However, unlike the case for a flux pinning limited  $J_c$ , quantification of connectivity effects is quite difficult. Whereas changes in flux pinning cause changes in the intragranular (true)  $J_c$ , connectivity changes may most significantly influence the effective superconducting cross section  $A_{eff}$ , which may be very close to the total cross section  $A$  for a well connected sample, or only a very small fraction of  $A$  in a poorly connected sample. Thus, when a macroscopic  $J_c$  is defined as is usual to be  $I_c/A$ , without any knowledge of the connectivity it is difficult to know if the “true”  $J_c$  of the material is changing, or just  $A_{eff}$ , or both. The intergranular connectivity of a 2223 tape can be fixed by any of several types of defects, or by combinations of defects, which include microcracks, porosity, and impurity phases.

It will be shown later that consideration of the effects of connectivity is not just hypothetical; there is now ample evidence showing that the current flow in 2223 tapes is percolative.

#### **1.4 Structure of this dissertation**

As illustrated in the following chapters, the materials science of Ag-clad BSCCO-2223 tapes is extremely complicated. Evidence will be given to show that the  $J_c$  of 2223 tapes can be determined by any of several intergranular connectivity limitations, and that the flux pinning strength of the percolative current path can play a role in determining the upper limit of  $J_c$  performance. The work is presented in a logical progression from wire fabrication to increasingly complex thermomechanical processing issues, with discussions of the  $J_c$  limitations that arise along the way. In Chapter 2 the details of the tape fabrication and metalworking processes are reported. A discussion and review of the knowledge regarding the phase formation and stability of the high- $T_c$  2223 phase is presented in Chapter 3. In Chapter 4 the general thermomechanical process that is used to convert the precursor tapes into the 2223 phase is described. Chapters 5 and 6 introduce one type of connectivity limitation, where it is shown that the microhardness and density of the 2223 phase can be correlated to  $J_c$ . In Chapter 7 evidence of residual (post-heat treatment) microcracks is presented, and the implications of cracks on the connectivity considered. A novel materials engineering approach to microcrack reduction is presented in Chapter 8, and the results of several experiments aimed at improving the process are discussed. A summary of several experiments studying the effect of the cooling rate on

the microstructure and superconducting properties is given in Chapter 9, with the results considered in the context of both connectivity and flux pinning. In Chapter 10 experiments are described that give further insight into the mechanism of the remarkable effect of the cooling rate on the superconducting properties, and it is shown that changes in both connectivity and flux pinning are induced by manipulation of the cooling rate. Finally, the conclusions to be drawn from the work are presented in Chapter 11, and the implications of the findings for improving  $J_c$  are discussed.

## 2. Fabrication of Ag-clad tapes

BSCCO tapes are most commonly made using the “oxide-powder-in-tube”, or OPIT, technique. The basic premise of the process is simple: fill a Ag tube with BSCCO precursor powder, plug the ends, draw it into a wire, and finally roll the wire into a tape. Although the OPIT process is essentially a short piece length process, it can be usefully scaled up for some industrial applications. An advantage of working with small billets made by the OPIT process is that only small amounts of raw material are required to make a length of tape sufficient for most laboratory experiments. The fabrication of composites is often a process of trial and error, with each made utilizing what was learned from its predecessor. In this chapter some of the procedures and important things learned about billet fabrication are discussed.

### ***2.1 Powder packing density and the Ag:Superconductor ratio***

Two of the many variables of composite design are the choices of the initial powder packing density and the Ag:superconductor area ratio (Ag:SC). The precursor

powders (which will be discussed in more detail in Chapter 3) can be conveniently packed into Ag tubes or “cans” with packing fractions ranging from  $< 20\%$  to about  $70\%$  of the BSCCO-2223 theoretical density, which is about  $6.3 \text{ g/cm}^3$ . Low packing fractions of  $\sim 25\%$  were obtained via an iterative process of pouring a small amount of powder into a can, and then hand packing the powder with a rod. This iterative process ensured a (somewhat) uniform density along the billet length.

Higher powder compact densities were achieved by cold isostatic pressing (CIP'ing). This was typically done using the following procedure. First, a clean rubber CIP bag (usually a 9.5 mm diameter bag) was filled with powder. The powder was worked so that it was all at the bottom of the bag, and then the powder slug was gently pinched off by hand. The powder slug/CIP bag was then gently rolled between the hands or on a table to get the powder uniformly packed in the bag, and to give the slug a nice cylindrical shape. During this rolling the powder was packed more firmly, and as much air as possible was let out of the bag. Then the CIP bag was tied off as close to the cylindrical powder slug as possible, and the end of the bag containing the powder was placed into a short length of snug-fitting stainless steel tube. The tube helped to keep the CIP bag and powder in a cylindrical shape during the CIP'ing process, and to define a maximum diameter for the green compact. A CIP pressure of  $\approx 340 \text{ MPa}$  was usually used, which resulted in packing density of  $\approx 70\%$ . After CIP'ing, the powder slug was cut from the bag, and then any rough edges were cut or ground away. The powder compact was later inserted into a can that was machined specifically for the slug, as this method resulted in green compacts that had slightly different diameters each time.

The initial powder packing method/density plays a large role in determining the final Ag:SC ratio of a composite. Although it is technically more correct to speak of a “Ag-to-hole-in-the-tube” area ratio, as the powders never achieve full density, it is common practice to use the term “Ag-to-superconductor” ratio. From a conductor application point of view, a Ag:SC substantially lower than 1:1 is desirable; however, to facilitate easy drawing of OPIT composites, a minimum Ag:SC of ~ 2:1 is required. Such a Ag:SC ratio can be achieved by either loosely packing a very thin wall can, or by loading a somewhat thicker wall tube with a CIP’ed slug. When a composite is drawn, a loosely packed powder is compacted, decreasing its cross section relative to that of the Ag can, thus increasing the apparent Ag:SC ratio. As CIP’ed powder densifies less upon drawing, one can start with a Ag can that is close to the desired Ag:SC. Data by Karuna et al. [13] are very useful for designing monofilament composites with a specific Ag:SC ratio. The packing method, initial Ag:SC ratio, and the Ag:SC ratio reached after wire drawing for several composites are listed in Table 2-1 to illustrate the relationship between these composite parameters. Several authors have reported that the maximum BSCCO powder density that can be achieved through wire drawing (and/or rolling) is about 75% [13,14]. The need to densify beyond this low green packing density is one of the reasons why tapes must be deformed between heat treatments. This will be discussed in Chapters 5 and 6, where it is shown that the density of the 2223 phase can be an important  $J_c$ -determining connectivity limitation.

Table 2-1. Initial billet fabrication parameters and the Ag to superconductor ratio achieved after wire drawing.

Composite identification	Initial O.D. of Ag tube	Packing method (% relative density)	Initial Ag:SC ratio (SC area fraction)	Ag:SC ratio after drawing to ~ 2 mm (SC area fraction)
UWB49	13.0 mm	CIP (~70%)	1.8:1 (36%)	2.0:1 (33%)
UWB59	14.6 mm	CIP (~70%)	3.5:1 (22%)	3.8:1 (21%)
UWB61	15.9 mm	CIP (~70%)	2.8:1 (26%)	3.2:1 (24%)
UWB72	13.4 mm	hand packed (~25%)	0.8:1 (56%)	1.4:1 (42%)
UWB90	11.4 mm	hand packed (~25%)	0.3:1 (77%)	0.7:1 (59%)

It is thus clear that the initial packing density of OPIT wires plays a significant role in determining the final Ag:SC. Essentially any desired ratio can be obtained at any given composite size through thoughtful composite design.

## **2.2 Aspects of billet design**

The design of the Ag cans and the plugs which closed them evolved over time, often building on what was learned with each prior composite. Several of the common types of can/plug assemblies used to make billets, and the specific needs/uses they filled are described in this section.

The standard type of billet was made from a Ag tube roughly 15 cm long of constant outer and inner diameters of ~ 15 mm and ~ 7.5 mm, respectively. Such tubes were closed by plugging both ends with cylindrical Ag plugs about 2.5 cm long, and swaging the tubes over the plugs to form a tight seal. This type of design required a relatively thick Ag tube wall, so that the tube had sufficient strength to co-reduce the plugs during drawing. This design was used primarily for CIP'ed powder slugs, so that the thick

tube walls would not result in relatively high final Ag:SC values; as CIP'ed slugs do not significantly further densify, the Ag:SC would be maintained at a reasonable level during drawing (Table 2-1).

When drawing composites made in this way, the tube wall would eventually thin relative to the Ag plug to the point where there was no longer a tube cross section sufficient to co-reduce the plug, and the wire would break at the point where the BSCCO meets the plug. This was not really important at small wire diameters, when the wire could easily be closed again with a hammer, but at large wire diameters it could be a major difficulty. This problem could usually be avoided by swaging over the plugs on both ends before each drawing die pass, so that the plugs would not be deformed in the die. However, this was not always a convenient solution, as it would become difficult after many swaging/drawing passes to keep track of the exact location of the plug ends, and unnecessarily swaging pieces longer than the plugs would reduce the yield of the high quality wire section.

A variation of the thick wall design for CIP'ed slugs designed to alleviate the problem of wire breaks at the plug interfaces used a solid rod with a hole drilled only partially through, instead of a tube open at both ends. This design needed only one plug to close the open end. Billets were made in this manner with either a long solid rod section, or with a short solid rod section and a long drilled section. A long solid rod section was useful for billets with Ag:SC close to or less than  $\sim 2:1$ , as the solid end could be used as the leading swage tip (i.e. the end of the wire the draw bench jaws grab on to), eliminating wire tip breaks that would occur with thinner wall tube/plug designs. The use of a short

solid section, with a long drilled portion of rod, eliminated the need to swage the back of the composite before every die pass when the solid section was used as the back of the composite (i.e. when the open tube/Ag plug end was used as the swage tip). This design was useful for long CIP'ed slugs, or when only Ag rod was available for billet fabrication.

A third type of can/plug assembly was useful for fabricating hand packed composites with low final Ag:SC ratios. As hand packed powders significantly densify upon drawing, a very low initial Ag:SC is required to achieve a low final Ag:SC. This was not possible using designs like those described above, as very thin Ag tube walls lack the strength to co-reduce solid Ag plugs. The successful method used to make such a composite was to first reduce the outer diameter of a portion of a Ag tube length by machining so as to create a section for the powder that would have a low Ag:SC. Then the remaining thick tube wall section was swaged shut, and used as the drawing and swage tip. Leaving the extra Ag thickness along this front section made it easier to close off the tube bore by swaging. The BSCCO powder was then hand packed into the thin wall back end, and was closed with a Ag plug which had been hollowed out along almost its entire length, except for the very end which contacted the powder. Machining a small point on this end of the plug helped to reduce the stress concentration of the thin wall/Ag plug junction. The back of the composite, containing the hollowed-out plug, was then swaged before each die pass so that the die would do no work on the plug section. The solid Ag front end of the wire (the swage tip) was the key to being able to draw such wires. It was very important not to cut off all of this solid Ag swage tip, because the wall thickness of the

BSCCO sections were usually not thick enough to withstand the force of drawing after swaging (i.e. the swage tips would break).

## **2.3 Composite metalworking**

### 2.3.1 Wire drawing

Although the initial powder packing density and Ag:SC ratio are important composite design parameters, the wire drawing and cold rolling procedures used to turn billets into tape also substantially influence the properties of the final tape product. For example, if too great a wire drawing area reduction per pass is used, it may make a composite impossible to draw down, and if a reduction too small is used, it may lead to centerburst problems, which can lead to sausaging (this is mainly a problem for multifilament wires [15]) and also make the composite difficult to draw. Furthermore, the cold rolling sequence which follows wire drawing can have a large effect on the powder packing density [13] and filament sausaging of the final tape product. As a complete theoretical analysis of all of the forces involved with OPIT wire drawing and rolling is a difficult problem, requiring the input of many unknown or essentially unmeasurable parameters, only the features relevant to practical composite processing are discussed here.

The first step in reducing a billet into tape is to draw it into a wire, typically between 1.5-2.0 mm in diameter. A wire is drawn to a smaller diameter by repeatedly passing it through successively smaller conical wire drawing dies. The leading end of the wire is swaged to produce a tip to fit through the outlet of the die (the swage tip), and this

tip is used by the draw bench jaws to pull the rest of the wire through the die. As shown in Figure 2-1, the required draw force  $P_d$  which is supplied by the draw bench is balanced by the horizontal component of the frictional force between the wire and the die surface and by the horizontal component of the normal pressure which reduces the wire diameter [16]. Here the drawing *force* is considered rather than the *stress* as the wire cross section  $A$  is not homogeneous; it consists of both Ag metal and a powder core. The powder core complicates the analysis, as it contributes (essentially) nothing to the effective tensile strength of the wire and/or swage tip, and yet it requires significant force to compress and elongate it through the die. The force needed to draw the wire through the die is thus the sum of the compressive and frictional forces:

$$P_d = pS \sin \alpha + \mu pS \cos \alpha$$

where  $\mu$  is the friction coefficient between the wire and the die,  $\alpha$  is the half angle of the die, and  $p$  is the mean pressure acting on the contact surface  $S$ , which is given by

$$S = \frac{A_i - A_f}{\sin \alpha}.$$

It can be shown [16] that the drawing force is approximately equal to

$$P_d \approx \sigma_0 A_f \ln \frac{A_i}{A_f} (\mu \cot \alpha + 1)$$

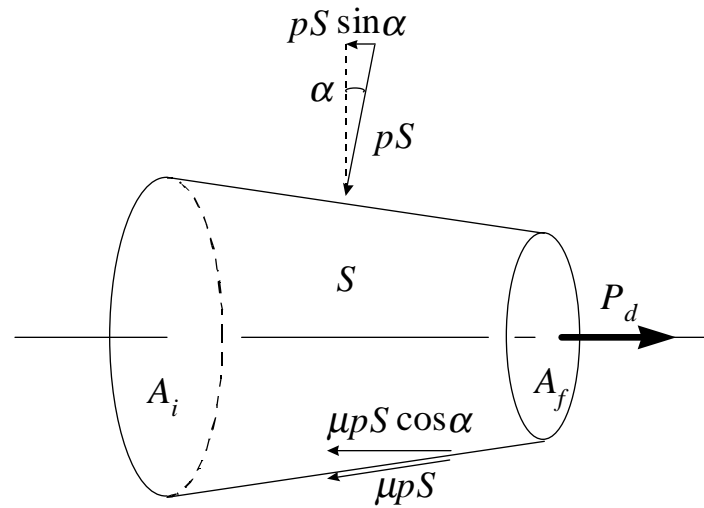


Figure 2-1. Forces acting on a conical element of wire having contact area  $S$  as it is drawn through a die of half angle  $\alpha$  under mean pressure  $p$  with drawing force  $P_d$  and friction coefficient  $\mu$  from initial area  $A_i$  to final area  $A_f$ . [16]

where  $\sigma_0$  is the effective yield strength (flow stress) of the wire. As the dies used in the drawing schedules had a constant half angle of  $\alpha = 6^\circ$ , for a constant value of friction  $\mu$  (a reasonable assumption since the same type of dies and lubricant were used throughout the drawing schedule), it can be seen that in this case the drawing force is solely a variable of the area reduction ratio and the composite flow stress.

The parameter that is of primary importance for OPIT wire drawing is the area reduction per pass. For composite fabrication two drawing schedules were used, corresponding to 10% and 20% area reductions per pass. For thick walled composites (high Ag:SC ratio), a 20% area reduction schedule could usually be used, as there was a sufficient amount of Ag in the cross section so that the swage tip and/or any wire that had

passed through the die could support the drawing force  $P_d$  required to pull the rest of the wire through the die. Such a schedule could also be used for the first few passes of a thin walled billet containing hand packed powder, as the flow stress of such a composite is relatively low until the powder gets compacted to a high density (i.e. until the interparticle friction reaches a high value). For thinner walled billets containing dense CIP'ed cores, or for hand packed billets with extremely thin walls, a reduction schedule of 10% per pass was needed to draw the wire, as this reduced the drawing force compared to the 20% schedule.

It was also found that some thin walled, dense powder composites were difficult to draw, even using when a 10% area reduction per pass schedule. The most common problem was frequent swage tip breaks; i.e., the wire could not be drawn through the die as the swage tip lacked sufficient strength to withstand the draw force. In such cases decreasing the drawing speed from  $\sim 10$  cm/sec to  $\sim 0.04$  cm/sec (corresponding to time average mean strain rates [16] of  $\sim 15$  s<sup>-1</sup> to  $\sim 0.05$  s<sup>-1</sup> over the wire diameter range where breaks usually occurred) would allow the wire to be drawn successfully. The reason for this effect was not determined, but it is known that the flow stress of metals is a function of the strain rate [16]. For example, Thiagarajan and Varma reported [17] that the yield stress of annealed Cu rod decreased from  $\approx 220$  MPa to  $\approx 150$  MPa when the tensile strain rate was decreased from  $\approx 0.1$  s<sup>-1</sup> to  $\approx 0.001$  s<sup>-1</sup>. Although in our case Ag was used instead of Cu, and noting that tensile tests and wire drawing are substantially different processes, it suggests the possibility that reducing the drawing speed increases wire drawability by reducing the flow stress of the Ag sheath. However, it is possible that deforming the

powder core at lower strain rates also reduces its flow stress, and thus may also contribute to the strain rate sensitivity of the drawability. A second interesting phenomena was also found to sometimes help improve the drawability of thin walled wires: annealing the *entire* wire improved drawability by decreasing swage tip breaks. Although this may seem counterintuitive, it probably can be explained by considerations of the drawing forces and flow stresses. Annealing the wire reduced the flow stress of the Ag, thus reducing the drawing force. Since the swage tip is cold worked before each die pass, it was sufficiently strengthened relative to the rest of the annealed wire to support the reduced drawing force of the annealed wire.

### 2.3.2 Rolling of wire into tape

After a wire was drawn to the desired diameter, it was then rolled into a tape. Rolling both further densifies the powder and aligns the BSCCO grains. The diameter to which a wire is drawn before rolling obviously influences the final tape width, but it also can influence the core packing density and tendency to sausage. Satou et al. [18] have shown that drawing to higher strains before rolling packs the core to higher densities (until a maximum of  $\approx 75\%$  density is reached [13]), and leads to less filament sausageing and higher  $J_c$  values. Similarly, Grasso et al. [19] found that there is an optimum wire diameter before rolling. They reported that drawing a wire having a Ag:SC ratio of  $\approx 1.3:1$  to a diameter of 1 mm before rolling led to a  $J_c$  (77 K, 0 T) of  $30 \text{ kA/cm}^2$ , whereas a wire drawn to 2 mm produced a tape with  $J_c = 22 \text{ kA/cm}^2$ . The standard procedure used for early composites in this thesis work was to draw the wire (which typically had Ag:SC  $\sim$

3:1) to  $\approx 2$  mm before rolling, but after the work of Satou [18] was recognized, wires were drawn to 1.52 mm diameter, and then through a rectangular die of height 1.19 mm and width 1.50 mm before rolling. Giving the wire a slightly rectangular shape in this way made it easier to keep the wire flat as it was rolled (using the wide edge) into a tape.

The important features of the rolling process as they pertain to OPIT tape fabrication are mainly those which control or produce defects in the tape. For example, the roll gap must be perfectly parallel to avoid a thickness gradient across the tape width, which causes curvature or waviness in the tape. Another tape defect which is controlled by the rolling parameters is filament sausaging. It was found that filament sausaging could be minimized by using small reductions in thickness per pass [20]. For example, decreasing the thickness reduction per pass from 20% to 5% reduced the sausaging of a  $\sim 20$   $\mu\text{m}$  thick filament from  $\approx 40\%$  to  $\approx 10\%$ . For this reason, almost all of the composites used for experiments discussed in this thesis were rolled at a nominal 5% thickness reduction per pass. However, it was not easy to precisely control changes in the roll gap with our rolling mill, and thus distributions of thickness reductions like that shown in Figure 2-2 were usually observed.

The mechanics of the rolling process will be described in more detail later in the context of tape thermomechanical processing. The details of rolling will not be addressed further here, except to note that samples were usually rolled without lubrication of the rolls or tape. Slight front and back tensions (supplied by hand) were applied to the tape entering and exiting the rolls. The lubrication state and front and back tensions are just a few of the variables involved in the rolling process. Other potentially important rolling

parameters include the reduction per pass, which was discussed earlier, and the roll diameter. The explicit effect on  $J_c$  of varying any of these parameters in rolled samples was not studied in this work.

## **2.4 Ag-Mg-Ni alloys**

Pure Ag (99.9%) is commonly used as the cladding material for BSCCO tapes because it is chemically compatible with 2223 (actually, it helps to form and stabilize the 2223 phase, as will be discussed in Chapter 3), and because oxygen can diffuse through it very quickly [21,22]. Although the strength of cold worked pure Ag is usually sufficient to withstand the forces involved in OPIT composite fabrication, the Ag becomes very soft after the 2223 formation heat treatments, which are typically given at  $\sim 825^\circ\text{C}$  and are hundreds of hours long. Although this is usually not important for laboratory experiments like most of those described in this thesis, the low strength is an issue for industrial applications like cables and magnets.

One way to increase the strength of the cladding is to use noble metal Ag alloys such as Ag-Au [23,24]. However, although such alloys work harden more than pure Ag, once the tapes are heat treated, their strengthening benefit is mostly lost. A more effective way to increase the post-heat treatment strength is to use oxide dispersion strengthened Ag alloys. As oxygen can diffuse through Ag, the oxide particles are usually formed during heat treatment in an oxygen-rich atmosphere. Many different oxide-forming alloying elements have been studied in the literature, including Al, Cu, Hf, Mg, Mn, Ti, Zr [25,26,27,28,29,30], with Ag-Mg and Ag-Mg-Ni alloys being the most extensively studied.

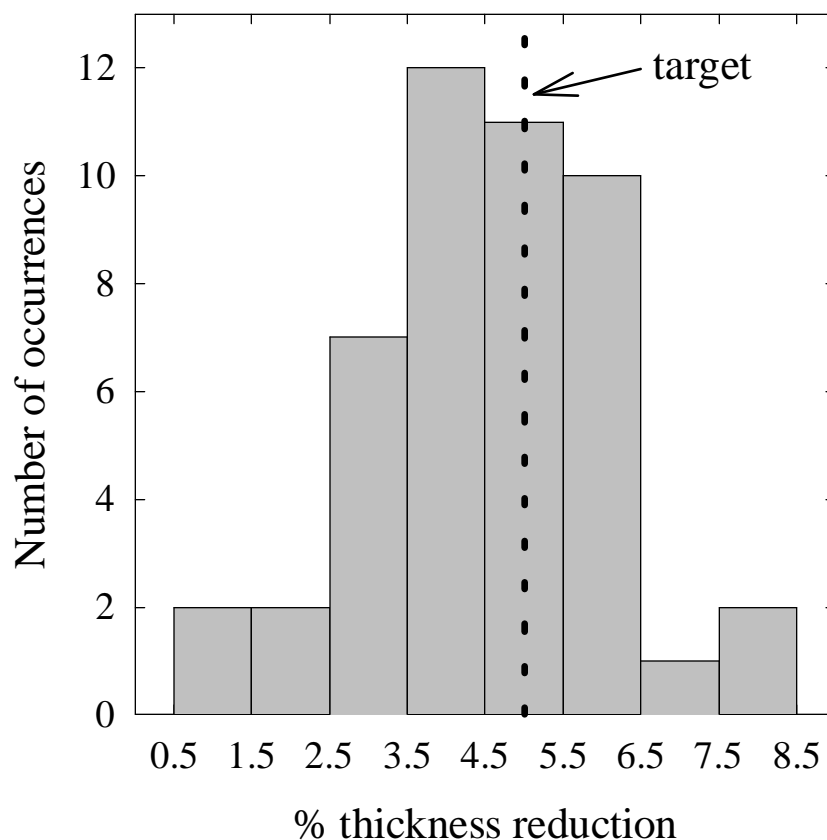


Figure 2-2. Typical thickness reduction distribution obtained when a wire was rolled into a tape with a nominal 5% thickness reduction per pass.

For some experiments Ag-Mg-Ni alloy sheaths were used. The particular alloy was Ag-0.25 wt% Mg-0.25 wt% Ni, sold by Handy and Harmon under the trade name Consil 995. The Mg is intended to form oxide particles for hardening, while the Ni is added as a grain refining agent, but in fact it was found that the Mg and the Ni tended to form a type of Mg-Ni-O particles. To keep Mg and Ni contamination of the 2223 to a minimum, the Consil cans were oxidized *before* powder insertion and metalworking. It was found that a

heat treatment of 42 hours at 800°C in air was sufficient to internally oxidize most cans (i.e. tubes or rods with holes drilled into them). Oxidation of solid rods of diameter 1.47 cm took longer, as only the outer surface of a rod is exposed to the atmosphere. After the oxidation heat treatment, the annealed but dispersion hardened Consil had a Vickers microhardness ( $H_V$ ) of  $\approx 140 \text{ kg/mm}^2$  (10 g, 15 sec.). This compares to a hardness of  $\approx 90 \text{ kg/mm}^2$  for cold worked 99.9% Ag, and  $H_V \approx 40 \text{ kg/mm}^2$  for annealed Ag.

It was possible to draw and roll hardened Consil composites into tape, with the following caveats. Consil wires tended to squeak and make very loud noises as they were drawn, suggesting a higher friction coefficient  $\mu$  between the wire and die than for pure Ag. This friction led to “chatter”, or vibration of the wire, as it was drawn through the die. This problem was alleviated by directing a stream of flowing drawing lubricant into the die exit, as well as the inlet. Occasionally cracks would form in the sheath, particularly in regions of high stress concentration such as plug/tube junctions, but usually such cracks would not lead to wire fracture. Once the wires were drawn to their rolling diameter, such cracked regions were cut away before rolling. Hardened Consil wires tended to develop small cracks during rolling that gradually formed a rough, jagged edge along the entire length of the tape. The formation of these edge cracks was probably due to the lateral spread of the tape and the limited ductility of the hardened Consil. Furthermore, the lateral spread was found to be higher in Consil tapes than for Ag tapes (for example, otherwise identical wires made with Ag and Consil sheaths resulted in tapes 3.22 mm and 3.51 mm wide, respectively [30]). This additional spread exaggerates the tendency for edge cracking [16]. Presumably this edge cracking could be reduced somewhat by

annealing the wire, which would increase its ductility, and/or through optimization of the reduction schedule to reduce inhomogeneous deformation in the thickness direction (which can also cause edge cracking [16]), although this was not explored in this thesis work.

### 3. Formation and stability of the 2223 phase

After an OPIT tape was fabricated, the precursor powder needs to be converted to the 2223 phase. However, converting a multiphase, overall  $(\text{Bi,Pb})_2\text{Sr}_2\text{Ca}_2\text{Cu}_3\text{O}_x$  composition powder into phase-pure BSCCO-2223 in a Ag-clad tape can be a difficult task. Relatively small variations in starting chemistry, reaction temperature, and oxygen partial pressure can move the system into regions in phase space where 2223 formation is not favorable. For example, even in the atmosphere optimum for 2223 formation (oxygen partial pressure  $\approx 0.075$  atm, often referred to as simply 7.5%  $\text{O}_2$ ), the activation energy for 2223 formation,  $E_a^{2223}$ , has been shown to change from  $\sim 2700$  kJ/mol to  $\sim 700$  kJ/mol [31,32] over just a few  $^\circ\text{C}$ . This sharp change in  $E_a^{2223}$  is believed to result from a change from a solid state to a liquid-assisted formation process. As the activation energy for formation of the impurity, or “second” phases in the system is only  $\sim 500$  kJ/mol [33], it is very difficult to form single phase 2223. Since the BSCCO system involves so many components and possible reaction pathways, the initial phase assemblage, in addition to

the overall chemical composition, has a large effect on the post-processing results. Furthermore, some of the components are volatile (e.g. Pb [34]), and therefore the overall composition of the system can shift during processing, resulting in a corresponding shift in the equilibrium (or metastable) phases. Many of the important details of the 2223 phase formation and stability are intertwined, which makes it difficult to separately discuss the individual aspects. In this chapter the main points relevant to tape processing are briefly reviewed.

### ***3.1 Formation mechanism***

At present, the mechanism by which 2223 forms from a largely 2212 and secondary phase powder mixture is a subject of debate. Formation mechanism models are often proposed on the basis of some analysis of the microstructural development during the conversion process, and/or by analysis of the kinetics of the formation reaction. Several mechanisms and reaction pathways for 2223 formation have been put forward, but thus far none have been convincingly proven to be solely responsible for the formation of 2223, and it may be that a combination of processes actually occurs. Most formation models fall into one of two broad categories: formation by intercalation, or by nucleation and growth. Almost all models involve a liquid phase in some capacity. The origins and significance of this liquid phase will be discussed first, followed by a brief review of the literature framed in the context of the intercalation and nucleation and growth models.

### 3.1.1 The importance of Pb, liquid, and the overall cation composition

It was discovered by Sunshine et al. [35] that the partial substitution of Bi by Pb enhances the formation and stability of the 2223 phase. In fact, appreciable amounts of 2223 are generally formed only when some Pb has been added to the mixture. Powders of overall composition  $\text{Bi}_{2-x}\text{Pb}_x\text{Sr}_{-2}\text{Ca}_{-2}\text{Cu}_{-3}\text{O}_y$  with  $0.2 \leq x \leq 0.5$  usually yield the greatest degree of 2223 conversion [36,37,38]. It was also found [37,38,39] that a slight excess of Ca and Cu can be helpful in increasing the rate and the extent to which a powder converts to the 2223 phase. Presumably, these somewhat empirical findings are related to the mechanism(s) by which the 2223 phase is formed.

Uzumaki et al. [40] proposed that a liquid responsible for rapid 2223 formation came from the melting of  $\text{Ca}_2\text{PbO}_4$  at  $\sim 822^\circ\text{C}$  in air. In their study they found that  $\text{Ca}_2\text{PbO}_4$  and 2201 formed below  $750^\circ\text{C}$  in air, and they suggested that 2223 is formed by a reaction between 2212 and  $\text{Ca}^{2+}$  in the liquid formed by the melting of 2201 and  $\text{Ca}_2\text{PbO}_4$ . Ikeda et al. [41] reported that the liquid with the lowest formation temperature ( $825^\circ\text{C}$  in air) was formed not just from  $\text{Ca}_2\text{PbO}_4$ , but from a reaction between 2201 and  $\text{Ca}_2\text{PbO}_4$ . They stated that this liquid wetted both 2201 and 2212, but not 2223 pellets. They proposed that this liquid from  $2201 + \text{Ca}_2\text{PbO}_4$  converts 2212 to Pb-2212, and that Pb-2212 reacts with  $(\text{Ca,Sr})_2\text{CuO}_3$  [2:1 alkaline earth cuprate (AEC)] and another liquid composition to form 2223. Several other researchers have reported similar findings [42,43,44,45,46,47,48,49].

The important role of Pb-2212 was not widely appreciated until Dorris et al. [50,51] demonstrated that introducing the Pb in the form of Pb-doped 2212 instead of as

PbO or  $\text{Ca}_2\text{PbO}_4$  improves the 2223 reaction rate, as well as increases the achievable 2223 phase purity. The introduction of Pb into 2212 changes the crystal structure from tetragonal to orthorhombic [52], which causes the separation of the (200) and (020) X-ray diffraction peaks between  $33^\circ$  and  $34^\circ$   $2\theta$  when Cu-K $\alpha$  radiation is used. Subsequent work by several groups [52,53,54] confirmed that putting the Pb into the 2212 phase is indeed a crucial step in the 2223 reaction. It seems that the final stage of the 2223 formation involves a reaction between Pb-2212 and a calcium cuprate phase. Thus it is not clear that  $\text{Ca}_2\text{PbO}_4$  is desirable after all, because if a large fraction of the Pb is present as  $\text{Ca}_2\text{PbO}_4$ , then the dissociation of  $\text{Ca}_2\text{PbO}_4$  may control the formation of 2223. For example, Koyama et al. [38] and Pierre et al. [55] have shown that the best conversion was obtained for  $x = 0.3-0.4$ , for which excess  $\text{Ca}_2\text{PbO}_4$  growth is avoided.

Because largely  $\text{Ca}_2\text{PbO}_4$  free, Pb-2212 powders react quickly with a high degree of phase purity, it was initially thought that  $\text{Ca}_2\text{PbO}_4$  is not necessary to form a reactive liquid to speed formation of 2223, and that the liquid phase and increased reactivity may instead be a result of the fact that the melting point of 2212 decreases with increasing Ca [39] and Pb content [51]. However, experiments of Grivel et al. [56] and Xu et al. [57] suggest that Pb-2212 is not a stable phase, and that Pb-rich phases such as  $\text{Bi}_{0.5}\text{Pb}_3\text{Ca}_2\text{Sr}_2\text{CuO}_x$  ("3221") and  $(\text{Ca,Sr})_2\text{PbO}_4$  are formed during the heat treatment ramp up. Thus, despite a considerable body of work, there is still some confusion about the role played by Pb-2212,  $\text{Ca}_2\text{PbO}_4$ , and other second phases in the formation of a liquid phase and the 2223 phase.

### 3.1.2 Nucleation and growth

In the context of 2223 processing, “nucleation and growth” is generally used to refer to a process by which new 2223 grains are somehow nucleated on existing 2212 grains, or directly from a liquid phase. Mechanisms such as disproportionation and dissolution-precipitation fall somewhere in between intercalation and nucleation and growth, but here they will be considered as variations of a nucleation and growth process.

Most 2223 formation work in the literature concludes that 2223 is formed by a nucleation and growth process, whereby 2212 reacts with a liquid phase, and new 2223 grains are nucleated either at sites on 2212 grains, or directly from the melt. Many authors have used X-ray diffraction studies of the 2223 conversion kinetics to come to this conclusion. As presented by Kingery et al. [58] and first shown by Avrami [59], an isothermal solid-state conversion process in which the fractional conversion  $f$  versus time curves exhibit sigmoidal behavior can be described by

$$f = 1 - \exp\left[-\frac{4\pi}{3} u^3 \int_0^t I_v (t - \tau)^3 d\tau\right]$$

where  $u$  is the isotropic growth rate per unit area of the interface of spherically-shaped transformed regions,  $I_v$  is the nucleation rate, and  $\tau$  is the nucleation time. An example of the fraction converted data as a function of time for a tape with a relatively small “incubation” period is shown in Figure 3-1. In general, variations in the functions for the nucleation and growth rates lead to expressions of the form

$$f = 1 - \exp(-Kt^n)$$

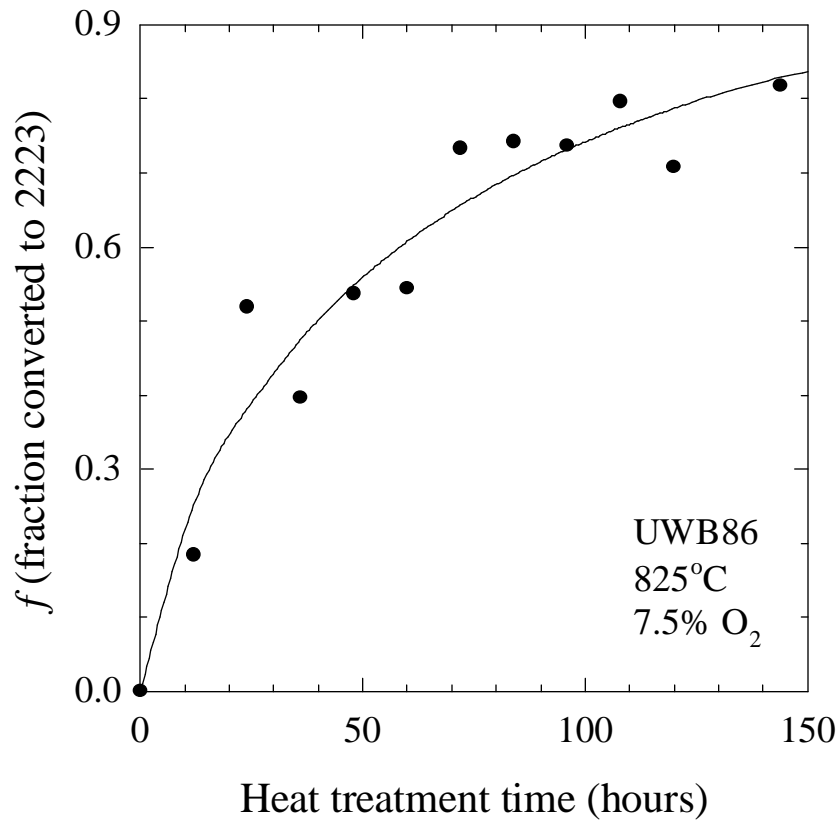


Figure 3-1. Volume fraction of 2223 (measured by X-ray diffraction) as a function of time for composite UWB86 heat treated at 825°C in 7.5% O<sub>2</sub>. [60] This data gives an Avrami exponent  $n$  of 0.73, suggesting that 2223 forms by a two dimensional, diffusion-controlled reaction.

where  $f$  is the fraction converted,  $K$  is a reaction rate constant which depends on the temperature-dependent, nucleation-and-growth rates, and the exponent  $n$  is referred to as the Avrami exponent, which can vary from  $\sim 1$  to 4 [61]. The Avrami exponent  $n$  can be determined from fits of the conversion as a function of time data, and can give some insight into the mechanism of the conversion process, as listed in Table 3-1.

Table 3-1. Values of the Avrami exponent for various formation mechanisms and sites of nucleation

Avrami exponent $n$	Rate-limiting mechanism [67,68]
1	diffusion controlled, two-dimensional
2	nucleation controlled, two dimensional
3	nucleation controlled, three dimensional

Using this type of analysis of the formation kinetics, most studies have found values of  $n$  between 1 [31,32,62,63] and 2 [64,65,66] for the 2223 formation reaction, indicating a two dimensional nucleation and growth process that is limited by either diffusion of material to the growth front, or by the formation of nuclei. The two dimensional growth mechanism is consistent with the observed anisotropic BSCCO grain growth (which is much faster within the ab-plane than in the c-direction) and/or the plate-like nature of the precursor 2212 grains, which confines the formation product (the 2223 phase). The fact that the 2223 conversion process (which involves a liquid) can be described quite well by solid-state formation models may be an indication that the quantity of liquid involved in the reaction is small. On the other hand, the variation of the Avrami exponent reported in the literature may be due to variations in the amount of liquid formed, which may be a result of variations in the complicated phase assemblage in tapes.

Microstructural studies have also been reported which lend support to formation by nucleation and growth process. Hatano et al. [69] suggested that 2223 forms by precipitation from a liquid phase which itself forms from the dissolution of 2212 and other second phases. The basis for this explanation is that a reactive liquid phase is needed to explain the rapid initial 2223 formation and increased density that is observed

experimentally. Thus 2223 precipitation from a liquid is the most likely formation mechanism. Morgan et al. [70] have shown evidence for a solution-precipitation 2223 formation mechanism. In their paper they show SEM micrographs of what appears to be a liquid droplet moving along a 2212 plate, leaving a trail of 2223 in its wake. Recently Grivel et al. [71] have also published microstructural evidence for a nucleation and growth process. SEM examinations of the same regions of a sintered pellet after increasing amounts of thermal treatment revealed that 2212 grains shrank during the heat treatment, while simultaneously new 2223 crystals appeared with their own distinct orientation and morphology. They concluded that 2223 grains were not using 2212 grains as formation templates, and that 2223 was forming by a nucleation and growth process.

There are additional formation models which do not fit entirely under either the nucleation and growth or intercalation umbrellas. They are mentioned here for completeness, although they all have less support in the literature. As they both involve precipitation of a phase from a liquid, they are included in this nucleation and growth section.

A formation mechanism called disproportionation refers to a cyclic process in which 2212 decomposes into 2223 and 2201, the new 2201 reacts with a liquid to form new precipitates of 2212, which in turn leads to more 2223, and so on [37,72,73,74]:

- (1)  $2(2212) \rightarrow 2223 + 2201$
- (2) 2201 melts into Pb-rich liquid flux
- (3) new 2212 grains nucleate and precipitate from the melt
- (4)  $2(2212) \rightarrow 2223 + 2201$  [back to step (1)]

This process repeats until the supply of 2212 is exhausted. Note that this mechanism should always result in a residue of 2201 at the end of the reaction. Since this is not usually the case, disproportionation is not well supported experimentally.

Another process, known as dissolution-precipitation, is similar to disproportionation. In this model [44,75],  $\text{Ca}_2\text{PbO}_4$  melts incongruently to form a liquid and CaO. Then CuO and CaO react with and are dissolved into the liquid. The 2212 grains are then melted, and new 2201 grains are precipitated from the melt. The 2201 grains react with Ca and Cu ions in the liquid to form the 2223 phase.

Thus, although there still is some disagreement between the exact details of the process, there is a wide body of evidence that suggests 2223 forms via a nucleation and growth process which involves precipitation of the 2223 grains from a reaction between a Pb-rich liquid phase and 2212. However, there is also ample evidence that intercalation also plays a role in 2223 formation, as is discussed next.

### 3.1.3 Intercalation

“Intercalation” refers to a process where 2212 grains are directly transformed into 2223 platelets via the insertion of additional Ca/Cu-O layers. In contrast to nucleation and growth proponents, which use kinetic analysis as the primary support with microstructural studies as secondary evidence, supporters of intercalation have the opposite situation; most intercalation evidence comes from TEM studies, with few reports of kinetic analysis confirmation.

Ikeda et al. [76] suggested that 2212 converts to 2223 by an intercalation mechanism, in which additional Ca and Cu diffuse into the structure and convert 2212 to 2223, layer by layer. The basis of this hypothesis came from a TEM study, in which it was observed that the superconducting grains often consisted of a banded structure of 2212 and 2223 intergrowths. A 2223 formation study at Wisconsin [77] has provided evidence that seems to support this intercalation formation mechanism. In this study, TEM micrographs show what appears to be an intercalation growth front, where it appears that a 2212 grain is undergoing the layer-by-layer transformation to 2223. Bian et al. [78] have published similar TEM results, and go a step further to claim that 2212 actually converts via intercalation to an complex intermediate phase denoted as 4435 (alternating layers of 2212 and 2223) before complete conversion to 2223.

To provide a more stable foundation for the intercalation model, Cai et al. [79] developed a theory to explain the kinetics of such an ion-diffusion controlled intercalation mechanism. Their model considers the cylindrical “void” that results from the edge dislocation-like feature caused by the insertion of a Ca/CuO plane at the 2212/2223 interface to be a short-circuit channel for fast ion diffusion. The 2223 formation rate is then controlled by one-dimensional diffusion down this dislocation “pipe”, the cations being supplied from a reactive liquid at the edges of the grain. Their model results in an Avrami exponent between 0.5 and 1.5, consistent with most of the published values.

Kinetic and microstructural support for 2223 formation by intercalation has been published recently by Wang et al. [80]. In their study, they used a transmission X-ray technique (using high intensity X-rays supplied by a synchrotron) to probe both the texture

and phase assemblage of the entire thickness of a tape, and used TEM for microstructural investigation. Their study revealed that before any 2223 formation was observed, the texture of the precursor 2212 grains was strongly increased, and that this resultant texture was the same as that of the 2223 that was later formed. They proposed a two-step process for the formation of aligned 2223 grains in a Ag-clad tape: during the ramp up and early stages of heat treatment (during the so-called “incubation” period before 2223 formation), 2212 grains are partially dissolved and then regrown [57,81] with a greater texture, and then the 2223 grains are formed by intercalation from the 2212 grains. This hypothesis is attractive because it can explain many of the phenomena that authors have used to reach differing conclusions, including the fact the conversion process involves a liquid phase, that 2223 forms with texture greater than that of the as-rolled precursor 2212 [82,83,84], and that 2223 grains with 2212 intergrowths are commonly observed [76,77,78,85,86,87,88].

### ***3.2 Role of Ag and the Ag cladding***

The details of 2223 phase formation described above generally apply to both bulk 2223 and tapes. However, it has been found that it is much easier to form high purity 2223 in Ag-clad tapes. Of many feasible metallic sheathing materials, pure Ag has been found to be the most chemically compatible with BSCCO [30,89]. Ag also has the fortuitous dual properties of remaining noble during heating in oxygen-containing atmospheres, while at the same time the diffusion of oxygen through the metal is very fast

Table 3-2. Literature summary of the effect of Ag additions on the temperature of partial melting of 2223 precursor powder

Atmosphere	$T_m^{partial}$ of undoped or bare powder	Amount of Ag added to powder	$T_m^{partial}$ with Ag addition or in Ag-clad tape	Reference
air	847°C	5 wt%	836°C	[92]
air	850°C	various	840°C	[93]
air	837°C	various	828°C	[94]
air	856°C	Ag clad tape	829°C	[95]
7.5% O <sub>2</sub>	820°C	5 wt%	805°C	[96]
7.0% O <sub>2</sub>	820°C	10 wt%	800°C	[97]

[90,91]. These are required properties for BSCCO tapes, which are heat treated for many hours at high temperatures in oxygen-containing environments.

There have been many studies of the effects of Ag on 2223 formation. The most common conclusions are that the addition of Ag results in a lowered precursor (partial) melting point  $T_m^{partial}$ , and accelerated 2223 formation. The reported effects of Ag additions (or the simply the effect of the Ag sheath) on the melting point of 2223 (which is also dependent on the heat treatment atmosphere) are summarized in Table 3-2.

Although there have been many reports of Ag lowering the melting point of 2223 precursors, there have been fewer studies of the actual mechanism of this effect. Dou et al. proposed that the addition of Ag causes the formation of a Ag-PbO-CuO low melting point eutectic liquid [98,99], which lowers the melting point of the Ag/2223 system and accelerates 2223 formation. McCallum et al. [100] studied the pseudobinary Ag/BSCCO-2212 phase diagram, and found an oxide-rich eutectic at  $\leq 4$  at% Ag which lowered the

melting point of 2212 by 30°C. A Ag/oxide eutectic may explain the results of several authors who found that 2223 tended to form first near the Ag interface [101,102,103]. It may take longer for the material in the central portions of a tape to convert to 2223 because Ag needs to diffuse into the core to form the low melting point eutectic; Ag tracer diffusion data from Fang et al. [104] have shown that diffusion through a typical ~ 100 µm BSCCO core at ~ 800°C takes a few hours. Also, Parrella et al. [105] and Sung and Hellstrom [96] have shown that mixing a small amount (~ 1 wt%) of Ag into the powder helps to evenly distribute liquid in the core, and leads to more homogeneous microstructures. However, the exact role of Ag still remains somewhat unclear. Indeed, several groups have reported finding no evidence of a reaction with Ag (i.e. Ag is inert), and that Ag does not enter the 2223 crystal structure, or that it can actually be detrimental to 2223 formation [96,98,106,107].

In addition to directly contributing chemically to the formation of 2223, the Ag sheath also helps 2223 phase formation by reducing the evaporation of Pb (and perhaps Bi) from the powder. Luo et al. [34] have shown that the Ag cladding effectively prevents evaporative Pb loss under typical heat treatment conditions. However, if the ends of a tape are just cut and left open during heat treatment, material can leave through the open ends. Evidence for this was witnessed in the form of the whitish/yellowish film that formed on the inside of the furnace work tubes that were used to heat treat samples. Recently, Thurston et al. [108] have shown that the conversion to 2223 is hindered in a ~ 2 mm long region near the open ends of a tape, confirming a composition change (Pb loss).

The Ag sheath of a tape also plays a role in the 2223 grain texture development. As 2223 often grows first along the Ag interface [101,102,103], a smooth interface will result in better textured 2223 than one that is irregular or jagged. Additionally, the Ag provides a geometrical constraint on the 2223 grain growth, and this also leads to some texturing [82,84]. The texturing benefit of the Ag sheath increases as the filament thickness decreases [108], because the fraction of the BSCCO core in close proximity to Ag increases.

### ***3.3 The stability of 2223 as a function of temperature and oxygen partial pressure***

A significant aspect of the thermomechanical processing of 2223 tapes is the understanding of the conditions under which the 2223 phase will form and remain stable. In addition to the overall cation composition and the effects of Pb and Ag discussed above, the temperature and oxygen partial pressure ( $pO_2$ ) of the heat treatments have considerable influence on 2223 processing.

Although most of the reported work on 2223 has been done in air, there have been a number of studies that examined the effect of the processing atmosphere on the formation of 2223, with sometimes conflicting results. For example, some groups reported that 2223 forms in nitrogen [109,110], while others showed that 2223 was unstable and decomposed when heated in nitrogen [111,112]; Jao et al. [113] reported substantial 2223 formation in oxygen, but Endo et al. [114] reported that 2223 did not form when  $pO_2 > 0.21$  atm, and claimed that  $pO_2 \approx 0.075$  atm (7.5%  $O_2$ ) was best. Rubin et al. [115]

examined the stability of the Pb-free Bi-2223 phase over a wide range of temperatures and oxygen partial pressures, and found that at low  $pO_2$  values, Bi-2223 decomposed to 2212 and other secondary non-superconducting phases. They reported that this decomposition reaction was not reversible. MacManus-Driscoll et al. [53] and Daümling et al. [116] have extended the work of Rubin et al. by performing similar experiments on Pb-doped 2223, and found similar results. Figure 3-2 is a 2223 stability diagram for temperatures from 650°C to 900°C, over 6 decades of  $pO_2$  values, using data taken from references [53,114,115,116]. The 2223 phase is stable (the shaded region) over a narrow range of temperatures and partial pressures. Zhu et al. [111] reported that the optimum 2223 formation conditions were  $0.01 \leq pO_2 \leq 0.35$  atm at  $820^\circ\text{C} \leq T \leq 880^\circ\text{C}$ , and that the single phase 2223 stability range is  $pO_2 \leq 0.5$  atm. They describe the influence of  $pO_2$  in terms of the valence state of the Pb ions; because the Pb in  $\text{Ca}_2\text{PbO}_4$  is  $\text{Pb}^{4+}$  and is reduced to  $\text{Pb}^{2+}$  in BSCCO, oxygen must be released. Thus, high oxygen partial pressures favor the formation of  $\text{Ca}_2\text{PbO}_4$  instead of 2223, while at lower  $pO_2$  values, the decomposition of the  $\text{Ca}_2\text{PbO}_4$  phase is favored. Work at Wisconsin [33] has confirmed that  $pO_2 \approx 0.075$  atm gives a wider 2223 temperature formation range than  $pO_2 = 0.21$  atm, and so  $pO_2 \approx 0.075$  atm has been used almost exclusively for the past four years for BSCCO tape processing.

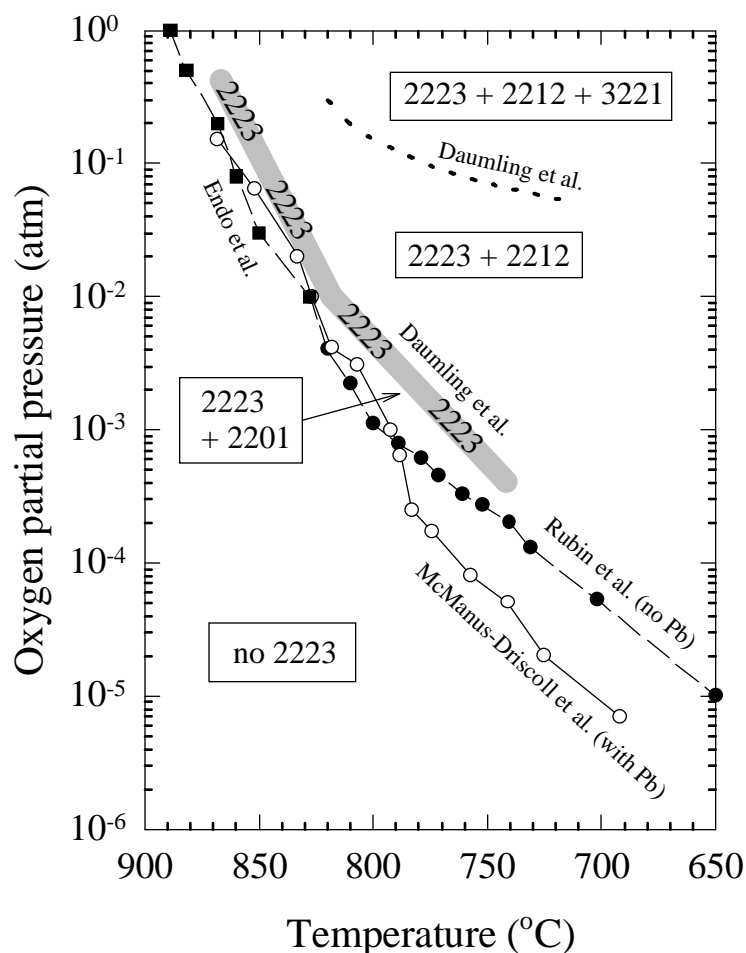


Figure 3-2. Stability diagram for BSCCO-2223 with data from references [53,114,115,116]. All phase fields also contain at least a small amount of various alkaline earth cuprate phases, not shown for clarity.

Several groups have examined in more detail the temperature dependence of the stability of (Bi,Pb)-2223 at a constant  $pO_2 \approx 0.075$  atm, and have found that the 2223 phase is stable between  $\sim 800^\circ\text{C}$  and  $830^\circ\text{C}$  [111,117,118]. At temperatures  $\leq 800^\circ\text{C}$ , they found that 2223 decomposes to 2212 and other non-superconducting phases, and that

2223 partially melts to 2201 and other non-superconducting phases at temperatures  $\geq 840^\circ\text{C}$ . Experiments done for this thesis on samples cooled slowly after the reaction heat treatment also indicate that 2223 is unstable and decomposes to 2212, 3221,  $\text{Ca}_2\text{PbO}_4$ , and other non-superconducting phases at lower temperatures [119].

In summary, despite a large amount of research, many details of the 2223 phase remain unclear. In general it can be said that 2223 forms via a reaction between 2212 and secondary phases, and is assisted by a small volume fraction of a Pb-rich liquid phase. The 2223 phase seems to form via a combined nucleation and growth and intercalation mechanism. In 7.5%  $\text{O}_2$ , which is the atmosphere which gives the widest temperature stability window, 2223 phase starts to form at  $\sim 800^\circ\text{C}$ , and is stable up to about  $830^\circ\text{C}$ . Many of the details of the conversion process vary from tape to tape, probably because of small and unintentional variations in the precursor powder composition or phase assemblage.

## 4. Thermomechanical processing

In the previous chapter some of the details of the precursor to 2223 conversion process were discussed in terms of the phase relations in the system. In this chapter details are given on how tapes were thermomechanically processed. Results from the literature are also reviewed. Some of the processing details and their effects are parts of experiments described in subsequent chapters, and so they are not discussed fully here.

A cyclic process of reaction heat treatment, mechanical deformation, and subsequent heat treatment is used to convert the precursor powders to (relatively) high density, well aligned, high phase purity 2223. The heat treatments are needed to form the 2223 phase, and the mechanical deformation steps are needed to densify and align the 2223, and to help break up the sintered structure to accelerate conversion to 2223. The process is illustrated in Figure 4-1.

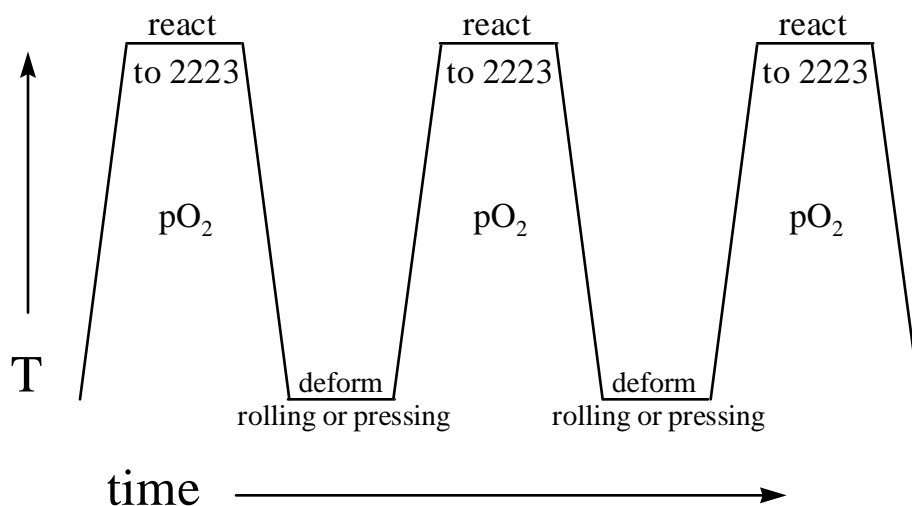


Figure 4-1. Schematic of the cyclical thermomechanical process of heat treatment, mechanical deformation, and heat treatment used to make BSCCO-2223 tapes. The heat treatments form the 2223 phase, and the deformation steps densify and align the grains, and break up the sintered structure to accelerate 2223 conversion.

#### 4.1 Heat treatments

It is commonly observed that changing the heat treatment temperature by as little as  $1^{\circ}\text{C}$  can have a significant effect on  $J_c$ . This is a result of the narrow 2223 formation temperature window, and the low levels of liquid that are involved in the conversion process. Most of the heat treatments in this work were done in low thermal mass furnaces with gold radiation shields, using quartz work tubes and Type K control thermocouples. Typically, the furnaces had zones uniform to  $\pm 1^{\circ}\text{C}$  over lengths of 5-8 cm, which dictated

the maximum straight tape length which could be processed. The temperature within the uniform zone of each furnace was calibrated against a Type S Pt/Pt-Rh probe and electronic ice point couple. This pair was used as an interfurnace standard and as an absolute measure of temperature. However, even with this method of furnace calibration, the measurement and control of the temperature of a furnace to a precision better than  $\pm 1\text{-}2^\circ\text{C}$  is extremely difficult. For this reason, it was not uncommon to be unable to reproduce results from furnace to furnace. Because of this problem, whenever possible, samples made for a given experiment reported here were produced in the same furnace, and at the same time.

Straight sections of tape were sandwiched between porous cordierite wafers and tied with nichrome wire. Cordierite wafers appear inert with respect to the Ag cladding, and their porous structure allowed uniform exposure of the tape surface to the reaction atmosphere. A flowing reaction atmosphere, usually 7.5%  $\text{O}_2$ /balance  $\text{N}_2$ , was supplied by gas cylinders from Liquid Carbonic Co. or AGA Gas Co. While a nominal oxygen content of 7.5% was desired, typically the actual oxygen content ranged from 7.35 to 7.80%.

## ***4.2 Intermediate deformation steps***

Between heat treatments, tape samples were mechanically deformed by either uniaxial pressing or cold rolling. Deformation steps are needed to develop a high quality microstructure and high  $J_c$  values, as will be shown in subsequent chapters. Depending on the experiment, tapes were either reduced to a certain thickness, or pressed at a certain

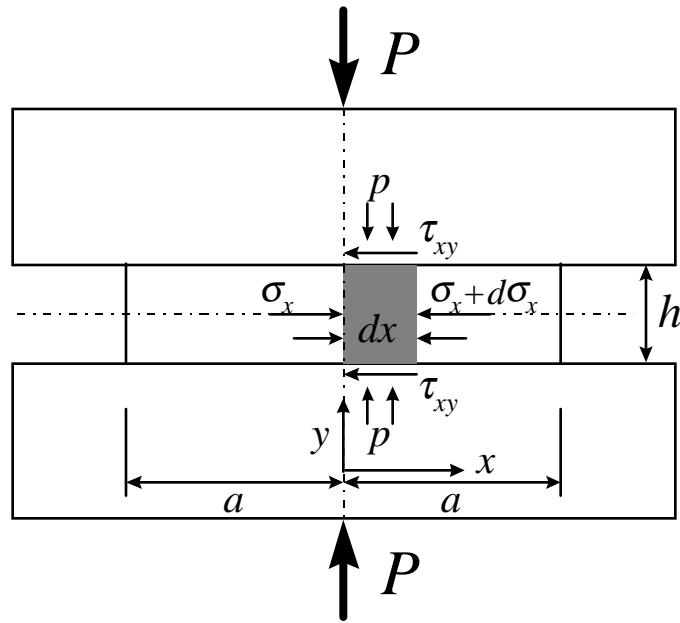


Figure 4-2. Stresses which act on an element  $dx$  of a plate of thickness  $h$  and width  $2a$  forged in plane strain conditions (in the  $xy$  plane) between flat platens with load  $P$ . The length of the sample is into the page in the  $z$  direction. An analogous stress balance is realized along the length of the sample.

pressure. It will be shown later that whether a tape is pressed or rolled, and the parameters used for doing so, has a large influence on the critical current density.

#### 4.2.1 Mechanics of uniaxial pressing

Samples were usually uniaxially pressed between polished WC cermet cutting tool blanks, with glycerin used as a lubricant. If the experiment called for a controlled reduction in thickness instead of a fixed pressing pressure, brass or stainless steel shim stock was used to limit the thickness to which the tapes were compressed. The use of WC

platens allowed tapes to be pressed thinner and more evenly than was possible with tool steel platens, which were also sometimes used. A possible explanation for this result can be found from consideration of the pressing mechanics.

The process of uniaxially pressing between two flat platens is known as open-die forging [16], as the workpiece (the tape in this case) is free to spread laterally between the platen surfaces. Figure 4-2 shows the stresses which act on a long sample (i.e. plane strain situation in the *transverse* tape plane) of thickness  $h$  as it is pressed with load  $P$  between two flat platens. Frictional shear stresses  $\tau_{xy} = \mu p$ , where  $\mu$  is the friction coefficient and  $p$  forging pressure, develop at the platen surfaces to oppose the flow of material away from the centerline. This friction causes a force imbalance in the  $x$  direction (i.e. along the tape width) which results a change of the lateral stress  $\sigma_x$  from one side of the element  $dx$  to the other. This leads to a friction hill, and causes both the lateral stress and forging pressure to vary across the sample width of  $2a$ . As shown in [16], the pressure is given by

$$p = \sigma'_0 \exp\left[\frac{2\mu}{h}(a - x)\right]$$

where  $\sigma'_0$  is the plane strain yield stress of the workpiece. The pressure is greatest along the centerline of the sample, at  $x = 0$ , and is distributed across the sample width (as well as the length) as shown in Figure 4-3. The mean forging pressure is given by [16]

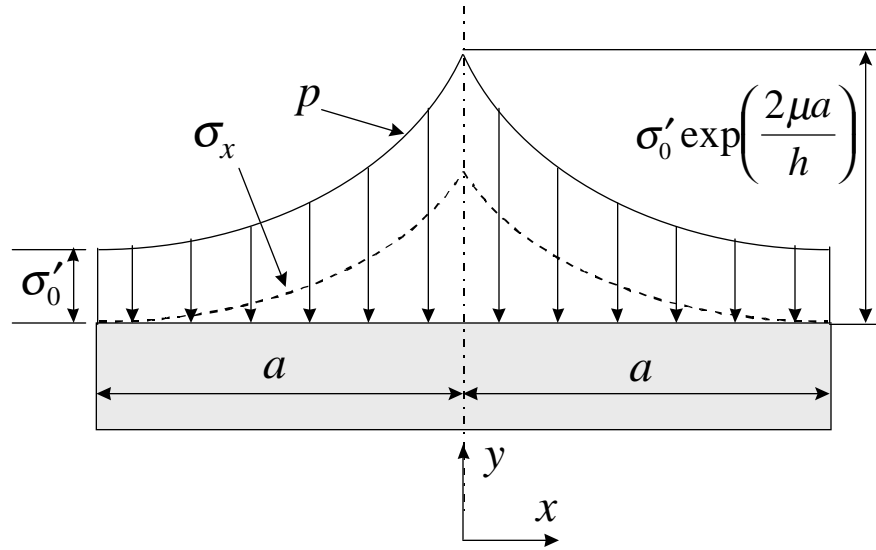


Figure 4-3. Distribution of the normal pressure  $p$  and the lateral pressure  $\sigma_x$  for uniaxial compression between flat plates.

$$\bar{p} = \int_0^a \frac{p dx}{a} = \sigma'_0 \frac{\exp(2\mu a / h) - 1}{2\mu a / h}$$

and thus the pressure required to compress a sample increases rapidly with the ratio of the sample width to thickness ( $2a/h$ ), and decreases when the friction  $\mu$  is decreased. For this reason, the use of a lubricant (glycerin in this case) reduces the friction  $\mu$  between the tape and the platens, lowering the pressing pressure (load) needed to deform the sample.

A possible reason why samples can be pressed thinner and more uniformly (i.e. with “dog-boning”) with WC platens than with tool steel can be also be proposed from a consideration of the forces involved in pressing. For a typical tape with a width to thickness ratio  $2a/h$  of  $\geq 20$ , and taking  $\mu$  to be as low as  $\sim 0.1$  [16], the peak pressing pressure is of the order of  $10\sigma'_0$ . The high pressures involved with pressing cause the

platens to deform elastically (bend) around the tape, especially when the platen is much longer than the tape (i.e. when the restoring force supplied by the tape does not reach the ends of the platens), and when the pressing load  $P$  is applied nominally uniformly along the length of the platen. These conditions were often realized, as the samples were at most  $\sim 8$  cm long, more typically  $\sim 6$  cm, and the platens were  $\sim 10$  cm in length so as to be useful to press a wide range of sample sizes. At a sufficiently high pressure and/or small sample thickness, the ends of the platens are thus forced closer together than at the center, resulting in tapes that are thinner and wider at the ends than at the center, being thus shaped like a dog bone. As WC cermets have a modulus of elasticity ( $\sim 450$  GPa) approximately twice that of tool steel ( $\sim 200$  GPa), they should have a lesser tendency than tool steel platens to bend in response to the pressing forces, and this was found to be the case experimentally.

#### 4.2.2 Mechanics of cold rolling

In contrast to uniaxial pressing, in which an essentially plane strain condition occurs in the transverse tape plane (i.e. pressed samples get thinner and wider, but not appreciably longer), near plane-strain conditions are developed in the longitudinal plane in rolling process (i.e. rolled samples get thinner and longer, but not appreciably wider).

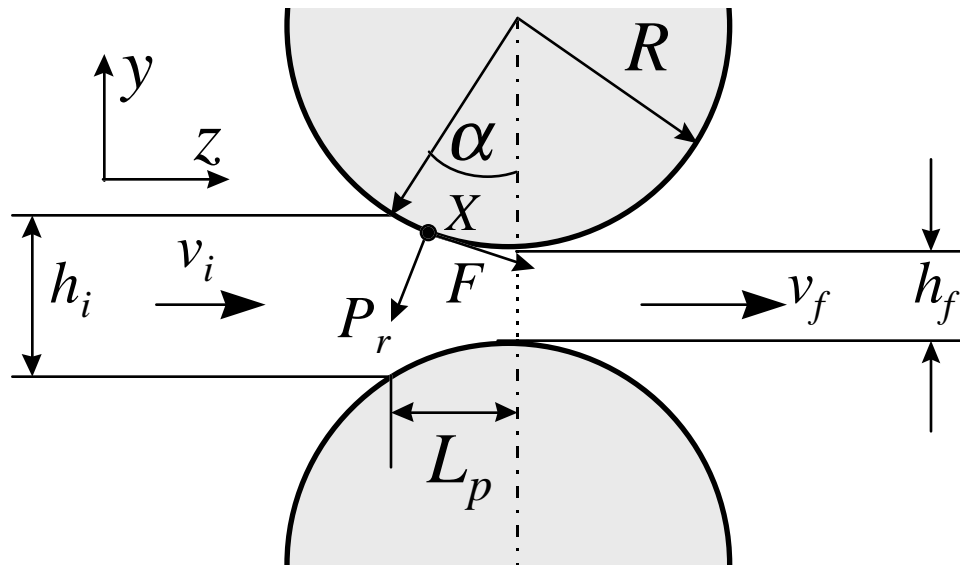


Figure 4-4. Forces acting during rolling a sheet from thickness  $h_i$  to  $h_f$  through rolls of radius  $R$  at initial velocity  $v_i$  with an angle of bite  $\alpha$ . The deformation is essentially plane strain in the  $yz$  plane (the  $x$  direction is along the width of the sheet, into the page).

The basic forces involved in rolling are shown in Figure 4-4, adapted from reference [16]. At any point such as  $X$  along the arc of contact, two forces act on a tape: the radial force  $P_r$  which reduces the tape thickness, and the frictional force  $F$  (equal to  $\mu P_r$ , where  $\mu$  is the coefficient of friction) which draws the tape into the rolls. The vertical component of  $P_r$  is known as the rolling load or separation force  $P$ , as it is the force acting to push the rolls apart. The specific roll pressure  $p$  is given by the rolling load divided by the contact area. The contact area is equal to the product of the tape width  $2a$  and the projected arc of contact  $L_p$ , which is given by [16]:

$$L_p = \left[ R(h_i - h_f) - \frac{(h_i - h_f)^2}{4} \right]^{1/2} \approx \left[ R(h_i - h_f) \right]^{1/2}.$$

Thus, the effective pressure applied to the tape by the rolls is

$$p = \frac{P}{2a\sqrt{R}} * \frac{1}{\sqrt{h_i - h_f}}.$$

The rolling load  $P$  can be approximated by [16]

$$P = \frac{2}{\sqrt{3}} \bar{\sigma}_0 \left[ \frac{1}{Q} (e^Q - 1)(2a)\sqrt{R(h_i - h_f)} \right]$$

where  $Q = 2\mu L_p / (h_i + h_f)$ .

As the roll radius  $R$  was fixed at 3.81 cm for these experiments, and the tape width  $2a$  near the end of the rolling sequence was consistently  $\approx 3$  mm, the rolling force (and therefore the pressure) was determined mainly by the thickness reduction  $h_i - h_f$ . The effect of the rolling pressure employed on *green* tapes (those which have not been reacted to 2223) on the final superconducting properties has not been considered in the literature, but it has been shown that large thickness reductions result in wider tapes (more width strain) than those made with smaller reductions per pass [120]. However, studies of the effect of the rolling parameters used when rolling *reacted* tapes between heat treatments have been reported [19], and show considerable influence the superconducting properties. Some of the reasons for this are described in the next section and in Chapter 7.

### 4.2.3 Cracking behavior

The pressing and rolling procedures described above have one important feature in common: both are used to plastically deform tape samples between heat treatments, significantly changing the thickness (typically by ~ 10% or more at each pass) and one other dimension of the tape. As the Ag cladding is a ductile metal, this large deformation can be easily accommodated. However, BSCCO-2223 is not significantly ductile (at least at room temperature), and the large deformations cause cracks in the core. As will be illustrated in upcoming chapters, some effects of deformation are very beneficial to 2223 tapes; the deformation steps increase the density (and perhaps the alignment) of the oxide grains, and they break up the sintered structure, increasing the reaction rate of the precursor powder to the 2223 phase. However, it will also be shown that cracks formed in the deformation process can remain in the core after the subsequent heat treatment, clearly an undesirable situation when one strives to make full use of the superconductor cross section of a tape.

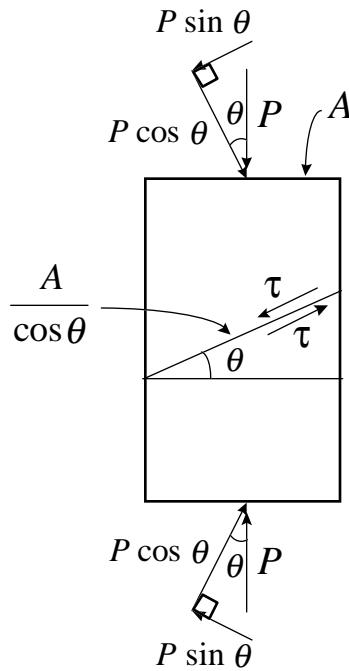


Figure 4-5. Resolved shear stresses  $\tau$  which develop in a material under a compressive stress  $P/A$  [121]. The shear stress is largest for  $\theta = 45^\circ$ .

Although rolling and pressing can both be thought of ideally as plane strain deformation processes, the crack structure formed by each is significantly different. For both processes, the compressive force supplied by either the platens or rolls acts principally to decrease the thickness of the tape. The compressive stress  $P/A$  creates shear stresses  $\tau$  on planes in the material that are at an angle to the direction compressive stress, as shown in Figure 4-5. The resolved shearing force  $P \sin \theta$  acts on the area  $A / \cos \theta$ , and thus the value of the shear stress  $\tau$  is given by

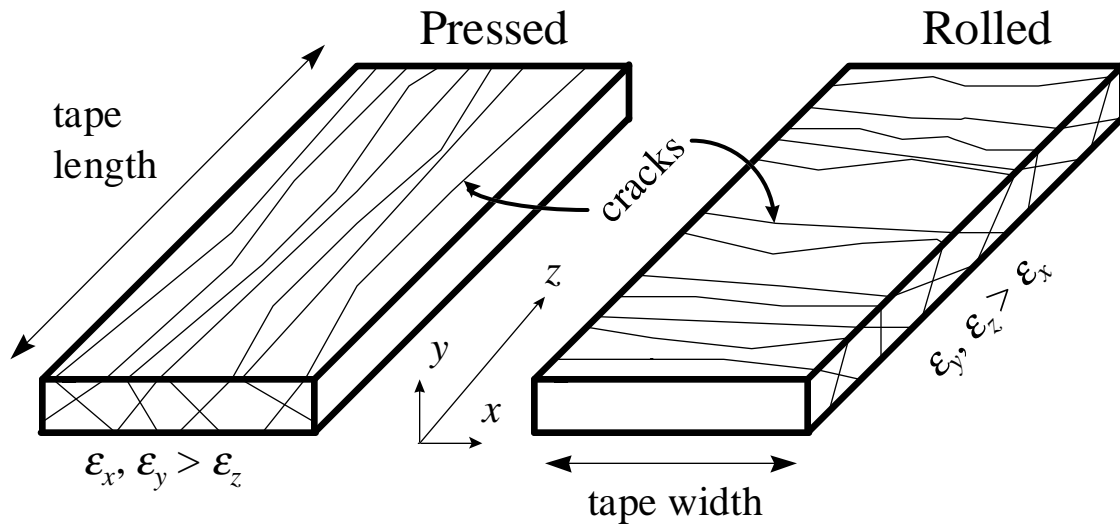


Figure 4-6. Characteristic cracking patterns formed in segments of pressed and rolled 2223 tape. The different orientations of the planes under plane strain result in cracks which run predominantly along the tape axis (parallel to the direction of current flow) in pressed tapes, and transverse to the long tape axis (and current flow) in rolled samples.

$$\tau = \frac{P \sin \theta}{A / \cos \theta} = \frac{P}{A} \sin \theta \cos \theta .$$

The shear stress is therefore maximized for  $\theta = 45^\circ$ , and thus the material under compression will tend to slip (if it is ductile) or fracture (if it is not) on planes at or close to  $45^\circ$  to the compressive stress. Thus, for both pressed and rolled tapes, cracks are formed preferentially at angles  $\sim 45^\circ$  to the direction of compression.

Since the plane strain conditions in pressing and rolling are different by  $90^\circ$  (plane strain in the  $xy$  plane for pressing, and the  $yz$  plane for rolling, as shown in Figure 4-2 and Figure 4-4), the characteristic crack structure formed by the two methods is also rotated

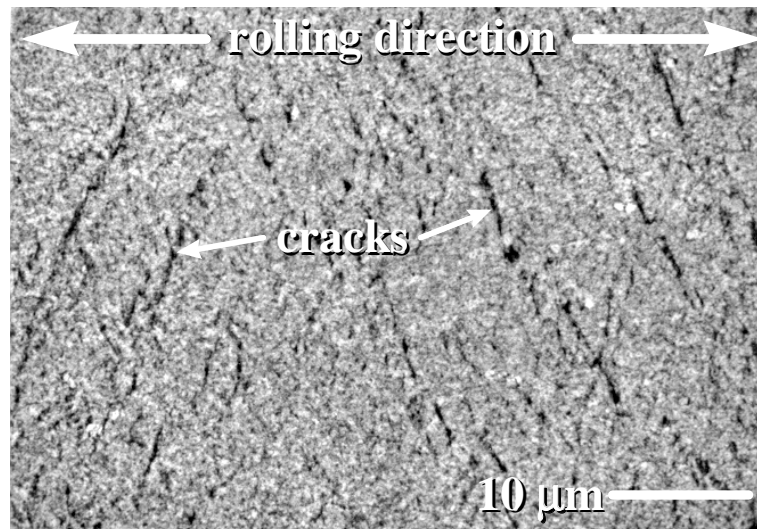


Figure 4-7. SEM micrograph of a longitudinal section (the  $yz$  plane) of a rolled powder core. Cracks oriented at  $\sim 45^\circ$  to the rolling direction are visible.

by  $90^\circ$  [120]. This means that cracks formed in pressed samples tend to be oriented along the  $z$  direction (parallel to the long tape axis), and those in rolled samples run in the  $x$  direction (transverse to the tape axis). The resulting cracking patterns are shown schematically in Figure 4-6, and a real example of cracks in rolled tapes is shown in Figure 4-7. As will be shown in Chapter 7, this fundamental difference in the orientation of the defects formed in rolled and pressed samples is very important in determining the critical current density in 2223 tapes.

## **5. The relationship between microhardness, density, connectivity, and $J_c$**

The material in this chapter is part of the publication:

J.A. Parrell, S.E. Dorris, and D.C. Larbalestier, “On the role of Vickers and Knoop microhardness as a guide to developing high critical current density Ag-clad BSCCO-2223 tapes”, *Physica C* 231 (1994) 137.

### ***5.1 Introduction***

As described in Chapter 4, Ag-clad 2223 tapes made by the OPIT process must be given precisely controlled thermal and deformation treatments in order to convert their precursor powder to the high- $T_c$  BSCCO-2223 phase. The best microstructures and highest critical current density values are obtained when the tapes are given multiple (typically 2-4) heat treatments for relatively long cumulative times (perhaps hundreds of hours) at a temperature slightly above that at which some melting of the precursor powder

occurs. The mechanical deformation step [122,123] between heat treatments is a vital part of the process. At the time of this study the role of the deformation step was not well understood; potential benefits of this intermediate deformation were hypothesized to include an improved reaction rate during the subsequent heat treatment, an increased density, and an improved grain alignment of the superconducting phase.

As discussed in Chapter 3, it is generally believed that BSCCO-2223 forms by a reaction between a eutectic liquid phase and the BSCCO-2212 phase [31,43,46,41,96,101,124]. Implicit in the efficacy of the deformation step is the belief that the cracks which form in the BSCCO core as a result of the mechanical deformation [120,125] will sinter shut during the subsequent heat treatment. However, microslice and other experiments led Larbalestier et al. [126,127] to explicitly question whether this assumption is always true, proposing that microcracks (microcracks are defined as those which are localized between grains or blocks of grains rather than those which have propagated through a significant fraction of the entire core thickness) are one of the major current-limiting mechanisms in BSCCO-2223 tapes. However, it is very difficult to determine the extent of microcracking in reacted BSCCO composites, and this conclusion was only inferred from local measurements of the variability of  $J_c$ .

Yamada et al. [25] and Satou et al. [18] found a strong correlation between the Vickers hardness of the *unreacted* powder core and the after-heat-treatment  $J_c$  in Ag-clad BSCCO-2223 tapes. They reasoned that the resistance to indentation (the definition of hardness) of the core would increase as the powder in the core densified during wire and tape fabrication. Because of the difficulty of directly measuring the density of the thin

BSCCO cores (these were 40-100  $\mu\text{m}$  thick), Vickers microhardness ( $H_V$ ) was used to infer the relative density changes which occurred during the fabrication of the tapes. This increased density prior to the reaction heat treatments was postulated to result in reacted BSCCO-2223 cores of higher density, which correlated directly to higher  $J_c$  values.

The goal of this study was to investigate the importance of the length of the first two heat treatment steps as a test of the following hypothesis: If a liquid phase controls the 2212 to 2223 phase conversion and if this liquid phase is consumed during the phase conversion reactions which occur during heat treatment, then it should get progressively more difficult to heal the cracking produced in the deformation steps between the heat treatments. Indeed, a BSCCO-2223 composition powder should exhaust its liquid in the later stages of reaction. Since any cracks formed during the deformation step must be healed if the  $J_c$  is not to be degraded below its potential, control of the thermomechanical processing during the later stages becomes rather critical. There is certainly a marked tendency for there to be a greater variability in superconducting properties with increasing numbers of deformation steps and heat treatments [30,123,128]. Although long heat treatments may still be necessary after the 2223 conversion is essentially complete (for example, to remove residual 2212 layers at the grain boundaries [85,86]), it may be that all the mechanical deformation steps used to densify and align the core should be given while sufficient amounts of liquid-forming phases remain to heal deformation damage. This chapter provides experimental data addressing this hypothesis, under the assumption that a low density and/or cracked core will provide a lesser resistance to indentation than a dense, well-connected core.

## 5.2 Experimental Details

BSCCO-2223 powder made by a "two-powder" process ( $\text{Bi}_{1.8}\text{Pb}_{0.4}\text{Sr}_2\text{Ca}_1\text{Cu}_2\text{O}_x$  and  $\text{CaCuO}_2$  powders were combined to give a powder having the overall composition of  $\text{Bi}_{1.8}\text{Pb}_{0.4}\text{Sr}_2\text{Ca}_2\text{Cu}_3\text{O}_x$ ) was packed into a Ag tube, closed shut, and swaged, drawn, and rolled to a tape  $\sim 0.25$  mm thick. At this point the BSCCO core thickness was  $\sim 100$   $\mu\text{m}$ . Twelve 5-cm lengths of the tape, known as ANLB17, were given heat treatments for various times with intermittent uniaxial pressings ( $\sim 2$  GPa), at a constant temperature of  $815^\circ\text{C}$  in a flowing 7.5%  $\text{O}_2$ /balance  $\text{N}_2$  atmosphere. The specific heat treatment times and sample identifications are listed in Table 5-1. Since all heat treatments were performed at  $815^\circ\text{C}$ , the individual samples are denoted in the text by the lengths of their heat treatments: for example, 12/50/100 indicates the tape which was given a 12 hour first heat treatment, an intermediate pressing, a 50 hour second heat treatment, an intermediate pressing, and finally a 100 hour third heat treatment. Tapes were monitored through 4 heat treatments and 3 intermediate pressing cycles.

Samples of each tape were then characterized by their  $I_c$  (77 K, 0 T), microhardness, and by examining their microstructure with a scanning electron microscope (SEM). The  $I_c$  of the tapes was taken as the current where the first sign of a non-zero voltage was resolvable ( $\sim 1$   $\mu\text{V}$ ), and this value was converted to  $J_c$  by dividing by the average of two transverse cross-sectional areas measured by image analysis.

Table 5-1. Identification and heat treatment times of reacted samples of composite ANLB17. All heat treatments were given at 815°C in 7.5% O<sub>2</sub>.

Sample Identity	HT1 time (h)	HT2 time (h)	HT3 time (h)	HT4 time (h)
12	12			
24	24			
12/50	12	50		
24/50	24	50		
12/100	12	100		
24/100	24	100		
12/50/100	12	50	100	
24/50/100	24	50	100	
12/100/100	12	100	100	
24/100/100	24	100	100	
12/100/100/100	12	100	100	100
24/100/100/100	24	100	100	100

The Vickers microhardness of two polished transverse sections of each tape was measured; the results were combined, resulting in 10-20 hardness measurements for each sample. Due to the thin core size and fragile nature of the BSCCO, a 10 g load was used (with a 15 second loading time). The hardness measurements were made in a row at the center of the transverse cross section, approximately one to two indentation widths away from the Ag sheath on either side of the core. Due to the difficulty of measuring the small hardness indentations and the variability of the local microstructure in the tapes, there was sometimes considerable scatter in the hardness data. In addition, it was found that the surface polish of the BSCCO sample was crucial in obtaining reproducible hardness data; even though samples appeared scratch-free under the light microscope, further polishing (with 0.05  $\mu\text{m}$  Al<sub>2</sub>O<sub>3</sub> in methanol) was needed to remove damaged layers. The Knoop microhardness ( $H_K$ ) was measured in a similar way. Since the elongated diamond shape of

the Knoop indenter is not symmetric, the long axis of the indenter was placed such that it was parallel to the rolling plane of the tape (i.e. nominally parallel to the “a-b”-direction), or orthogonal to the rolling plane, such that the long axis of the indenter was nominally parallel to the “c”-direction.

The BSCCO microstructure was recorded by examining polished longitudinal cross-sections of each tape with an SEM operated at 15 kV in both backscatter (BS) (for as-polished samples) and secondary electron (SE) (for samples etched with 1% perchloric acid in 2-butoxyethanol) imaging modes. The BS imaging mode emphasizes phase identification, while the SE mode is best for examining the alignment of the BSCCO grains and for imaging cracks that may be present in the core.

### **5.3 Results**

Figure 5-1 shows  $J_c$  (77 K, 0 T) versus total heat treatment time and the heat treatment number for all of the samples prepared for this study. It is clear that there is a strong positive correlation between  $J_c$  (77 K, 0 T) and total heat treatment time, the relationship being approximately linear.  $J_c$  increases from 0 to  $\sim 22,000$  A/cm<sup>2</sup> as the heat treatment time increases from 12 to  $\sim 320$  hours. It can also be noted that the sensitivity of  $J_c$  to heat treatment time and number of heat treatments depends on the duration of the first heat treatment;  $J_c$  increased linearly from  $\sim 1000$  to  $\sim 22,000$  A/cm<sup>2</sup> with heat treatment time for samples given a 24 hour first heat treatment (the line drawn connects these points), while  $J_c$  depended only on the number of heat treatments for samples which

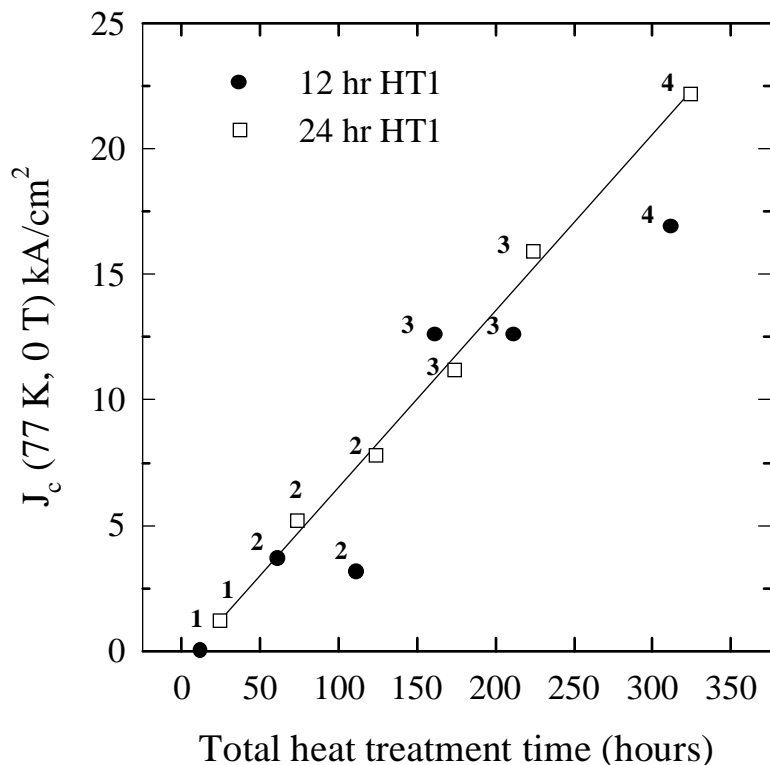


Figure 5-1.  $J_c$  (77 K, 0 T) as a function of total heat treatment time. The numbers next to the data points are the number of heat treatments which the tape was given. The line is drawn through the 24 h first heat treatment data points.

had 12 hour first heat treatments. The most heavily reacted sample (24/100/100/100) had the highest  $J_c$  (77 K, 0 T) value of all of the tapes in this study, 22,200 A/cm<sup>2</sup>.

Figure 5-2 shows the  $H_V$  of the transverse BSCCO cross sections as a function of the total heat treatment time. The data points in the plots are average values, and the error bars represent one standard deviation on each side of the average value. It can be seen that there is a marked hardness decrease between the first and second heat treatments (from  $\sim 100$  to  $\sim 70$  kg/mm<sup>2</sup>), but that  $H_V$  then increases with each subsequent heat

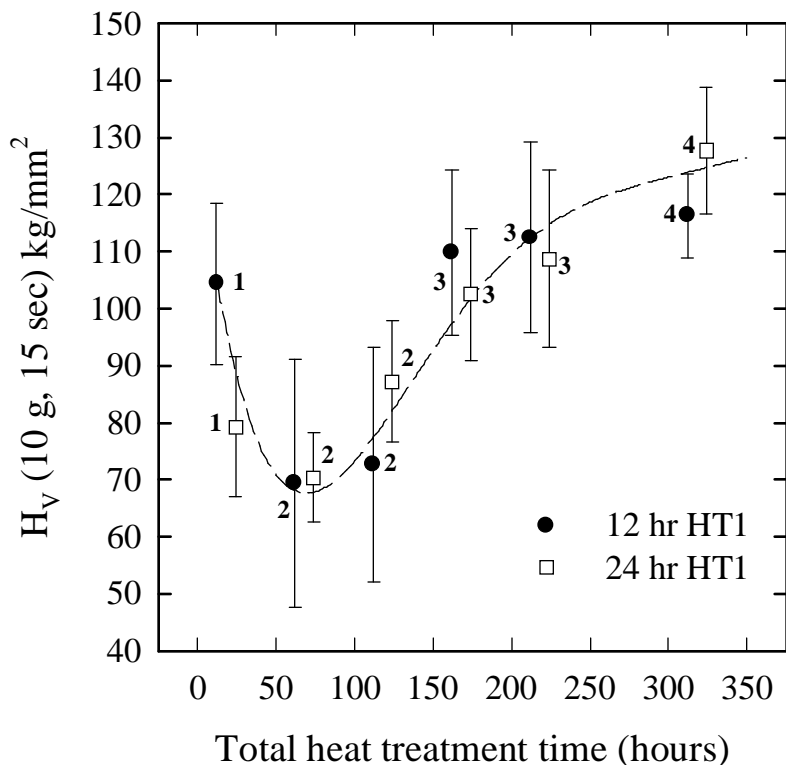


Figure 5-2. Vickers microhardness of the transverse BSCCO cross-sections of composite ANLB17 as a function of total heat treatment time. The numbers next to the data points are the number of heat treatments which the sample was given. The curve is provided as a guide to the eye. The error bars represent one standard deviation on each side of the mean.

treatment up to a maximum value of  $\sim 130 \text{ kg/mm}^2$ . The initial decrease can be attributed to two factors, one being the disappearance of hard second phase (as shown later) and the second to retrograde sintering [129,130] which occurs during the 2212 to 2223 phase transformation, the major part of which takes place during the first and second heat treatments.

Figure 5-3 shows the  $J_c$  of the second through fourth heat treatment samples as a function of Vickers microhardness. The first heat treatment samples were excluded from this figure because of the large amounts of hard non-superconducting alkaline earth cuprate (AEC) particles which were still present after the first heat treatment. It can be seen that there is a strong positive, nearly linear correlation between the Vickers microhardness of the reacted BSCCO-2223 core and  $J_c$ . On going from the second to the fourth heat treatment  $J_c$  increased from  $\sim 3000$  to  $22,000 \text{ A/cm}^2$  while  $H_V$  increased from  $\sim 70$  to  $130 \text{ kg/mm}^2$ .

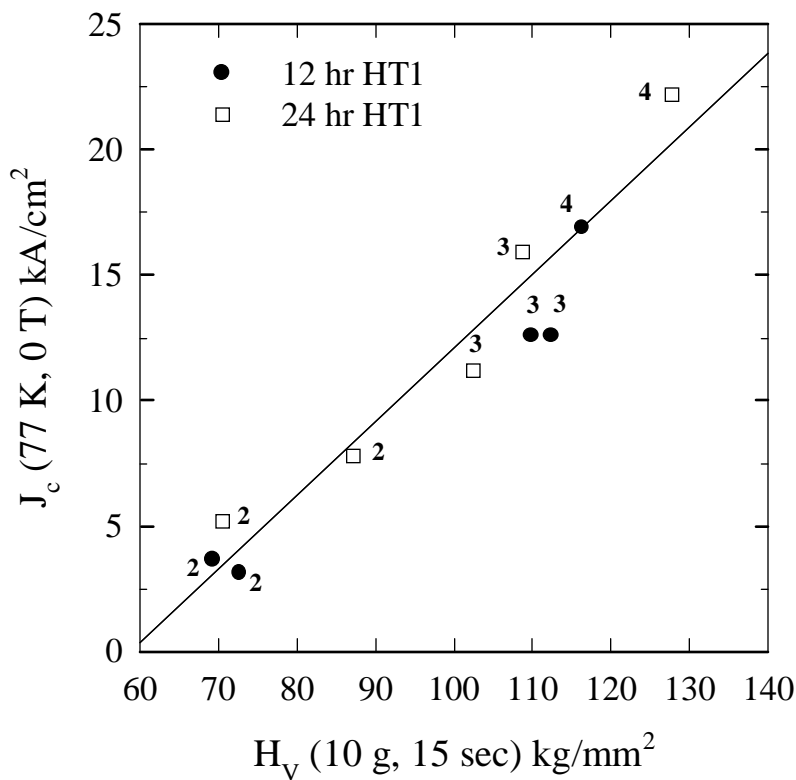


Figure 5-3.  $J_c$  (77 K, 0 T) as a function of the Vickers hardness of the transverse BSCCO cross-sections. The line is provided as a guide to the eye. The numbers next to the data points are the number of heat treatments which the tape was given.

Figure 5-4 is similar to Figure 5-3, but shows  $J_c$  as a function of the  $H_K$  of the transverse BSCCO cross-sections. The open symbols on the left hand side of the figure show  $J_c$  as a function of Knoop hardness with the long axis of the indenter placed parallel to the broad axis of the transverse cross section (i.e. approximately parallel to the a-b planes), while the closed symbols on the right hand side plot  $J_c$  against the Knoop hardness measured with the long axis of the Knoop indenter placed parallel to the short axis of the

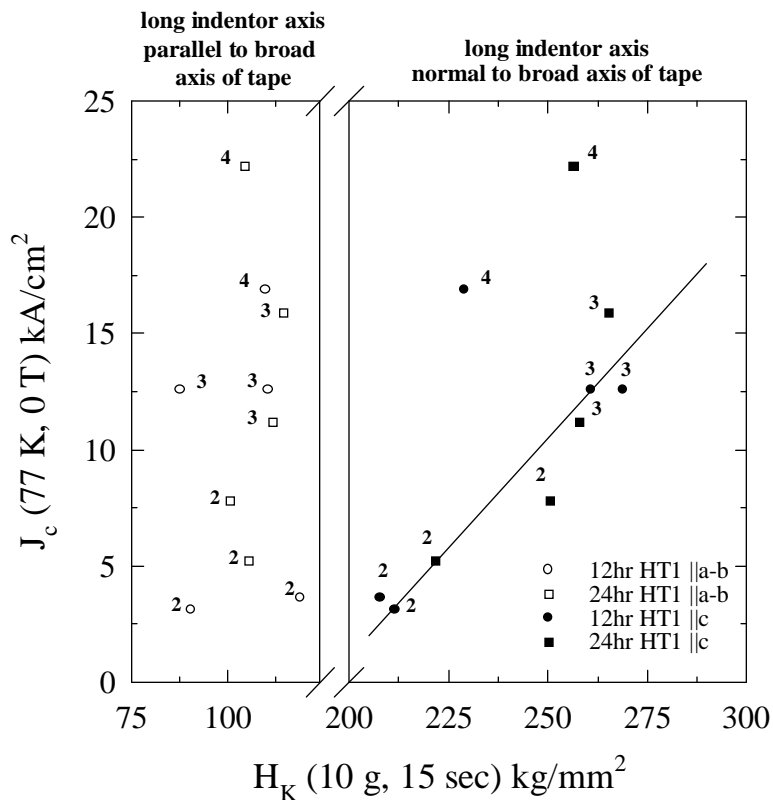


Figure 5-4.  $J_c$  (77 K, 0 T) as a function of Knoop microhardness of the transverse BSCCO cross-sections. The data to the left of the axis break is for  $H_K$  parallel to the rolling plane (i.e. approximately ||a-b), and the data to the right is  $H_K$  perpendicular to the rolling plane (i.e. approximately ||c). The numbers next to the data points are the number of heat treatments which the tape was given. The line is provided as a guide to the eye.

transverse section (i.e. approximately parallel to the c-axis). The data show almost no correlation between  $J_c$  and  $H_K$ (||a-b), but there is a reasonable correlation between  $J_c$  and  $H_K$ (||c), except for the two fourth heat treatment samples, whose  $H_K$  is about 20% lower than would be expected based on their  $J_c$  value.

Figure 5-5 compares SEM backscatter micrographs of longitudinal sections of the 12 and 24 hour first heat treatment samples to those obtained after a second 50 hour heat treatment. In these micrographs three major phases are evident by their atomic number contrast. The lightest phase is BSCCO-2212, the plate-like darker gray phase is BSCCO-2223, and the angular, relatively equiaxed dark phase is principally  $(\text{Ca,Sr})_2\text{CuO}_3$  (2:1 AEC). In all four micrographs it appears that the reaction occurs relatively uniformly throughout the cross-section and that increasing time drives the reaction towards the BSCCO-2223 phase. The quantity of black non-superconducting AEC phase is greatest in the first heat treatment: only limited 2212 to 2223 conversion has occurred after 12 hours at  $815^\circ\text{C}$  (Figure 5-5a) and since  $J_c$  (77 K, 0 T) was zero, the BSCCO-2223 current path cannot be above the percolation limit. For the 24 hour first heat treatment sample (Figure 5-5c), the BSCCO-2223 phase conversion was more evident and a finite  $J_c$  ( $1200 \text{ A/cm}^2$ ) was obtained. In both cases the second heat treatment of 50 hours (Figure 5-5b and Figure 5-5d) caused the BSCCO-2212 phase to almost disappear under the imaging conditions chosen.

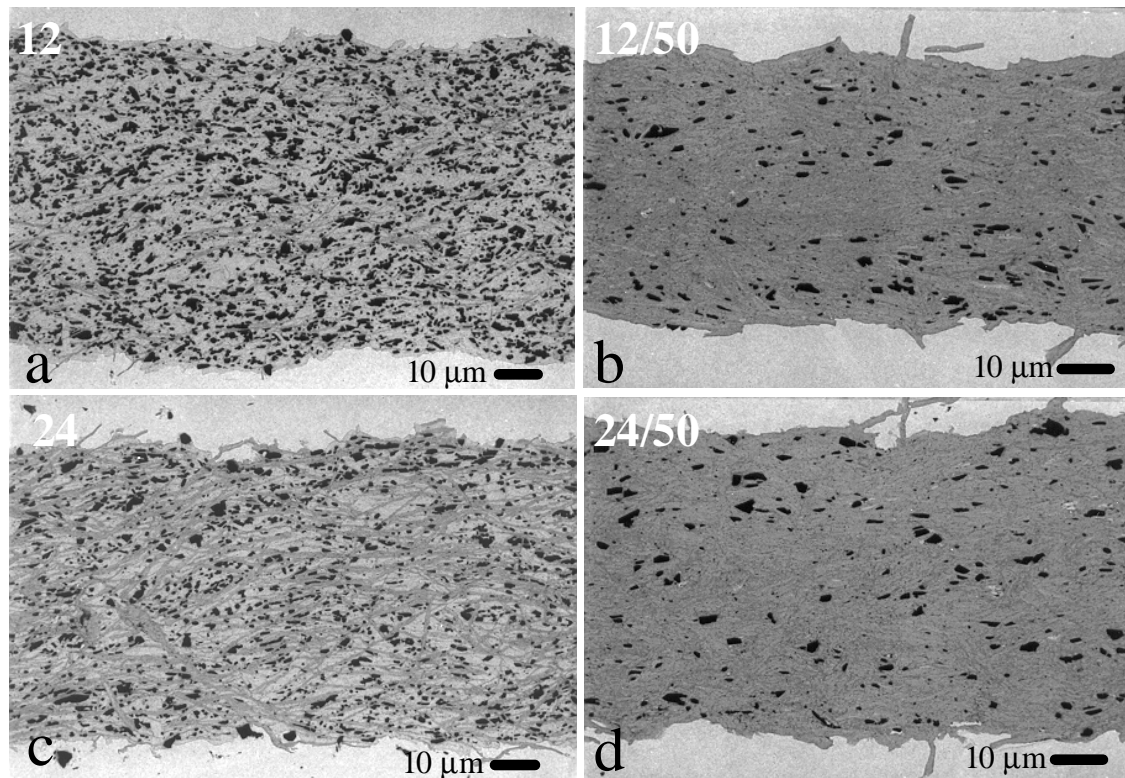


Figure 5-5. SEM backscatter micrographs of the 12 h ( $J_c$  (77 K, 0 T) = 0) and 24 h ( $J_c$  = 1200 A/cm<sup>2</sup>) first heat treatment samples (a and c, respectively) compared to the microstructures after an intermediate pressing step and a further 50 h heat treatment (b,  $J_c$  = 3700 A/cm<sup>2</sup>, and d,  $J_c$  = 5200 A/cm<sup>2</sup>). All heat treatments were at 815°C in 7.5 % O<sub>2</sub> atmosphere.

Figure 5-6 compares the grain structure of the samples after the 12 and 24 hour first heat treatments (Figure 5-6a and Figure 5-6b, respectively) to those obtained after a 50 hour second heat treatment (Figure 5-6c and Figure 5-6d) more explicitly by viewing them in the etched condition under secondary electron imaging mode. The grains are several times smaller and less aspected in the 12 hour heat treated tape (Figure 5-6a) than the tape which was given a longer 24 hour heat treatment (Figure 5-6b). The shorter

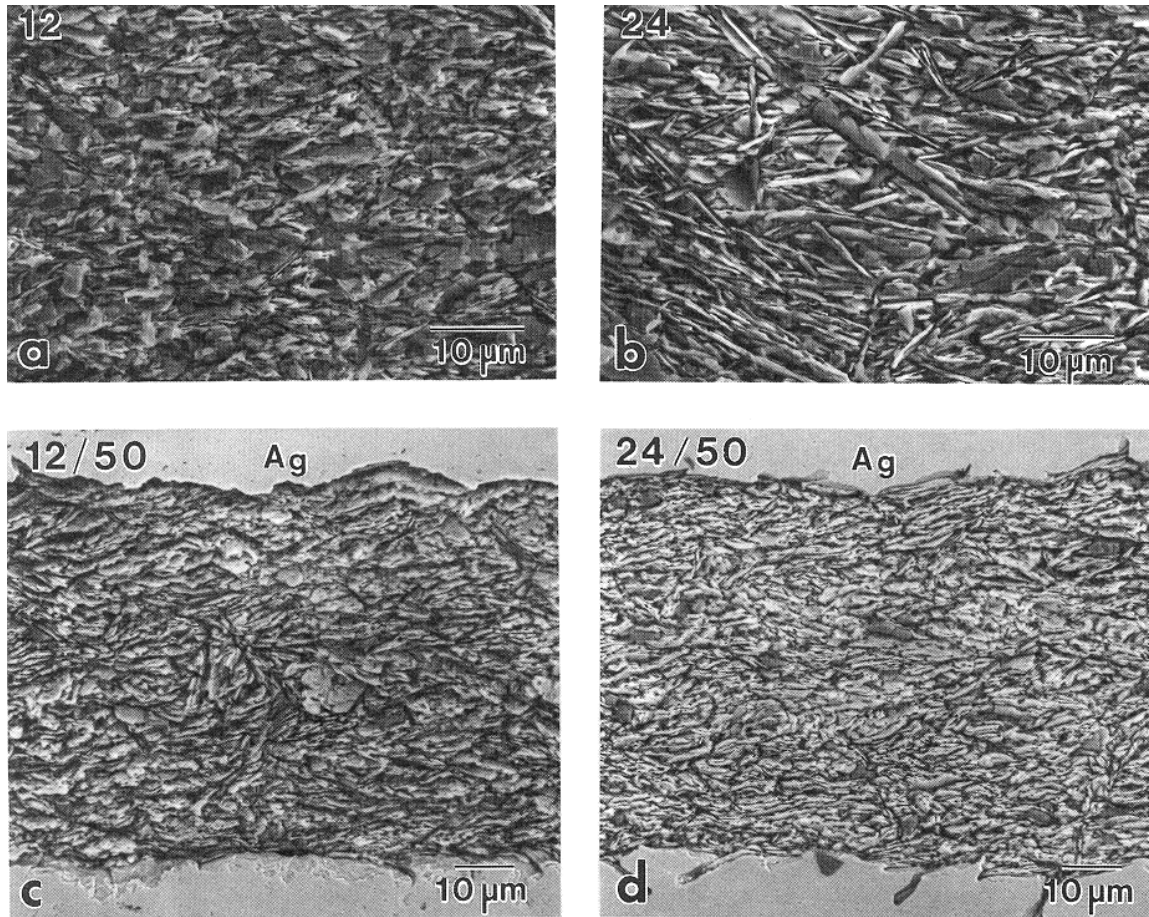


Figure 5-6. SEM secondary electron images of the etched 12 and 24 h first heat treatment samples (a and b, respectively) compared to the etched microstructures after an intermediate pressing step and a further 50 h heat treatment (c and d).

length heat treatment sample also appears to have a less evident grain-to-grain alignment; this implies that it has a less dense microstructure. Note that this difference in alignment and density still appears to exist after the second heat treatment (compare Figure 5-6c and Figure 5-6d).

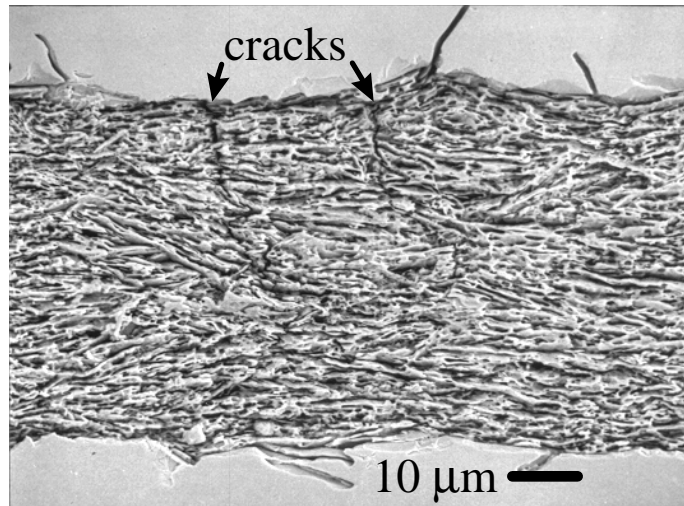


Figure 5-7. SEM-SE micrograph of the etched 24/100/100/100 fourth heat treatment sample illustrating the cracks which were observed in both this sample and the 12/100/100/100 fourth heat treatment sample.

Figure 5-7 is an SEM-SE micrograph of an etched longitudinal cross section from the 24/100/100/100 fourth heat treatment sample which illustrates the cracks which were found in both this sample and the 12/100/100/100 fourth heat treatment sample. These cracks are believed to be examples of unhealed deformation damage from the uniaxial pressing which separated the third and fourth heat treatments.

#### **5.4 Discussion**

There are at least three limits on the grain-to-grain connectivity of a BSCCO-2223 filament, and together or separately these largely determine the  $J_c$ . The first connectivity limit is imposed by the difficulty in forming largely phase-pure 2223 grains

[33,50,51,85,86,103]. Extending the number of deformation and heat treatment cycles is beneficial to this goal. A second limit may be posed by misaligned grains of the 2223 phase, across which the supercurrent connections are poor [131]. A third limit is introduced if macrocracks (i.e. those cracks which completely sever the filament) or more localized microcracks which are introduced during each deformation step cannot be healed in the subsequent heat treatment. All of these current-limiting mechanisms are operative to some extent, and they all act to reduce the active cross-section of the composite [126,127]. Their relative importance depends on the stage that the sample is at in the processing sequence. Attempting to eliminate the first and second connectivity limits (the phase purity and alignment of the 2223 grains) by adding additional heat treatment and deformation cycles may simply result in  $J_c$  being limited by unhealed cracks. Evidence for all three of these mechanisms is found in the samples studied in this experiment.

The plot of  $J_c$  as a function of total heat treatment time (Figure 5-1) has two interesting features. For samples given a 12 hour first heat treatment (the filled circles in Figure 5-1), it appears that  $J_c$  increases in a step-wise fashion with the *number* of heat treatments, and does not seem dependent on the *length* of the subsequent heat treatments. In other words, the 12/50 and 12/100 samples (two heat treatments each) had essentially the same  $J_c$  values, as did the 12/50/100 and 12/100/100 samples (three heat treatments each). However, for samples given 24 hour first heat treatments (the open squares), it appears that  $J_c$  is dependent on both the number *and* total length of heat treatment and that  $J_c$  increases linearly with the total length of all heat treatments. The difference in

behavior is believed to originate from the very different grain morphology of the 12 and 24 hour first heat treatment samples just prior to their first uniaxial pressing, as described below. This difference in grain morphology is clearly visible in Figure 5-6a and Figure 5-6b.

For the 24 hour first heat treatment sample, there was already significant conversion to BSCCO-2223 and growth of the 2223 grains during the first heat treatment (Figure 5-5c and Figure 5-6b). A subsequent uniaxial pressing can align the c-axes of such plate-like grains. During the second heat treatment, this aligned 2223 grain structure can constrain new or growing 2223 grains, both in where they nucleate and along which directions they grow. Both of these factors promote alignment of new grains with the existing 2223 network, and thus make it possible for the density of the BSCCO core to increase with further thermal processing.

The situation is rather different for the samples that received the shorter 12 hour first heat treatment. Due to the relatively long incubation period required to initiate the 2212 to 2223 phase transformation [31,62], there is less 2223 transformation and grain growth in briefly heat treated samples. The largely 2212 grains of the 12 hour first heat treatment sample were smaller and less aspected than those produced by the 24 hour heat treatment (compare Figure 5-6a and Figure 5-6b), and the pressing between the first and second heat treatments was correspondingly less effective in improving the grain alignment and density. Thus, the new 2223 grains which formed during the second heat treatment were relatively freer to nucleate and grow in arbitrary directions. The net result is a less well aligned (and thus less dense) grain structure (compare Figure 5-6c and Figure

5-6d), and so it is not surprising that the 12/50 sample had a lower  $J_c$  value than that of the 24/50 sample (3700 A/cm<sup>2</sup> compared to 5200 A/cm<sup>2</sup>). For both samples, it seems likely that incomplete conversion to 2223 is still limiting the  $J_c$  after the second heat treatment, but the poorer alignment of the 2223 grains in the 12 hour first heat treatment sample set also exerts an important role in limiting  $J_c$ .

Since liquid is believed to be formed by the reactions between the 2212, AEC, and CuO phases [50,51], it is evident that the quantity of liquid will diminish (in principle to zero) as the reaction proceeds. Figure 5-5b and Figure 5-5d confirm that the major step in the conversion to BSCCO-2223 occurred during the first and/or second heat treatment. Due to limited amounts of residual liquid-forming phases and the reduced porosity remaining after the second heat treatment (both of which reduce the ability of grains to rotate into alignment), solid state diffusion is likely to be the dominant densification and grain growth mechanism in the later (third and fourth) heat treatments. Thus it is likely that the alignment and overall grain morphology obtained after the first two liquid-bearing heat treatments remains essentially unchanged through later heat treatments, since the solid state processes of densification and grain growth are slower than their liquid-assisted counterparts. Because solid state diffusion in BSCCO is anisotropic (orders of magnitude faster in the a-b plane than in the c-direction), microstructures with poorly aligned grains tend to push themselves apart during sintering, producing the well-known retrograde densification [129,130] which disrupts the grain-to-grain connectivity. By contrast, when the grains are well aligned, retrograde densification is not so pronounced, and grain-to-grain connectivity improves during sintering. In summary, it appears that the degree of

2223 phase conversion and grain alignment which develops during the first heat treatment and its subsequent deformation step can play a decisive role in determining the density, connectivity, and  $J_c$  throughout all the subsequent process steps.

Two distinct trends can be seen in the Vickers hardness versus total heat treatment time plot shown in Figure 5-2. The first is the drop in the microhardness which occurs in the first and second heat treatments. The dominant factor is believed to be the marked reduction of hard AEC particles as the Ca and Cu of the AEC phases is consumed during the 2212 to 2223 conversion reaction. After these are consumed the properties of the BSCCO-2223 phase dominate. A comparison of Figure 5-5a and Figure 5-5c with Figure 5-5b and Figure 5-5d illustrates the dramatic changes which occur in the microstructure between the first and second heat treatments. The second main feature of Figure 5-2 is the increase in  $H_V$  that occurs following the second heat treatment. Evidently the mechanical deformation and subsequent heat treatments cause the density (and hardness) of the cores to increase. As shown in Figure 5-3, this hardness increase is directly and positively correlated with increases in  $J_c$ .

The Knoop microhardness results (Figure 5-4) indicate that the hardness parallel to the a-b plane of the tape is essentially constant ( $H_K(\parallel a-b) \approx 100$ ), while the hardness parallel to the c-direction increases with thermal treatment (except after the fourth heat treatment). This latter result can be directly attributed to increases in the density of the core due to heat treatment and the intermediate uniaxial pressings. The constant value of the Knoop hardness parallel to the a-b plane is somewhat harder to explain. One interpretation is that the density of the core does not increase in the a-b plane of the tape

(which is consistent with the fact that the tapes are uniaxially pressed normal to this plane). A second explanation is that  $H_K(\parallel a-b)$  represents the stress required to cleave the BSCCO grains apart at the Bi-O bilayer in the a-b plane. This quantity should be intrinsic to the 2223 phase crystal structure, rather than be determined by the connections of the sintered polycrystalline multi-phase assembly. The Vickers indenter is symmetric in shape, and thus is not as sensitive as the Knoop indenter to the anisotropic nature of BSCCO (there were variations in the lengths of the two diagonals of a Vickers indentation in some cases, but there appeared to be no obvious trend or pattern to these variations). It can be seen that the two data points in Figure 5-4 corresponding to the 12/100/100/100 and 24/100/100/100 samples do not follow the trend of the data from the earlier heat treatments since  $H_K(\parallel c)$  is significantly lower than expected for these two samples. As mentioned earlier, cracks in the BSCCO core were observed in etched sections of the 12/100/100/100 and 24/100/100/100 samples (Figure 5-7). It is possible that the measured hardness deficit is due to such micro- and macrocracks. However, a hardness deficit was not observed in the Vickers hardness measurements, perhaps because of the larger and more symmetric shape of the indenter. It is interesting to note that  $J_c$  increased through the fourth heat treatment in spite of these cracks. For this to occur, the local  $J_c$  of the continuous current path must have increased such that the overall tape  $J_c$  would also be increased, despite the cracks which reduce the active cross-section of the core [126,127]. Thus it is not anticipated that the linear relationships of Figure 5-1 and Figure 5-3 are fundamental ones since the cross-section appropriate for normalizing the critical current ( $A_{eff}$ ) is very unlikely to be the whole core cross-section ( $A$ ).

Whatever the subtleties of the Knoop versus the Vickers hardness tests, it is very valuable that such simple tests yield such positive correlations to the  $J_c$ . The next task is to more precisely define the current-limiting mechanism at different steps in the process. The ensemble of data presented in this paper provides further support for the idea that current flow in these tapes is largely percolative and dominated by the active cross-section of good connections between grains [126,127].

## **5.5 Summary**

In summary, a linear correlation between the Vickers microhardness and  $J_c$  (77 K, 0 T) of reacted BSCCO-2223 tapes with critical current densities up to 22,000 A/cm<sup>2</sup> was observed. A correlation between the  $J_c$  and Knoop microhardness measured with the long indenter axis placed normal to the rolling plane of the tape was also observed. These results are consistent with the belief that a significant limit on the  $J_c$  of BSCCO-2223 tapes is provided by a lack of full density and thus a compromised grain-to-grain connectivity in the BSCCO core. The length of the first heat treatment was found to be very important in determining the final properties of the 2223 tapes. Appropriate heat treatment schedules should be developed that allow for the maximum densification of the 2223 phase through mechanical deformation and subsequent heat treatment without forming cracks which cannot heal due to the lack of a liquid phase or insufficient solid state mass transport during later heat treatments.

## **6. The effect of sheath material and deformation method on the microhardness, connectivity, and $J_c$**

The material in this chapter is part of the publication:

J.A. Parrell, S.E. Dorris, and D.C. Larbalestier, “The effect of sheath material and deformation method on the oxide core density, filament uniformity, and critical current density of  $(\text{Bi,Pb})_2\text{Sr}_2\text{Ca}_2\text{Cu}_3\text{O}_x$  tapes”, *Advances in Cryogenics Engineering (Materials)* 40 (1994) 193.

### **6.1 Introduction**

As discussed in prior chapters, the  $J_c$  of Ag-clad 2223 tapes appears to be controlled by a combination of factors, reviewed briefly here. The first problem is to fully convert the precursor powder to the high  $T_c$  2223 superconducting phase. This effort is hampered by the formation of non-superconducting second phases which not only wastefully take up conductor cross-section, but disturb the local alignment of the 2223

grains in their vicinity, further reducing  $J_c$  [33]. Dorris et al. have reported a more reproducible method for obtaining 2223 tapes having reduced amounts of second phase [50,51]. However, the fact that record critical current densities have not as of yet been reported in tapes made from this so-called "two-component powder" process may indicate that other variables are still important in obtaining high  $J_c$  values in a 2223 tape.

Since it has been shown that the formation of 2223 is enhanced next to Ag, and that alignment of the BSCCO grains is essentially perfect at the Ag/BSCCO interface [103], it seems that the smoothness of the Ag/BSCCO interface plays a major role in controlling the long range alignment of the 2223 grains. A thin, yet "unsausaged" BSCCO core would take advantage of this preferential 2223 formation and alignment near the Ag/BSCCO interface. However, thin ( $\sim 15 \mu\text{m}$  or less) cores in conventionally processed oxide-powder-in-tube (OPIT) tapes are often severely "sausaged" [7], producing a condition which results in a misaligned BSCCO microstructure and an irregular filament cross section. It has been proposed that a stronger sheath could reduce the Ag/BSCCO interface irregularity [132].

It has been shown in Chapter 5 that the density of the BSCCO-2223 core (as measured by microhardness) can be directly correlated to  $J_c$  [25,133]. Since it is thought by many that the  $J_c$  in these tapes is limited by grain to grain (or colony to colony) connectivity [85,86,131,134,135], it seems reasonable to assume that a well-aligned, phase-pure, and highly dense BSCCO core is essential for obtaining high critical current densities.

Due to the micaceous, plate-like nature of BSCCO-2223 grains, BSCCO wires made by the common OPIT method must be mechanically deformed into thin tapes in order to produce a dense, aligned BSCCO microstructure. The details of this process were described in Chapter 4. The 2223 superconducting phase is formed by two or more reaction-deformation cycles. It seems that the deformation increases the density of the oxide core, improves the alignment of the grains, and perhaps helps break up regions of second phase so that the 2223 formation reaction can continue during the next heat treatment. In addition, for reasons not fully understood at the time of this work, uniaxial pressing between heat treatments usually results in a tape of higher  $J_c$  than is obtained by rolling between heat treatments. Indeed, the highest  $J_c$  values reported thus far in a 2223 OPIT tape were obtained by pressing between heat treatments [25]. Unfortunately, uniaxial pressing is not useful for making long lengths of conductor. For this reason, long length manufacture of BSCCO-2223 involves rolling as the mechanical deformation step between reaction heat treatments.

The purpose of this study was to examine the effects of sheath strength and the intermediate mechanical deformation method on the oxide core density and  $J_c$ , with the goal of clarifying the differences between rolled and pressed samples. Two different sheathing materials were chosen for this study: pure Ag, and a Ag-0.25wt%Mg-0.25wt%Ni oxide-dispersion hardenable alloy, having the trade name Consil 995. Two OPIT tapes were made in an identical fashion from these materials. Samples of the tapes were heat treated together and then deformed by rolling or pressing between heat treatments, as discussed in more detail next.

## 6.2 Experimental details

Approximately 20 g of 2223 two-component ( $\text{Bi}_{1.8}\text{Pb}_{0.4}\text{Sr}_2\text{Ca}_1\text{Cu}_2\text{O}_x$  and  $\text{CaCuO}_x$ ) powder [50] with an overall composition of  $\text{Bi}_{1.8}\text{Pb}_{0.4}\text{Sr}_2\text{Ca}_2\text{Cu}_3\text{O}_x$  was cold isostatically pressed (CIP'ed) at 340 MPa into a rod  $\sim 10.2$  cm long and  $\sim 7.5$  mm in diameter. The rod was then cut in half, and inserted into one of two machined cans (O.D. = 13.0 mm, I.D. = 7.7 mm). The first can was of pure Ag, and the second of Consil 995, which had been oxide dispersion hardened by a heat treatment of 42 hours in air at 800°C. The hardened Consil can (Vickers microhardness ( $H_V$ ) = 140 kg/mm<sup>2</sup>, 10 g load, 15 second loading time) was approximately 50% harder than the cold-worked pure Ag can ( $H_V$  = 90 kg/mm<sup>2</sup>) at the starting size (13.0 mm O.D.). Machined plugs ( $\sim 2.5$  cm long, 7.6 mm O.D.) made from the same material as the sheaths were used to close the cans.

The billets were then swaged and cold drawn to a diameter of 2.11 mm, and rolled to a thickness of  $\sim 0.2$  mm with a nominal thickness reduction of 5% per pass in a two-high rolling mill with 3.81 cm diameter rolls. Even though the two composites were passed through the rolling mill right after each other (without adjusting the rolls), they did not finish at the same thickness, presumably due to the elastic spring back of the rolling mill with respect to the different sheath hardnesses. The Ag-clad composite (also known as UWB48) had a final thickness of 0.198 mm and a width of 3.223 mm, while the harder Consil composite (UWB49) was 0.239 mm thick and 3.505 mm wide. The Consil-clad composite developed small cracks that gradually formed a rough, ragged edge along the entire length of the tape as it was rolled down.

Seven 7.6 cm-long pieces were cut from each tape. Heat treatments were performed at 815°C in a flowing 7.35%O<sub>2</sub>/balance N<sub>2</sub> atmosphere. After the first heat treatment of 24 hours, one Ag and one Consil sample were placed aside, and the remaining samples were then deformed in preparation for a second heat treatment. Half of the samples of each sheath type were pressed to ~ 0.18 mm at ~ 2 GPa between polished tungsten carbide platens separated by brass shim stock, using glycerin as a lubricant. The other samples were rolled to ~ 0.18 mm with a nominal thickness reduction of 5% per pass. The samples were then heat treated for the second time. The second and all subsequent heat treatments were each for 100 hours. After the second heat treatment, the remaining tapes were then pressed or rolled to ~ 0.15 mm, and heat treated again. Following the third heat treatment, the remaining four samples were then pressed/rolled to ~ 0.13 mm, and heat treated for a fourth time.

Two transverse cross-sections of each tape were dry ground with SiC, and polished with 0.05 μm Al<sub>2</sub>O<sub>3</sub> in methanol. The hardness of the center of the core was measured 5 times using a 15 second load time, as described in Chapter 5. The samples were reground and repolished, and the center of each tape was then indented 5 more times, so as to yield a total of 20 hardness measurements per tape condition.

Longitudinal midsections of each sample were mounted and polished as above. A scanning electron microscope (SEM) operated at 15 kV in backscatter mode was used to record the microstructure of each tape. The same longitudinal samples were then used to quantify the filament uniformity (sausaging) of each tape. A high resolution 1024 × 1024 image analysis system was used to overlay 512 lines across the longitudinal BSCCO

section. The image analysis system then measured the length of each line and computed the average core thickness, as well as the BSCCO core thickness standard deviation. Five different areas were measured and the  $\sim 2500$  measurements were combined for each sample. The core thickness standard deviation divided by the average core thickness was used as the measure of filament uniformity. This measurement takes into account the presence of intrusions of BSCCO-2223 "plates" into the Ag (e.g. Figure 6-6) since the core thickness is defined by the first crossing of the Ag-BSCCO interface. Thus cores with many intrusions into the sheath will have a slightly higher variability than those without.

Short section ( $\sim 2$  cm)  $I_c$  measurements were made at 77 K and 0 T.  $I_c$  was determined using a  $1 \mu\text{V}/\text{cm}$  criterion, and  $J_c$  was calculated by dividing  $I_c$  by the average core area from two measured transverse cross-sections.

The temperature dependence of the zero-field-cooled (ZFC) AC susceptibility of some samples were measured in a Lakeshore model 7225 AC susceptometer. Samples were measured in a 125 Hz AC field of 0.1 mT, which was applied parallel to the rolling plane of the tape (i.e. nominally parallel to the c-axis of the 2223 grains).

### **6.3 Results**

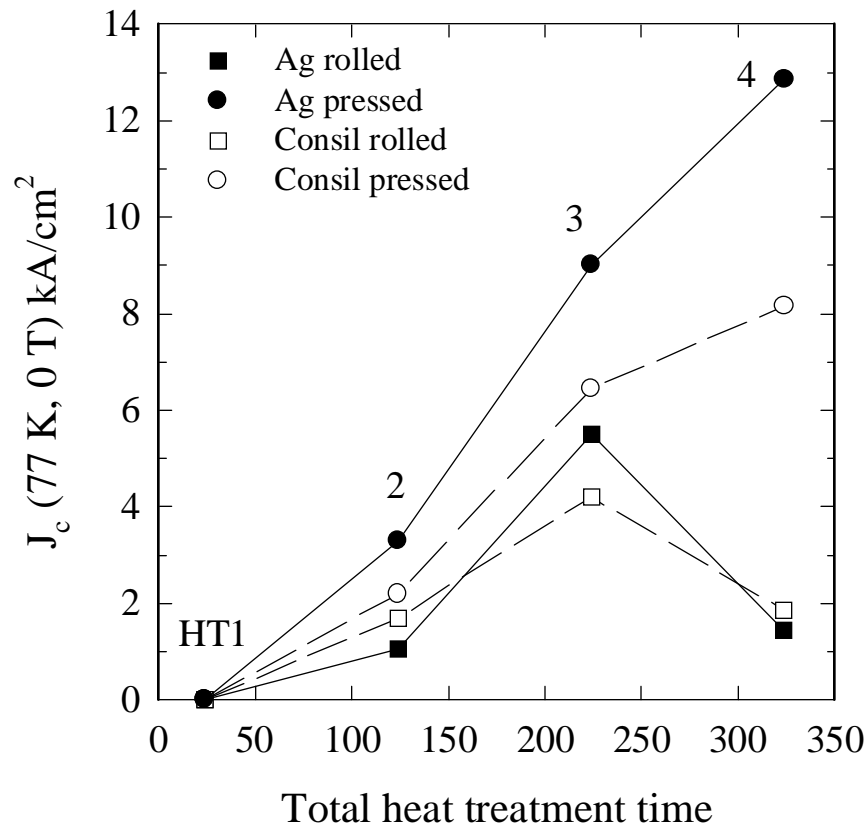


Figure 6-1.  $J_c$  (77 K, 0 T) as a function of heat treatment time and number for samples made for this study. Pressed samples developed higher  $J_c$  values than rolled samples.

Figure 6-1 plots  $J_c$  versus total heat treatment time for all of the samples prepared for this study. Note that the pressed tapes, regardless of sheath type, had  $J_c$  values than rolled tapes. In addition, the pressed Ag-sheathed tapes had higher  $J_c$  values than the corresponding Consil-clad tapes. However, the type of sheath did not seem to make a difference as to the final  $J_c$  for the rolled tapes. The  $J_c$  of the rolled tapes dropped

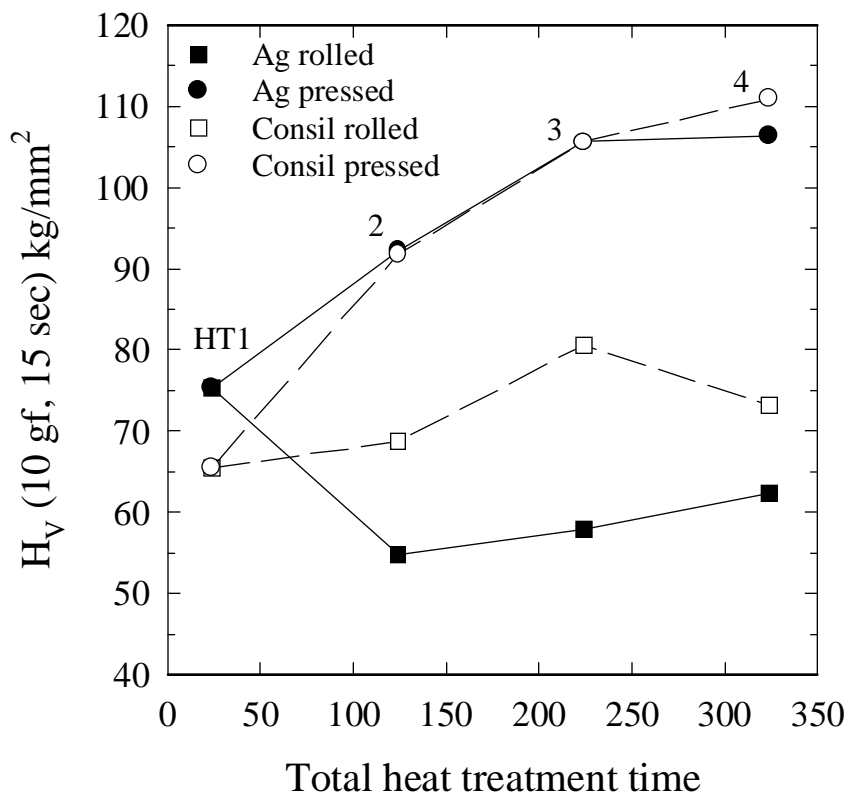


Figure 6-2. Vickers microhardness as a function of heat treatment time and number. Pressed samples were consistently harder than rolled samples.

considerably after the third heat treatment, presumably due to cracks that did not heal during the final sintering, as discussed in Section 4.2.3 and Chapter 5.

Figure 6-2 shows the Vickers microhardness of the BSCCO cores after heat treatment, as a function of total heat treatment time. After the initial 24 hour heat treatment, the hardness of the pressed BSCCO filaments increased with each additional heat treatment. The hardness of the pressed tapes was 50% to 100% higher than the rolled tapes. The type of sheath alloy did not seem to make a difference in the hardness of the

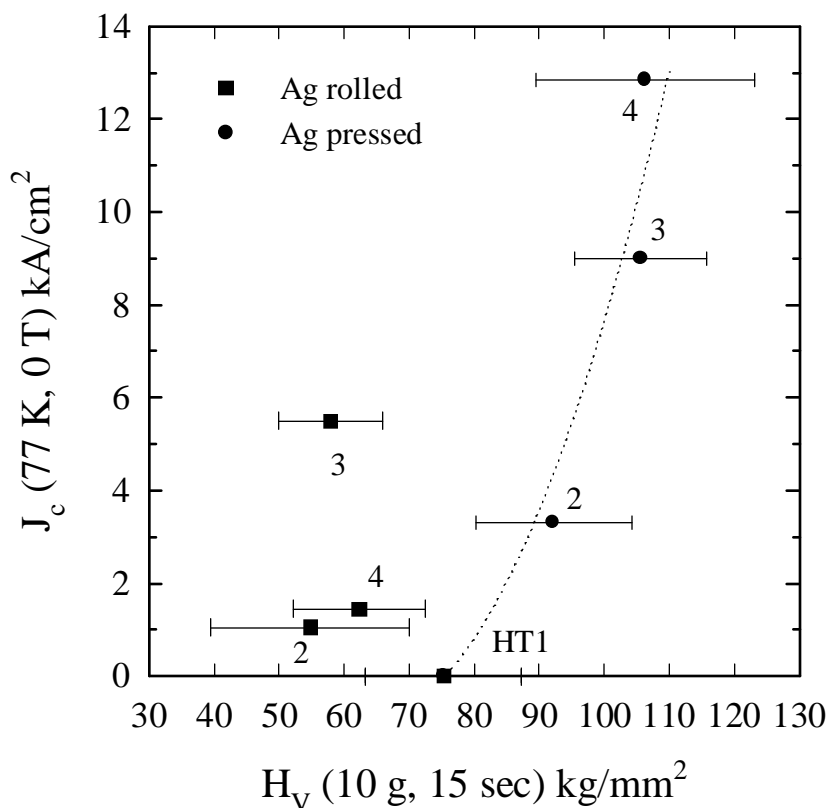


Figure 6-3. The dependence of  $J_c$  (77 K, 0 T) on the Vickers microhardness of the BSCCO cores of Ag-clad samples. The line is provided a guide to the eye. The correlation is not good for rolled samples (see discussion).

pressed tapes, but for the rolled tapes it appears that the Consil-clad tapes had harder BSCCO cores than the Ag-clad tapes.

Figure 6-3 plots  $J_c$  versus microhardness for the Ag-clad tapes. As the hardness increased, the  $J_c$  of the BSCCO core increased also, but the hardness and the  $J_c$  of the rolled tapes did not reach the hardness and  $J_c$  of the pressed tapes even after four reaction heat treatments. Figure 6-4 is a similar plot of  $J_c$  versus  $H_V$  for the Consil-clad tapes. The

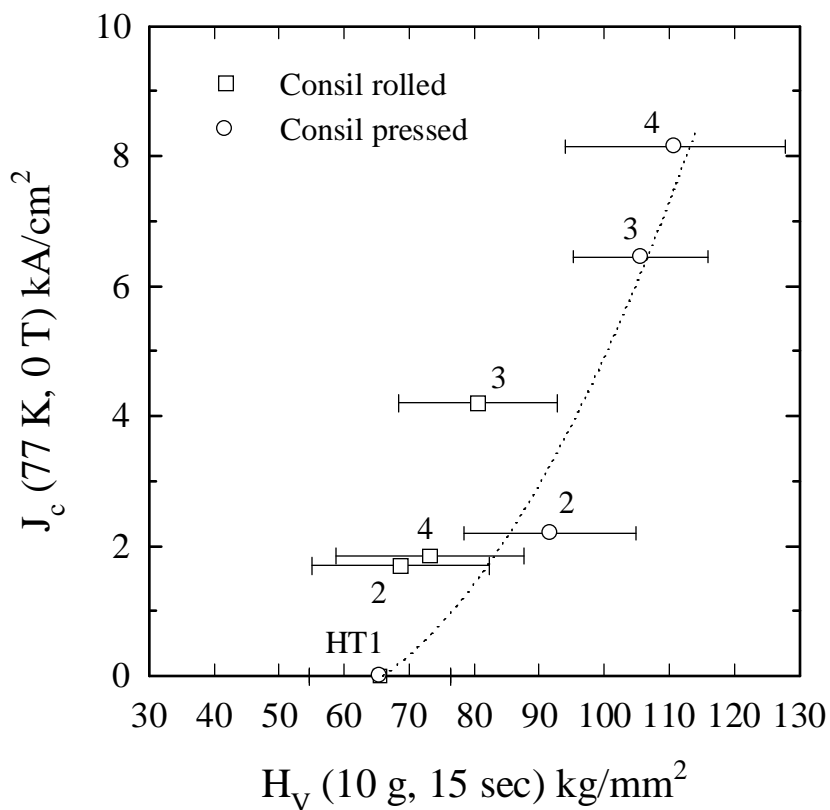


Figure 6-4. The dependence of  $J_c$  (77 K, 0 T) on the Vickers microhardness of the BSCCO cores of Consil-clad samples. The line is provided as a guide to the eye. The correlation is not good for rolled samples (see discussion).

hardness and  $J_c$  for both the pressed and rolled tapes followed the same trends as the Ag-clad tapes; the hardness and  $J_c$  of the pressed samples were again higher than those of the rolled samples.

The BSCCO core thickness variability (sausaging) as a function of overall core thickness for all tapes is shown in Figure 6-5. In general, the sausaging increased as the core was made thinner by mechanical deformation between each heat treatment. For the

Ag-sheathed tapes, rolling between heat treatments caused a greater increase in sausaging than pressing between heat treatments. The opposite was found for the Consil-clad tapes; pressing caused more sausaging than rolling. In addition, it was found that the Consil-clad BSCCO cores were more sausaged overall than the Ag-clad BSCCO cores. One factor contributing to the higher variability of the core thickness in the Consil-clad tapes was that many more BSCCO plates had grown into the sheath for the Consil-clad tapes than the Ag-clad tapes.

Figure 6-6 and Figure 6-7 are SEM backscatter micrographs of the pressed Consil and Ag-clad samples, respectively, after the fourth heat treatment. Note that many more plates of BSCCO have grown into the sheath of the Consil-clad tape. Figure 6-8 and Figure 6-9 show the microstructures of the Ag-clad rolled and pressed samples, respectively, after third heat treatment. The reaction to 2223 is more advanced in the pressed sample. Figure 6-10 shows the microstructure of the rolled Consil-clad sample after the fourth heat treatment. The Mg-Ni-O precipitates are visible as black particles in the Ag cladding.

Figure 6-11 is a plot of the AC susceptibility of the Ag-clad third and fourth heat treatment samples as a function of temperature. The kink in the  $T_c$  transition, denoted as  $T'$  [85,86], appears at higher temperatures for pressed samples than for rolled samples. This suggests that rolled samples contain more residual 2212 intergrowths than pressed samples that have otherwise received that same thermal treatment.

## **6.4 Discussion**

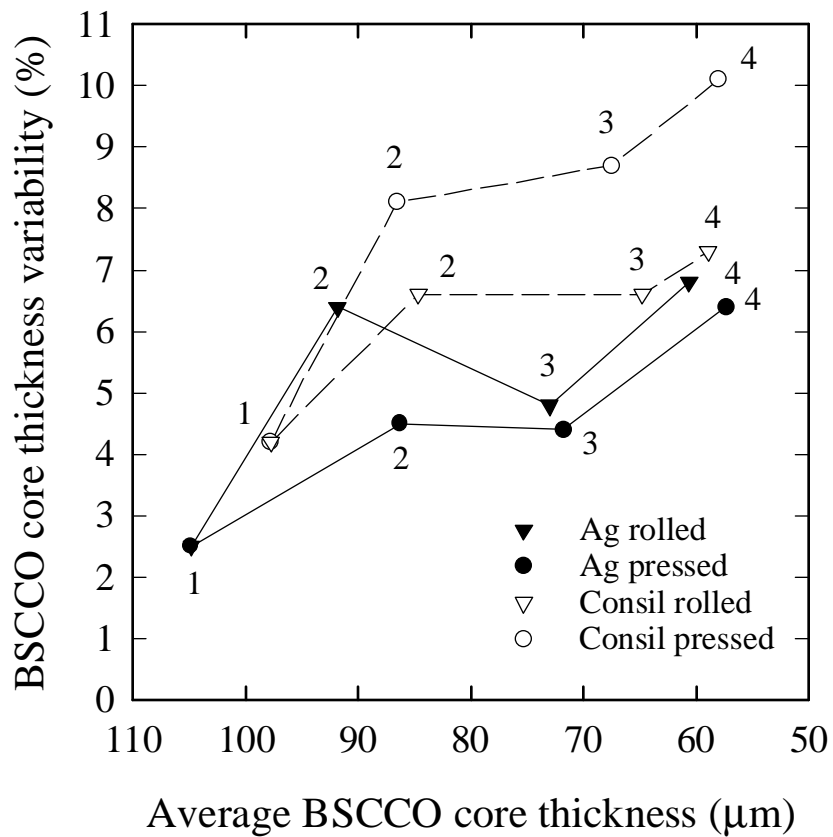


Figure 6-5. BSCCO core thickness variability as a function of the average core thickness. The numbers next to the data points indicate the number of heat treatments. Sausaging increased as the cores were made thinner.

As shown in Figure 6-3 and Figure 6-4, there is a strong correlation between the after-heat-treatment microhardness of the BSCCO and  $J_c$ . The results confirm the findings of Yamada et al. [25] and Parrell et al. [133] who reported that the microhardness and bulk density of the BSCCO core are directly correlated and that high  $J_c$  requires a high density BSCCO phase.

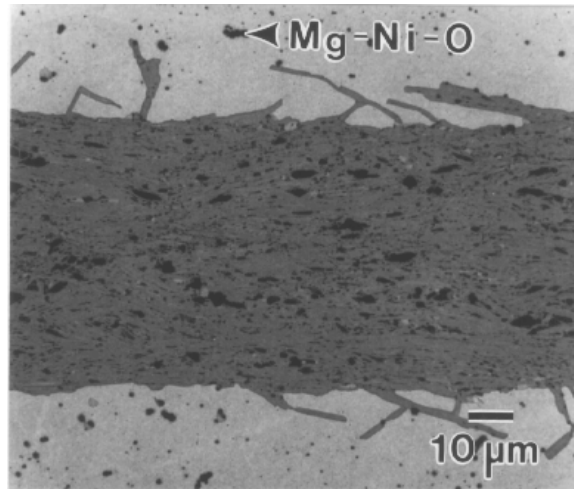


Figure 6-6. SEM backscatter micrograph of the pressed Consil-clad sample (UWB49) after the fourth heat treatment (324 hours total at 815°C in 7.35% O<sub>2</sub>).

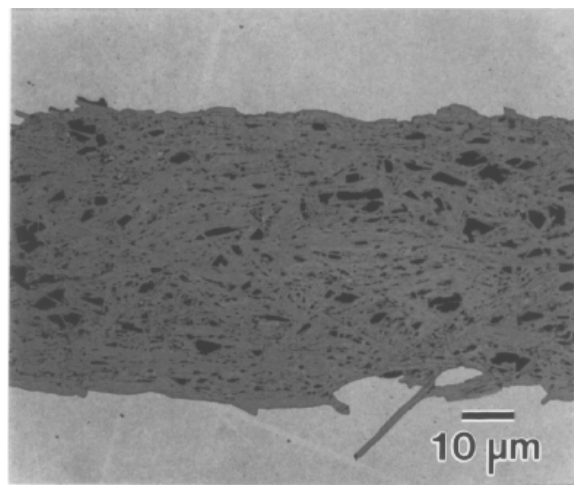


Figure 6-7. SEM backscatter micrograph of the pressed Ag-clad sample (UWB48) after the fourth heat treatment (324 hours total at 815°C in 7.35% O<sub>2</sub>).

From the microhardness and  $J_c$  data presented here, it appears that pressing the tapes between heat treatments results in a greater increase of the oxide core density than rolling, and the  $J_c$  values are indeed much higher. The BSCCO cores in the pressed Consil-clad tapes, although having hardness values comparable to the cores of pressed Ag-clad tapes, had lower overall critical current densities. A possible reason for this is that there is a chemical reaction between the alloying elements of the Consil sheath and the BSCCO core.

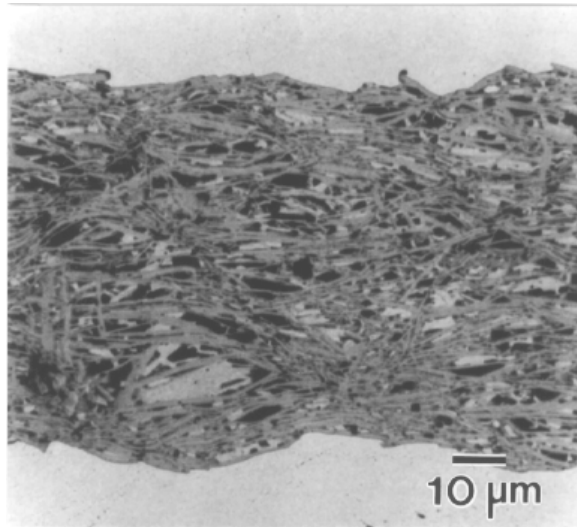


Figure 6-8. SEM backscatter micrograph of the rolled Ag-clad sample after the third heat treatment. 2212 phase (light gray) is still visible in 2223 matrix.

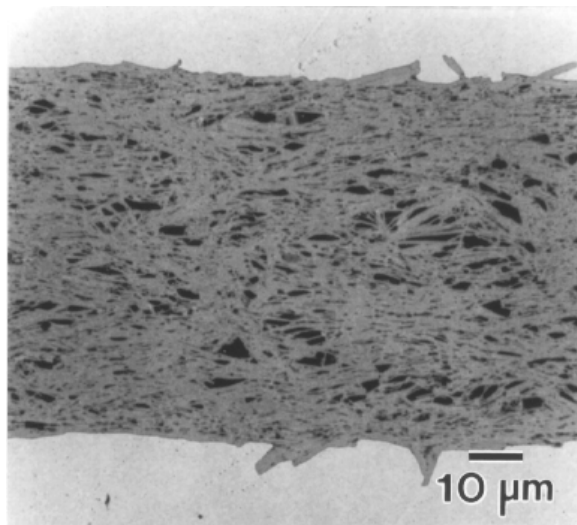


Figure 6-9. SEM backscatter micrograph of the pressed Ag-clad sample (UWB48) after the third heat treatment. No 2212 phase is visible.

Support for this hypothesis can be seen in Figure 6-6, where there appears to be a lack of Mg-Ni-O precipitates (the dark spots in the sheath) in the region immediately adjacent to the BSCCO core of the Consil clad tape. This may indicate that no Mg-Ni-O precipitates formed in this region because the alloying elements diffused into the BSCCO core, causing a lowering of  $J_c$ . Strong reactions were seen in a separate experiment involving reaction heat treatment of a previously non-hardened Consil sheath with BSCCO-2223 powder. Because of this problem, it is now common practice to insert a pure Ag “diffusion barrier” between the BSCCO and the outer alloy sheath.

The stronger Consil sheath appears to be less detrimental to the rolled tapes; as shown in Figure 6-2, the BSCCO core in Consil-clad tapes rolled between heat treatments had a higher microhardness (i.e., bulk density) than the rolled Ag-clad tapes. However, the benefit of increased oxide core density in the rolled Consil-clad samples seemed to be negated by reaction with the alloying elements, since  $J_c$  for the Ag-clad and Consil-clad tapes were similar (Figure 6-1). Thus it appears that pressing between heat treatments results in a greater densification of the BSCCO core than rolling between heat treatments, and that the harder Consil sheath helps increase the bulk oxide core density during rolling more than does the softer Ag. The reason for the latter effect may be that because the Consil-clad samples spread laterally during rolling more than the Ag-clad samples, the deformation may have been more pressing-like.

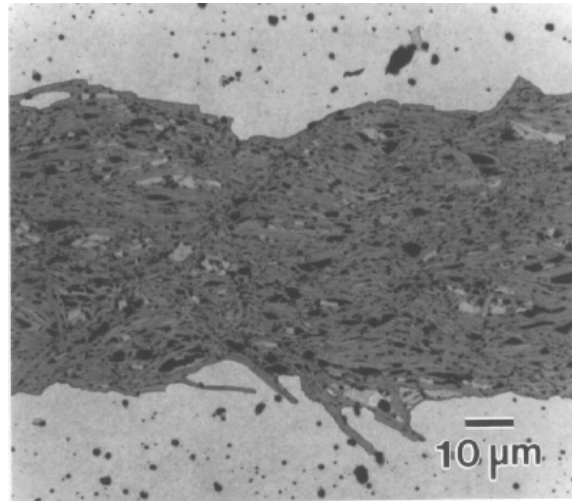


Figure 6-10. SEM backscatter micrograph of the rolled Consil-clad sample (UWB49) after the fourth heat treatment.

Examination of the microstructure of these tapes supports this hypothesis; rolled tapes with a lower microhardness and  $J_c$  appeared to have a less dense microstructure than the more dense, higher microhardness and  $J_c$  pressed samples. Figure 6-8 and Figure 6-9 are SEM micrographs after the third heat treatment of the rolled and pressed Ag-clad tapes. Note that the BSCCO grain structure appears to be less well connected in the rolled sample. Also note that the degree of alignment of the 2223 grains is less in the rolled tape than in the pressed Ag-clad tape (Figure 6-9). Of even greater note may be that the conversion from BSCCO-2212 to 2223 was less advanced in the rolled tapes. This is evident both in the SEM backscatter images (Figure 6-8 and Figure 6-9) and in measurements of the  $T_c$  transition shown in Figure 6-11.

As mentioned earlier, the degree of sausaging of the BSCCO core in the Consil-clad tapes was higher than in the Ag-clad tapes. Some of this higher variability was due to the fact that the Consil induced the growth of more plates of misaligned BSCCO into the sheath, resulting in a higher measured filament thickness variability. Between the Consil-clad samples, pressing caused a higher degree of sausaging than rolling. Part of this difference can be attributed to the fact that the rolled Consil-clad tapes had fewer plates of BSCCO protruding into the sheath than the pressed Consil-clad tapes. Figure 6-10 is an SEM micrograph of the rolled Consil-clad tape after the final heat treatment. Compare this with Figure 6-6, which shows the pressed Consil tape after final heat treatment. The reason for the growth of fewer plates of BSCCO into the sheath for the rolled samples is not entirely known, but perhaps it is related to the bulk density of the oxide core; the oxide core density is lower in the rolled samples, so the misaligned 2223 grains are relatively free to grow into the core, whereas in the higher bulk density pressed samples, growth of the misaligned grains into the dense core is less favorable, and thus the misaligned grains grow into the sheath. It does not appear that the Ag-clad tapes exhibit this behavior; however, it may just be that because there were far fewer plates growing into the Ag cladding that no trends were noticeable.

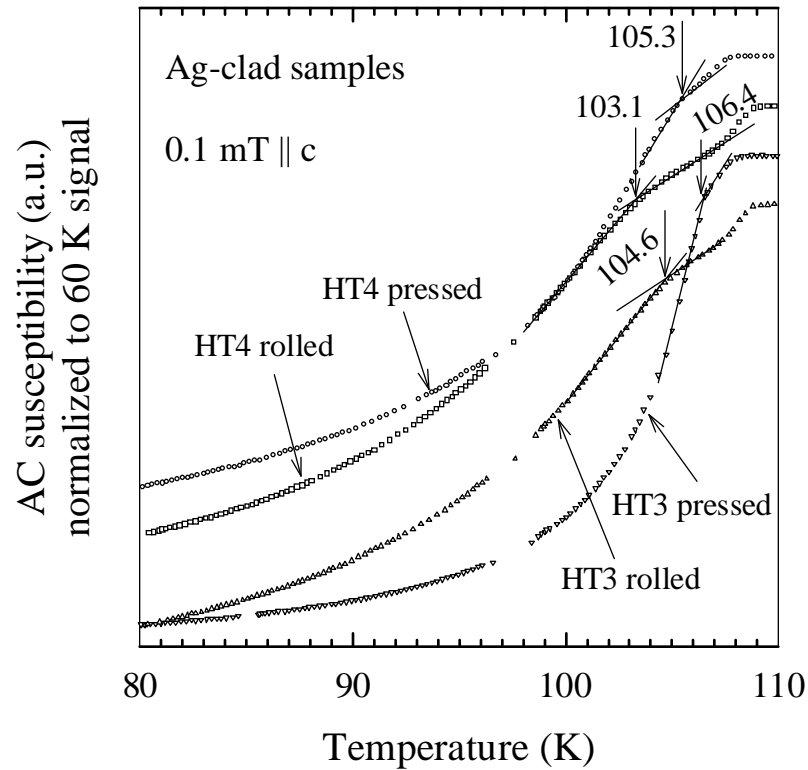


Figure 6-11. Normalized AC susceptibility of the third and fourth heat treatment Ag-clad samples (UWB48). The kink in the  $T_c$  transition occurs at higher temperatures for the pressed samples, suggesting that there are fewer residual 2212 intergrowths within the 2223 grains.

As shown in Figure 6-5, the sausaging behavior of the Ag-clad tapes was slightly different than that of the Consil-sheathed tapes; although the degree of sausaging did increase for both the pressed and rolled tapes as the BSCCO core thickness was reduced, the rolled Ag-clad tapes had a higher amount of sausaging at a given core thickness than the pressed Ag-clad tapes. However, in most cases this difference was small, and thus it may be that for core thickness ranging from  $\sim 100 \mu\text{m}$  to  $\sim 50 \mu\text{m}$ , rolling and pressing

between heat treatments causes essentially the same amount of sausageing. It is not known if the trend holds true at thinner core sizes ( $\sim 10 \mu\text{m}$ ) such as those in multifilamentary tapes.

## **6.5 Summary**

BSCCO-2223 OPIT tapes were made with pure Ag and oxide dispersion hardened Ag-Mg-Ni alloy sheaths. Samples of these tapes were reaction heat treated, and deformed between heat treatments either by pressing or rolling. A strong positive correlation between Vickers microhardness and critical current density was observed. Based on the observed greater microhardness values, it is thought that the higher  $J_c$  of the pressed tapes is due to a greater oxide core density than is present in the rolled tapes. While the hardened Ag-alloy sheath did increase the microhardness (bulk density) of the BSCCO core in the rolled tapes more effectively than the pure Ag sheath, any  $J_c$  increase as a result of this higher bulk density appeared to be negated by reactions between the BSCCO and the Mg and Ni alloying elements. The degree of transformation from the 2212 to the 2223 phase was always found to be greater in the pressed tapes. In addition, it was found that the hardened Ag-alloy-clad tapes actually exhibited greater sausageing than the pure Ag-clad tapes over the range of oxide core thicknesses observed in this study.

## 7. Residual microcracks in processed tapes

This chapter contains material from the publication:

J.A. Parrell, A.A. Polyanskii, A.E. Pashitski, and D.C. Larbalestier, “Direct evidence for residual, preferentially-oriented cracks in rolled and pressed Ag-clad BSCCO-2223 tapes and their effect on the critical current density”, *Superconductor Science and Technology* 9 (1996) 393.

### 7.1 Introduction

The fabrication of Ag-clad 2223 tapes involves one or more cycles of heat treatment, mechanical deformation, and subsequent heat treatment. The deformation steps improve the alignment of the micaceous 2223 grains [7,123,136,137], and as shown in Chapters 5 and 6, increase the density of the core [25,30,106,133,138,139] and break up the sintered structure, bringing the reactants into more intimate contact, and facilitating greater conversion of the precursor powder to the 2223 phase [30,140]. All of these effects are correlated to higher critical current density ( $J_c$ ) values. Thus, deformation is a beneficial and vital step in the fabrication of high-performance 2223 tapes.

The two most common methods for deforming 2223 tapes are cold rolling, which is the process most suitable for producing long lengths of conductor, and uniaxial pressing, which is appropriate for short lengths. To date, pressing usually results in higher  $J_c$  values than rolling, although  $J_c$  values in rolled tapes comparable to those achieved by pressing have been recently reported [19,141,142]. In Chapter 6 it was shown that one of the reasons why pressing results in higher  $J_c$  values is that rolling is less effective in densifying the oxide core [30,143], but an additional important reason for the difference is believed to be due to the different residual crack structures which the two methods produce.

As described in Section 4.2.3, rolling tends to produce cracks in the oxide core which run transverse to the long axis (rolling direction) of the tape, and uniaxial pressing tends to cause cracks which run parallel to the tape axis. The difference in crack orientation is due to the different stress states induced in the oxide core [13,120,125,128,144]. Since the reaction to form the 2223 phase from a 2212 and multiphase precursor mixture involves a liquid [40,43,45,46,47,50,51,62,145,146,147], it is implicitly believed that cracks produced during the deformation step can be healed during the subsequent heat treatment step. However, as speculated in Chapter 5, it may be that the cracks that are formed during the later stages of processing, for example during a second deformation step, are more difficult to heal [133,148], as very little liquid-formation capacity remains in a tape that is almost fully converted to 2223. When unhealed cracks remain in the oxide core after the final heat treatment, the core connectivity and fraction of the cross-section actively carrying transport current are reduced, resulting in a decrease in the macroscopic transport  $J_c$ , where  $J_c$  is defined as the

transport critical current  $I_c$  divided by the whole superconductor cross-section [127]. Cracks that run transverse to the long axis of the tape (like those produced by rolling) are thought to have a larger deleterious effect on the transport  $J_c$ , because they tend to sever the whole filament. Cracks oriented parallel to the long axis of the tape (like those produced by pressing), have a lesser effect on the axial transport  $J_c$  because the oxide core acts like an array of multiple, parallel conductors. Thus, cracks that are formed by rolling that go unhealed are much more detrimental to the transport  $J_c$  than cracks produced by pressing. Figure 4-6 illustrates the different crack structure produced in pressed and rolled tapes.

One of the central optimization problems of BSCCO-2223 tapes is that the deformation process responsible for cracking also exerts a beneficial effect on the grain alignment and the density of the core (as shown in Chapters 5 and 6), both factors which tend to raise the  $J_c$ . However, the cracks must be healed in the subsequent heat treatment if the maximum benefit of the deformation is to be obtained. Alignment and density can be measured but it is extremely hard to measure the crack density and thus to quantify the effect of residual cracks. Several authors have reported indirect electromagnetic evidence for the existence of cracks which have retained their preferential orientation, even after a subsequent heat treatment [125,149,150]. However, at the filament surface, only large cracks can be convincingly observed by light or scanning electron microscopy in heat treated samples. This implies that cracks disappear from metallographic view long before their effect on the transport critical current density disappears. This chapter directly addresses this problem in a novel way by using magneto-optical (MO) imaging to observe

how magnetic flux enters rolled and pressed samples at different stages in the processing. It was found that there is a direct correlation between the direction from which flux penetrates and the crack network produced by deformation. The MO images provide strong evidence that it is very easy to leave residual cracks in the tape after the last heat treatment, confirming the working hypothesis of Chapters 5 and 6.

## **7.2 Experimental details**

Monocore tape was made by packing  $\text{Bi}_{1.8}\text{Pb}_{0.4}\text{Sr}_{2.0}\text{Ca}_{2.0}\text{Cu}_{3.0}\text{O}_x$  powder made by a two-powder process [50,51] into a Ag tube, drawing the composite to a diameter of 1.5 mm, and by rolling the round wire into a flat tape having a width of ~ 2.5 mm and an overall thickness of ~ 175  $\mu\text{m}$ . Sections of this tape (UWB65) were given three heat treatments of 50, 100, and 100 hours length, respectively, at 825°C in a flowing 7.5%  $\text{O}_2$ /balance  $\text{N}_2$  atmosphere. Samples were either uniaxially pressed to a defined thickness using brass shim stock with glycerin as a lubricant, or cold rolled without lubricant between 3.81 cm diameter rolls to reduce their thickness by approximately 10 - 15% between each heat treatment. The final thickness of the oxide core after thermomechanical processing was ~ 60  $\mu\text{m}$  for both the pressed and rolled samples. Since pressing causes samples to spread laterally, while rolling predominantly increases the length, pressed samples tend to be slightly wider than rolled samples for a given core thickness, as can be observed in the MO images shown below.

The transport critical currents (defined at 1  $\mu\text{V}/\text{cm}$ ) of two or three 2-cm-long samples of each condition were measured at 77 K, 0 T. The critical currents were

converted to  $J_c$  by dividing by the average area of two transverse cross-sections measured by image analysis.

Samples were prepared for MO imaging [151,152,153,154,155,156] by chemically removing the Ag cladding from a rolling plane face (the broad face of the tape) using a  $\text{NH}_4\text{OH}/\text{H}_2\text{O}_2$  etch [13]. The samples were then attached to thin Cu disks with varnish, and lightly ground with 1200 grit SiC paper so as to produce a flat surface on which to place the MO film. It should be noted that samples were also examined before grinding, and that the same features were observed that are reported below. Thus, lightly grinding the surface just made the samples more flat, resulting in sharper, more detailed images, and did not modify the samples' intrinsic defect structure. MO imaging was performed by placing a ~ 2 mm thick ferromagnetic Bi-doped Y-iron-garnet film directly on the broad surface of the tape. Samples were zero field cooled to  $T = 13$  K, and then all were imaged in a magnetic field of 24 mT applied perpendicular to the tape rolling plane (i.e. nominally parallel to the c-axis of the 2223 grains). MO images were also taken at  $\mu_0 H = 40$  mT to more clearly reveal the defect structure of the sample being imaged. A schematic of the MO imaging arrangement is shown in Figure 7-1.

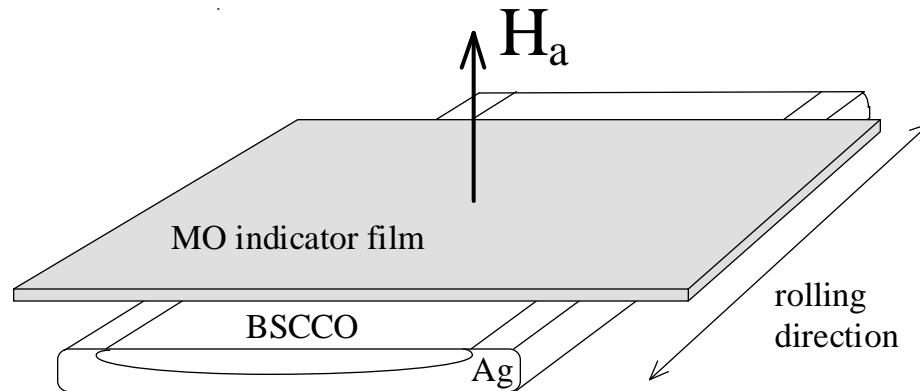


Figure 7-1. Schematic diagram of the plan-view magneto-optical imaging geometry used to reveal the residual defect structure in 2223 tapes.

To check for a correlation between the details observed on the MO images and physical features on the samples' surfaces, some samples were examined after MO imaging with a scanning electron microscope operated at 15 kV.

### 7.3 Results

Figure 7-2 shows  $J_c$  (77 K, 0 T) as a function of heat treatment time and number for the five types of samples produced in this study. After one heat treatment (HT1) of 50 hours at 825°C in 7.5% O<sub>2</sub>, the samples had a critical current density of 3 kA/cm<sup>2</sup> and contained about 70% 2223 and 30% 2212 phase, as determined by X-ray diffraction. Samples were then either rolled or pressed before a second heat treatment (HT2-rolled and HT2-pressed) of 100 hours. The  $J_c$  of both the rolled (open circles) and pressed (solid circles) samples increased to 11 kA/cm<sup>2</sup>. At this point the samples contained ~ 95% 2223.

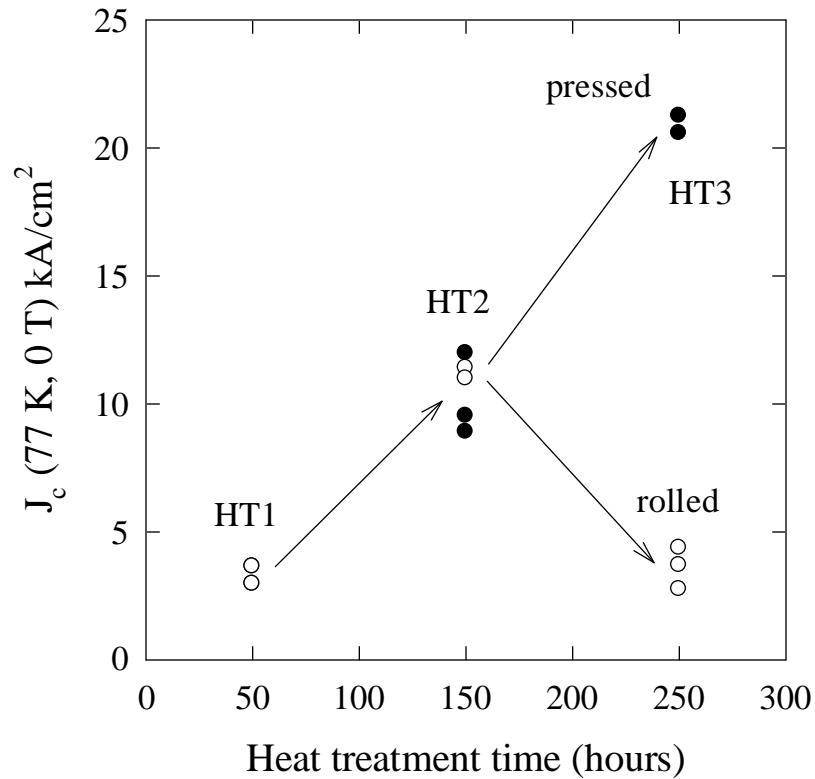


Figure 7-2.  $J_c$  (77 K, 0 T,  $1 \mu\text{V}/\text{cm}$ ) as a function of heat treatment time and number for the rolled and pressed samples of UWB65 produced in this study.

After a second deformation and a third heat treatment of 100 hours (HT3-rolled and HT3-pressed), the samples contained essentially no 2212 phase. The  $J_c$  of the pressed samples increased to  $21 \text{ kA}/\text{cm}^2$ , while the  $J_c$  of the rolled samples decreased sharply to  $4 \text{ kA}/\text{cm}^2$ . This  $J_c$  fall off for the rolled samples has been observed previously in 2223 tapes (e.g. Chapter 6 and references [30,128]).

Figure 7-3 is a representative collection of plan-view MO images of the samples whose  $J_c$  values are plotted in Figure 7-2. All samples were imaged after their individual final heat treatment, at which point it is generally assumed that deformation damage has healed. Under the imaging conditions used, the light regions indicate areas where the magnetic flux has preferentially entered the samples, and darker regions correspond to areas of lower magnetic flux densities, where induced supercurrents shield the applied field. Figure 7-3a through Figure 7-3e were taken at a constant field of  $\mu_0 H = 24$  mT, and clearly show the relative changes produced by thermomechanical processing. Figure 3a is an image of the first heat treatment (HT1) sample. This sample had a low  $J_c$  value (3 kA/cm<sup>2</sup>), and the image is of relatively low contrast. The image has a granular structure with a scale length of order 100  $\mu\text{m}$ , or several grain diameters. There appears to be no directionality associated with the flux leakage. Figure 7-3b and Figure 7-3c show the HT2-pressed and HT2-rolled samples, respectively. Both images are of higher contrast than the HT1 sample, consistent with their approximately four times greater overall  $J_c$  values. Darker bands that are visible along their centerlines indicate regions of strong flux exclusion resulting from the shielding currents induced in the samples. The width of these dark regions depends on both the overall  $J_c$  of the sample and the sample geometry. In the present case the samples' geometry only varied slightly (as mentioned earlier, pressed samples are wider than rolled samples because pressing causes samples to spread laterally, whereas rolling makes the samples longer but does not significantly increase their width), and thus the width of the dark band is an indicator of the overall  $J_c$ . For instance, the HT2 samples shown in Figure 7-3b and Figure 7-3c have approximately the same transport  $J_c$

values ( $11 \text{ kA/cm}^2$ ), and have dark regions of roughly equal widths. Figure 7-3d and Figure 7-3e compare the HT3-pressed sample, which had the highest  $J_c$  value ( $21 \text{ kA/cm}^2$ ), and the HT3-rolled sample, which had a low  $J_c$  value ( $4 \text{ kA/cm}^2$ ). There is indeed a strong difference in contrast between the two images. The rolled sample shows markedly worse shielding and clear evidence of transverse flux penetration, while the central dark region of the HT2-pressed sample grew wider in the HT3-pressed sample. The images are qualitatively in accord with the transport  $J_c$  values, the HT1 and HT3-rolled samples having  $J_c$  values of 3 and  $4 \text{ kA/cm}^2$ , and having very similar contrasts.

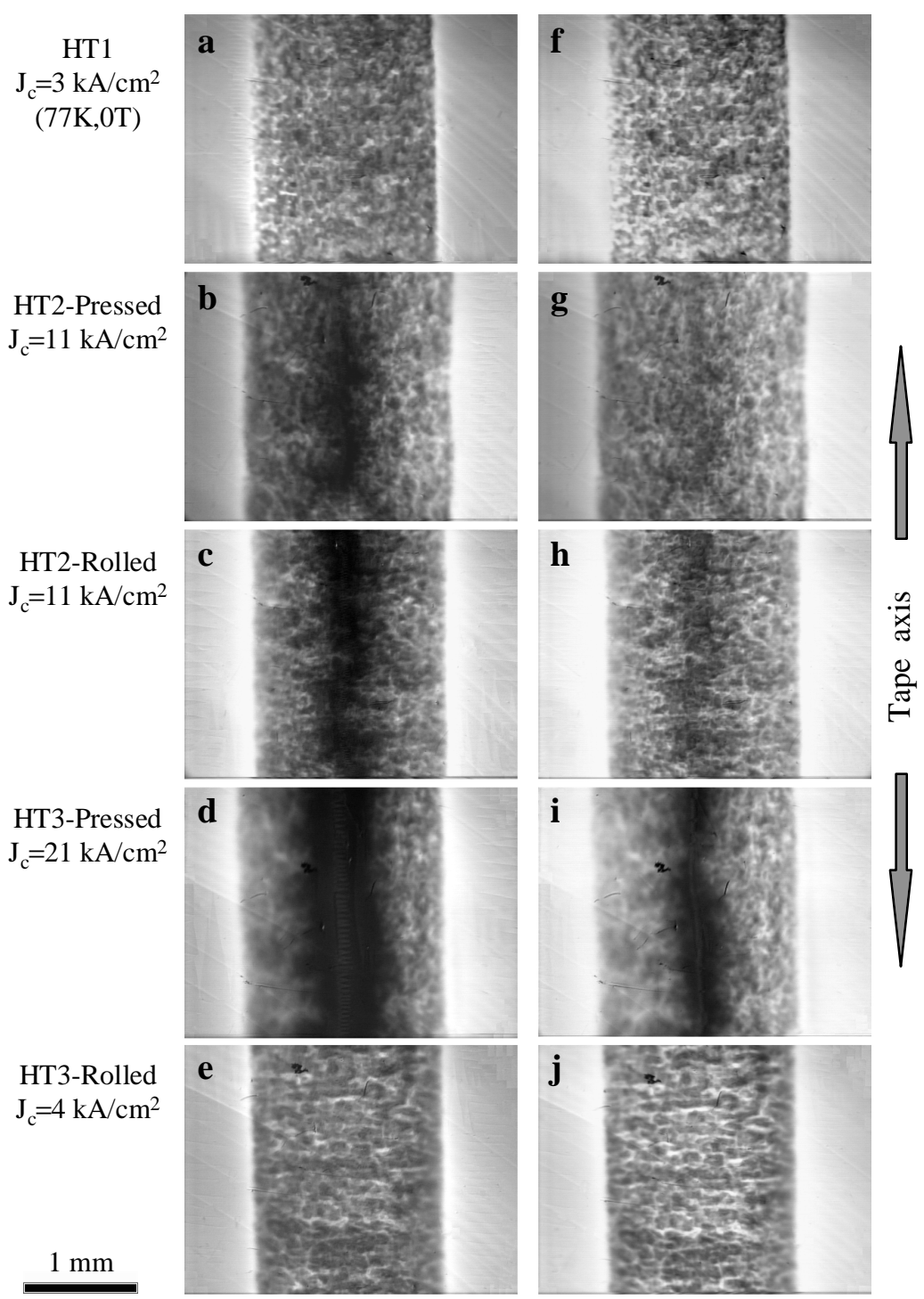


Figure 7-3. MO images of the samples whose  $J_c$  values are shown in Figure 7-2. Note that pressed samples have defects (the lighter regions) which run parallel to the original rolling direction, whereas the defects run across the core width in rolled samples.

Figure 7-3f through Figure 7-3j are images of the same samples as in Figure 7-3a- Figure 7-3e, but taken at  $\mu_0 H = 40$  mT so as to more clearly show each sample's defect structure. Figure 7-3f is an image of the HT1 sample. The granular nature noted at 24 mT in Figure 7-3a is more apparent, perhaps due to the fact that the sample is only  $\sim 70\%$  converted to 2223, and thus still contains a relatively large amount of 2212 phase. Figure 7-3g shows the HT2-pressed sample. In this sample, the flux-admitting defects run parallel to the core length, which is also the expected behavior of cracks in pressed samples. Figure 7-3h is an image of the HT2-rolled sample. It clearly shows that flux has entered transversely across the core width, as would be expected of cracks in a rolled sample. Figure 7-3i images the HT3-pressed sample, and shows that the dominant defect structure is again thin, elongated regions running parallel to the long tape axis, as in Figure 7-3g. Figure 7-3j is an image of the HT3-rolled sample, which shows many defects running across the core width, as in Figure 7-3h, but now more pronounced. Thus it appears that the principal defects visible in all the samples except the HT1 sample are cracks produced by the rolling or pressing process which were not fully healed by the subsequent heat treatment. This is particularly clear in the HT3 samples. In all cases it is clear that the samples are not fully connected, suggesting that the current flow must be percolative through the BSCCO core, as earlier shown in quantitative analysis of similar pressed samples [155,156].

Figure 7-4 is an secondary/backscattered electron mixed signal SEM image taken from the same area of the HT3-rolled sample that is shown in Figure 7-3e and Figure 7-3j, but at substantially higher magnification. Small fissures that run along the transverse

direction are visible in the micrograph, and correspond to the defects observed in the MO images. For this sample, which appeared by MO imaging to be the most heavily damaged, such defects could be detected by SEM. Cracks in the other, substantially less heavily damaged samples, were much more difficult to find. It thus appears that MO imaging is useful as a qualitative diagnostic tool for characterizing the connectivity of BSCCO tapes.

## **7.4 Discussion**

Taken together, the critical current density results of Figure 7-2 and the MO imaging results in Figure 7-3 qualitatively illustrate what takes place during the thermomechanical processing of 2223 tapes. After the first heat treatment (Figure 7-3a and Figure 7-3f), the penetration of magnetic flux into the samples is substantial but uniform. We believe this is because the conversion to 2223 is not yet complete (~ 70% 2223), and the density of the core is low [133]. After two heat treatments, regardless of deformation method, the samples become much more flux resistant, presumably because of the increased 2223 volume fraction (~ 95% 2223) and the increased core density [133]. The MO images after two heat treatments (Figure 7-3b and Figure 7-3c) show that the core structure is relatively uniform, probably because sufficient liquid-forming phases (2212 and secondary phases) remained before the second heat treatment. These were able to heal most of the deformation damage, although some evidence of residual cracks is still visible in Figure 7-3g and Figure 7-3h. After a second deformation and third heat treatment, the situation deteriorated. The deformation step was still beneficial for the pressed samples, as  $J_c$  increased from 11 kA/cm<sup>2</sup> to 21 kA/cm<sup>2</sup> even though longitudinal

cracks remained in the core (Figure 7-3d and Figure 7-3i). The  $J_c$  increase is possible because the principal crack orientation in pressed samples does not interrupt axial current flow, and because the quality of the well-connected regions of the core was improved due to the increased densification which pressing provided [133], and because the extended heat treatment time helped eliminate 2212 intergrowths [85,86]. For the rolled samples, however, the additional heat treatment time was of little value, because the more  $J_c$ -detrimental (compared to cracks produced by pressing) transverse cracks were not healed, as Figure 7-3e, Figure 7-3j, and Figure 7-4 clearly illustrate. In this case, the quality improvement of the remaining percolative current paths brought about by the additional rolling and heat treatment cycle is apparently not great enough to overcome the effect of the cracks. An additional factor may be that rolling is less effective than pressing in densifying the core [30], a supposition consistent with the markedly lower contrast of the MO image. This conclusion is also consistent with the influence of rolling and pressing on hardness and  $J_c$ , as described in Chapter 6.

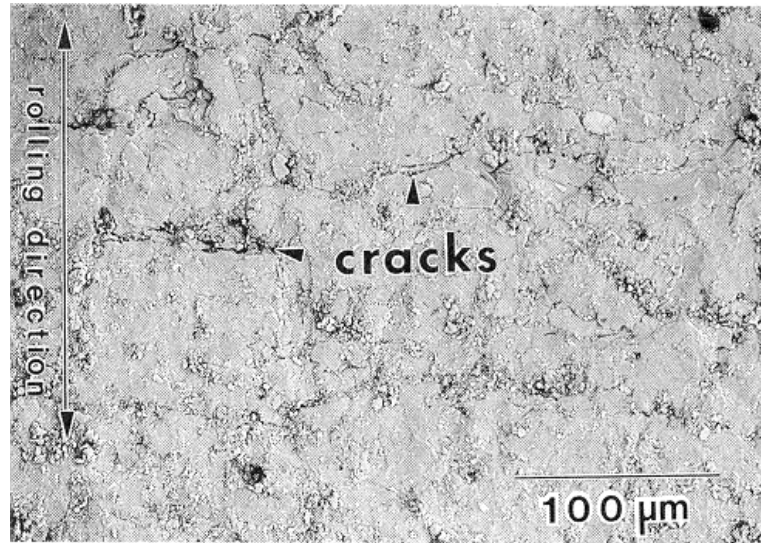


Figure 7-4. Plan-view scanning electron micrograph of the HT3-rolled sample whose MO images are shown in Figure 7-3e and Figure 7-3j. Small cracks that run transverse to the rolling direction are visible in some regions.

This experiment clearly illustrates the diminishing returns of continuing to deform and heat treat 2223 tapes after the conversion to 2223 is essentially complete, and no liquid phase is available [133,148]. Although cracks in pressed samples which do not heal during heat treatment are less detrimental to the transport  $J_c$  than cracks formed in rolled tapes (because of their more favorable alignment, and the improved density and properties of the remaining well-connected percolative path), eventually the cracking can become so severe that the transport  $J_c$  will decrease even for pressed tapes [e.g. references 45,123,128,139,140,157,158]. It is thus concluded that it is very important to optimize heat treatment and deformation parameters [19,133] so as to avoid the formation of large

cracks which cannot be healed during heat treatment because the conversion to 2223 has already been largely completed.

## **7.5 Summary**

Magneto-optical imaging was used to visually expose the deformation-induced defect structure that remains in Ag-clad BSCCO-2223 monocoil tapes, even after heat treatment. Through two heat treatments, tapes rolled or uniaxially pressed exhibited similar  $J_c$  values ( $11 \text{ kA/cm}^2$ ), although different defect structures were observed using magneto-optical imaging. After another deformation and heat treatment step, however, while the  $J_c$  of pressed samples increased to  $21 \text{ kA/cm}^2$ , the  $J_c$  of rolled samples decreased to  $4 \text{ kA/cm}^2$ . Magneto-optical imaging revealed many defects where magnetic flux easily penetrated, even after heat treatment, in both pressed and rolled samples. These defects were confirmed by SEM to be cracks, believed to have been produced during the deformation steps, which could not be healed during the final heat treatment because insufficient residual liquid phase. The defects were more detrimental to the transport  $J_c$  of rolled samples than of pressed samples, because cracks in rolled samples tend to run transverse to the direction of current flow, thus severing the filament, whereas cracks in pressed samples tend to run parallel to the direction of current flow, breaking the oxide core up into multiple parallel paths for superconducting current flow. It was shown that magneto-optical imaging can be used as a fast and relatively simple method to obtain valuable information about the connectivity of a BSCCO core.

## **8. Control of the liquid phase and the healing of microcracks**

### ***8.1 Controlled, reversible decomposition of 2223 tapes in oxygen atmospheres into pseudoprecursor phase mixtures***

This section contains material from the publication:

J.A. Parrell, Y. Feng, S.E. Dorris, and D.C. Larbalestier, "Controlled decomposition and reformation of the 2223 phase in Ag-clad  $(\text{Bi,Pb})_2\text{Sr}_2\text{Ca}_2\text{Cu}_3\text{O}_x$  tapes and its influence on the microstructure and critical current density", *Journal of Materials Research* 11 (1996) 555.

#### **8.1.1 Introduction**

As discussed in previous chapters, the fabrication of Ag-clad 2223 tapes requires a process of one or more heat treatment, mechanical deformation, and subsequent heat treatment cycles. This process has developed empirically and many of its details are still

not understood. It is generally believed that the deformation steps are necessary to develop the alignment of the plate-like 2223 grains [7], although recent work by Thurston et al. [108] shows that this may not always be true. The deformation steps do increase the density of the core [25,30,133], thus increasing its connectivity. Both effects correlate to an increased  $J_c$ . As shown in Chapter 6, an additional benefit of the deformation steps is that they break up the sintered structure and bring the reactants into more intimate contact, facilitating greater conversion of the precursor powder to 2223 [30]. For these multiple reasons, deformation is a beneficial and vital step in the fabrication of high-performance 2223 tapes. However, as shown in Chapter 7, if the deformation causes cracks in the oxide core that do not heal during the final reaction heat treatment [125,128,133], the active cross-section of the core will be reduced, resulting in a decrease in the effective conductor  $J_c$  [30,127,133] (recall that  $J_c$  is conventionally defined as the critical current  $I_c$  divided by the entire BSCCO cross-section  $A$ , irrespective of how much of the cross-section is carrying current). This potentially deleterious effect of deformation is difficult to quantify because only large cracks ( $\sim 5 \mu\text{m}$  or longer) are obvious in polished cross-sections, and such cracks are relatively rare. Smaller scale cracks, voids, or unbonded interfaces may exert a far greater effect, while being essentially invisible to standard metallographic observation. Figure 8-1 illustrates schematically the conventional thermomechanical processing schedule of heat treatment, deformation and cracking, and partial crack healing during subsequent heat treatment.

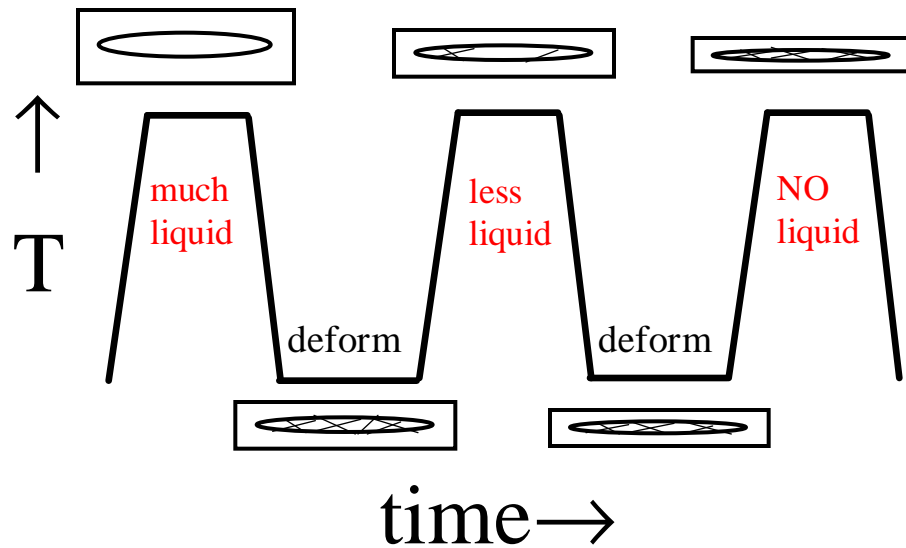


Figure 8-1. Illustration of the conventional thermomechanical processing of 2223 tapes. Deformation (pressing in this case) makes the tape thinner and densifies the core, but also causes cracks to form, as shown in the schematic transverse tape cross sections. These cracks may only be partially healed during the subsequent heat treatment.

The formation of the 2223 phase is believed to proceed by a reaction between  $\text{Bi}_2\text{Sr}_2\text{Ca}_1\text{Cu}_2\text{O}_y$  (hereafter referred to as "2212"), alkaline earth cuprate phases, and a liquid phase [40,43,45,46,47,50,51,62,145,146]. One of the most effective ways to make a nearly phase-pure 2223 microstructure is to blend Pb-doped 2212 powder with a mixture of  $\text{Ca}_2\text{CuO}_3$  and  $\text{CuO}$  [50,51]. Such a "two-powder" mixture reacts quickly to the 2223 phase, leaving only small  $(\text{Ca,Sr})_2\text{CuO}_3$  particles as the principal residual second phase. While such a powder mixture can yield reproducible  $J_c$  (77 K, 0 T) values in the 15 - 30  $\text{kA/cm}^2$  range [50,51,30,133], these values are not as high as might be expected on the

basis of their high phase purity. Their apparent  $J_c$  shortfall focuses attention on other factors which control the  $J_c$ , one of which may be the residual crack network left after each deformation step, as shown in Chapter 7. It is plausible that a liquid can heal these crack networks. However, an inherent problem with the established process for fabricating BSCCO-2223 tapes is that the liquid-forming precursors are consumed as the reaction to 2223 moves toward completion, and there may thus be little or no liquid-formation capacity in a nearly fully converted tape.

In principle, two distinct types of liquid are available in the 2223 system: one type that forms "naturally" from eutectic reactions between 2212 and secondary phases within the 2223 stability range ( $\approx 800\text{-}830^\circ\text{C}$  in 7.5%  $\text{O}_2$ ), and a second type formed by partially melting the 2223 at temperatures above the stability limit [33,43,53,118]. It is generally but not universally [159,160] believed that the high-temperature 2223 stability limit should not be exceeded, because 2223 does not re-form upon cooling [44] due to extensive phase segregation during partial melting. Thus, it is may be more advantageous to control the liquid phase content by manipulating the volume fraction of phases that form eutectics, namely 2212,  $(\text{Ca,Sr})_2\text{PbO}_4$ , and alkaline earth cuprates. This can be done by decomposing 2223 below its melting point, as will be shown later.

The volume fraction of liquid-forming 2212 and secondary phases present in a tape can be controlled to some degree by closely monitoring the extent of 2223 formation throughout the thermomechanical processing sequence. An optimized schedule could involve reacting the tape to form the optimum volume fraction of 2223 before the final deformation step, then giving the final reaction heat treatment after the last deformation

step. The final heat treatment would then explicitly have dual purposes: first to convert the remaining precursor phases into 2223, and second to use the residual eutectic liquid to heal deformation damage, as discussed in Chapter 5 [133]. However, as 2223 generally does not form uniformly throughout the core thickness (the reaction often starts at the Ag interface [33,103]), liquid is not always available uniformly throughout the core. Furthermore, as  $J_c$  has been shown to be directly correlated to the density of the 2223 core [25,30,133], and because 2223 formation is known to be accompanied by a decrease in density (due to the retrograde densification which occurs during reaction [69,129,133]), it is desirable to deform a core which is already fully converted to 2223 in order to achieve the highest possible density.

The two goals of thermomechanical processing thus require a difficult compromise; it is desirable from a  $J_c$  point of view to form a 2223 structure that is as phase-pure, dense, and aligned as possible, but at the same time there should remain enough precursor phases to form sufficient liquid to heal any deformation-induced cracks. We believe that the inherent conflicts in this compromise are a major factor in explaining the difficulty of reliably achieving high  $J_c$  values in BSCCO-2223 tapes.

In this study, an alternative method of controlling the liquid-producing secondary phases was developed, through a controlled solid-state decomposition process. This process was developed in parallel with work by Grivel and Flükiger, who proposed a similar process on the basis of an X-ray diffraction study, which showed that 2223 tapes could be reversibly decomposed in air [161].

In this controlled decomposition/reformation (CDR) process, a tape is fully processed so as to form a 2223 structure which is as phase-pure, dense, and aligned as possible, without concern for residual cracks. The 2223 is then partially decomposed to form a controlled amount of 2212,  $(\text{Ca,Sr})_2\text{PbO}_4$ , and other secondary phases. Since these are the same phases often found in 2223 precursor powder mixtures, this decomposition can be considered as a "back-reaction" into precursor phases. When the tape is subsequently heated under 2223 formation conditions, these decomposition by-products react again to form 2223, and the liquid that forms in the process helps to heal the cracks. Thus, the essence of the process is that the initial thermomechanical processing produces a fully reacted, highly aligned, and highly dense 2223 core, which is likely to contain cracks. The tape is then slightly decomposed to produce some liquid forming phases without greatly perturbing the aligned 2223 grain structure. A final heat treatment is then given to re-form the 2223 phase, and the liquid that is formed from the decomposed phases heals residual cracks left over from the deformation steps.

An overview of the CDR processing schedule is illustrated in Figure 8-2. The schematic microstructural changes at each stage of processing are shown in Figure 8-3. This chapter describes experimental tests of both the microstructural and critical current density aspects of the CDR process.

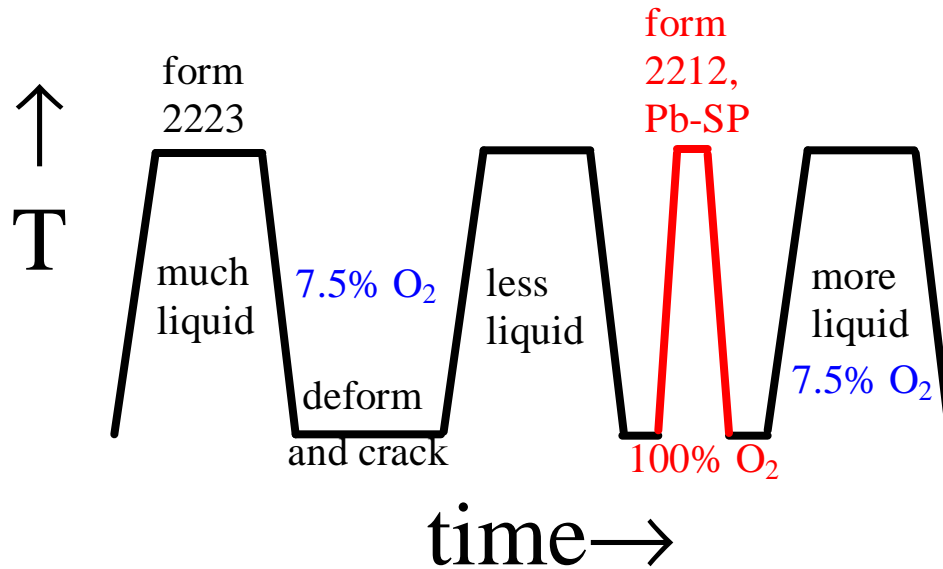
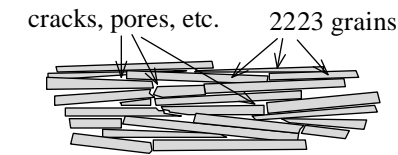


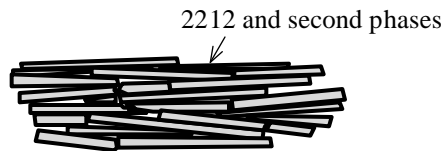
Figure 8-2. Schematic of the controlled 2223 decomposition/reformation (CDR) thermomechanical processing schedule. A decomposition step is added between heat treatments to re-form a controlled quantity of the liquid producing second phases in the 2223 microstructure. The decomposition step may or may not require a change of temperature.

### 8.1.2 Experimental details

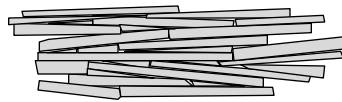
Samples of Ag-clad 2223 tape (UWB65) made from a two-powder process [50,51] ( $\text{Bi}_{1.8}\text{Pb}_{0.4}\text{Sr}_{2.0}\text{Ca}_{1.0}\text{Cu}_{2.0}\text{O}_x$  and "CaCuO<sub>y</sub>" powders mixed to give an overall composition of  $\text{Bi}_{1.8}\text{Pb}_{0.4}\text{Sr}_{2.0}\text{Ca}_{2.0}\text{Cu}_{3.0}\text{O}_z$ ) were given two reaction heat treatments of first 50 and then 150 hours at 825°C in a 7.5% O<sub>2</sub>/balance N<sub>2</sub> atmosphere, with a 1 GPa uniaxial pressing applied between heat treatments. After this thermomechanical processing, the samples were approximately 95% converted to 2223, as estimated by X-ray diffraction (XRD) intensity ratios for the 2212 (008) and 2223 (0010) peaks. At this point some samples



As-processed 2223 microstructure:  
contains cracks and unbonded  
regions (white areas)



After 2223 decomposition in 100% O<sub>2</sub>:  
liquid-forming phases (black) coat 2223  
grains (see text)



After 2223 reformation in 7.5% O<sub>2</sub>:  
liquid phase produced during 2223  
formation improves core connectivity

Figure 8-3. A schematic illustration of the hypothesized microstructural changes in the controlled decomposition/reformation (CDR) process. Liquid-forming phases are produced in a 2223 tape by partially decomposing the 2223 phase in 100% O<sub>2</sub>. When 2223 is re-formed in 7.5% O<sub>2</sub>, the liquid phase helps to heal cracks and increases the core connectivity. Secondary phases such as alkaline earth cuprates have been omitted for clarity.

were given a solid-state decomposition, before then being given a final pressing and 2223-formation heat treatment, as described below.

Although 2223 can be reversibly decomposed below  $\sim 800^\circ\text{C}$  in both 7.5%  $\text{O}_2$  and in air [161,162], previous experiments on two-powder tapes have shown that decomposition to 2212 and secondary phases in 7.5%  $\text{O}_2$  occurs rather slowly [119,163]. However, the kinetics of decomposition are faster in 100%  $\text{O}_2$ , because 2223 is unstable at all temperatures up to the melting point and thus the decomposition can be done at higher temperatures. Decomposition in 100%  $\text{O}_2$  results in the formation of 2212,  $(\text{Ca,Sr})_2\text{PbO}_4$ , and other secondary phases [111,164]. For these reasons, 100%  $\text{O}_2$  (total pressure 1 atmosphere) was used for this study.

In order to control the amount of 2223 that was decomposed (and thus the amount of liquid-producing phases formed), the kinetics of the decomposition reaction at  $825^\circ\text{C}$  in 100%  $\text{O}_2$  were studied by XRD. Using this information, we prepared three sample sets for a third and final 2223-formation heat treatment: a) a control set which did not undergo any decomposition and contained  $\approx 5\%$  2212; b) a partially decomposed set produced by heating at  $825^\circ\text{C}$  in 100%  $\text{O}_2$  for 3 hours to form  $\approx 10\%$  2212; and c) a partially decomposed set produced by heating at  $825^\circ\text{C}$  in 100%  $\text{O}_2$  for 48 hours to form  $\approx 30\%$  2212. All three sample sets were then given a final 1 GPa uniaxial pressing followed by a 2223 re-formation heat treatment of 200 hours at  $825^\circ\text{C}$  in 7.5%  $\text{O}_2$ , and were then slowly cooled from  $825^\circ\text{C}$  to  $730^\circ\text{C}$  at  $\approx 9^\circ\text{C}/\text{hour}$ . This cooling rate was found to give the highest  $J_c$  for this particular composite [119]. After the samples reached  $730^\circ\text{C}$ , they were furnace cooled at  $\sim 500^\circ\text{C}/\text{hour}$ . The dimensions of the control and decomposed samples

were nominally identical both before and after the final 1 GPa pressing, and thus all of the samples were equally strained by the final pressing.

After the final heat treatment, the three sample sets were examined by XRD and scanning electron microscopy (SEM). The decomposed samples were also examined by transmission electron microscopy (TEM). Longitudinal TEM specimens were made by gluing several tape segments together along their broad faces. Slices were cut and ground to about 40  $\mu\text{m}$  thickness and were then mounted on gold grids. The samples were dimpled, Ar-ion milled at 4.5 kV in a liquid nitrogen cooled stage, and then examined in a Philips CM200 Ultratwin HRTEM at 200 kV. The critical currents (defined at 1  $\mu\text{V}/\text{cm}$ ) of one to six 2-cm-long samples for each condition were measured at 77 K, 0 T with five voltage taps spaced 2 mm apart. The critical currents were converted to  $J_c$  by dividing by the average area of three transverse cross-sections.

### 8.1.3 Results

The kinetics of the decomposition reaction at 825°C in 100% O<sub>2</sub> are shown in Figure 8-4, where it can be seen that the amount of 2212 (determined by comparing the intensities of the 2212 (008) and 2223 (0010) lines) formed by decomposition increases linearly with the square root of time. As no liquid phase should exist in the system under these heat treatment conditions, the parabolic kinetics of the process suggest that the decomposition of 2223 in 100% O<sub>2</sub> occurs via solid-state diffusion.

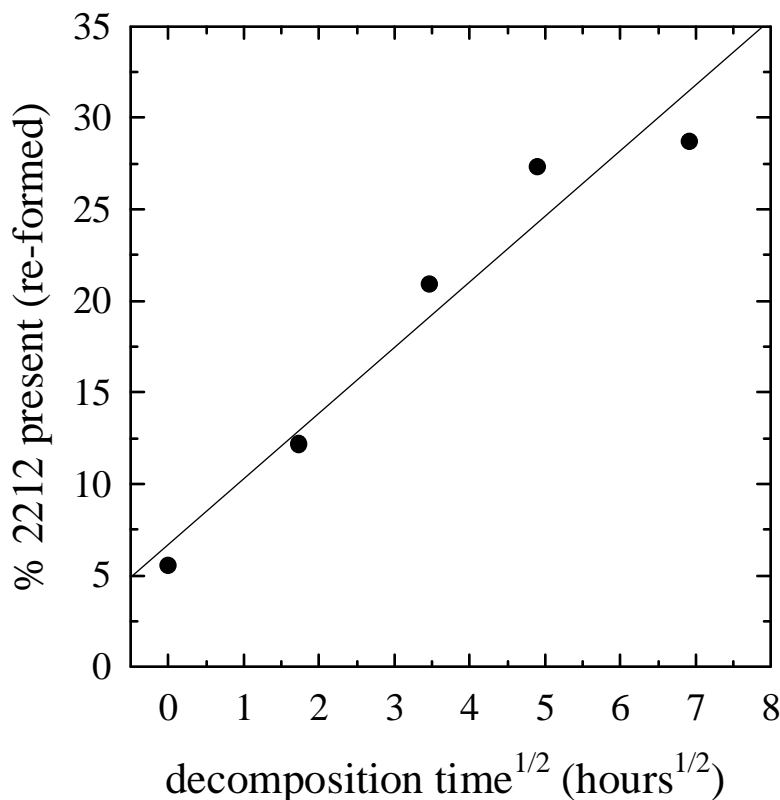


Figure 8-4. The amount of 2212 present in samples of UWB65 (as determined by XRD) as a function of the square root of time held at 825°C in 100% O<sub>2</sub>. The decomposition reaction exhibits parabolic kinetics.

Figure 8-5 shows the XRD traces after each stage in the processing sequence for all of the sample sets. Figure 8-5a shows the XRD pattern after the first heat treatment, at which point the samples contained  $\approx 70\%$  2223. Figure 8-5b shows the trace taken after the second heat treatment, when the samples contained  $\approx 95\%$  2223. Figure 8-5c and Figure 8-5d are the diffraction patterns for samples decomposed for 3 and 48 hours in 100% O<sub>2</sub>, respectively. After decomposition, the amount of 2212 had increased from  $\approx$

5% to  $\approx 10\%$  for the 3 hour decomposition, and to  $\approx 30\%$  for the 48 hour decomposition. Strong alkaline earth cuprate (AEC) signals, believed to be mainly due to  $(\text{Ca,Sr})_{14}\text{Cu}_{24}\text{O}_{41}$  based on SEM-EDS results, are clearly visible in both of the decomposed sample traces, and a  $(\text{Ca,Sr})_2\text{PbO}_4$  peak is apparent in the sample decomposed for 48 hours (Figure 8-5d). The  $(\text{Ca,Sr})_{14}\text{Cu}_{24}\text{O}_{41}$  phase is more prominent in the samples that were treated in 100%  $\text{O}_2$  than in the samples only treated in 7.5%  $\text{O}_2$  (Figure 8-5a and Figure 8-5b), because this phase is more stable in higher oxygen partial pressures [33]. Figure 8-5e and Figure 8-5f show the diffraction patterns from the 3 and 48 hour decomposed samples after the final pressing and 2223-formation heat treatment. Figure 8-5g shows the diffraction pattern from a control sample (which received no decomposition) after the final 2223-formation heat treatment. The pattern from the 3 hour decomposed sample after the final heat treatment (Figure 8-5e) is essentially identical to that of the control sample (Figure 8-5g), but greater amounts of residual 2212 and second phase are visible in the trace from the 48 hour decomposed sample after the final heat treatment (Figure 8-5f). The amount of residual second phase in the control sample (particularly  $(\text{Ca,Sr})_2\text{PbO}_4$  and a phase believed to be  $(\text{Bi,Pb})_3\text{Sr}_2\text{Ca}_2\text{Cu}_1\text{O}_x$ , hereafter referred to as "3221" [161,162,165]) is higher after the third heat treatment (Figure 8-5g) than after the second heat treatment (Figure 8-5b) because all of the samples were slowly cooled after the final 2223-formation heat treatment. This slow cooling, although beneficial to the superconducting properties, reduces the 2223 phase purity [119]. The Ag peak appears to grow throughout the processing sequence because the XRD samples were prepared by cutting the edges of the tapes and peeling them apart to expose the BSCCO core. The tapes were much thinner

after the second and third heat treatments than after the first heat treatment (because they were been pressed between heat treatments), and when thinner tapes are peeled apart, there is a greater likelihood of the BSCCO core being thin enough in some sections for the X-rays to penetrate through to the Ag cladding. Thus the apparent growth of the Ag peak is not relevant to the phase transformations described in this chapter.

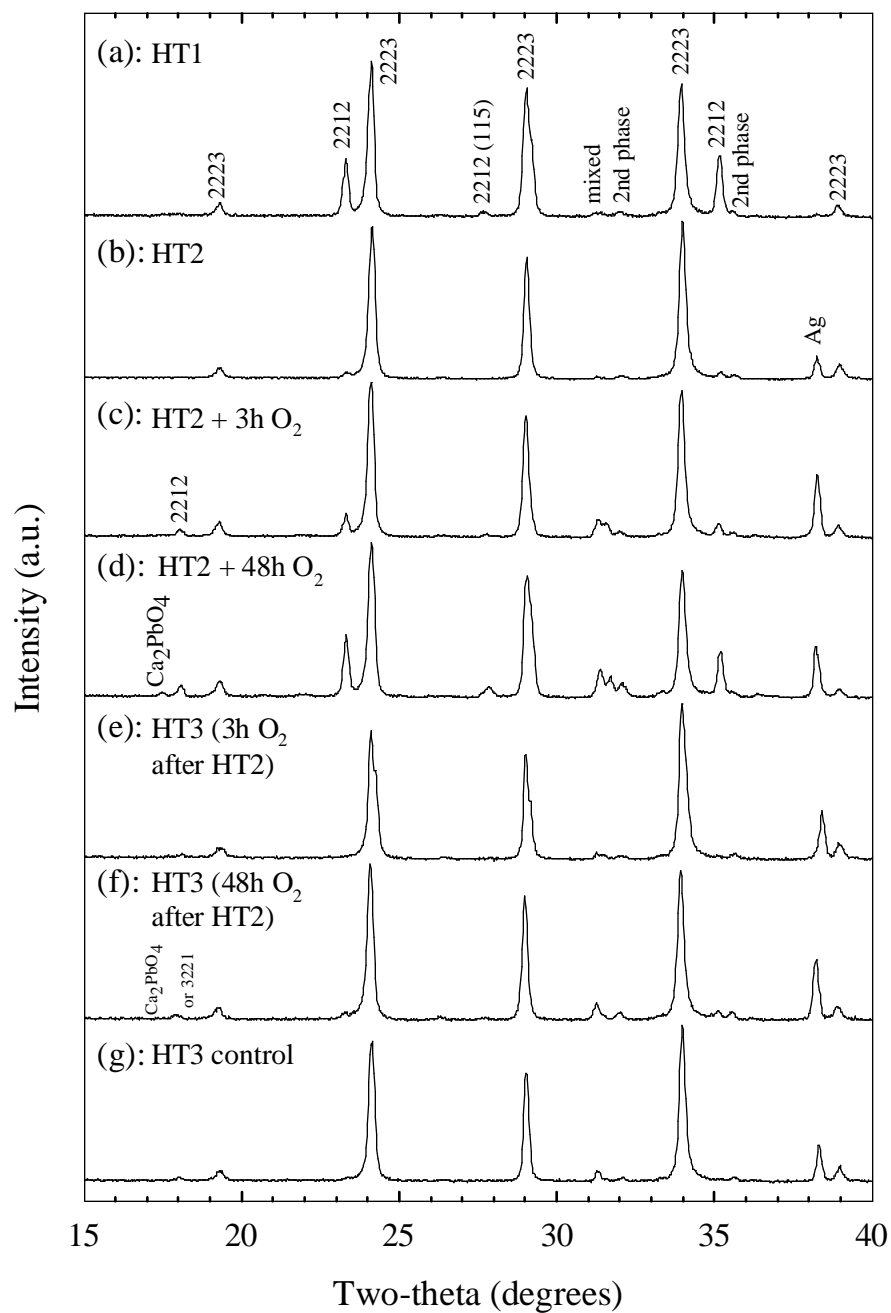


Figure 8-5. XRD spectra of samples from the decomposed samples sets. Heating 2223 tapes in 100% O<sub>2</sub> resulted in 2212 and secondary phase formation, which converted back to 2223 in the final 7.5% O<sub>2</sub> heat treatment. The peaks are identified in the figure in which they first appear.

Figure 8-6 presents a series of SEM backscatter photomicrographs corresponding to the XRD traces of Figure 8-5. The series follows each step of the processing sequence of the CDR-processed sample sets. Figure 8-6a shows the microstructure after the first heat treatment. Large regions of 2212 (light gray) are rather uniformly mixed with the 2223 grains (darker gray) throughout the entire core thickness. At this stage, the principal non-superconducting phase is  $(\text{Ca,Sr})_2\text{CuO}_3$  (black particles). Figure 8-6b shows the microstructure after two heat treatments totaling 200 hours at 825°C in 7.5%  $\text{O}_2$ . Essentially no 2212 is visible, and only a few non-superconducting second phase particles (still mainly  $(\text{Ca,Sr})_2\text{CuO}_3$  at this point) are present. Figure 8-6c and Figure 8-6d show the microstructure of samples after decomposition in 100%  $\text{O}_2$  at 825°C for 3 and 48 hours, respectively. A large number of mostly fine (but some  $> 5 \mu\text{m}$  in diameter) well dispersed  $(\text{Ca,Sr})_2\text{PbO}_4$  particles appear throughout the core in both cases, as do large alkaline earth cuprate particles (now mostly  $(\text{Ca,Sr})_{14}\text{Cu}_{24}\text{O}_{41}$  instead of  $(\text{Ca,Sr})_2\text{CuO}_3$  as before). Long, thin 2212 grains that have grown in an apparently random manner throughout the core are plainly visible in the sample decomposed for 48 hours (Figure 8-6d). A phase similar to  $(\text{Ca,Sr})_2\text{PbO}_4$ , which is believed to be the 3221 phase, was also observed in the decomposed samples. Figure 8-6e and Figure 8-6f show the microstructures of samples that were decomposed for 3 and 48 hours, respectively, and then pressed and given a third heat treatment of 200 hours at 825°C in 7.5%  $\text{O}_2$ . In neither case are 2212 grains visible and most of the fine  $(\text{Ca,Sr})_2\text{PbO}_4$  and 3221 particles have disappeared. The samples appear to have converted back to 2223. Large alkaline earth cuprate particles, mainly  $(\text{Ca,Sr})_{14}\text{Cu}_{24}\text{O}_{41}$ , remain in the structure, as do some large  $(\text{Ca,Sr})_2\text{PbO}_4$ -like particles

(probably the 3221 phase). Figure 8-6g shows the microstructure of the control set after the third 2223-formation heat treatment. Some alkaline earth cuprate and  $(\text{Ca,Sr})_2\text{PbO}_4$ -like particles are also present in the microstructure of the control samples (Figure 8-6g), which as mentioned before, is a result of the slow cooling rate used after the final heat treatment of all the sample sets. Taken as a whole, this sequence of photomicrographs is consistent with and augments the XRD traces of Figure 8-5. Both sequences show that the decomposition of the 2223 phase is apparently reversible. However, the 2223 and non-superconducting phase balance is not the same at the end of the decomposition and re-formation treatment as at the beginning; the second phase content is higher and the particle size is noticeably larger in both Figure 8-6e and Figure 8-6f than in Figure 8-6b. Although some of this second phase volume fraction increase can be attributed to the slow cooling treatment, not all of it can be, as the amount of second phase in the CDR-processed samples after the last heat treatment is greater than the amount in the final heat treatment control samples (Figure 8-6g).

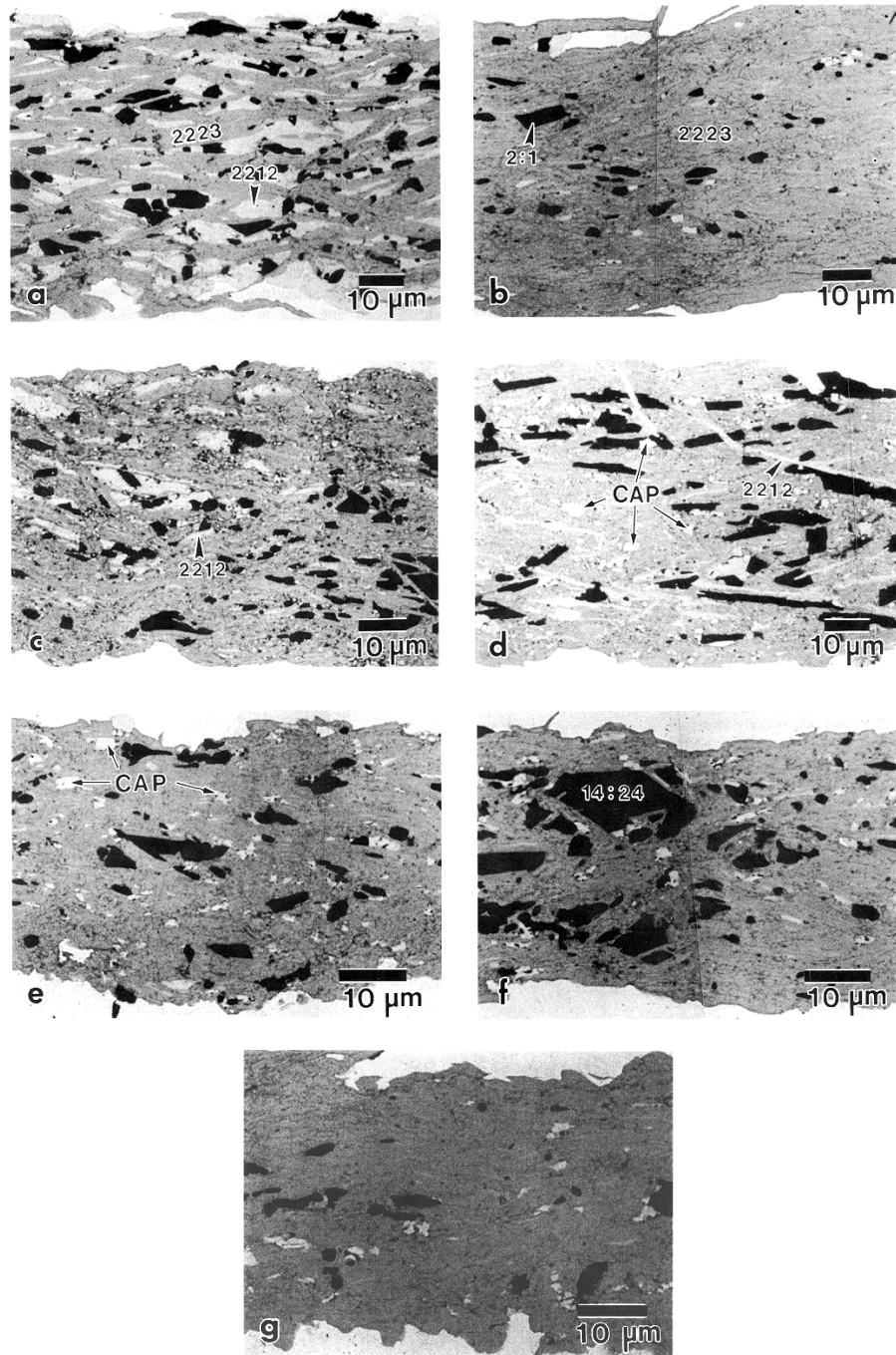


Figure 8-6. Microstructures of the decomposed samples. (a) and (b) show the microstructure development through the first and second heat treatments in 7.5% O<sub>2</sub>. (c) and (d) show how the 2223 phase decomposed to 2212 and Pb-rich phases (“CAP”) after heating in 100% O<sub>2</sub> for 3 and 48 hours at 825°C. (e) and (f) show the samples from (c) and (d) after a final 7.5% O<sub>2</sub> heat treatment, and (g) shows the control sample after the heat

Figure 8-7 plots  $J_c$  (77 K, 0 T) as a function of heat treatment time and number for the three sample sets. Figure 8-7a shows how  $J_c$  developed through three 2223-formation heat treatments for the control samples without decomposition. The behavior observed is typical. The critical current density increased with each deformation and heat treatment step, from  $\sim 4 \text{ kA/cm}^2$  after the first heat treatment, to 10-15  $\text{kA/cm}^2$  after the second heat treatment, and to 12-20  $\text{kA/cm}^2$  after the third heat treatment. Figure 8-7b and Figure 8-7c show the data sets from the samples that were decomposed in 100%  $\text{O}_2$  for 3 and 48 hours, respectively, and then pressed and given a final 2223-formation heat treatment. The data for the first and second heat treatments in Figure 8-7b and Figure 8-7c are the same as for the control data set in Figure 8-7a, because the decomposition step was given after the second heat treatment. After the decomposition,  $J_c$  decreased to almost zero in both cases, as indicated by the downward arrows in Figure 8-7b and Figure 8-7c. After the last pressing and final 2223 formation heat treatment, the  $J_c$  values sharply increased. The  $J_c$  of the samples decomposed for 3 hours increased back to about the same level as the control set (12-20  $\text{kA/cm}^2$ ), while those decomposed for 48 hours in 100%  $\text{O}_2$  increased to slightly lesser  $J_c$  values (10-17  $\text{kA/cm}^2$ ).

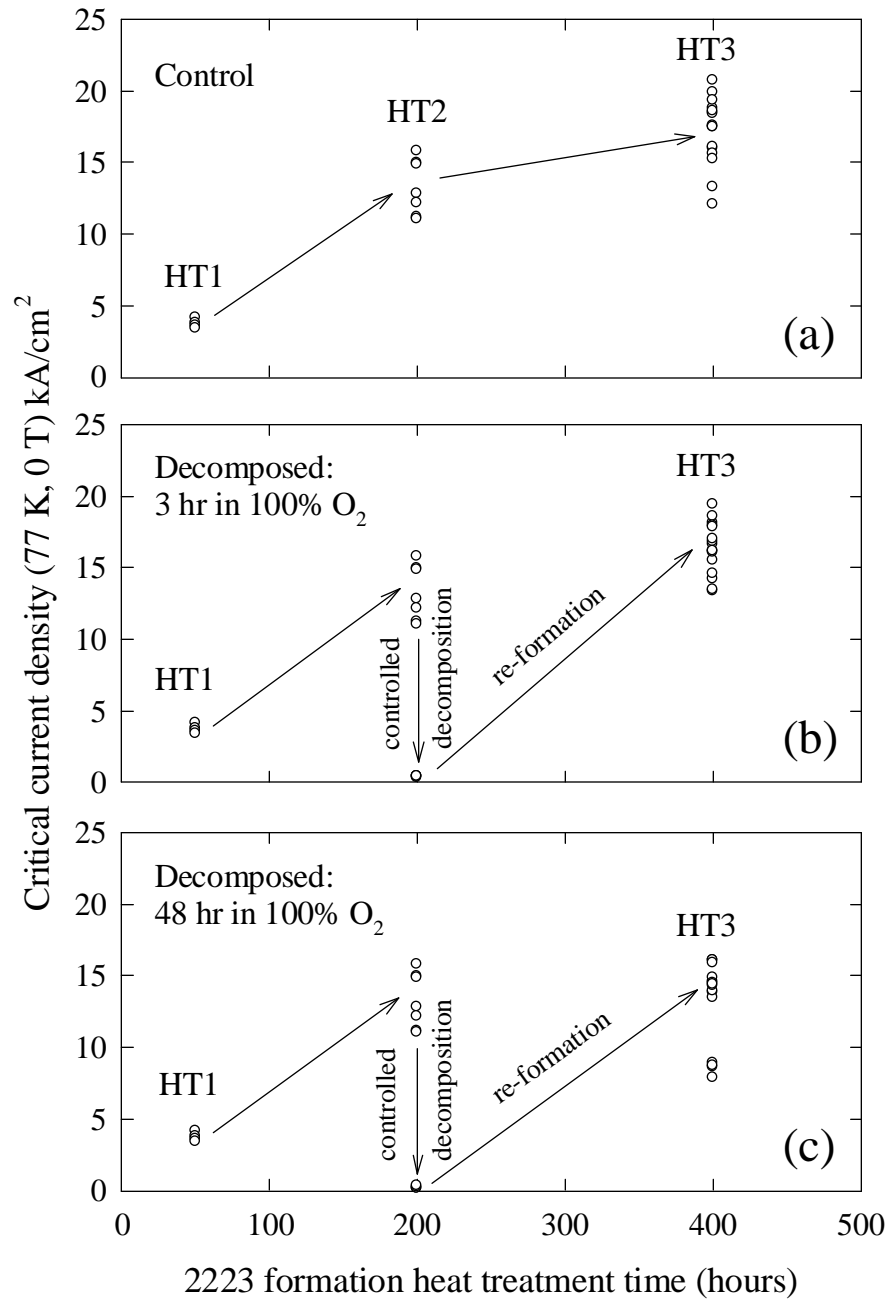


Figure 8-7.  $J_c$  (77 K, 0 T) as a function of heat treatment time and number for all three sample sets of UWB65. Heating in 100%  $\text{O}_2$  caused  $J_c$  to fall sharply to nearly zero for both of the decomposed sample sets, but in both cases in recovered to nearly the control set value after the 2223 re-formation heat treatment in 7.5%  $\text{O}_2$ .

Figure 8-8 shows a series of transmission electron micrographs from the sample decomposed in 100% O<sub>2</sub> for 48 hours which illustrates the mechanism of the decomposition process. Figure 8-8a is a low magnification image taken near the Ag interface which shows that AEC phases have formed layer-like grains between newly formed 2212 grains. The shape of the AEC grains conforms to that of the plate-like 2212 grains. Figure 8-8b is a high resolution image taken at the Ag interface, which shows a pure 2212 grain containing no 2223 intergrowths. It is worth noting that the interface layer between the Ag and 2212 grain is a half cell having the BSCCO-2201 phase c-axis spacing, as found earlier by Feng et al. [103]. Figure 8-8c is a high resolution image of a 2223 grain that contains a (001) twist boundary and just a few layers of 2212. These photomicrographs are representative of what was observed throughout the decomposed sample: small layers of non-superconducting secondary phases conforming to the shape of the 2212 and 2223 phases had grown along BSCCO colony boundaries, while the BSCCO grains tended to be either pure 2212 or pure 2223, containing few intergrowths of the other compound.

#### 8.1.4 Discussion

The most essential feature of this experiment is that it has showed that the 2223 phase can be decomposed and reformed. The transport  $J_c$  was reversibly reduced to nearly zero and then restored essentially to its full original value. However, a full evaluation of the results suggests that fine details of the experiment are important and that the full potential of the process has not yet been attained.

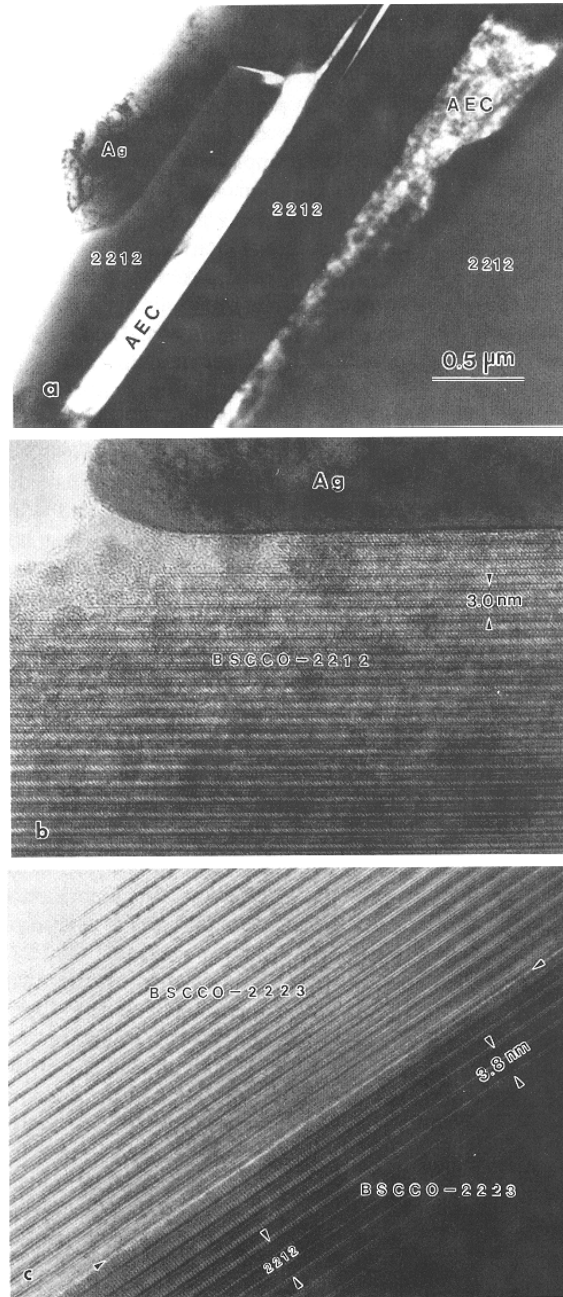


Figure 8-8. TEM micrographs from the 2223 sample decomposed for 48 hours at 825°C in 100% O<sub>2</sub>. (a) shows how small alkaline earth cuprate particles (marked “AEC”) had grown in layers between BSCCO grains, and (b) is an image of a 2212 grain taken near the Ag interface. (c) is an image of a 2223 grain containing a (001) twist boundary (indicated by arrows) and a few 2212 layers. Throughout the sample the BSCCO grains were essentially pure 2212 or pure 2223, and contained very few intergrowths.

Although the experiments do show that there is a substantial reversible component to the 2212-2223 formation reaction, the results also show that there are some important differences of detail. The phase assemblage after decomposition in 100% O<sub>2</sub> (Figure 8-5c, Figure 8-5d, Figure 8-6c, and Figure 8-6d) differs somewhat from that after one heat treatment in 7.5% O<sub>2</sub> (Figure 8-5a and Figure 8-6a). The samples decomposed for 48 hours and the first heat treatment samples contain about the same amount of 2212 (compare Figure 8-5a and Figure 8-5d), but the decomposed sample exhibits strong (Ca,Sr)<sub>2</sub>PbO<sub>4</sub> and alkaline earth cuprate peaks, whereas after one heat treatment in 7.5% O<sub>2</sub>, no (Ca,Sr)<sub>2</sub>PbO<sub>4</sub> was detectable by XRD, and the alkaline earth cuprate peaks were much weaker. Although it has been shown that powders containing Pb in the form of Pb-2212 rather than (Ca,Sr)<sub>2</sub>PbO<sub>4</sub> often react more quickly and completely to 2223 [50,51], powders containing (Ca,Sr)<sub>2</sub>PbO<sub>4</sub> and 2212 will also react to 2223, forming a eutectic liquid in the process, even though their conversion may be slower and their end 2223 product less phase pure [51]. As shown in Figure 8-6, the morphology of the precursor phases also differs between the first heat treatment and decomposed samples. The 2212 grains in the first heat treatment samples (Figure 8-6a) are small (< 10 μm long) and grouped together, whereas in the samples decomposed for 48 hours (Figure 8-6d), the 2212 grains are larger (~ 10-20 μm long) and more isolated, even though both samples contain the same volume fraction of 2212 (≈ 30%). The 2212 grains in the samples decomposed for 3 hours (Figure 8-6c) are more difficult to see by SEM, although ≈ 10% 2212 was detected by XRD. Furthermore, it appears by both SEM and XRD that the 2212 grains in the decomposed samples have a more random orientation, as evidenced by the

appearance of the 2212 (115) peak at about  $27.8^\circ 2\theta$  in Figure 8-5d. This peak was also visible in the samples after the first heat treatment (Figure 8-5a), but had disappeared after the second heat treatment (Figure 8-5b), thus indicating that the 2212 grains did receive some deformation-induced texturing during rolling [83,84,166].

Implicit in the effort of eliminating microcracks in the BSCCO core is the assumption that microcracks are an important limit on the connectivity [127,133,167] and  $J_c$  of BSCCO-2223 tapes. Although qualitative evidence for the presence and detrimental effects of microcracks was clearly demonstrated in Chapter 7, the typical microcrack density and total microcrack length for an average 2223 tape are not known and are very difficult to quantify. Added to this uncertainty are other important unknown quantities about the 2223 system, specifically the amount of liquid created during the 2223-formation reaction, the amount of liquid needed to heal cracks in a tape, and what liquid composition(s) are useful for healing cracks. Because of the difficulty of studying microcracks directly, attempts at reducing the microcrack density must use indirect measures to gauge their effectiveness. The simplest analysis to perform is the measurement of the 77 K, 0 T critical current. However, because of the large number of factors which can control  $I_c$  and  $J_c$  defined over the entire superconductor cross section ( $I_c/A$ ), the interpretation of  $I_c$  measurements and their relationship to  $J_c$  may be complicated, as discussed below.

The abrupt decrease in  $J_c$  with decomposition to a value much lower than that obtained after the first heat treatment (at which point the volume fraction of 2212 was comparable to or even greater than the amount in the decomposed samples, as shown in

Figure 8-5) indicates that the decomposition step quickly destroys the connectivity between the 2223 grains. This implies that decomposition occurs first at interfaces (e.g. colony or grain boundaries), which is consistent with samples decomposed at low temperatures in nitrogen [112]. This behavior is illustrated schematically in Figure 8-3. The TEM analysis (Figure 8-8) provides experimental support for this interpretation, as it seems that secondary phases and pure 2212 grains (Figure 8-8b and Figure 8-8c) have formed along 2223 grain boundaries, rather than forming from the 2223 grains (Figure 8-8c) by an intergrowth mechanism. Had the decomposition occurred uniformly throughout the 2223 grains instead of just at the interfaces, it would be expected that the 2212 and 2223 grains would each contain many intergrowths of the other compound [85,86], and this was not observed. Although decomposition in 100% O<sub>2</sub> quickly destroyed the  $J_c$ , it recovered in the subsequent 2223-formation heat treatment. This indicates that the decomposition by-products do indeed re-react to form 2223. However, as shown in Figure 8-5 and Figure 8-6, some 2212 and large second phase particles did remain in the decomposed samples even after the final 2223-formation heat treatment. The quantity of these phases is above and beyond the amount that can be attributed to the slow cooling treatment. These unwanted phases undoubtedly reduce the local  $J_c$  of the decomposed tapes [85,86,126,155], particularly in the central part of the samples where the second phase particles cluster. Nonetheless, despite this additional second phase (Figure 8-5 and Figure 8-6), the CDR-processed samples have  $J_c$  values comparable to those of the control samples (Figure 8-7). Detailed magneto-optical imaging studies of the current path in conventionally processed samples from the same starting composite show that the local  $J_c$

is highly variable from place to place [155,156]. The results obtained with this new controlled 2223 decomposition/reformation process are all consistent with the hypothesis that cracks have been healed by a liquid produced by the decomposition/2223 reformation process, and that the local  $J_c$  of the active current path is higher in the CDR-processed tapes than in the control tapes.

### 8.1.5 Summary

Heating fully reacted Ag-clad BSCCO-2223 tapes in 100% O<sub>2</sub> at 825°C leads to partial decomposition of the 2223 into 2212, (Ca,Sr)<sub>2</sub>PbO<sub>4</sub>, 3221, and alkaline earth cuprates. This decomposition occurs initially at the 2223 grain boundaries, destroying the grain-to-grain connectivity, and abruptly decreasing the 77 K, 0 T transport  $J_c$ . When such decomposed samples are subsequently deformed and heated in 7.5% O<sub>2</sub>, the decomposition by-products re-react to form 2223, and the connectivity and original  $J_c$  are nearly recovered, despite the growth of large alkaline earth cuprate particles. The recovery of  $J_c$ , despite a deterioration in overall phase purity, suggests that the connectivity in the 2223 matrix has been improved, through the healing of microcracks. Optimization of this controlled decomposition process could produce volume fractions of liquid-forming phases sufficient for healing residual microcracks without growing large second phase particles that do not disappear during the final heat treatment. Such a process may allow for the fabrication of more aligned and dense 2223 structures, because deformation-induced damage can potentially be healed at any time by liquid produced via controlled decomposition and subsequent 2223 reformation heat treatments.

## 8.2 Experiments designed to improve the CDR process

From the initial experiments on decomposing samples in 100% O<sub>2</sub>, it was clear that the CDR process had potential, but needed some refinements. In this section some additional work aimed at improving the process is described. In the end, although there was some success in improving the connectivity and  $J_c$  of some samples, the process was not able to be successfully widely applied to all samples. Possible reasons for this disappointing conclusion and its implications will be discussed at the end of this chapter.

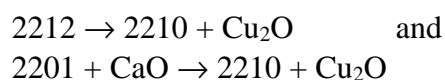
### 8.2.1 Decomposition in nitrogen

In parallel with the initial decomposition studies in oxygen, the consequences of decomposing samples in nitrogen atmospheres was also examined. As shown previously, decomposition of 2223 tapes in a 100% oxygen atmosphere leads to the formation of 2212, (Ca,Sr)<sub>2</sub>PbO<sub>4</sub>, (Pb,Bi)<sub>3</sub>Sr<sub>2</sub>Ca<sub>2</sub>Cu<sub>1</sub>O<sub>x</sub>, and alkaline earth cuprates (mainly (Ca,Sr)<sub>14</sub>Cu<sub>24</sub>O<sub>41</sub>). However, as described in Chapter 3 (where the formation mechanism(s) of the 2223 phase was discussed) in general higher phase purity and better conversion comes from a mixture of Pb-doped 2212 and cuprate phases, rather than a powder which contains Pb in the form of (Ca,Sr)<sub>2</sub>PbO<sub>4</sub> (or perhaps (Pb,Bi)<sub>3</sub>Sr<sub>2</sub>Ca<sub>2</sub>Cu<sub>1</sub>O<sub>x</sub>). As (Ca,Sr)<sub>2</sub>PbO<sub>4</sub> is not stable in low  $pO_2$  atmospheres, the decomposition and reformation of the 2223 phase in nitrogen was studied.

MacManus-Driscoll et al. [53] studied the decomposition of 2223 in  $pO_2$  atmospheres, and found that for  $T < 785^\circ\text{C}$  and  $pO_2 < 2 \times 10^{-4}$  atm, 2223 decomposed via the following reaction pathway:



but simultaneously:



so the overall reaction is:



Thus, low temperature decomposition in N<sub>2</sub> atmospheres will produce 2212 and 2201 as intermediate phases. To try to take advantage of the plumbate-free 2223 decomposition by-products available in nitrogen, the decomposition kinetics of 2223 were studied as a function of temperature. The volume fractions of 2223, 2212, and 2201 phase (determined by XRD) formed in 5 hours at various temperatures is shown in Figure 8-9. The results indicated that heat treating for 5 hours at 750°C could produce 2212 without much 2201 formation.

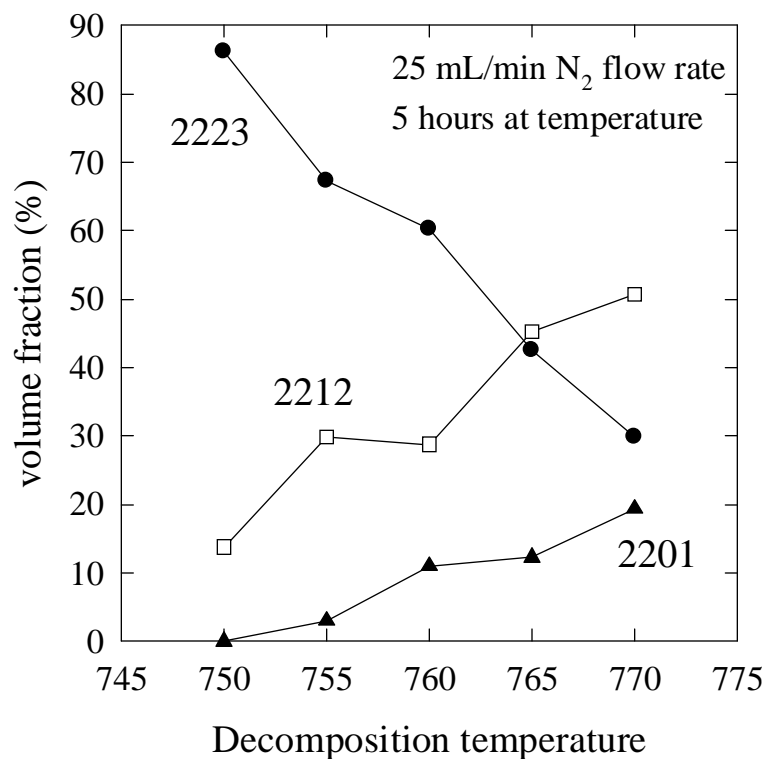


Figure 8-9. The volume fraction of 2223, 2212, and 2201 in samples decomposed at various temperatures for 5 hours in N<sub>2</sub> gas flowing at 25 mL/min.

Upon further experimentation, it was soon found that the decomposition kinetics are strongly affected by the flow rate of N<sub>2</sub> gas through the furnace; the faster the flow rate, the faster the decomposition. This may be an indication that oxygen is given off in the low  $pO_2$  decomposition process, and that the local  $pO_2$  near the sample surface has a substantial influence on the process.

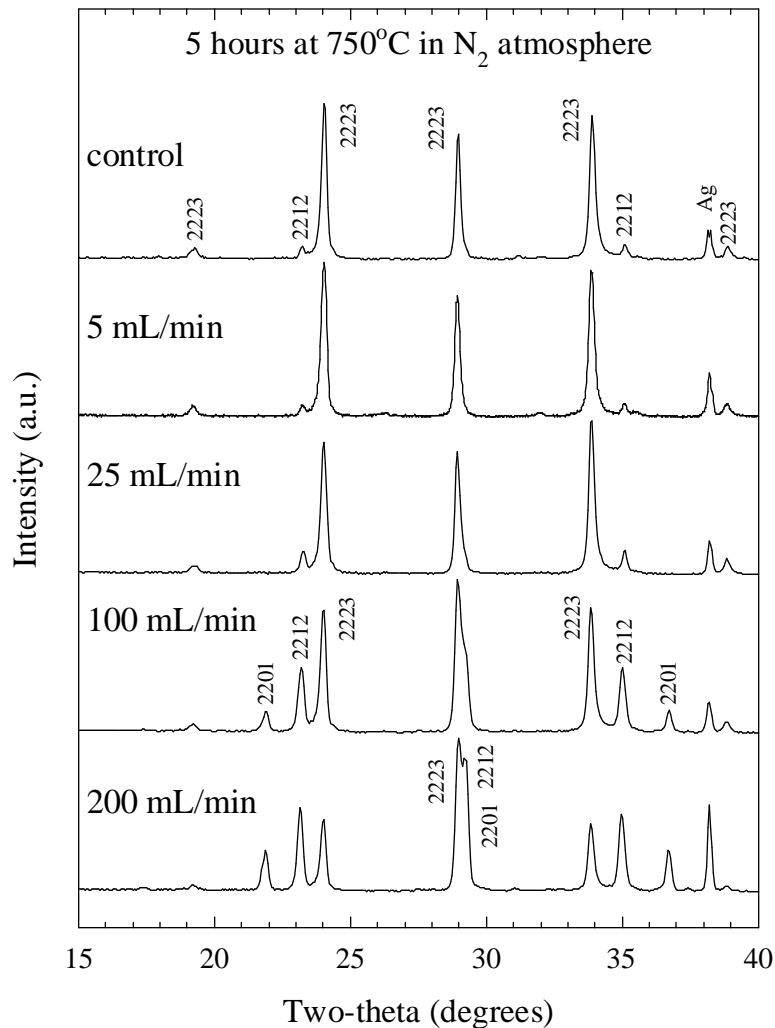
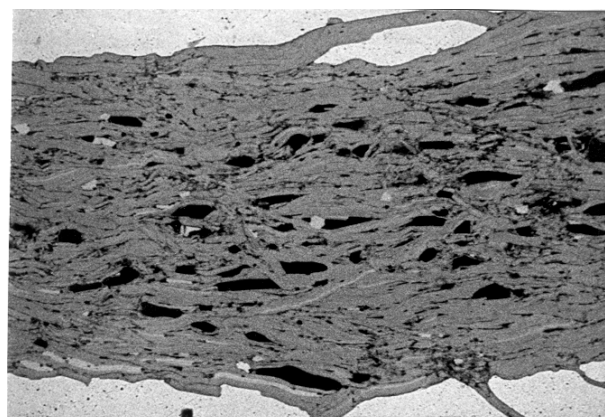


Figure 8-10. XRD spectra of 2223 tapes heat treated at 750°C for 5 hours with different N<sub>2</sub> gas flow rates. Decomposition occurs more quickly at high flow rates.

Figure 8-10 shows the results of an XRD study of the effect of the N<sub>2</sub> flow rate on the decomposition of fully reacted samples of UWB65. From top to bottom, the plot shows the XRD pattern of a control sample (as reacted) showing a small amount of 2212, and the spectra of samples decomposed at 750°C for 5 hours at N<sub>2</sub> flow rates between 5

mL/min and 200 mL/min (the inner diameter of the quartz furnace work tube was ~ 35 mm). As the flow rate was increased, the volume fraction of the decomposition by-products of 2212 and 2201 increased. Based on these results, a flow rate of 25 mL/min was chosen as the “standard” flow rate. This rate was high enough so that a reasonably precise and reproducible gas flow controller setting could be used, and low enough to avoid quickly draining the gas cylinder.

Samples of UWB65 were then processed through 3 heat treatments of 50, 100, and 100 hours, at 825°C in 7.5% O<sub>2</sub> with pressings between heat treatments. This extensive processing developed a dense, high phase purity 2223 microstructure, which should have provided a good test for the ability of CDR processing in nitrogen to heal residual deformation damage. Samples of this fully processed tape were then decomposed for 5 and 10 hours at 750°C in a N<sub>2</sub> atmosphere flowing at 25 mL/min. The 5 hour decomposition produced ~ 10% 2212 as determined by XRD, and the 10 hour N<sub>2</sub> treatment resulted in the formation of ~ 25% 2212 phase. The microstructures of the control and partially decomposed samples are shown in Figure 8-11.



HT3 control

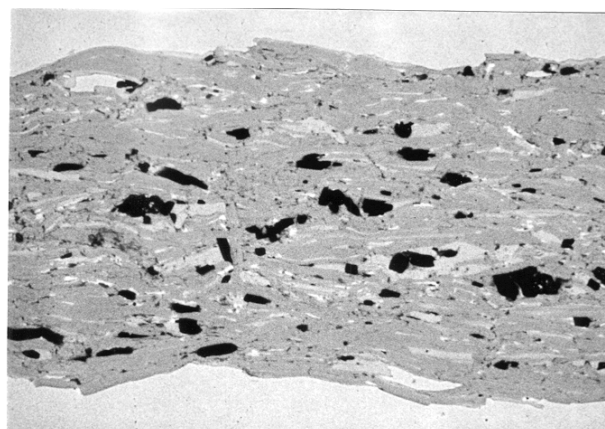
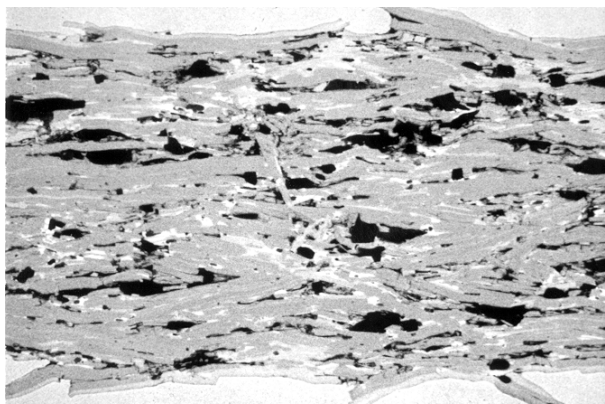
10  $\mu\text{m}$ HT3+5 h N<sub>2</sub> (~10% 2212)10  $\mu\text{m}$ HT3+10 h N<sub>2</sub> (25% 2212)10  $\mu\text{m}$ 

Figure 8-11. SEM backscatter micrographs of fully processed UWB65 samples, after the third heat treatment (top) and after partially decomposing in N<sub>2</sub> for 5 hours (middle) and 10 hours (bottom) at 750°C.

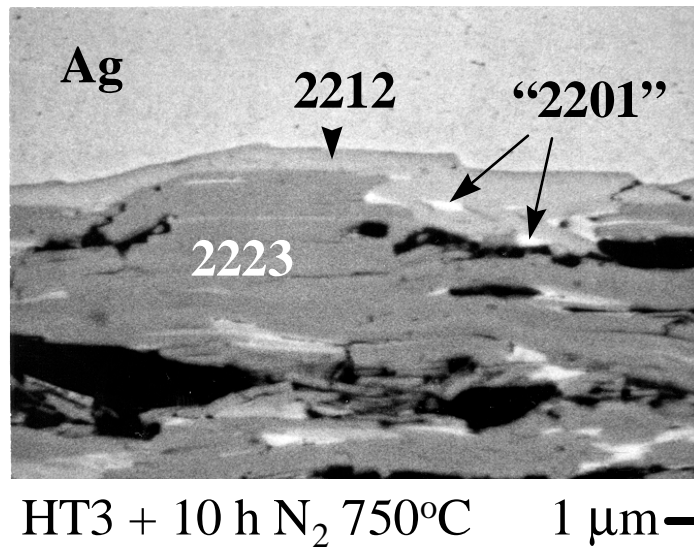
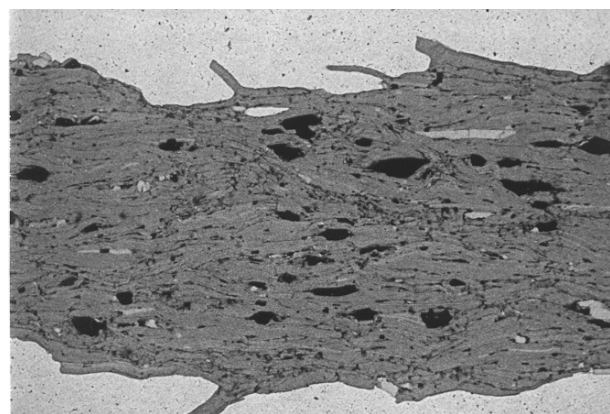


Figure 8-12. SEM backscatter image near the Ag interface of the sample decomposed for 10 hours in N<sub>2</sub> at 750°C. A layer of 2212 formed along the Ag, and pockets of white 2201/liquid phase are indicated.

As shown more clearly in Figure 8-12, the SEM backscatter images also revealed that the samples decomposed in N<sub>2</sub> also contained a small amount of 2201 phase (the small white pockets in the micrographs). Based on their morphology, these regions appear to have been liquid at some point in the processing, but SEM-EDS determined that their composition was similar to 2201, and samples containing large amounts of this phase also show a 2201 peak in XRD scans. The importance of pockets of this 2201/liquid phase in controlling the connectivity of samples will be discussed in Chapter 10. It may also be noted that Figure 8-11 and Figure 8-12 show a layer of 2212 phase at the Ag interface in the samples decomposed in N<sub>2</sub>. This was not observed in samples decomposed in O<sub>2</sub>.

After the decomposition treatment these samples, along with control samples, were pressed and then given a fourth 100 hour heat treatment at 825°C in 7.5% O<sub>2</sub> to re-form the 2223 phase. The microstructures of the samples after this fourth 2223 formation heat treatment are shown in Figure 8-13. It appears by SEM that most of the 2212 and 2201 phase present in the decomposed samples shown in Figure 8-11 has been converted back to 2223 phase. In fact, the samples treated in N<sub>2</sub> appear to have a higher quality microstructure after four heat treatments than does the control sample. In the control sample (top), small light gray particles of Bi,Pb-rich phases such as (Ca,Sr)<sub>2</sub>PbO<sub>4</sub> and 3221 are visible, but it appears that the samples treated in N<sub>2</sub> (middle and bottom) are free of this phase. This is likely because the N<sub>2</sub> treatment caused the Bi,Pb-rich phases to dissolve [164], so they could not grow large during the fourth heat treatment.



HT4 control

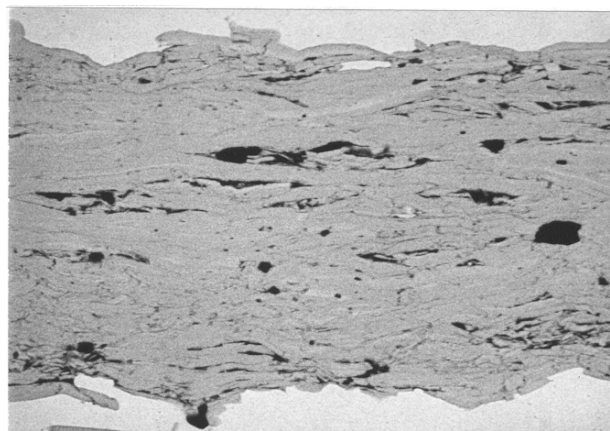
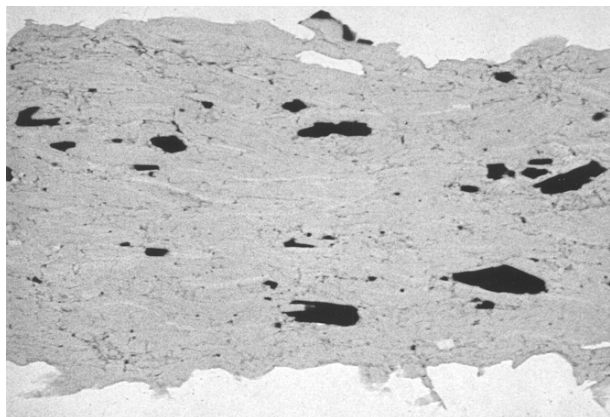
10  $\mu\text{m}$ HT3 + 5 h N<sub>2</sub> + HT410  $\mu\text{m}$ HT3 + 10 h N<sub>2</sub> + HT410  $\mu\text{m}$ 

Figure 8-13. SEM backscatter micrographs of the N<sub>2</sub>-decomposed sample sets after the fourth 2223 formation heat treatment. The samples treated in N<sub>2</sub> appear free of Bi,Pb-rich second phase particles.

The 77 K, 0 T  $J_c$  results from all of the N<sub>2</sub>-decomposed sample sets is shown in Figure 8-14. For the control set,  $J_c$  increased significantly with each of the first three heat treatments, but did not change much with the fourth heat treatment. This may be expected, as residual cracking from the pressing step may negate any other microstructural improvement. The  $J_c$  of the two sample sets that received the decomposition in N<sub>2</sub> decreased to essentially zero after the decomposition step, as was observed previously for decomposition in oxygen, but recovered after the 2223 phase was re-formed by the fourth heat treatment. However, the final  $J_c$  of both decomposed sample sets was not as high as the control set, and in fact were reduced from the control set value in scale with the amount of decomposition (i.e. the control set was highest, followed by the 5 hour decomposed samples, and then the 10 hour samples). The fact that the final microstructures of the decomposed samples appeared better than the control samples at the SEM level suggests that fine intergrowths of 2212 or 2201 may be present in the samples, lowering  $J_c$ .

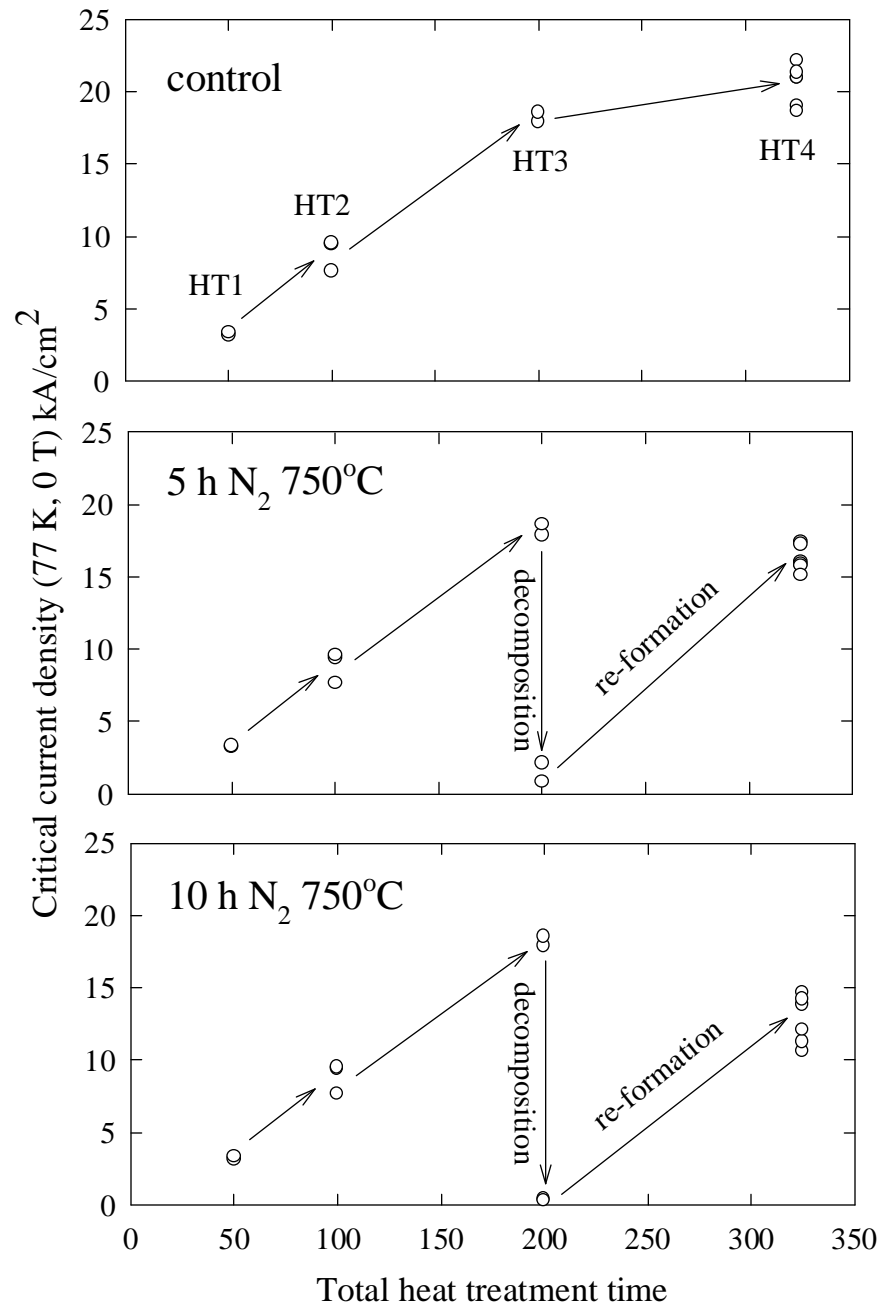


Figure 8-14.  $J_c$  (77 K, 0 T) results for the  $\text{N}_2$  decomposition study.  $J_c$  decreased to essentially zero for samples partially decomposed in  $\text{N}_2$ , but recovered after the fourth 2223 formation heat treatment.

Thus, the results in N<sub>2</sub> seemed less promising than those obtained in oxygen. Since the goal of CDR processing was to improve the intergranular connectivity by reducing residual microcracking, and it was not clear if (sufficiently) large quantities of liquid could be formed in samples free of (Ca,Sr)<sub>2</sub>PbO<sub>4</sub> (and 3221), this work was stopped after this study. The focus was turned to improving the CDR process using a 100% O<sub>2</sub> atmosphere, as discussed next.

### 8.2.2 Testing of a minimal-decomposition hypothesis

The original CDR study in oxygen showed that one problem with the process was that the second phase particles, particularly alkaline earth cuprates such as 14:24, tended to grow very large when the decomposition time was long. One way to limit the second phase growth is to reduce the time spent decomposing in 100% O<sub>2</sub>. As the goal of the CDR process was to heal microcracks, it was hypothesized that just a short time decomposition could be effective, if it formed the liquid-producing second phases just where they were needed; that is, near cracks or voids. Since the TEM results showed that decomposition of the 2223 phase tended to occur from the grain boundaries inward (Figure 8-8), rather than by a reverse-intercalation process, it was surmised that the liquid-producing phases would indeed be formed initially at unbonded interfaces and grain boundaries.

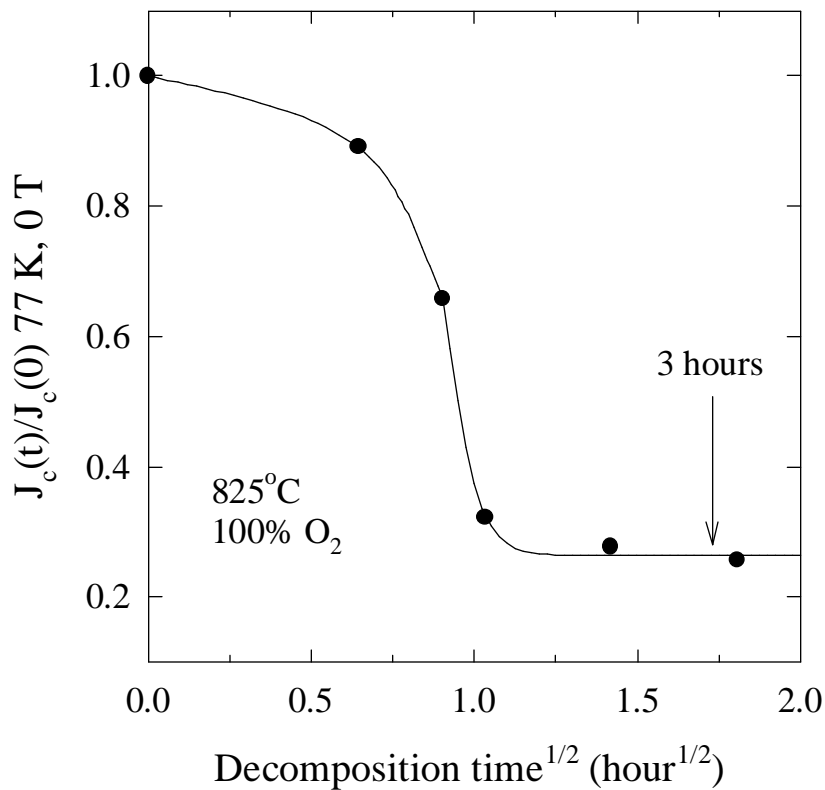


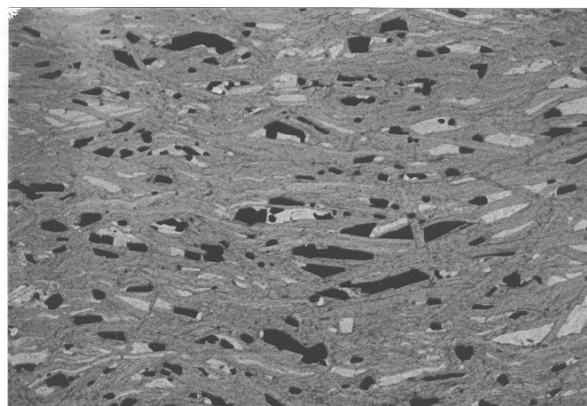
Figure 8-15. Normalized  $J_c$  as a function of the square root of decomposition time at 825°C in 100%  $O_2$ . The 2223 grain boundaries appear to be coated with non-superconducting phases after  $\sim 1$  hour of heat treatment.

The next step was to define a critical time for the decomposition heat treatment. Ideally, it would be long enough to form liquid-producing phases at the grain boundaries, but short enough to avoid large second phase growth. Since it seemed that the 77 K  $J_c$  was very sensitive to the decomposition at the grain boundaries (Figure 8-7), the change in  $J_c$  with short decomposition times was studied. The idea was that a sharp decrease in  $J_c$  would indicate a grain boundary coating of liquid-producing second phases. For these

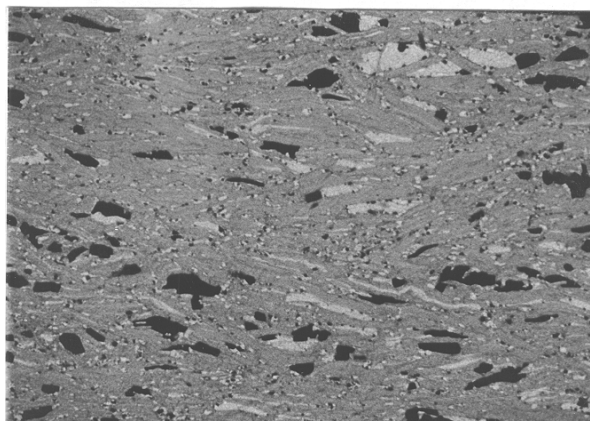
experiments a new composite had to be used, UWB90, which contained the same two-powder precursor as UWB65, but had a much lower Ag:SC ( $\sim 0.7:1$  as opposed to  $\sim 3:1$ ), and therefore relatively thicker BSCCO core at the usual working tape thickness of about  $150\ \mu\text{m}$ . A plot of the normalized  $J_c$  as a function of decomposition time at  $825^\circ\text{C}$  in 100%  $\text{O}_2$  is shown as Figure 8-15, from where it was determined that a decomposition time of about 1 hour is sufficient to coat the 2223 grains with non-superconducting phases.

As there was some variability in the volume fraction of by-products obtained by decomposing samples, a 3 hour decomposition time was chosen to (hopefully) ensure sufficient decomposition. Samples of composite UWB90 were processed by a standard thermomechanical schedule, like that shown in Figure 8-1, and with a CDR schedule like that shown in Figure 8-2, using a 3 hour decomposition time. All heat treatments were given at  $825^\circ\text{C}$ , in either 7.5%  $\text{O}_2$  or in 100%  $\text{O}_2$ , as required.

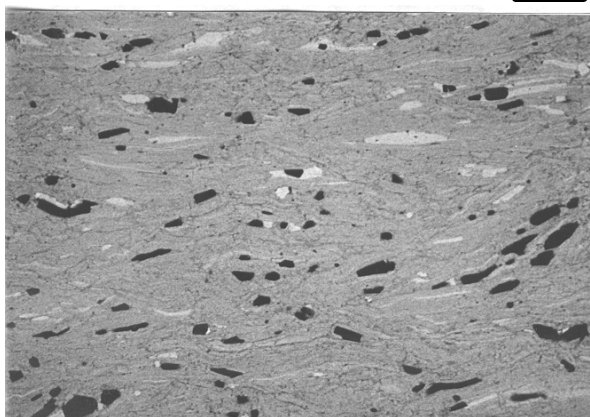
Figure 8-16 shows SEM backscatter micrographs of UWB90 samples after two heat treatments, after the 3 hour decomposition step, and after the final 2223 re-formation heat treatment. As can be seen in the middle micrograph of Figure 8-16, the 3 hour decomposition was sufficient to produce small non-superconducting, liquid-producing second phase particles at the 2223 grain boundaries (the small light and dark particles which dot the sample) and avoid large alkaline earth cuprate growth.



After 2 HT 50/100 825°C 10 μm



2 HT + 3 h 100% O<sub>2</sub> 825°C 10 μm



After 2223 reformation 10 μm

Figure 8-16. SEM micrographs of samples at various stages of processing. The center micrograph shows how small second phase particles (2212, Pb-rich phases, and alkaline earth cuprates) formed within the 2223 matrix.

The zero-field, 77 K  $J_c$  results of the control and short-time decomposition sample sets are shown in Figure 8-17.  $J_c$  increased between the first and second heat treatments, but for the control samples did not improve upon a second deformation step and third heat treatment. However,  $J_c$  (actually,  $I_c$ ) was increased substantially after third heat treatment for the CDR processed sample set. Thus, although the decomposition after the second heat treatment almost completely destroyed the intergranular connectivity, the connectivity and  $J_c$  did improve when the 2223 phase re-formed in the third heat treatment.

To verify that the active cross section  $A_{eff}$  was indeed increased by the CDR processing, the critical current of the third heat treatment samples from Figure 8-17 was measured in magnetic fields. If only the active cross section were changed by processing, one would expect that the behavior of the normalized  $I_c$  as a function of magnetic field would be the same for both sample sets. As shown in Figure 8-18, the behavior of both sample sets in field is essentially the same, suggesting that  $A_{eff}$  was increased in the CDR processed samples. It is tempting to ascribe this apparent increased  $A_{eff}$  to a reduced microcrack density, leading to an improvement in  $J_c = I_c/A$ .

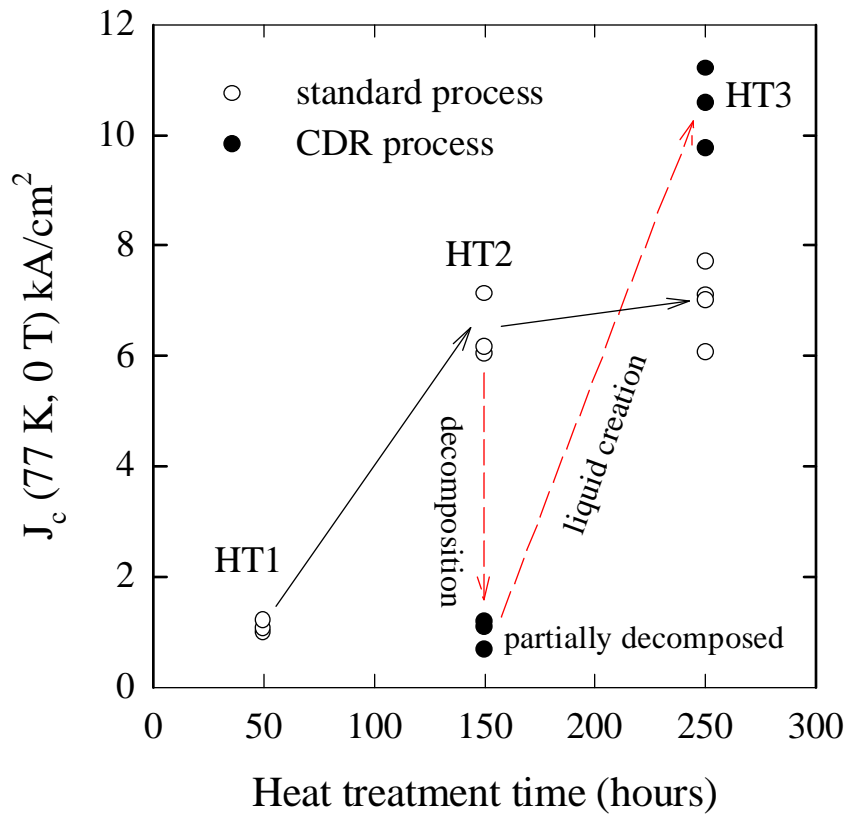


Figure 8-17.  $J_c$  (77 K, 0 T) of the control and CDR sample sets as a function of heat treatment time and number. CDR processing improved the  $J_c$  of the third heat treatment (HT3) samples.

As a further test to check that the microcrack density was reduced in these samples by CDR processing, magneto-optical imaging (as described in Chapter 7) was used to reveal the defect (crack) structure. Figure 8-19 shows the plan view MO images of the third heat treatment samples, imaged at 14 K and  $\mu_0 H = 40$  mT after zero field cooling. The Ag was removed from the top surface of the samples by etching in  $\text{NH}_4\text{OH}/\text{H}_2\text{O}_2$ . The light regions in Figure 8-19 indicate where magnetic flux has penetrated into the

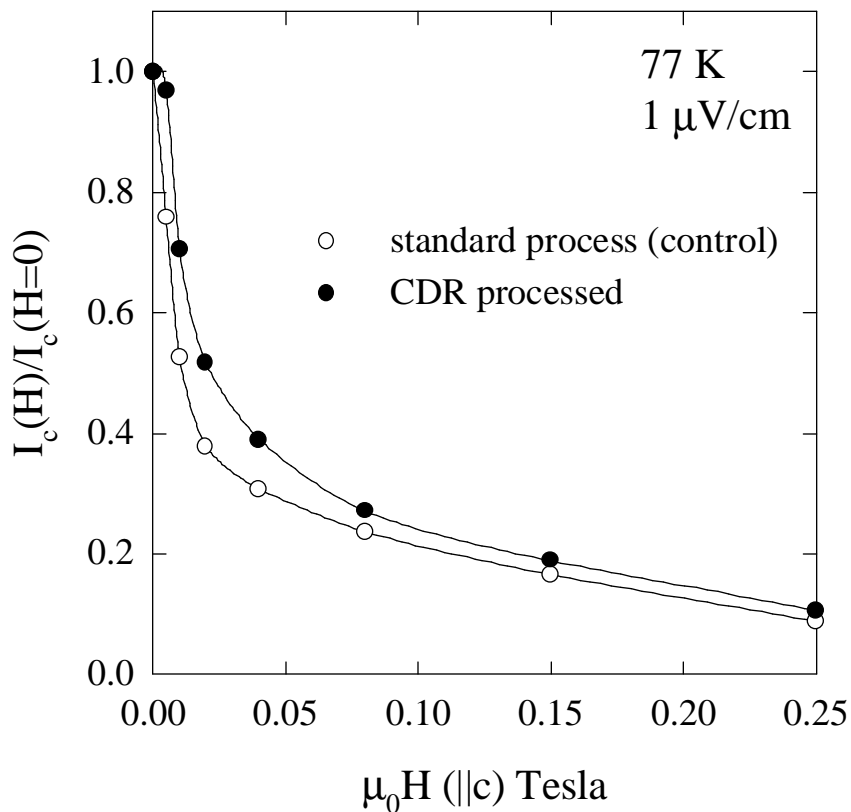


Figure 8-18. Normalized critical current as a function of applied magnetic field for the third heat treatment UWB90 control and CDR processed sample sets. The  $I_c$  response of both sample sets is similar.

sample, as was discussed in Chapter 7. The MO images show qualitatively that the core connectivity has been improved by CDR processing, in agreement with the  $J_c$  results presented in Figure 8-17 and Figure 8-18.

Although the short-time decomposition was effective in increasing  $J_c$  in these thick-core ( $\sim 100 \mu\text{m}$ ) UWB90 samples, similar implementations of the CDR process with

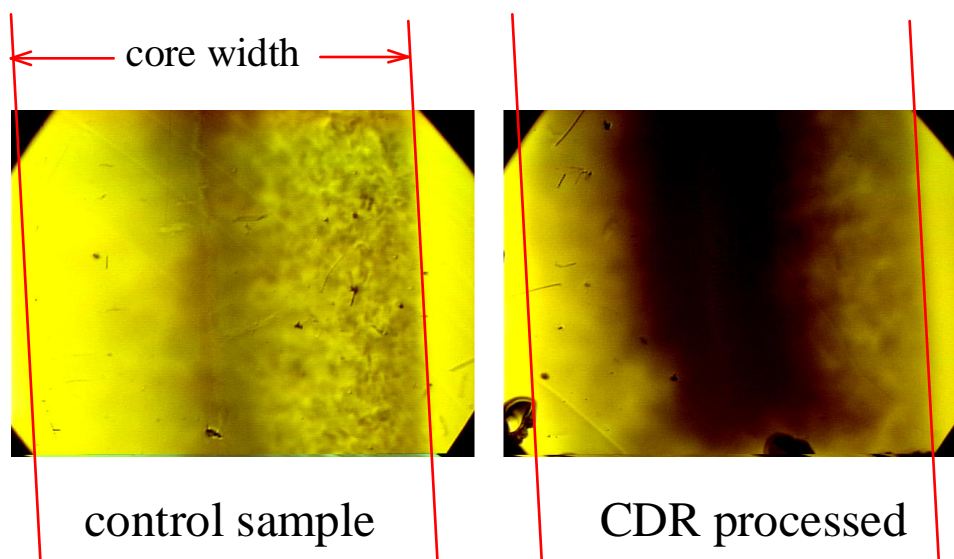


Figure 8-19. Plan view magneto-optical images of a conventionally processed UWB90 tape after three heat treatments (left) and a controlled decomposition-reformation processed sample (right). The images were taken at  $\mu_0 H = 40$  mT after zero field cooling to 14 K. The left hand side of the control image is out of focus because the MO indicator film was not resting perfectly flat on the sample. Less magnetic flux has penetrated into defects in the CDR processed sample than in the control sample.

thin core samples (UWB65, UWB92, and others) did not lead to significant improvements in  $J_c$ . Possible reasons for this are discussed next.

### 8.2.3 DTA and XRD studies of the pseudoprecursor phase mixtures produced by 2223 decomposition in oxygen

As there had not been consistent successes with the CDR process, the behavior of decomposed samples was examined more closely, to find the reason why tapes that were partially decomposed in oxygen (into what were believed to be liquid-producing phases)

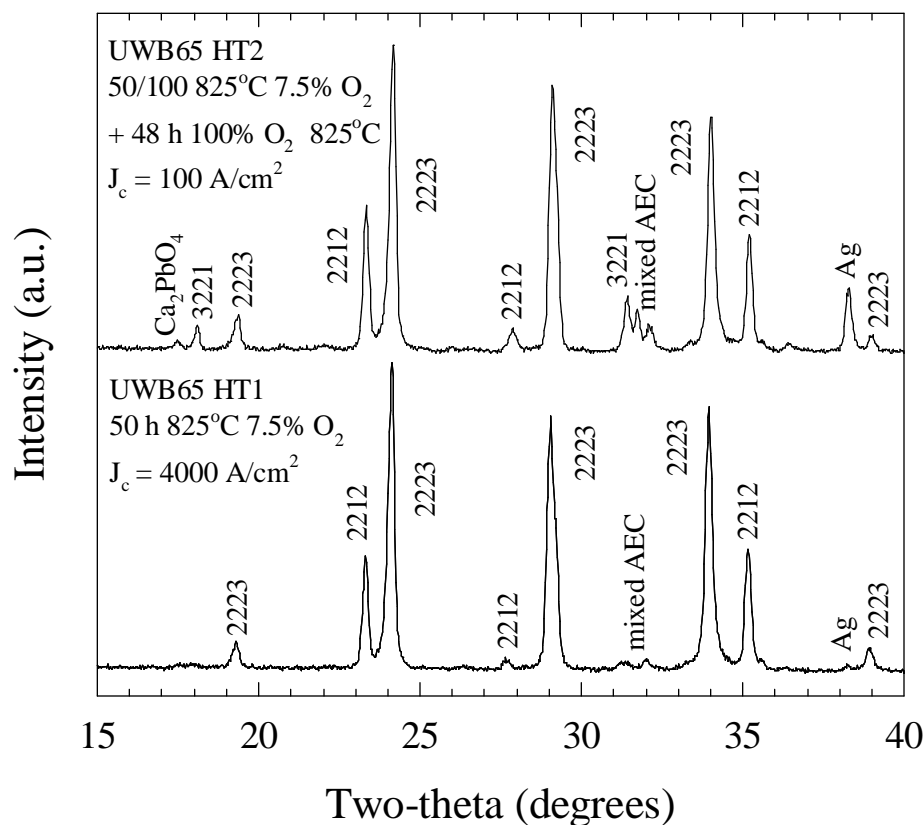


Figure 8-20. Comparison of the XRD patterns (Cu-K $\alpha$  radiation) of a first heat treatment sample (bottom) and of a fully processed sample after partial decomposition (top). The decomposed sample contains much more 3221 and (Ca,Sr)<sub>2</sub>PbO<sub>4</sub> phase than a first heat treatment sample with a comparable volume fraction of 2212.

did not regularly show a substantial improvement in the intergranular connectivity upon 2223 re-formation. X-ray diffraction was used to study the phase assemblage, and differential thermal analysis (DTA) was used to quantify endothermic (melting) events during the heat treatment of samples.

As a first experiment, the XRD patterns of samples that had received just one short 2223 formation heat treatment, and thus still contained some of the liquid-producing phases of the precursor powder, were compared to fully-processed samples that had partially decomposed into “pseudoprecursor” phase mixtures. A comparison of the spectra of samples that had been given one heat treatment, and two heat treatments followed by a substantial decomposition in oxygen, is given in Figure 8-20. Although the samples contained approximately the same amount of 2212 phase, there was in fact a significant difference in the minority phases in the two samples. The XRD patterns show that the sample decomposed to re-form the 2212 phase contains more Bi,Pb-rich phases such as  $(\text{Ca,Sr})_2\text{PbO}_4$  and  $(\text{Pb,Bi})_3\text{Sr}_2\text{Ca}_2\text{Cu}_1\text{O}_x$  (3221) than does the first heat treatment sample that has still contains the “natural” precursor phase assemblage. Furthermore, as discussed earlier, the samples decomposed in oxygen also have a different mixture of alkaline earth cuprates (AEC); while the principal AEC in samples processed in 7.5%  $\text{O}_2$  is 2:1, in decomposed samples the main AEC phase is 14:24.

To check if these differences in the phase assemblages of “naturally”-processed and intentionally-decomposed samples would result in different behavior when more 2223 was formed or re-formed, tapes were studied by DTA. Figure 8-21 shows the DTA curves of three samples at different stages of processing, which were taken while heating at  $5^\circ\text{C}/\text{min}$  in 7.5%  $\text{O}_2$ . The top curve is from an unreacted or “green” sample of composite UWB90. This unreacted sample contained raw precursor powder, which was a two powder mixture of Pb-doped 2212 and alkaline earth cuprates. The first endothermic event, occurring at  $\sim 817^\circ\text{C}$ , is likely associated with the formation of a liquid phase

involved in the 2212 to 2223 conversion reaction; in the literature this peak is usually attributed to a reaction between 2212 and  $(\text{Ca,Sr})_2\text{PbO}_4$ . The large endothermic peak at  $\sim 845^\circ\text{C}$  is from the melting of the 2212 phase. The middle curve is from a sample that had received one heat treatment of 50 hours at  $825^\circ\text{C}$  in 7.5%  $\text{O}_2$  to partially convert the powder to the 2223 phase. The endothermic peak at  $\sim 817^\circ\text{C}$  is smaller, but still visible, indicating that some liquid is still produced upon heating of this tape for a second time, as would be done for a second heat treatment step. This liquid is thus available to heal cracks during the second heat treatment, as demonstrated in Figure 7-3. The large endothermic peak at  $\sim 865^\circ\text{C}$  is from the melting of the 2223 phase. The bottom curve is from a fully processed, third heat treatment sample, that had been partially decomposed by heating at  $825^\circ\text{C}$  for 100 hours in 100%  $\text{O}_2$  to re-form about 40% 2212 and other second phases. Figure 8-20 already showed that this pseudoprecursor mixture is not exactly the same as the natural precursor phase assemblage, and indeed it appears from the DTA heating curve that no endothermic event occurs below  $\sim 840^\circ\text{C}$ . The large endothermic event starting at  $\sim 840^\circ\text{C}$  is actually comprised of two peaks, one from 2212 and one from 2223. However, it does not seem that a liquid forms at  $\sim 817^\circ\text{C}$  in the pseudoprecursor phase mixture produced by decomposition in oxygen, at least in quantities sufficient to cause a temperature difference detectable by the DTA instrument.

To study this difference in more detail, some post-decomposition heat treatments were given to samples that were partially decomposed in oxygen, with the goal of more closely recreating the natural phase assemblage present in partially-reacted samples. The

results of one such experiment are shown in the XRD patterns of Figure 8-22. The bottom trace is from a fully processed UWB90 sample that had been given a 100 hour decomposition heat treatment at 825°C in 100% O<sub>2</sub>, like the bottom sample in Figure 8-21. The diffraction peak positions corresponding to the 2212 and several Bi,Pb-rich phases are marked in the figure. The position of the peak of the 3221 phase which occurs at ~ 17.9° 2θ (with Cu-Kα X-rays) is not strongly dependent on composition [168], but the position of the (Ca,Sr)<sub>2</sub>PbO<sub>4</sub> peak at ~ 17.3° 2θ changes with composition over a range of almost 0.5° 2θ [169]. The as-decomposed sample trace shown at the bottom of Figure 8-22 contains both 3221 and (Ca,Sr)<sub>2</sub>PbO<sub>4</sub>, the latter having a composition close to Ca<sub>1</sub>Sr<sub>1</sub>PbO<sub>4</sub>. As there does not seem to be a large quantity of 3221 in naturally processed samples (Figure 8-20), a low *pO*<sub>2</sub> anneal was given to try to eliminate the 3221 phase, perhaps forming more (Ca,Sr)<sub>2</sub>PbO<sub>4</sub> and/or Pb-2212, which as discussed in Chapter 3 are believed to be the important liquid producing phases. The XRD pattern of this sample, heated for 24 hours at 800°C in a 1% O<sub>2</sub> atmosphere, is shown as the top trace in Figure 8-22. While the low *pO*<sub>2</sub> treatment was effective at eliminating the 3221 phase from the sample, it also dissolved most of the (Ca,Sr)<sub>2</sub>PbO<sub>4</sub>.

After samples processed in this more complicated way still showed no improvement in *J<sub>c</sub>* values, indicating that the connectivity was not significantly improved by the CDR process, work in this area was stopped to focus on other, more promising areas of research, as discussed in the following chapters.

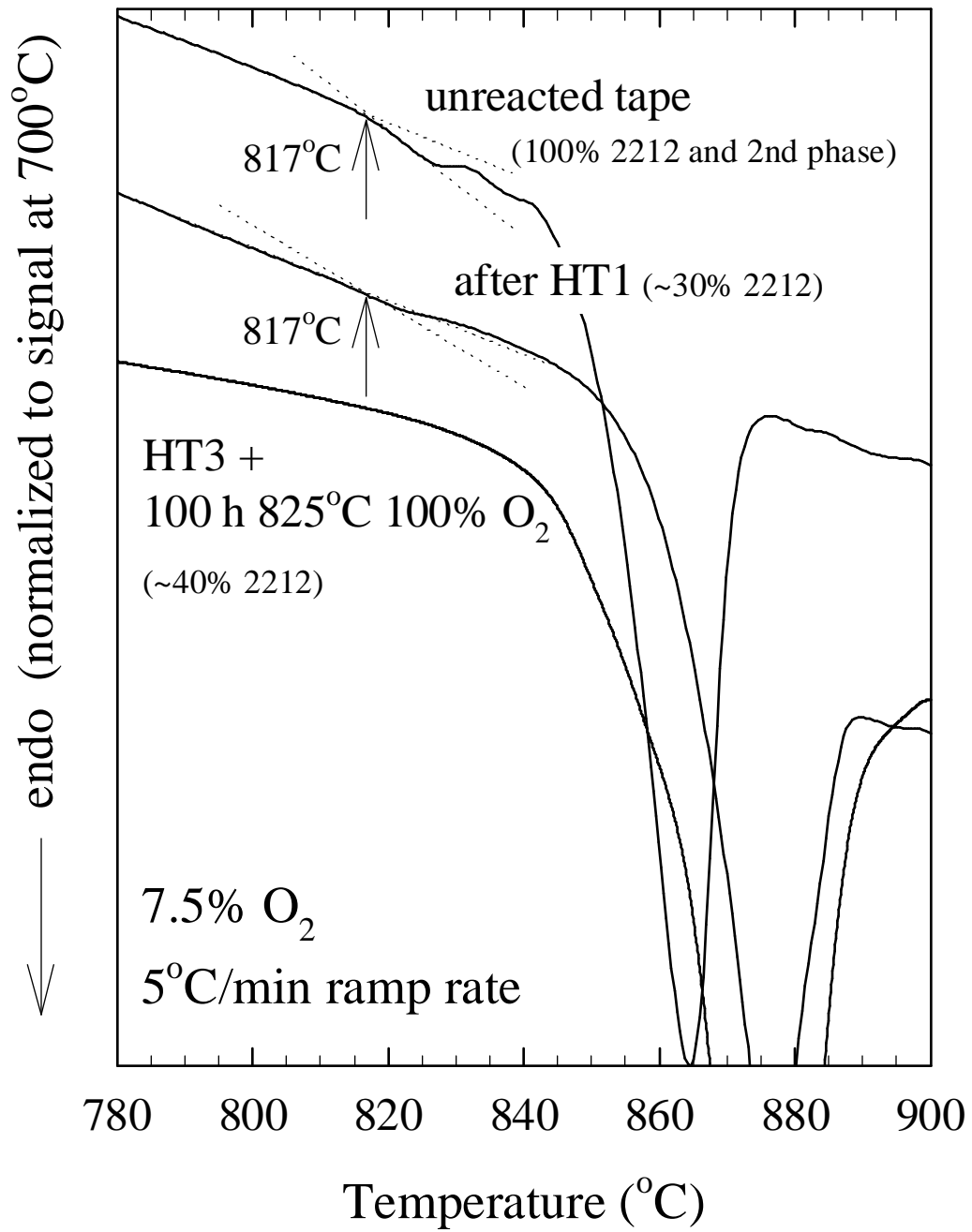


Figure 8-21. DTA heating curves of samples of UWB90 at different stages of processing. The sample decomposed in oxygen does not exhibit an endothermic peak at 817°C, unlike the conventionally-processed samples.

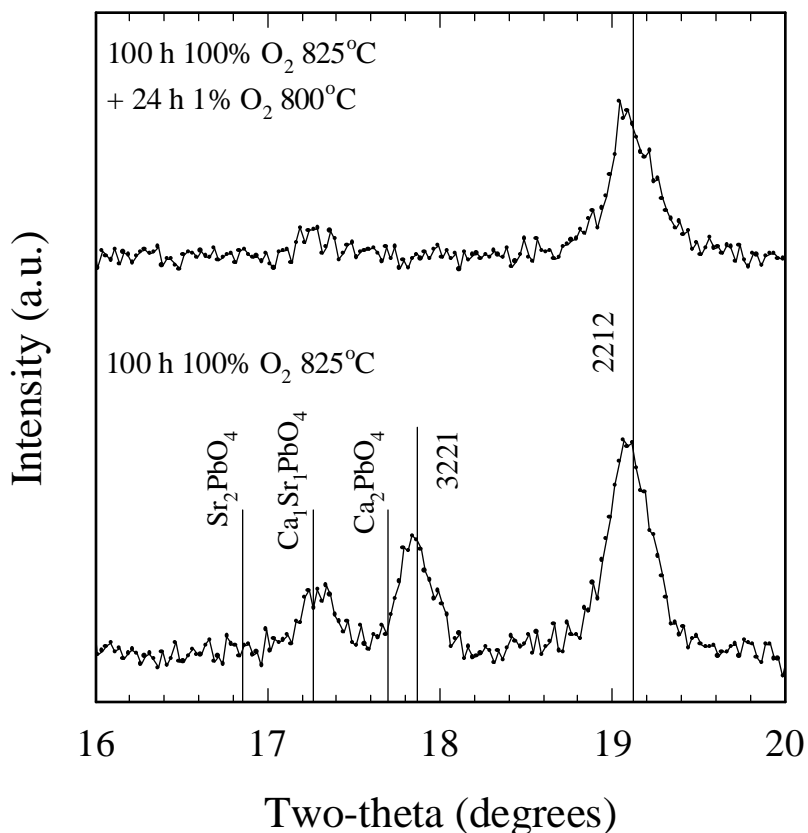


Figure 8-22. XRD patterns of samples first decomposed in 100% O<sub>2</sub> (bottom) and then given a low  $pO_2$  anneal in 1% O<sub>2</sub> (top). The low  $pO_2$  anneal eliminated the 3221 phase, and greatly decreased the amount of (Ca,Sr)<sub>2</sub>PbO<sub>4</sub>.

#### 8.2.4 Summary

As it had been clearly shown by magneto-optical studies like those described in Chapter 7 that the presence of residual microcrack networks was very real, and that indeed in most cases the connectivity of 2223 tapes appears to be limited by cracks, a large improvement in the connectivity and  $J_c$  was expected in CDR processed tapes.

When this was not regularly realized, many experiments were devised in order to clarify the reason why this was so. One of the central puzzles was that while decomposed samples contained significant quantities of 2212 and Bi,Pb-rich phases (e.g. Figure 8-20), which are believed to react to 2223, forming an important liquid in the process, DTA studies of such samples showed no evidence of a liquid formation event. It is now obvious that the real situation is more complex than was originally conceived in the cartoon of Figure 8-3, that all of the phase relationships in 2223 are not clearly understood, and that the resolution of the liquid-shortage/crack healing problem would not come so easily.

The samples produced in the one successful implementation of the CDR process, described in Section 8.2.2, seemed to perhaps hold the key to unlocking some of the mysteries. However, the only significant differences that could be found between these UWB90 samples, and all of the other samples that undergone CDR processing, was that the BSCCO core was significantly thicker ( $> 100 \mu\text{m}$ ) than others (typically  $\sim 70 \mu\text{m}$ ), and that the second heat treatment samples still contained some precursor 2212 prior to the decomposition and reformation step. It is conceivable that this remaining precursor 2212 had a different stoichiometry than the 2212 formed by decomposition in oxygen, and as the melting point of 2212 is sensitive to the cation composition [39,51], that this may be why a liquid did not form in CDR samples. Unfortunately, the encouraging results obtained in that experiment could not be reproduced, even in samples of the same composite.

In the end, the main conclusions to be drawn from this work are as follows. It is easy to destroy the intergranular connectivity of 2223 samples by decomposing the

material, which happens primarily at the grain boundaries. It is possible to reconnect the grains by giving samples a subsequent 2223 formation heat treatment. Although the oxygen atmosphere decomposition by-products are similar to the phases present in unreacted or partially reacted tapes, for some reason they do not form a large quantity of a liquid which is useful for healing microcracks in the core. This could be a result of the cation composition of one or many of the decomposition by-products being slightly different than that required to form a useful liquid.

One final possible explanation for the results is proposed. It may be that a small quantity of liquid is indeed formed in CDR processed samples, but that the liquid is not effective at healing cracks. This could be because the cracks are not easily bridged by the liquid, and/or that the liquid does not wet the 2223 grains, and as a result there is little mechanical driving force to close the cracks. As most evidence suggests that 2223 forms by liquid-assisted intercalation of pre-existing 2212 grains, it may be that when the new, discrete 2212 grains created by decomposition (e.g. Figure 8-6 and Figure 8-8) are converted back to 2223, the result is only new, distinct 2223 grains, with new grain boundaries. In this scenario, the liquid only serves to convert 2212 to 2223, and does not act a mortar which more strongly connects pre-existing 2223 grains.

Although these experiments were not useful in themselves for learning how to improve  $J_c$ , some of the things learned in these studies about the decomposition and phase relationships in 2223 tapes did play a role in subsequent studies which did result in  $J_c$  improvements, as discussed in the next two chapters.

## 9. Effect of the cooling rate on the microstructure, $T_c$ , and $J_c$ of 2223 tapes

This chapter contains material from the publication:

J.A. Parrell, D.C. Larbalestier, and S.E. Dorris “Cooling Rate Effects on the Microstructure, Critical Current Density, and  $T_c$  Transition of One- and Two-Powder BSCCO-2223 Ag-Sheathed Tapes”, IEEE Transactions on Applied Superconductivity 5 (1995) 1275.

### 9.1 Introduction

Many parameters must be controlled and optimized during the fabrication and thermomechanical processing of Ag-clad 2223 tapes. The effects of powder composition, mechanical deformation, and heat treatment temperature, time, and atmosphere on the  $J_c$  of 2223 tapes have been studied extensively. One aspect that has received less attention in the literature is what occurs during the cool-down after the 2223 formation reactions. Lay [170] found that cooling at 1°C/min in air resulted in a ~ 15%  $J_c$  (77 K, 0 T) increase

over tapes cooled at  $\sim 3^\circ\text{C}/\text{min}$ , and reported that holding below the 2223 reaction temperature of  $\sim 830^\circ\text{C}$  in 2-5%  $\text{O}_2$  after processing in air could in some cases increase the  $J_c$  by a factor of two. Other groups have reported that the  $T_c$  transition of bulk 2223 samples can be sharpened by post-annealing above  $700^\circ\text{C}$  for  $\sim 10$  hours in 6-10%  $\text{O}_2$  [47,171].

We have found, as have others [111,114], that processing tapes in 7.5%  $\text{O}_2$  is more favorable for 2223 formation than processing in air. In this chapter several experiments on 2223 tapes which were reacted and cooled in 7.5%  $\text{O}_2$  are summarized, and the effect of cooling rate on the superconducting properties and microstructure is described.

Many advances in the  $J_c$  of Ag-clad BSCCO-2223 tapes have come from improving the degree of 2223 phase purity. Microstructures containing a large volume fraction of non-superconducting "second phase" particles are not desirable because these particles are typically many  $\mu\text{m}$  in size, and thus disturb the local alignment of the plate-like 2223 grains [33] and decrease the superconducting fraction of the conductor cross section. The importance of the 2223 phase purity extends to an even finer scale; it has been shown that intergrowths of even one or a few half-unit-cells of residual BSCCO-2212 within 2223 grains can be detrimental to  $J_c$  [85,86]. Thus, since many experiments to improve  $J_c$  have the goal of producing a more homogenous 2223 microstructure, it was interesting to find a contradiction to this general rule. It was found that cooling at rates sufficiently slow as to allow some decomposition of the 2223 phase often resulted in better superconducting properties, even though the 2223 phase purity was evidently degraded on a scale of  $\mu\text{m}$ .

## 9.2 Experimental details

Ag-clad tapes about 3 mm wide and 0.2 mm thick were made by rolling round wires produced by standard oxide-powder-in-tube methods. Tapes were fabricated with a standard "one-powder" uncontrolled phase balance powder of nominal composition  $\text{Bi}_{1.8}\text{Pb}_{0.3}\text{Sr}_{1.9}\text{Ca}_{2.0}\text{Cu}_{3.0}\text{O}_x$  purchased from Seattle Specialty Ceramics Inc., and with "two-powder" controlled phase assemblage powders ( $\text{Bi}_{1.8}\text{Pb}_{0.4}\text{Sr}_{2.0}\text{Ca}_{1.0}\text{Cu}_{2.0}\text{O}_x$  and  $\text{CaCuO}_2$  powders mixed to give an overall composition of  $\text{Bi}_{1.8}\text{Pb}_{0.4}\text{Sr}_{2.0}\text{Ca}_{2.0}\text{Cu}_{3.0}\text{O}_x$ ) obtained from Argonne National Laboratory [50,51]. The tapes were then thermomechanically processed as described below. All heat treatments and cool-downs were given in a 7.5%  $\text{O}_2$ /balance  $\text{N}_2$  atmosphere, and tapes were uniaxially pressed at  $\sim 1$  GPa between heat treatments.

### 9.2.1 One-powder tape processing

The one-powder tapes were given three heat treatments of 72 hours each at  $818^\circ\text{C}$ . The cooling rate to  $730^\circ\text{C}$  from the reaction temperature after the third reaction heat treatment was either  $4^\circ\text{C}/\text{min}$  or  $0.05^\circ\text{C}/\text{min}$ . After reaching  $730^\circ\text{C}$ , the samples were furnace cooled at  $\sim 20^\circ\text{C}/\text{min}$ .

### 9.2.2 Two-powder tape processing

Two separate experiments were performed with the two-powder tapes. In the first experiment, only one heat treatment was given (and thus the conversion to 2223 was incomplete), and the cooling rate after this single heat treatment was varied. The second

experiment was similar to the one-powder tape experiment described above, in that the cooling rate after the final heat treatment was varied.

### 9.2.2.1 Cooling rate varied after the first heat treatment

A sample was given a 30 hour heat treatment at 825°C, and cooled to 725°C at 5°C/min. After this short heat treatment the conversion of the precursor powder to BSCCO-2223 was not complete. A second sample was given the same 30 hour reaction heat treatment, and then cooled to 725°C at 0.05°C/min. Because the length of the cool-down of this sample was comparable to the length of the 30 hour reaction heat treatment (during cool-down the sample was between 825°C and 725°C for ~ 33 hours), a third sample was given a 63 hour reaction heat treatment at 825°C, and was cooled at 5°C/min to 725°C.

### 9.2.2.2 Cooling rate varied after three heat treatments

Two-powder tapes were given a 50 hour first heat treatment at 825°C, followed by 100 hour second and third heat treatments. After the third heat treatment and subsequent cool-down (at 4°C/min), the samples were quickly (~ 15°C/min) re-heated to 825°C in the 7.5% O<sub>2</sub> atmosphere (with no intermediate pressing), held for 1 hour at 825°C, and then cooled to 725°C at four different rates: 5, 0.5, 0.16, and 0.05°C/min.

The transport critical current values (1 μV/cm) were converted to  $J_c$  by dividing by the average of two or three cross-sections measured by image analysis. All critical currents were measured at 77 K, 0 T. The temperature dependence of the zero-field-

cooled AC susceptibility of many of the samples was measured at 0.1 and 2 mT, at 125 Hz, with the field applied normal to the rolling plane of the tape (i.e. nominally parallel to the c-direction of the aligned 2223 grains). A scanning electron microscope (SEM) operated at 15 kV was used to examine the microstructures of the tapes. X-ray diffraction (XRD) using Cu-K $\alpha$  radiation was also used to examine the phase purity of some samples.

### **9.3 Results**

#### **9.3.1 Fully processed one-powder tape experiments**

Figure 9-1 is a plot of the AC susceptibility of the fast (4°C/min) and slow (0.05°C/min) cooled samples as a function of temperature. The inset in Figure 9-1 shows  $J_c$  as a function of heat treatment time for the fully processed one-powder tapes. Slow cooling at 0.05°C/min to 730°C in 7.5% O<sub>2</sub> increased the  $J_c$  by almost 50% to ~ 12,000 A/cm<sup>2</sup> compared to the tape that was fast cooled at 4°C/min. The slow cooled sample has a sharper  $T_c$  transition than the fast cooled sample, and no T' kink indicative of BSCCO-2212 intergrowths [85,86] is visible, whereas a kink in the transition is apparent for the fast cooled sample.

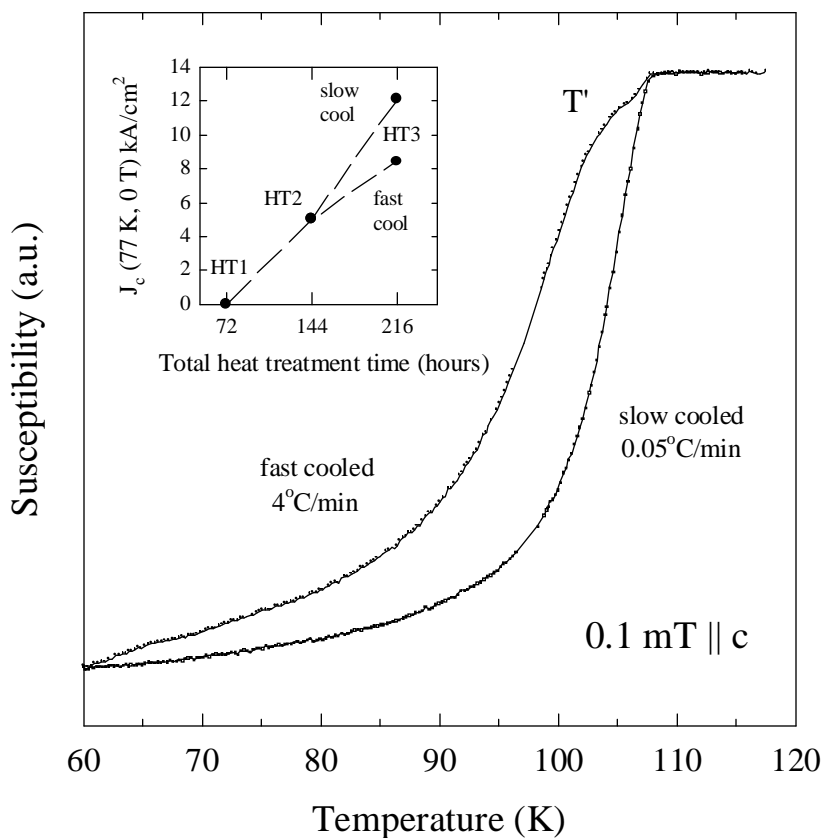


Figure 9-1. Normalized AC susceptibility (0.1 mT) of the fast cooled (4°C/min) and slow cooled (0.05°C/min) fully processed (3 heat treatments) one-powder samples (UWB41). The inset shows the critical current density (77 K, 0 T) as a function of heat treatment time and number. Slow cooling sharpened the  $T_c$  transition and increased  $J_c$ .

Figure 9-2a and Figure 9-2b are SEM backscatter micrographs of typical fast cooled (4°C/min) and slow cooled (0.05°C/min) one-powder tape microstructures, respectively. Many large BSCCO-2212 grains (light gray "needles") are visible throughout the thickness of the slow cooled sample (Figure 9-2b). These 2212 grains were seldom seen in the second heat treatment or in the fast cooled (4°C/min) third heat treatment

samples (Figure 9-2a), which suggests that slow cooling at 0.05°C/min to 730°C caused the regular formation of these 2212 grains. Presumably these 2212 grains formed as a result of 2223 decomposition, as 2223 is unstable below ~ 790°C in 7.5% O<sub>2</sub>, decomposing to 2212, (Ca,Sr)<sub>2</sub>PbO<sub>4</sub>, and other non-superconducting phases [111,117].

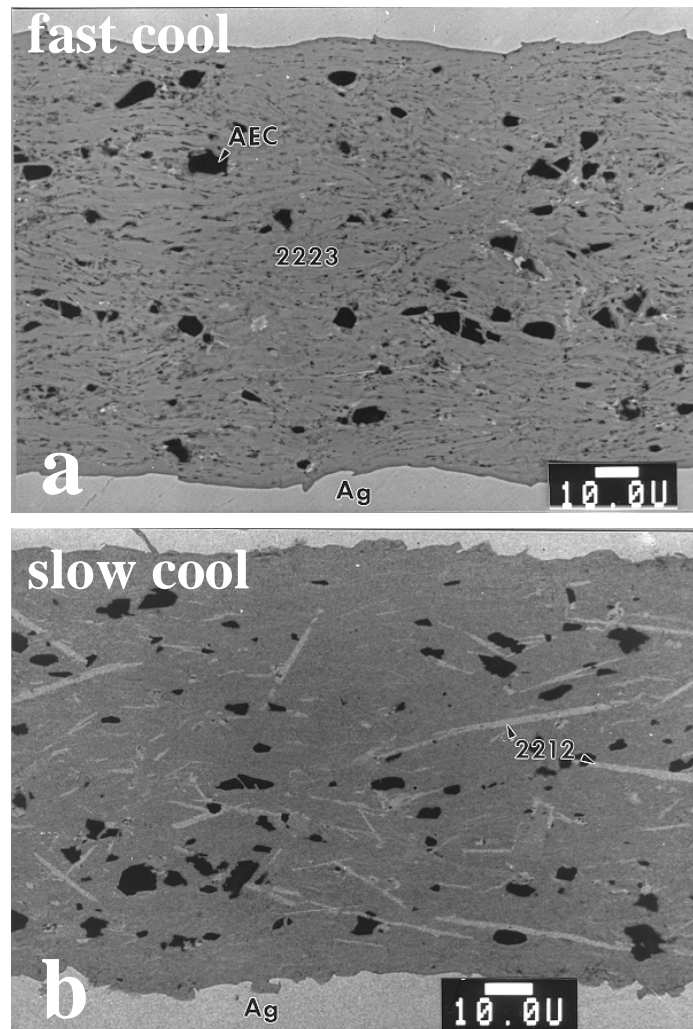


Figure 9-2. SEM micrographs of typical (a) fast (4°C/min) and (b) slow (0.05°C/min) cooled fully processed one-powder samples (UWB41). Large 2212 grains (light gray needles) are dispersed throughout the slowly cooled core.

In summary, cooling fully processed one-powder tapes at 0.05°C/min to 730°C in 7.5% O<sub>2</sub> resulted in a sharper  $T_c$  transition and a 50% higher  $J_c$  than tapes cooled more quickly at 4°C/min. The superconducting properties improved, despite many large 2212 grains in the sample.

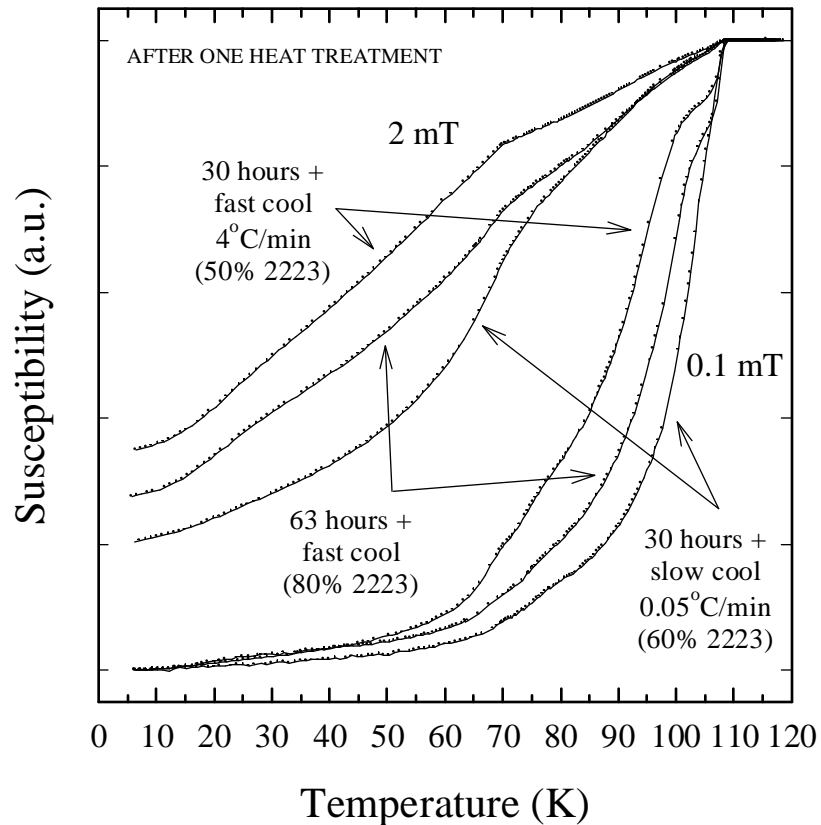


Figure 9-3. AC susceptibility (normalized to the 5 K, 0.1 mT signal) of the partially reacted two-powder samples (UWB63). The slowly cooled sample has a sharper transition than even the more extensively converted fast cooled sample (heat treated for 63 hours).

### 9.3.2 Two-powder tape experiments

#### 9.3.2.1 Cooling rate varied after the first heat treatment

It was found that the cooling rate has an effect on the critical current density and  $T_c$  transition of two-powder tapes after the first heat treatment, when the 2223 conversion

is far from complete. The sample that was heat treated for 30 hours and cooled at 5°C/min contained ~ 50% 2223 (by XRD) and had a  $J_c$  of 1,100 A/cm<sup>2</sup>, compared to the sample given a 30 hour heat treatment and cooled at 0.05°C/min, which was ~ 60% converted and had a  $J_c$  of 2,800 A/cm<sup>2</sup>. This slowly cooled sample had a  $J_c$  value greater than that of the sample given the longer 63 hour heat treatment ( $J_c = 2,300$  A/cm<sup>2</sup>), even though this more completely reacted sample contained ~ 80% 2223. AC susceptibility results for these three partially reacted samples, shown in Figure 9-3, show that the  $T_c$  transition was substantially sharpened by slow cooling at 0.05°C/min, as was also found in the fully processed one-powder tapes. Note that the slowly cooled sample (containing 60% 2223) has a sharper transition than the sample that was 80% converted to 2223 (the 63 hour heat treated sample), and that at 2 mT the slowly cooled sample exhibited a greater fraction of its 0.1 mT signal than did the fast cooled tapes.

### 9.3.2.2 Cooling rate varied after three heat treatments

Figure 9-4 shows XRD patterns for the samples that were cooled to 725°C at 5, 0.16, and 0.05°C/min. Note that as the cooling rate was decreased, the diffraction peak heights for (Ca,Sr)<sub>2</sub>PbO<sub>4</sub> and other second phases (mainly alkaline earth cuprates) increased, presumably because of 2223 phase decomposition. However, unlike what was observed for the one-powder tapes (Figure 9-2b), the relative amount of 2212 did not noticeably increase (as determined by SEM and XRD).

Figure 9-5 shows  $J_c$  as a function of cooling rate for the two-powder samples that received three heat treatments, were re-heated to 825°C, and then cooled at different rates

in 7.5% O<sub>2</sub>. The  $J_c$  increased as the cooling rate was decreased, reached a maximum value at a rate of 0.16°C/min, and then decreased at still slower rates. Thus, as was found for the one-powder samples, slow cooling can increase the  $J_c$  of fully processed two-powder tapes, even though the 2223 phase homogeneity was reduced. However, the fractional  $J_c$  increase (~ 20%) was less than for one-powder tapes.

## **9.4 Discussion**

In the earlier microhardness experiments described in Chapters 5 and 6, it was shown that even if the 2223 bulk density is made high by many deformation and heat treatment cycles,  $J_c$  need not increase if another factor, in that case cracks, becomes the dominant  $J_c$  limitation. In similar manner, the experiments described in this chapter clearly show that the phase purity of a polycrystalline 2223 filament is not necessarily an indicator of  $J_c$ , and suggests that another factor, either related to the connectivity or flux pinning, is important in determining  $J_c$ .

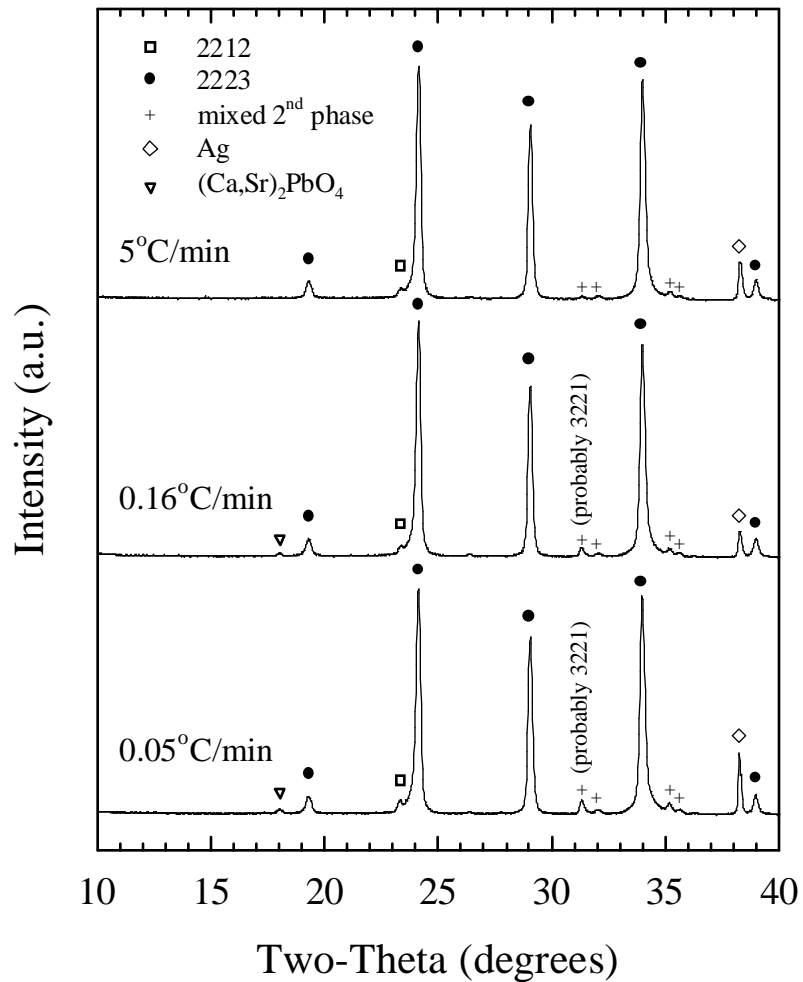


Figure 9-4. XRD spectra for the fully processed two-powder tapes (UWB65) that were cooled from 825°C to 725°C at 5, 0.16, and 0.05°C/min in 7.5% O<sub>2</sub>. The fraction of impurity phases, particularly those that are Pb-rich, increases with decreasing cooling rate.

Whether or not the current path in BSCCO tapes is dominated by "brick wall" [172] or "railway switch" [135] linkages, the dominant experimental evidence has been that there is a strong positive correlation between a higher  $J_c$  (77 K, 0 T) and a higher or absent kink in the AC or DC susceptibility trace [85,86]. The source of the kink is 2212

intergrowths, one to a few half-unit-cells thick, remaining from the unconverted precursor powder. In the present case, the 2212 is on a much larger scale,  $\mu\text{m}$  rather than nm, and is formed by decomposition of the 2223 phase. It is possible to rationalize both sets of data by postulating that the 2212 formed by decomposition has a very different morphology than that of residual 2212. Whereas residual 2212 was found in almost all 2223 grains [85,86] and thus exerted a large effect on the current path, the 2212 formed by decomposition of the 2223 phase is larger (Figure 9-2b) and seems to form discrete grains, similar to the decomposition in pure oxygen described in Chapter 8.

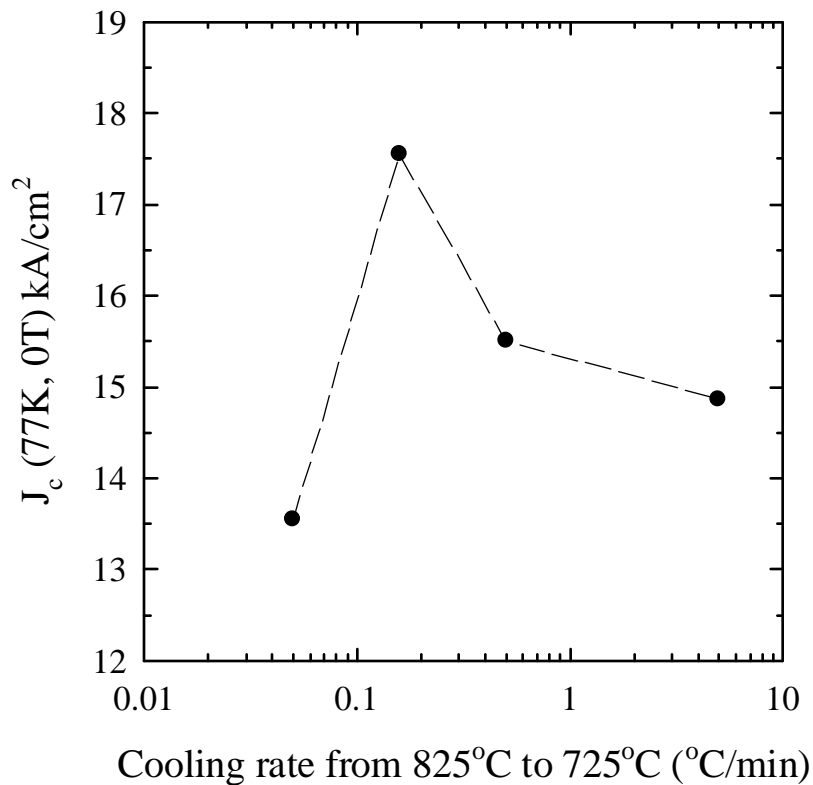


Figure 9-5. Critical current density as a function of cooling rate from 825°C to 725°C for the fully processed two powder samples (UWB65).

The encouraging and rather unexpected results of these initial studies of the effect of the cooling rate suggested that a more thorough analysis was in order. Such a study was needed to gain an understanding of both this new or misunderstood current limiting mechanism, as well as the control that the cooling rate has on this mechanism(s). These more detailed studies are the focus of the next chapter.

## 9.5 Summary

Although in general it is desirable to achieve a phase-pure 2223 microstructure to maximize  $J_c$  in BSCCO-2223 tapes, an exception to this rule is found for tapes that are cooled slowly after reaction heat treatment.  $J_c$  increases of 20-50% and marked sharpening of the  $T_c$  transition were observed for both one- and two-powder tapes when samples were cooled at a rate of  $\sim 0.15$ - $0.05^\circ\text{C}/\text{min}$  in 7.5%  $\text{O}_2$ . These improvements in superconducting properties were observed despite a reduced microstructure phase purity caused by 2223 decomposition. However, once the decomposition of the 2223 phase to 2212 and other non-superconducting phases became too extensive, the  $J_c$  decreased. This behavior is attributed to changes in the connectivity of the polycrystalline core as the cooling state is varied.

## **10. Connectivity and flux pinning improvements in 2223 tapes produced by changes in the cooling rate**

This chapter contains material from the publications:

J.A. Parrell, D.C. Larbalestier, G.N. Riley, Jr., Q. Li, R.D. Parrella, and M. Teplitsky, "Enhancement of the 77 K irreversibility field and critical current density of  $(\text{Bi,Pb})_2\text{Sr}_2\text{Ca}_2\text{Cu}_3\text{O}_x$  tapes by manipulation of the final cooling rate", *Applied Physics Letters* 69 (1996) 2915.

J.A. Parrell, D.C. Larbalestier, G.N. Riley, Jr., Q. Li, R.D. Parrella, and M. Teplitsky, "Connectivity and flux pinning improvements in Ag-clad BSCCO-2223 tapes produced by changes in the cooling rate", to be submitted (1996).

### **10.1 Introduction**

The superconducting properties of 2223 tapes are strongly dependent on several microstructural features which can determine the macroscopic  $J_c$  of the polycrystalline

oxide filament(s).  $J_c$  is defined here once again in the usual macroscopic sense as the critical current  $I_c$  divided by the whole superconductor cross-section. However, changes in  $J_c$  defined in this manner are not necessarily directly related to local factors. As shown in the previous chapters, the grain alignment [7,123,134,135,136,137,173], bulk density [25,30,106,133,138,139], microcrack density [125,128,133,148,167], and phase purity [33,85,86,174] are all factors which can impose limits on the grain-to-grain connectivity, and thus the macroscopic  $J_c$ , of a 2223 tape. These properties are largely determined by specific details of the tape heat treatment and deformation processing sequence.

As shown in Chapter 9, the rate at which 2223 tapes are cooled after heat treatment has a large effect on the transport  $J_c$ , critical temperature ( $T_c$ ) transition, and filament microstructure [119]. Slow cooling ( $< 0.1^\circ\text{C}/\text{min}$ ) in 7.5%  $\text{O}_2$  increased the  $J_c$  (77 K, 0 T) by as much as 50% over tapes more quickly cooled, considerably sharpened the  $T_c$  transition, and in some cases, increased the onset  $T_c$  by 1-2 K, despite decomposition of the 2223 phase caused by cooling slowly at temperatures below the 2223 phase stability limit ( $\sim 800^\circ\text{C}$  in 7.5%  $\text{O}_2$  [53,117]). Several other groups have reported similar findings during the course of tape processing [170,175,176,177]. These beneficial effects of slow cooling were even observed in samples that still contained substantial amounts ( $\sim 50\%$ ) of precursor (unreacted) 2212 phase. These results were surprising in light of earlier work by Umezawa et al. [85,86], who found that the  $J_c$  and the  $T_c$  transition of fully-processed 2223 tapes were very sensitive to the number density of residual 2212 intergrowths within the 2223 grains. This apparent paradox suggests that the cooling rate influences an additional, perhaps previously unappreciated,  $J_c$ -limiting factor.

The increased  $J_c$  values indicate that cooling slowly reduces the effect of one or more significant active  $J_c$ -limiting mechanisms. Although it is well documented that the connectivity factors mentioned above have a large influence on  $J_c$ , many authors have concluded that, at temperatures above  $\sim 30$  K and/or in high magnetic fields,  $J_c$  can be limited by the intragranular [131,178,179,180,181] or intergranular (i.e. grain boundary) [182,183,184] flux pinning strength of the 2223 microstructure. It is likely that either connectivity or flux pinning can limit  $J_c$ , with the active limitation in any given sample (or at any given point within a sample) being dependent on the sample processing history. From this viewpoint the large scatter in reported  $J_c$  results and the irreproducibility of high  $J_c$  values is not surprising; it is just a consequence of not understanding the influence of many specific details of the process that are not tightly controlled, or even recognized as significant.

To find the reason why the cooling rate can have such a strong effect on the superconducting properties of 2223 tapes, samples were examined using a number of analysis techniques. Scanning electron microscopy (SEM) with wavelength dispersive spectroscopy (WDS) and x-ray diffraction (XRD) were used to characterize the microstructure and phase balance of fully-processed tapes, as well as tapes which were quenched from various temperatures. Several techniques were used to characterize the superconducting properties, including: Transport  $J_c$  measurements ( $1 \mu\text{V}/\text{cm}$ ) at 77 K and 4.2 K in both zero field and in applied magnetic fields; high-sensitivity electric field-transport current density ( $E$ - $J$ ) measurements at 77 K, to determine the irreversibility field of the percolative current path,  $H^*$  [134,180,184,186]; SQUID magnetization

measurements as a function of field at 77 K, to determine the irreversibility field as measured by magnetization; and SQUID magnetization measurements at constant field as a function of temperature, to examine the effect of cooling rate on the  $T_c$  transition.

After considering the results, the complicated behavior of slowly cooled samples is discussed. It is deduced that slow cooling improves *both* the connectivity and the flux pinning properties of 2223 tapes.

## **10.2 Experimental Procedure**

Multifilament tape having 85 filaments was made by American Superconductor Corporation. Powder of nominal composition  $\text{Bi}_{1.74}\text{Pb}_{0.29}\text{Sr}_{1.84}\text{Ca}_{1.94}\text{Cu}_{3.00}\text{O}_x$  was packed into a Ag tube, and this wire was drawn and restacked into an 85 filament bundle which was in turn drawn and rolled into tape. Samples of this tape were then thermomechanically processed by two heat treatments separated by an intermediate rolling step to develop a dense and aligned 2223 phase structure. The final heat treatment was given at 825°C for 100 hours in a flowing 7.5%  $\text{O}_2$ /balance  $\text{N}_2$  atmosphere. The samples were then cooled from 825°C to 730°C under electronic furnace programmer control at rates of 5, 1.6, 0.5, 0.16, 0.05, 0.016, and 0.005°C/min. Below 730°C, the samples were furnace-cooled in low thermal mass furnaces at  $\sim 20^\circ\text{C}/\text{min}$ . A set of samples controllably-cooled at 0.05°C/min to 775°C instead of 730°C before furnace-cooling was also produced, in order to examine the effect of changing the lower temperature limit.

Some samples were also quenched from various temperatures to check for sub- $\mu\text{m}$  scale microstructural changes caused by slow cooling. Samples heated in 7.5%  $\text{O}_2$  were oil-quenched after a 24 hour hold at  $825^\circ\text{C}$  (the 2223 reaction temperature) to preserve the microstructural features present at that temperature. Samples were also slowly cooled from  $825^\circ\text{C}$  at  $0.016^\circ\text{C}/\text{min}$ , and then quenched from  $782^\circ\text{C}$ . A scanning electron microscope operated at 15 kV in backscatter mode was used to record the microstructures of polished longitudinal and transverse cross-sections of both quenched and fully-processed samples. X-ray diffraction using  $\text{Cu-K}\alpha$  radiation was also used to examine the phase content of some of the fully processed samples.

The 77 K, 0 T critical currents defined at  $1 \mu\text{V}/\text{cm}$  were measured for at least six 2.5 cm long samples for each of the seven cooling rate conditions. These critical currents were converted to  $J_c$  by dividing by the average of 12 transverse cross sections of the superconductor area measured by image analysis. The critical currents of some samples were measured at 77 K and at 4.2 K in magnetic fields from 0 to 10 T applied perpendicular to the rolling plane of the tape (i.e. nominally parallel to the c-axis of the 2223 grains).

Extended voltage-transport current ( $V$ - $I$ ) measurements were made at 77 K on at least two samples for each cooling rate using a Keithley 1801 nanovolt preamplifier and a 2001 digital multimeter. A sample cooled to  $730^\circ\text{C}$  at  $0.016^\circ\text{C}/\text{min}$  was also measured after it had been doubly bent to  $\varepsilon_b = 0.4\%$  (where  $\varepsilon_b = \text{tape thickness divided by the bending diameter}$ ) and straightened, for reasons that will be described in the results and discussion sections. The thermoelectric noise was kept to  $\pm 3 \text{ nV}$  in the best cases by

using continuous Cu voltage leads from the liquid N<sub>2</sub> to the preamplifier inputs. The voltage, measured between contacts spaced  $\approx 5$  mm apart, ranged from  $\sim 0.005$  to  $\sim 50$   $\mu\text{V}$ , corresponding to nominal electric fields of 0.01 to 100  $\mu\text{V}/\text{cm}$ .

Although it is desirable to remove the Ag cladding [184] in order to measure the true  $E$ - $J$  characteristics of the 2223 cores above  $\sim 1$   $\mu\text{V}/\text{cm}$  (where current sharing with the Ag becomes appreciable [181,184,186]), this was not feasible for the 85-filament samples used in this study. To correct for current sharing between the Ag sheath and the 2223 filaments, the current flowing in the superconductor,  $I_s$ , was calculated from  $I_s = I - V/R_{Ag}$ , where  $I$  is the measured current,  $V$  is the measured voltage, and  $R_{Ag}$  is the measured resistance of the Ag cladding.  $R_{Ag}$  was determined by measuring a sample which had been severely bent to  $\epsilon_b = 3.1\%$ , thus destroying the continuous 2223 paths. This bent and straightened sample was annealed at 400°C for 30 min before measurement to eliminate any cold work effect on the Ag resistivity caused by the bending. The Ag sheath resistance at 77 K was found to vary by less than 2% between 20 and 300 mT, as shown in Figure 10-1. For this reason the magnetic field dependence of  $R_{Ag}$  was ignored, and the value measured at  $\mu_0 H = 300$  mT was used. The  $E$ - $J$  characteristics of samples before and after this correction for current sharing were identical below  $\sim 1$   $\mu\text{V}/\text{cm}$ , which agrees with what Edelman et al. found for samples measured with and without the Ag cladding [183,184], indicating that subtracting the effect of the Ag sheath does not change the low  $E$  characteristics, and only has an appreciable effect at higher electric fields.

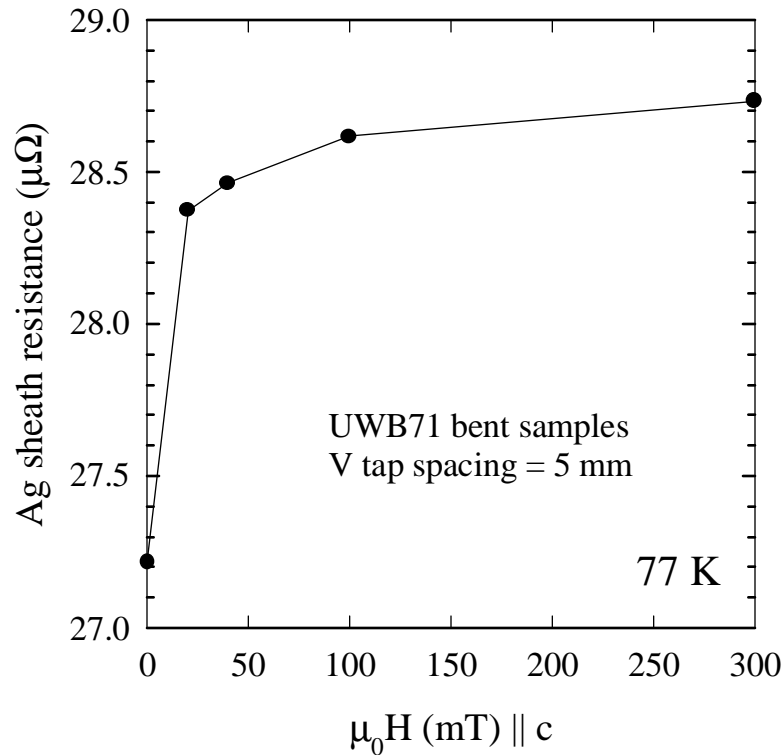


Figure 10-1. Resistance of the Ag sheath ( $R_{Ag}$ ) of composite UWB71 measured at 77 K as a function of magnetic field.  $R_{Ag}$  was nearly constant above  $\sim 20$  mT.

Following convention [134,180,184,186],  $H^*$  is defined as the field at which the curvature of the  $\log E$ - $\log J$  characteristics changes from negative to positive. A quadratic fit to the measured data was used to provide an unbiased determination of the curvature of each  $\log E$ - $\log J$  characteristic, and  $H^*$  was taken as the field at which the value of the coefficient of square term of the quadratic passed through zero [183,184,185,186].

The  $T_c$  transitions of some samples were measured in a SQUID magnetometer (Quantum Design MPMS) in a field of 0.1 mT applied parallel to the nominal c-axis. Magnetization loops of some samples were also recorded with a SQUID magnetometer, at 77 K, in fields from -240 mT to +240 mT also applied parallel to the c-axis. The irreversibility field determined by magnetization was defined as the field of loop closure.

### **10.3 Results**

Figure 10-2 shows  $J_c$  (77 K, 0 T), determined at  $1 \mu\text{V}/\text{cm}$ , as a function of cooling rate for all of the fully processed samples produced in this study. The data for samples cooled to  $730^\circ\text{C}$  is shown as the open circles within the shaded scatter band. As the cooling rate was decreased from  $5^\circ\text{C}/\text{min}$  to  $0.005^\circ\text{C}/\text{min}$ , the critical current density increased from  $\sim 8 \text{ kA}/\text{cm}^2$  to a maximum value of  $\sim 24 \text{ kA}/\text{cm}^2$  for a cooling rate of  $0.016^\circ\text{C}/\text{min}$ , and then decreased for the slower cooling rate of  $0.005^\circ\text{C}/\text{min}$ . Similar behavior has been observed previously [119,176,186], as shown in Chapter 9. The solid triangles show the data for the samples cooled at  $0.05^\circ\text{C}/\text{min}$  to the intermediate temperature of  $775^\circ\text{C}$ . These samples had  $J_c \sim 19 \text{ kA}/\text{cm}^2$ , which was slightly lower than the  $\sim 22 \text{ kA}/\text{cm}^2$  obtained in samples cooled at  $0.05^\circ\text{C}/\text{min}$  all the way to  $730^\circ\text{C}$ . These data suggest that the improvement of the superconducting properties occurs continuously during the entire cooling cycle.

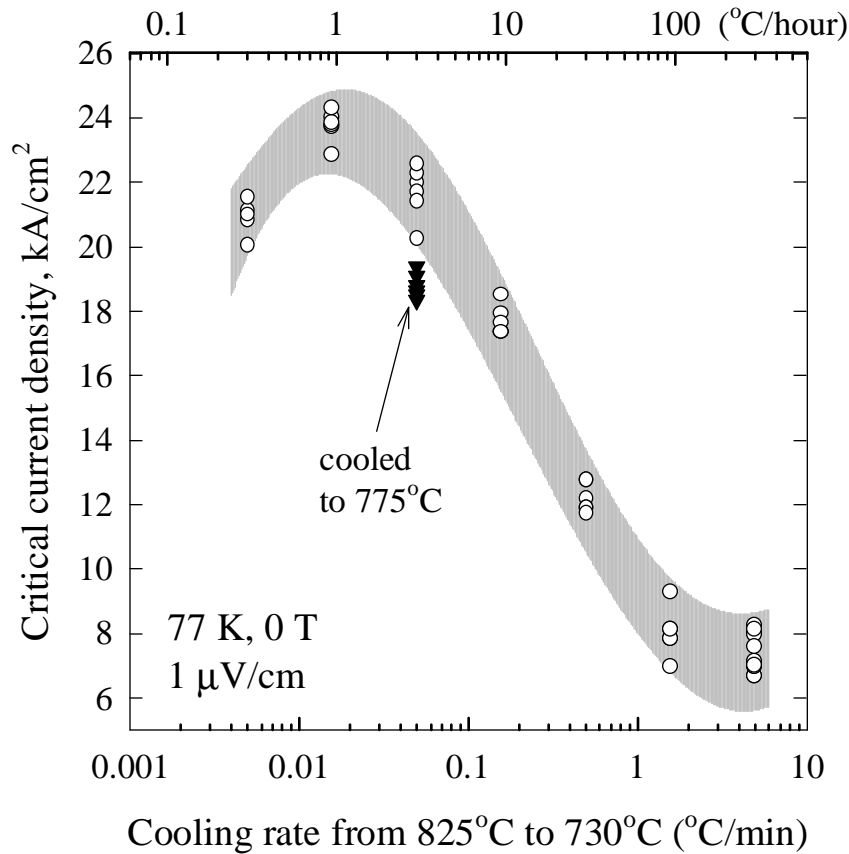


Figure 10-2.  $J_c$  (77 K, 0 T) as a function of cooling rate for samples of UWB71. The circles within the scatter band were cooled to  $730^\circ\text{C}$  before furnace cooling, and the triangles indicate samples cooled to  $775^\circ\text{C}$  before furnace cooling.  $J_c$  was maximized at a cooling rate of  $\sim 0.016^\circ\text{C/min}$ .

SEM images of the longitudinal microstructures of fully-processed samples cooled at the fastest rate,  $5^\circ\text{C/min}$ , and at an intermediate rate,  $0.16^\circ\text{C/min}$ , are shown as Figure 10-3. Although the  $0.16^\circ\text{C/min}$  samples contained more non-superconducting second phase particles, particularly  $(\text{Bi,Pb})_3\text{Sr}_2\text{Ca}_2\text{CuO}_z$  (or "3221") [148,161,162,165] and  $(\text{Ca,Sr})_2\text{PbO}_4$ , they had  $J_c \sim 18 \text{ kA/cm}^2$ , which was substantially higher than the  $J_c \sim 8$

kA/cm<sup>2</sup> of the 5°C/min samples, even though those samples contained less second phase. This somewhat surprising result confirmed what was observed in Chapter 9 [119], and suggests that the microstructural features apparent at the μm scale do not necessarily control the macroscopic  $J_c$ .

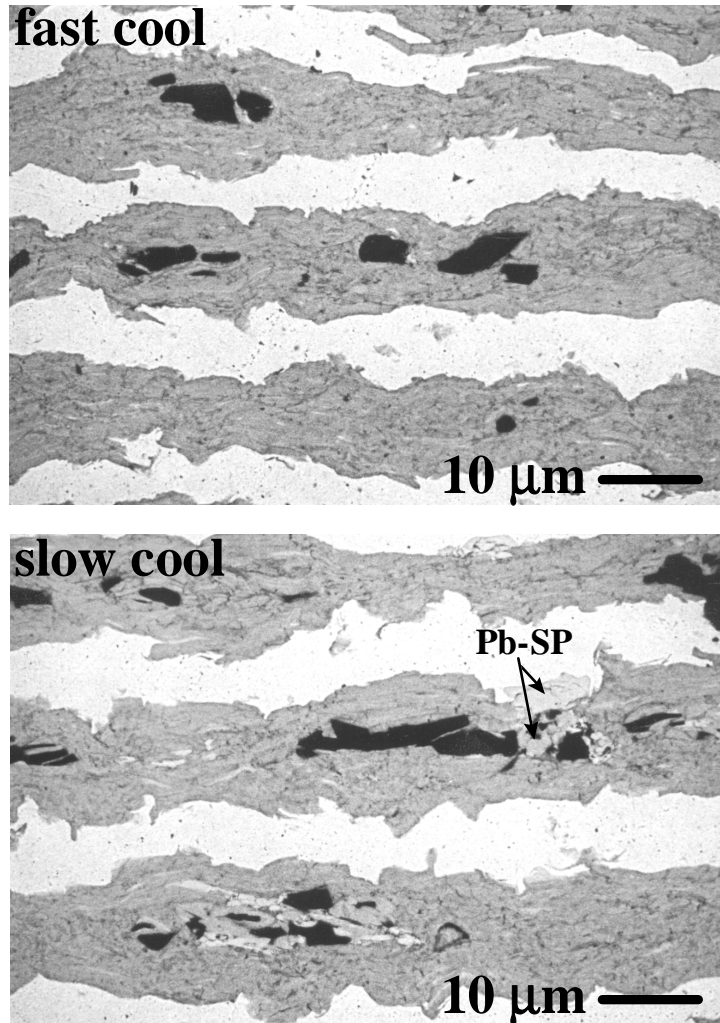


Figure 10-3. SEM micrographs of samples cooled to 730°C at 5°C/min (top) and 0.16°C/min (bottom). Cooling slowly caused the 2223 phase to decompose, increasing the volume fraction of second phase particles in the microstructure, particularly those that are Pb-rich (“Pb-SP”).

Figure 10-4 shows XRD patterns for fully processed samples cooled from 825°C to 730°C at 5°C/min (the fastest rate) and 0.016°C/min (the  $J_c$ -optimal rate). The slowly cooled sample contained more 3221 and  $(\text{Ca,Sr})_2\text{PbO}_4$  phase (i.e. more Pb,Bi-rich phases),

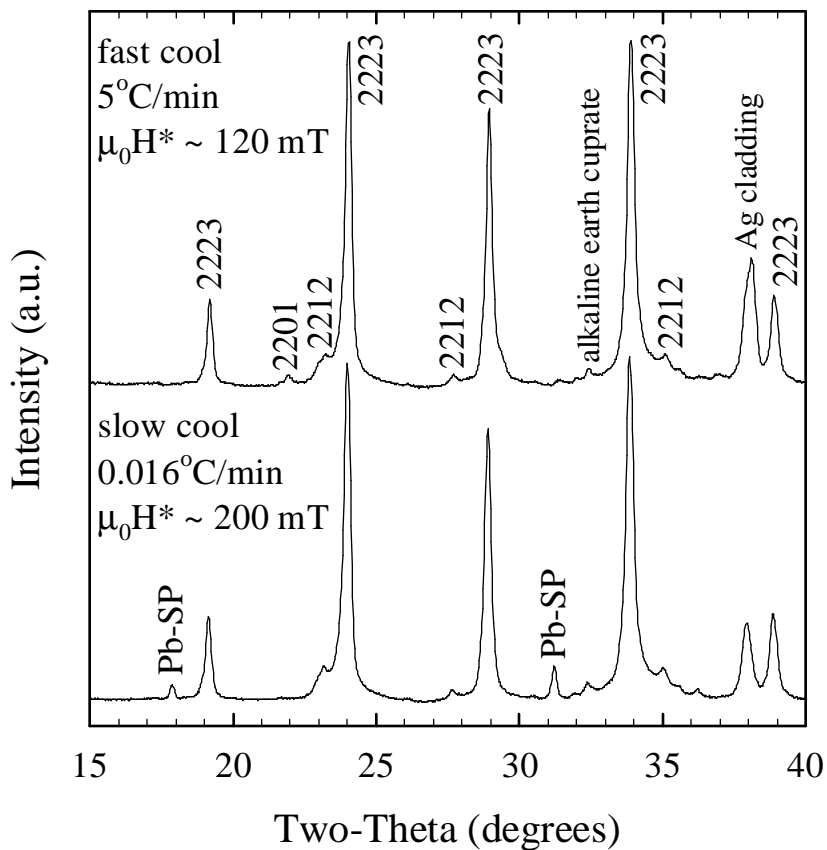


Figure 10-4. X-ray diffraction patterns of samples cooled at  $5^{\circ}\text{C}/\text{min}$  and  $0.016^{\circ}\text{C}/\text{min}$ . The more slowly cooled sample contains more Pb-rich impurity phase, and less 2201.

as evidenced by the diffraction peaks labeled "Pb-SP" in the figure at  $2\theta \sim 17.9^{\circ}$  and  $\sim 31.1^{\circ}$ , in agreement with what was observed by SEM (Figure 10-3). The slowly cooled sample also contained less BSCCO-2201 phase than the sample cooled at  $5^{\circ}\text{C}/\text{min}$ .

Figure 10-5 shows  $J_c$  (77 K,  $1 \mu\text{V}/\text{cm}$ ) as a function of magnetic field applied parallel to the c-axis for samples cooled at  $5^{\circ}\text{C}/\text{min}$ , which had the lowest  $J_c$ ,  $0.16^{\circ}\text{C}/\text{min}$ ,

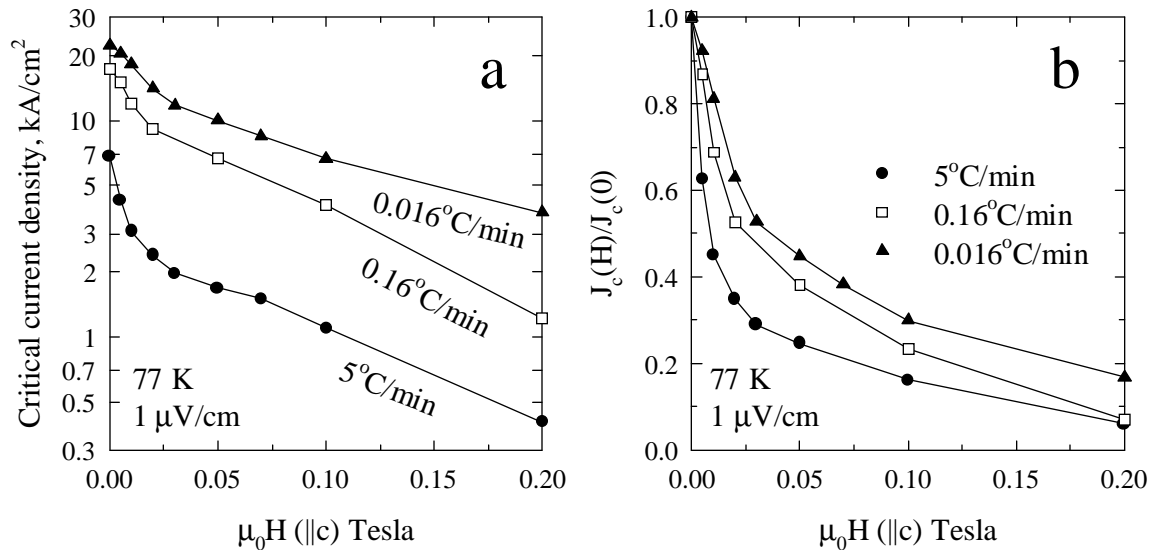


Figure 10-5. (a)  $J_c$  (77 K, 0 T, 1  $\mu\text{V/cm}$ ) of selected samples as a function of magnetic field applied parallel to the nominal c-axis of the 2223 grains. (b) Normalized  $J_c$  values as a function of field. Slow cooling increased both the zero field and in-field  $J_c$  values.

which had a mid-range  $J_c$ , 0.016°C/min, which had the highest  $J_c$ . Figure 10-5a plots the absolute value of  $J_c$  as a function of field, and Figure 10-5b plots  $J_c(H)$  normalized to the zero-field  $J_c$ . Each data point is the average of three samples. It can be seen that both the maximum value of  $J_c$  and the  $J_c$  resistance to an applied field increased as the cooling rate was decreased.

Figure 10-6 is similar to Figure 10-5, but shows absolute and normalized  $J_c(H)$  data measured at 4.2 K. The fact that slow cooling improved  $J_c$  (4.2 K, 0 T) suggests a change in the intergranular connectivity, as the irreversibility field (i.e. flux pinning limit) at 4.2 K

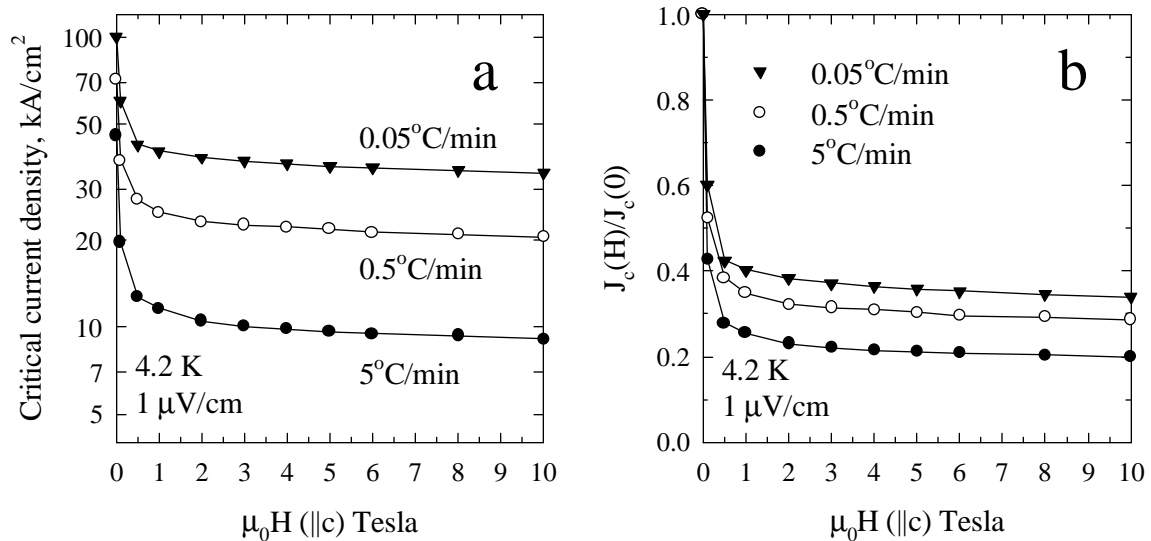


Figure 10-6. (a)  $J_c$  (4.2 K,  $1 \mu\text{V}/\text{cm}$ ) of selected samples as a function of magnetic field applied parallel to the nominal c-axis of the 2223 grains. (b) Normalized  $J_c$  values as a function of magnetic field. Both the 77 K and 4.2 K properties were improved by slow cooling.

is many times the field range of the measurement. The slowly cooled samples exhibit better in-field  $J_c$  retention at 4.2 K, just as they did at 77 K.

Figure 10-7 plots the magnetic moment of samples cooled at  $5^\circ\text{C}/\text{min}$  (the fastest rate) and  $0.016^\circ\text{C}/\text{min}$  (the  $J_c$ -optimal rate) measured at  $0.1 \text{ mT} \parallel c$  as a function of temperature. Note that slow cooling sharpens the  $T_c$  transition, as has been previously reported [119]. Additionally, as shown more clearly in the inset of Figure 10-7, slow cooling increased the onset  $T_c$  from  $\sim 107 \text{ K}$  to  $\sim 109 \text{ K}$ .

An example of the extended  $E$ - $J$  data used for determination of  $H^*$  is shown as Figure 10-8. Figure 10-8a plots the  $E$ - $J$  data from a sample cooled at  $0.016^\circ\text{C}/\text{min}$ , which had a 77 K, 0 T,  $1\ \mu\text{V}/\text{cm}$  critical current of 37.5 A. The open circles are the measured data points (which have been corrected for current sharing with the Ag), and the solid curves are quadratic fits to the data. Below  $H^*$ , the  $\log E$ - $\log J$  characteristics have a negative curvature, whereas the  $\log E$ - $\log J$  characteristics above  $H^*$  have a positive curvature. Figure 10-8b shows the data from Figure 10-8a collected at 200 mT, both as-measured and after correcting for current sharing with the Ag sheath. Note that above  $\sim 1\ \mu\text{V}/\text{cm}$ , current sharing becomes appreciable, and causes the measured characteristic to bend towards lower electric field values. Figure 10-8c is a plot of the curvature parameter (the coefficient of the square term of the quadratic fit) as a function of applied magnetic field, for the  $E$ - $J$  curves of Figure 10-8a. The field at which the curvature parameter changes from negative to positive is defined as  $H^*$ .  $\mu_0 H^*$  for this sample was  $197 \pm 5\ \text{mT}$ .

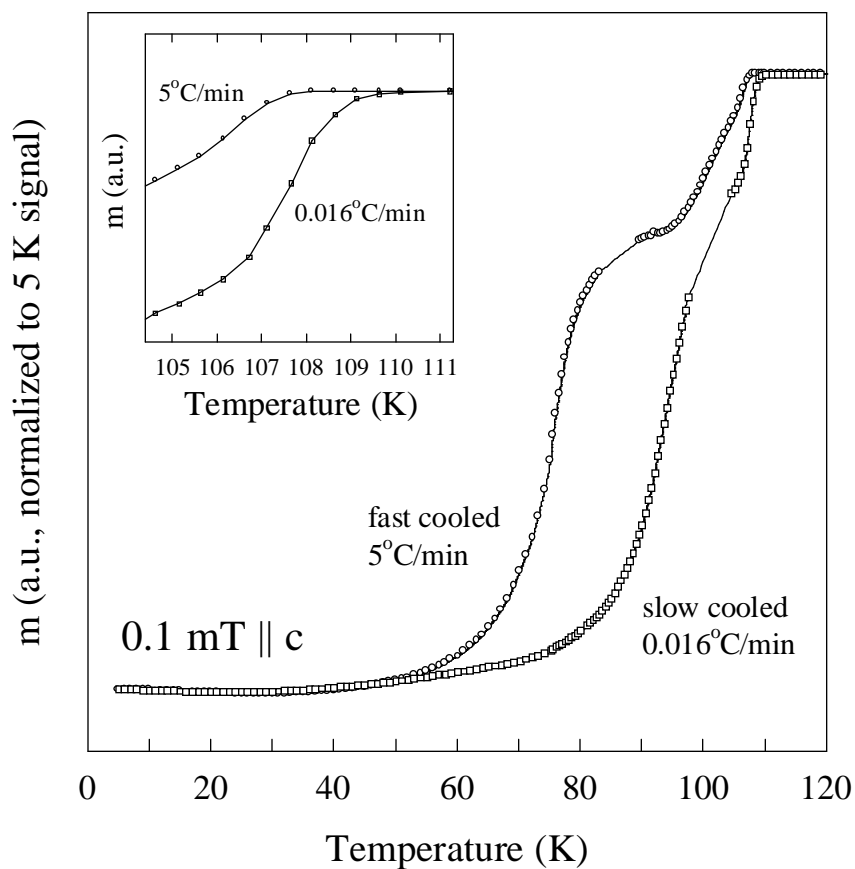


Figure 10-7. The  $T_c$  transitions of samples cooled at  $5^\circ\text{C}/\text{min}$  and  $0.016^\circ\text{C}/\text{min}$  as measured in a SQUID magnetometer. The signals are normalized to their values at 5 K. Cooling slowly sharpened the  $T_c$  transition, and increased the onset  $T_c$  from  $\sim 107$  K to  $\sim 109$  K (see inset).

Figure 10-9 shows  $H^*$ , determined as shown in Figure 10-8 and as determined from magnetization measurements, as a function of cooling rate from  $825^\circ\text{C}$  to  $730^\circ\text{C}$ . Note the non-zero origin of the  $H^*$  axis. The error bars represent the error associated with the determination of the field at which the curvature parameter of the quadratic fit changed sign. As the cooling rate was decreased from  $5^\circ\text{C}$  to  $0.005^\circ\text{C}/\text{min}$ ,  $\mu_0 H^*$  increased from  $\sim$

120 to  $\sim 200$  mT. The general behavior of  $H^*$  as a function of cooling rate is similar to that of  $J_c$ , as shown in Figure 10-2.

Figure 10-10 shows  $H^*$  of the samples from Figure 10-9 as a function of their 77 K, 0 T, 1  $\mu\text{V}/\text{cm}$  critical current density. It can be seen that there is a strong positive correlation between  $H^*$  and  $J_c$ .  $\mu_0 H^*$  rises from  $\sim 120$  mT in samples that have  $J_c$  (77 K, 0 T, 1  $\mu\text{V}/\text{cm}$ )  $\sim 8$   $\text{kA}/\text{cm}^2$  to over 200 mT in samples with  $J_c \sim 23$   $\text{kA}/\text{cm}^2$ . This correlation indicates that at least part of the  $J_c$  improvement caused by slow cooling is due to an increase in the irreversibility field of important components of the percolative current path.

Figure 10-11 shows the extended  $E$ - $J$  data of the same  $0.016^\circ\text{C}/\text{min}$  sample shown in Figure 10-8, after it had been doubly bent to  $\varepsilon_b = 0.4\%$  and then straightened. This treatment reduced the 1  $\mu\text{V}/\text{cm}$  critical current from 37.5 A to 13.9 A. The sample was annealed at  $400^\circ\text{C}$  for 30 minutes prior to measurement to remove cold work effects in the Ag cladding caused by the bending.  $\mu_0 H^*$  for this bent sample was  $205 \pm 5$  mT, which is the same value ( $197 \pm 5$  mT) as determined for the undamaged sample of Figure 10-8. Thus, although bending and cracking the sample reduced the critical current by  $\sim 60\%$ ,  $H^*$  was not affected. This supports the interpretation that  $H^*$  is measuring the intragranular, flux pinning properties.

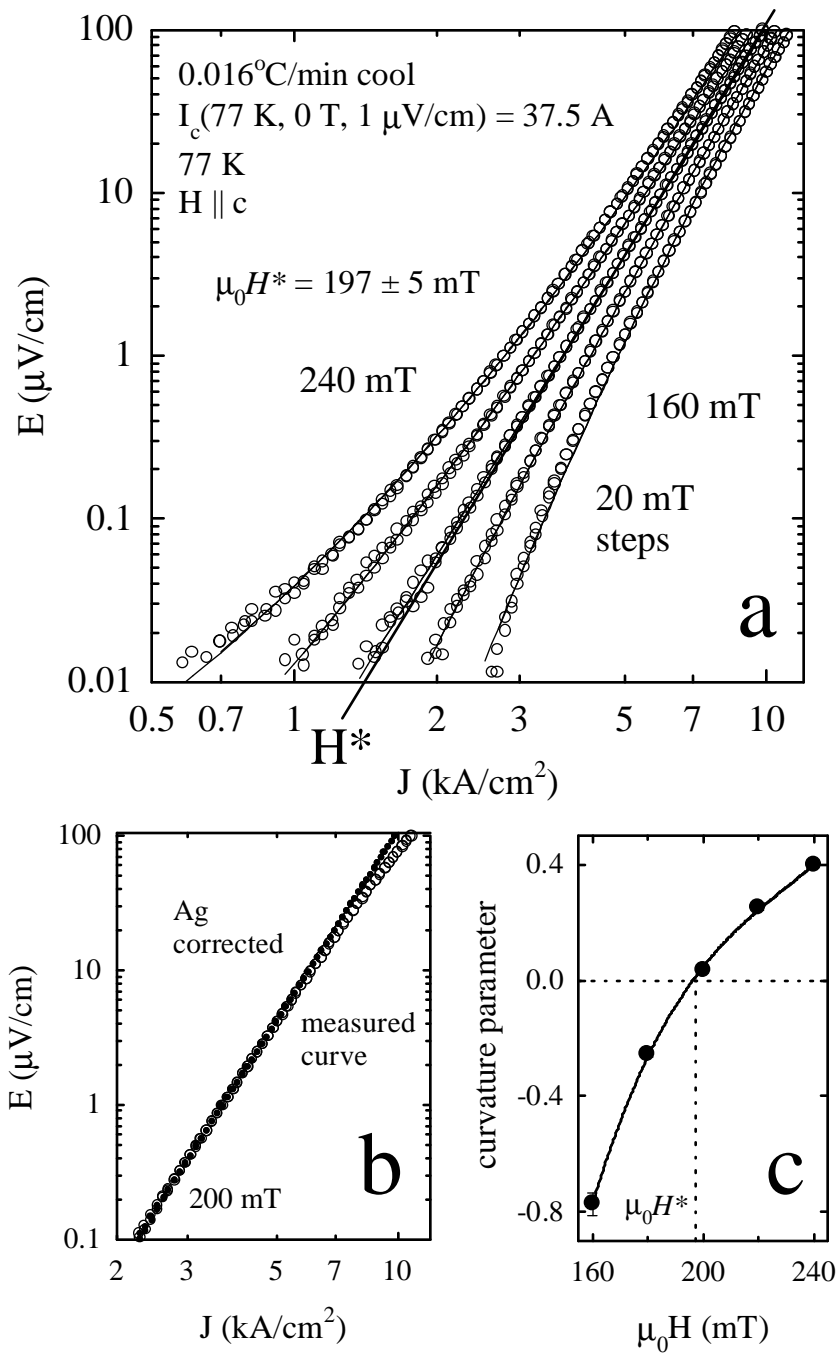


Figure 10-8. (a) Extended  $E$ - $J$  characteristics as a function of field for a sample cooled at  $0.016^\circ\text{C}/\text{min}$ . (b) Plot of the  $200\text{ mT}$  data from (a), both as-measured and after correction for current sharing with the Ag matrix. Current sharing becomes appreciable above  $\sim 1\ \mu\text{V}/\text{cm}$ . (c) Plot of the curvature parameter fit as a function of field.  $H^*$  was taken as the field where the curvature changed sign.  $\mu_0 H^*$  for this sample was  $197 \pm 5\text{ mT}$ .

Figure 10-12 shows high magnification SEM backscatter micrographs of one sample oil-quenched directly from the heat treatment temperature of 825°C, and of a second sample cooled at 0.016°C/min to 782°C and then quenched. Figure 10-12a shows the transverse microstructure of a filament from a sample quenched from 825°C. Small pockets of a phase which appears white under backscatter imaging mode are visible throughout the filament. Although in this case their composition could not be verified, from experience (e.g. Figure 8-12) such white regions have a composition close to 2201, and are Bi- and Pb-rich [33,187]. Based on their grain-wetting morphology, the regions presumably are amorphous, frozen pockets of liquid. The liquid pockets were commonly observed at the junctions between slightly misaligned 2223 platelets. Figure 10-12b shows a sample which was slow cooled (0.016°C/min) to 782°C and then quenched. Regions of the white Bi,Pb-rich phase could not be found. However, this sample contained much more 3221 and (Ca,Sr)<sub>2</sub>PbO<sub>4</sub> phase than the sample quenched from 825°C, and also had regions that looked like 2212 phase, based on their atomic number contrast, as indicated by the black arrows in Figure 10-12b. These micrographs suggest that the white liquid phase present at 825°C transformed into crystalline Bi,Pb-rich phases during the slow cooling to 782°C, changing from what appears to be a wetting phase (Figure 10-12a) to discrete point-like phases (bottom micrograph of Figure 10-3) in the process.

#### **10.4 Discussion**

The fact that slow cooling markedly improves  $J_c$ ,  $T_c$ , and  $H^*$ , while at the same time significantly degrading the microstructural quality, appears to violate one of the

central paradigms of BSCCO tape development, namely that higher phase purity samples have better superconducting properties than those of lower phase purity. This presents an apparent paradox which raises vital questions about the current limiting mechanisms of 2223 tapes. Here we discuss the flux pinning and connectivity contributions to  $J_c$ , again emphasizing that only the measurement of  $I_c$  is certain. Because the superconductor cross section over which current actually flows is uncertain, the derived  $J_c = I_c/A$  is also unsure, and certainly underestimated.

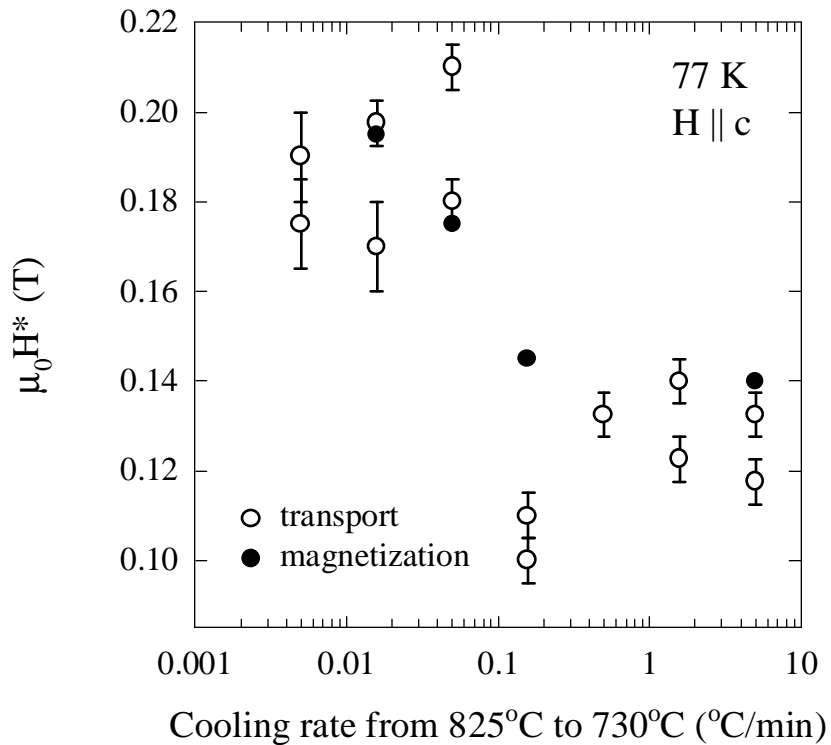


Figure 10-9. The irreversibility field, measured by the current transport method and by magnetization, as a function of cooling rate.  $H^*$  increased as the cooling rate was decreased. The behavior is similar to that observed for the  $J_c$  values shown in Figure 10-2.

#### 10.4.1 Intragranular flux pinning

Clear evidence that the intragranular properties are improved during slow cooling comes from the increased  $H^*$  values (Figures 7, 8, and 10), the increased in-field  $J_c$  retention (Figures 4 and 5), and the improved  $T_c$  transition (Figure 6). In this chapter  $H^*$  is used as a measure of flux pinning. In the case of BSCCO we can expect that  $H^*$  could be

increased by at least two independent means, one due to a lessening of anisotropy [12], and the other due to an increase in the pinning center density.

A reduction in the anisotropy (i.e. better coupling between Cu-O planes) could be caused by an optimization of the oxygen content of the 2223 phase during the cooling cycle [188]. Although it has been well documented that the  $T_c$  of 2212 is very sensitive to oxygen content [189,190,191], there have been relatively few reports on the relationship between the  $T_c$  (and  $H^*$ ) and oxygen content of the 2223 phase. Brauer et al. [192] have reported that decreasing the cooling rate of Ag-clad  $\text{Bi}_{1.79}\text{Pb}_{0.34}\text{Sr}_{1.84}\text{Ca}_{2.03}\text{Cu}_{3.00}\text{O}_x$  tapes treated in air from a very high rate, obtained by quenching, to  $\sim 0.5^\circ\text{C}/\text{min}$  increased the onset  $T_c$  from 102 K to 108 K, and changed the oxygen content from  $x = 10.05$  to  $x = 10.28$ . Tetenbaum and Maroni have also reported that the oxygen content of the 2223 phase increases during cooling [193]. Additionally, Özdás and Firat have shown [171] that the  $T_c$  transition can be substantially sharpened, and the onset changed by  $\sim 3$  K, by post-annealing bulk  $\text{Bi}_{1.7}\text{Pb}_{0.3}\text{Sr}_{1.8}\text{Ca}_2\text{Cu}_{2.8}\text{O}_x$  samples for 12 hours at  $750^\circ\text{C}$  in atmospheres ranging from 1.5-11%  $\text{O}_2$ . They found that the sharpest transition and maximum onset  $T_c$  of 109 K occurred in a 6.5%  $\text{O}_2$ . These findings are consistent with those reported here and in Chapter 9 [119], in that the  $T_c$  (and  $J_c$ ) improvements were obtained in samples cooled from  $825^\circ\text{C}$  to  $730^\circ\text{C}$  in 7.5%  $\text{O}_2$ , at rates between  $5^\circ\text{C}/\text{min}$  and  $0.005^\circ\text{C}/\text{min}$ . Thus, in an analogy to the BSCCO-2212 system, it may be that 2223 quickly cooled in 7.5%  $\text{O}_2$  is underdoped with respect to oxygen. Cooling slowly increases the oxygen content, which both increases  $T_c$  and reduces the anisotropy. Both factors should cause an increase in  $H^*$ .

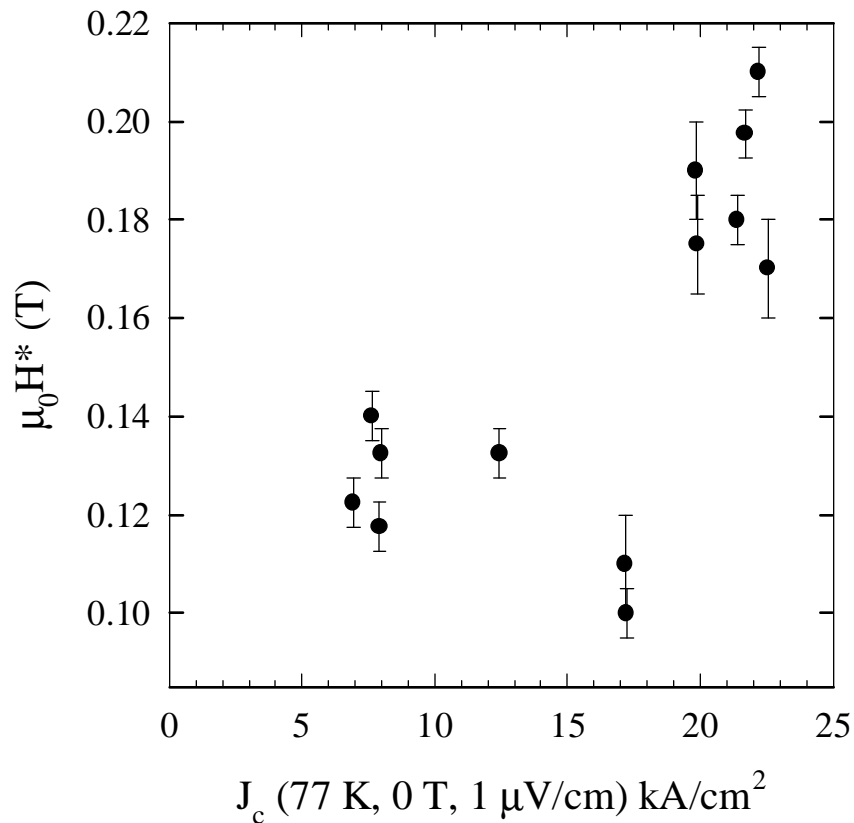


Figure 10-10.  $H^*$  versus the 77 K, 0 T, 1  $\mu\text{V}/\text{cm}$  critical current density for the samples whose  $H^*$  values are shown in Figure 10-9. As  $J_c$  increased from  $\sim 8$   $\text{kA}/\text{cm}^2$  to  $\sim 23$   $\text{kA}/\text{cm}^2$  as a result of slow cooling,  $\mu_0 H^*$  was observed to increase from  $\sim 120$  mT to  $\sim 200$  mT.

Another possible cause for the observed intragranular improvements could be that there is a shift of the cation stoichiometry of the 2223 phase due to the decomposition. Although there are few reports in the literature for such an effect, Hudáková et al. [194] have reported that the sharpness of the  $T_c$  transition and of bulk  $\text{Bi}_{2-y}\text{Pb}_y\text{Sr}_2\text{Ca}_2\text{Cu}_3\text{O}_x$  samples is a function of the Pb content, and found that  $y \approx 0.3$  is the optimum

composition. The decomposition of the 2223 phase during slow cooling results in the formation of Bi,Pb-rich phases (Figure 10-3 and Figure 10-4), suggesting that the 2223 phase is preferentially rejecting Bi and Pb [195]. A composition change caused by slow cooling was confirmed by WDS analysis. As shown in Table 10-1, slowly cooled 2223 (0.05°C/min) contained less Pb than a more quickly cooled (5°C/min) sample. It is also possible, though in our opinion unlikely (due to the large particle size), that the  $H^*$  improvements could be the result of an increased number of flux pinning centers caused by decomposition by-products [160,196,197]. It seems more plausible that this compositional change, which moves the 2223 composition away from stoichiometry (Table 10-1), should cause atomic scale, cation defects in the remaining 2223. Such fine defects could act as effective pinning centers.

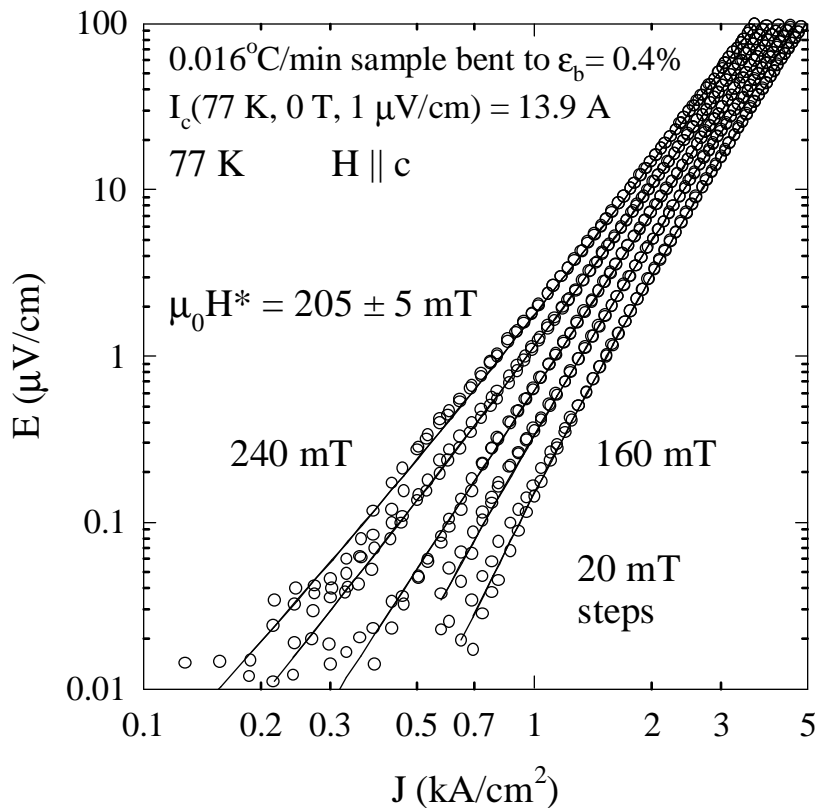


Figure 10-11. Extended  $E$ - $J$  characteristics for the 0.016°C/min sample of Figure 10-8 after it had been doubly bent to  $\epsilon_b = 0.4\%$  and then straightened. Although bending decreased  $I_c$  (77 K, 0 T, 1  $\mu\text{V/cm}$ ) from 37.5 A to 13.9 A,  $H^*$  did not change, within the precision of the measurement, and remained at  $\sim 200$  mT.

Additional support for a cation or anion adjustment mechanism for the improved intragranular properties is that cooling at 0.05°C/min to 775°C led to most but not all of the  $J_c$  improvement of cooling to 730°C (Figure 10-2). This indicates that the improvement in the superconducting properties does not occur abruptly, which suggests a

gradual microstructural change consistent with diffusion of either oxygen or cations in the 2223 phase.

#### 10.4.2 Intergranular connectivity

Although it is clear that cooling slowly improved the flux pinning, there is also evidence that the cooling rate influences the electromagnetic connectivity of the 2223 filaments. The fact that both  $J_c$  (77 K, 0 T) and especially  $J_c$  (4.2 K, 0 T) values were improved by slow cooling (Figure 10-5 and Figure 10-6) suggests that the intergranular connectivity, as well as  $H^*$ , was improved by slow cooling. In this section, the possible  $J_c$  and microstructural effects of cooling rate on several of the connectivity limits listed earlier is discussed.

The first two connectivity limitations to consider are misaligned grains and porosity. It does not seem likely that the 2223 alignment can be changed significantly during the cooling cycle: Whether the alignment is determined more by deformation-induced [137] or reaction-induced texturing [82,84], the texture is fixed after the reaction heat treatment, and should not be affected by even long times spent at lower temperatures. Changes to the density of the filament during the cooling cycle are uncertain but are unlikely [133]. Thus, we rule out significant effects of the cooling rate on these two connectivity parameters.

The next connectivity limit to consider is the effect of cooling rate on the microcrack density. The thermal expansion coefficients for the anisotropic BSCCO-2223 phase are not equal, being  $\sim 25 \times 10^{-6} \text{ }^\circ\text{C}^{-1}$  in the c-direction, and  $\sim 15 \times 10^{-6} \text{ }^\circ\text{C}^{-1}$  in the a-

and b-directions [198,199]. Since the thermal expansion coefficient of Ag lies between these two values at  $\sim 19 \times 10^{-6} \text{ }^\circ\text{C}^{-1}$  [200], we might expect that the ceramic filaments would be placed into compression along the a- and b-directions, and into tension in the c-axis direction during cooling. Recently, Goretta et al. [201] have used neutron diffraction to show that cores in Ag-clad tapes have residual stresses after cooling to room temperature. They reported that the 2223 cores in tapes made with an unspecified cooling rate were under an average tensile strain of 0.034%. Note that even nominally compressive stresses could result in cracks, as 2223 tapes always have misaligned grains, are multiphase, and are somewhat porous due to the plate-like 2223 grain growth and its accompanying retrograde densification [129,133]. Thermal stresses large enough to crack the BSCCO would certainly degrade the critical current. It is possible that slow cooling relaxes stress in the oxide filaments (by allowing time for creep of either the Ag and/or BSCCO to occur), thus reducing microcracking and increasing the core connectivity, thereby raising  $J_c = I_c/A$  by increasing the effective cross section. However, cracks alone should have no effect on the  $H^*$  (except when filaments are very inhomogeneous), a result borne out in the comparison of the not bent and bent sample characteristics in Figure 10-8 and Figure 10-11. Thus, it seems that the changes observed in the  $H^*$  (77 K) as a function of cooling rate can not solely be due to changes in the microcrack density of the filaments, as  $H^*$  is simultaneously changing.

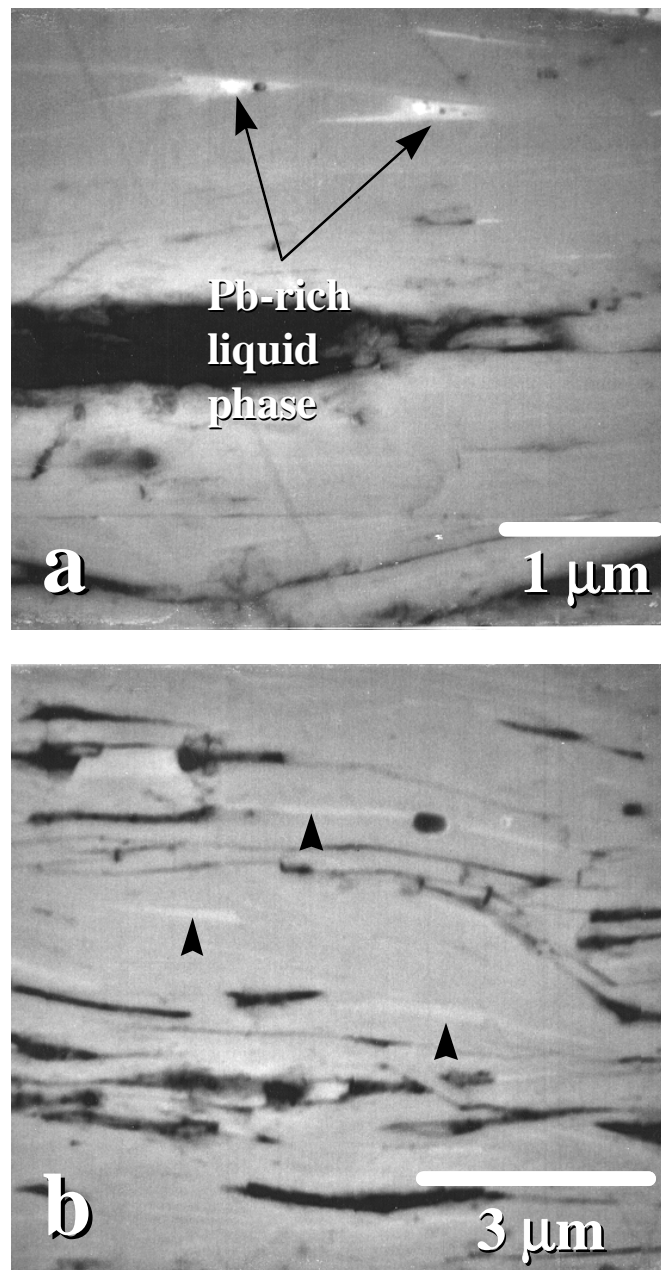


Figure 10-12. SEM backscatter micrographs of quenched samples. (a) is from a sample quenched from 825°C. Note the white Pb-rich regions. (b) is from a sample cooled from 825°C at 0.05°C/min and then quenched from 782°C. Pb-rich pockets are no longer visible. Regions of 2212 phase are indicated by the black arrows.

The final connectivity limit to consider is that posed by impurity or "second" phases within the 2223 microstructure. As shown in Figure 10-3 and Figure 10-4, slow cooling decreases the 2223 phase purity, causing the formation of second phase particles large enough to locally block a significant fraction of the filament thickness. Thus, reducing the volume fraction of second phase cannot be the reason for the observed  $J_c$  benefits of slow cooling. However, it is possible that changes in the microstructure at a smaller scale could be responsible for the improved  $J_c$  values. Since the formation of the 2223 phase involves a liquid [40,43,45,46,47,50,51,62,97,145,146,147,202], it is plausible that small quantities of a wetting liquid remain spread over many grain boundaries or particle surfaces, even in an essentially fully converted tape. Such liquid regions may result from inevitable localized chemical inhomogeneities. They will be difficult to convert into the 2223 phase, if there is no interconnected fast-mass-transfer liquid path, because solid state diffusion in BSCCO is slow. Figure 10-12a suggests that these liquid pockets may be frozen in place, producing significant local interruptions to the current path when samples are quickly cooled. Thus the improvement in  $J_c$  (especially at 4.2 K and in low magnetic fields) could be due to crystallization of such a wetting liquid into non-wetting, discrete precipitates like those shown in the bottom micrograph of Figure 10-3. More evidence of this change comes from the XRD patterns of Figure 10-4, where it is shown that cooling slowly reduces the amount of the 2201 phase, which presumably forms from the Bi,Pb-rich pockets (Figure 10-12a) upon cooling. Even if this liquid is not able to form 2223 phase because it does not have the proper composition (such regions may be

Table 10-1. WDS analysis of the cation composition of fast and slow cooled 2223.

Sample Condition	Bi	Pb	Sr	Ca	Cu	Comments
Nominal powder composition	1.74	0.29	1.84	1.94	3.00	measured by ICP
Fast cooled 5°C/min	2.02	0.38	1.95	1.99	3.00	few Bi,Pb-rich phase particles
Slow cooled 0.05°C/min	1.99	0.35	1.94	1.97	3.00	more Bi,Pb-rich second phase

too Bi,Pb-rich [33,168,203,204]), changing from a wetting, amorphous to a non-wetting, crystalline phase should still increase the density of percolative current paths.

There are supporting data for this liquid phase/connectivity effect in the literature. Several authors have observed amorphous regions or layers in TEM studies [87,102,203,205,206]. For example, Li et al. [205] found amorphous layers at c-axis twist boundaries in 2223 tapes, and concluded that current must flow primarily through low-angle a-b axis grain boundaries (that were free of such layers), as it would be difficult for current to pass in the c-direction through these amorphous, insulating layers. Yan et al. [203], Wang et al. [87], and Luo et al. [206], have also reported the existence of amorphous regions on 2223 grain boundaries, particularly within the "triangular regions" found at 2223 grain facets or high angle boundaries. Holesinger et al. [204] have recently reported a  $J_c$  increase in 2223 samples for which the  $pO_2$  was changed during the final heat treatment from a low ( $\sim 7.5\%$   $O_2$ ) to a higher  $pO_2$  (air). They report the appearance of Bi,Pb-rich impurity phases in such samples, consistent with the crystallization of a Bi,Pb-rich liquid or amorphous phase. The relevance of this latter experiment to the present discussion is that the change to a higher  $pO_2$  reduces the effective temperature of

the 2223 heat treatment [33,111,114], making the phase changes similar to those obtained by cooling slowly in a fixed 7.5% O<sub>2</sub> atmosphere.

This microstructural mechanism is also consistent the results presented in Chapter 9, where the  $J_c$  and the  $T_c$  transition sharpness was greatly improved in slowly cooled tapes that still contained large amounts of precursor 2212. Such samples contain large amounts of the liquid associated with the 2223 transformation. Clearing the 2223 grain boundaries of this liquid should also greatly improve the connectivity of the 2223 network, resulting in more effective magnetization screening currents, thus sharpening the  $T_c$  transition.

As evidenced by this discussion, it seems it is not possible to attribute all of the effects that the cooling rate has on the superconducting properties of 2223 tapes to just one mechanism. It seems clear that decreasing the cooling rate leads to improvements in both the connectivity *and* the flux pinning properties of the 2223 filaments. It is possible to rationalize all of data in Chapters 9 and 10 by concluding that two major changes occur in BSCCO-2223 filaments during slow cooling: 1) the active cross section (i.e. the size of the percolative path) is increased by a reduction of amorphous phase at grain boundaries, and 2) that the flux pinning of the percolative path is increased by slow cooling.

## **10.5 Summary**

Both the connectivity and flux pinning of Ag-clad 2223 tapes are improved by slowly cooling after the final 2223 formation heat treatment. An increase in  $J_c$  (77 K, 0 T) from  $\sim 8$  to  $\sim 24$  kA/cm<sup>2</sup> was observed when the cooling rate to 730°C was decreased from 5°C to 0.005°C/min. A similar trend was observed in samples measured at 4.2 K. In

addition to this increase in the zero field  $J_c$ , slow cooling increased the 77 K irreversibility field from  $\sim 120$  to  $\sim 200$  mT, decreased the sensitivity of  $J_c$  to an applied magnetic field, and also sharpened the  $T_c$  transition and increased the onset from  $\sim 107$  to  $\sim 109$  K. An overall increase in the second phase content (especially Bi,Pb-rich phases) was observed in slowly cooled tapes, which may have formed from the crystallization of a Bi,Pb-rich liquid found between 2223 grains, and/or by slowly cooling outside of the 2223 stability temperature range. Additionally, the Pb content of the 2223 phase was decreased by slow cooling. It is concluded that the improved superconducting properties result from a change in the oxygen content and/or cation stoichiometry of the 2223 phase, which increases both  $T_c$  and the irreversibility field, and a reduction of an amorphous phase at the 2223 grain boundaries, which improves the intergranular connectivity.

## 11. Review and conclusions

The experiments described in this dissertation were designed to help deconvolute the complex interplay of materials processing and  $J_c$  limitations of BSCCO-2223 tapes. To this end, many analysis techniques were used to study several important aspects of thermomechanical processing.

The role that deformation plays in increasing the density and intergranular connectivity of the superconducting core was discussed in Chapters 5 and 6. The microhardness of the 2223 filament was used as a qualitative measure of the density, and it was found that in general, there is a strong correlation between the hardness of a filament and  $J_c$ , as summarized in Figure 11-1. It was also found that uniaxial pressing is more effective than rolling at densifying the BSCCO core (Figure 6-2), and that this density difference is one of the reasons why pressed tapes typically have higher  $J_c$  values than rolled tapes. However, it seems that at some point in the iterative deformation/heat treatment cycle, porosity ceases to be the dominant connectivity and  $J_c$ -limiting factor. As cracks were observed by SEM in samples that had already been given several heat

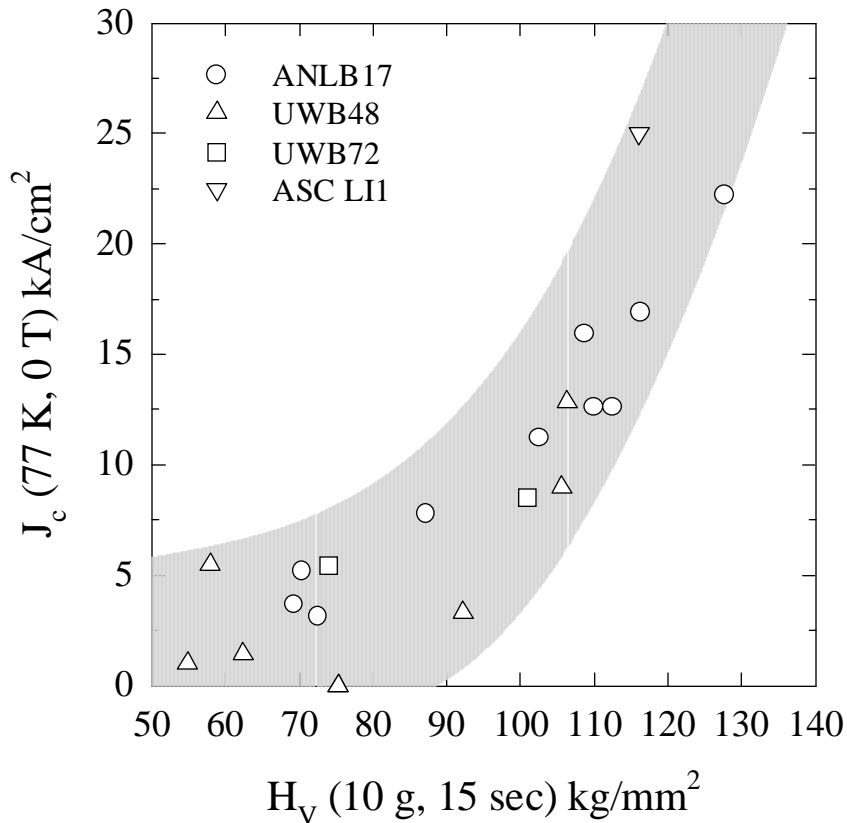


Figure 11-1. Summary plot of  $J_c (77 \text{ K}, 0 \text{ T})$  as a function of the after heat treatment Vickers microhardness of the BSCCO core of monofilament samples. The correlation is strong for many different composites.

treatments, it was postulated that an explicit crack-healing process step was required. The method chosen to implement this step was by control of the liquid phase associated with the precursor powder-to-2223 conversion process.

To prove both the existence and the strong  $J_c$  influence of residual deformation-induced microcracks, magneto-optical imaging was used as described in Chapter 7 to reveal the 2223 filament connectivity. As shown in Figure 7-2 and Figure 7-3, both the

existence and the orientation of the cracks with respect to the direction of current flow are important features; cracks that run transverse to the tape axis are more detrimental to  $J_c$  than cracks which run parallel to the tape axis and direction of current flow. Figure 11-2 shows MO images which convey the main result of this study: Because of insufficient crack-healing liquid, it is easy to leave behind deformation-induced microcracks in tapes even after final heat treatments of 50-200 hours. Since the principal microcrack orientation is determined by the deformation technique, as discussed in Section 4.2.3, this is another reason why rolled tapes in general perform more poorly than pressed tapes.

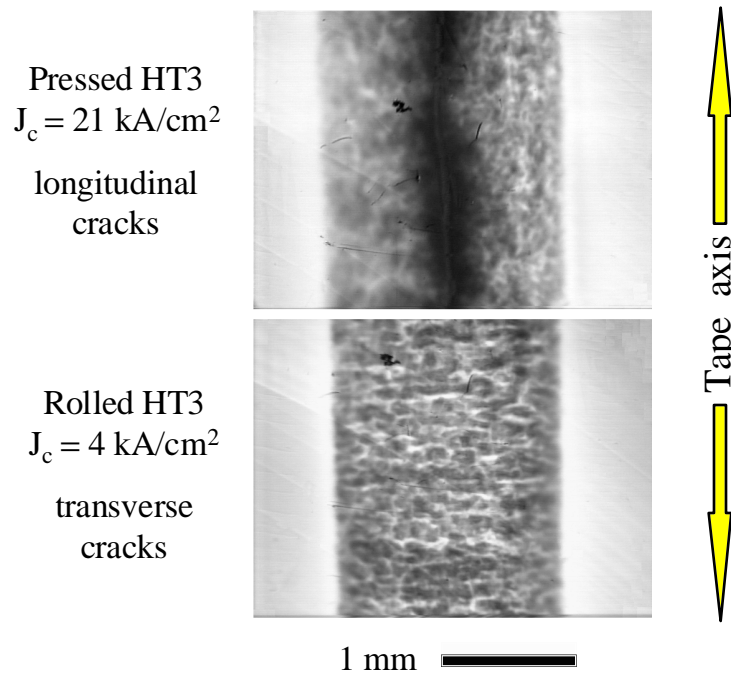


Figure 11-2. Plan view magneto-optical images of pressed and rolled 2223 tapes. The images were recorded at  $T = 13 \text{ K}$  and  $\mu_0 H = 40 \text{ mT}$  after zero field cooling. Magnetic flux penetrates into defects which run parallel to the direction of current flow in pressed samples, and in the transverse direction in rolled samples.

Since control of a liquid phase which could heal cracks seemed so important, processing methods intended to lend greater control over the presence of a liquid phase were developed. These experiments were described in Chapter 8. It was found that decomposing a fully converted 2223 core in oxygen (or nitrogen) would lead to the reformation of 2212 and various second phases, as shown in the micrographs of Figure 11-3. As these phases are essentially the same as those which occur “naturally” during processing, they should form a liquid phase when they are reacted back to the 2223 phase

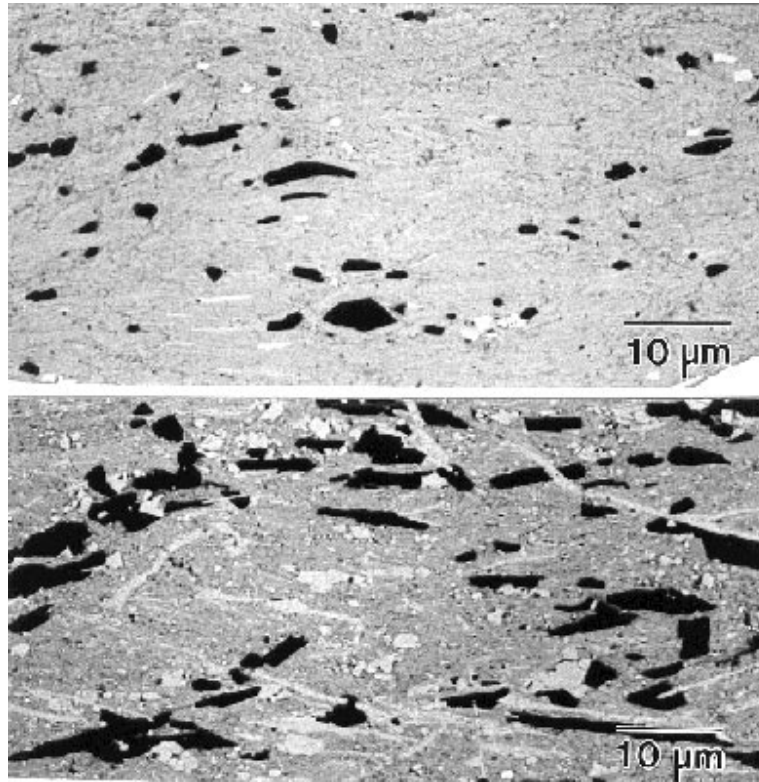


Figure 11-3. SEM backscatter micrographs of 2223 samples (top) before and (bottom) after decomposition in 100% O<sub>2</sub>. The 2223 phase decomposed into 2212 (light needles), alkaline earth cuprates (black), and Pb-rich second phases (gray equiaxed particles).

in 7.5% O<sub>2</sub>. However, despite much effort, large  $J_c$  gains caused by connectivity improvements were not regularly achieved. Studies of natural and decomposed phase mixtures by SEM, XRD, and DTA revealed that the phase assemblage achieved through decomposition was not quite the same as that in precursor powders. Moreover, such partially back-reacted mixtures did not seem form a liquid when heated. Those results were shown in Figure 8-20 and Figure 8-21.

The final two chapters of the dissertation described the large effect that the post-heat treatment cooling rate has on the microstructure,  $J_c$ , and  $T_c$  of 2223 tapes. In Chapter 9 it was shown that cooling slowly caused decomposition of the 2223 phase, but at the same time improved  $J_c$  (77 K, 0 T) and the sharpness of the  $T_c$  transition. Figure 11-4 shows an example of the observed behavior on pressed monofilament samples. A more detailed microstructural and superconducting property analysis of this effect was described in Chapter 10. Measurements of the extended electric field-current density characteristics of samples cooled at different rates as a function of magnetic field were used to determine the irreversibility field,  $H^*$ , of the percolative current path. It was found that one of the reasons why slow cooling improves  $J_c$  is that the flux pinning is improved during the slow cooling cycle, as summarized in the plot of  $H^*$  versus  $J_c$  in Figure 11-5. However, the fact that cooling slowly improved the zero field  $J_c$  values at both 77 K and 4.2 K, as well as the in-field  $J_c$  retention, indicated that an increase in the intergranular connectivity was also occurring. Analysis by SEM and XRD revealed that small pockets of a Pb- and Bi-rich liquid existed at the heat treatment temperature at the grain boundaries in some regions of the samples. It was concluded from the microstructural evidence that these grain-wetting liquid regions crystallized to non-wetting second phase particles during slow cooling. Removal of this insulating layer from between the 2223 grain boundaries resulted in an overall improvement in the intergranular connectivity, despite the isolated growth of large second phase particles.

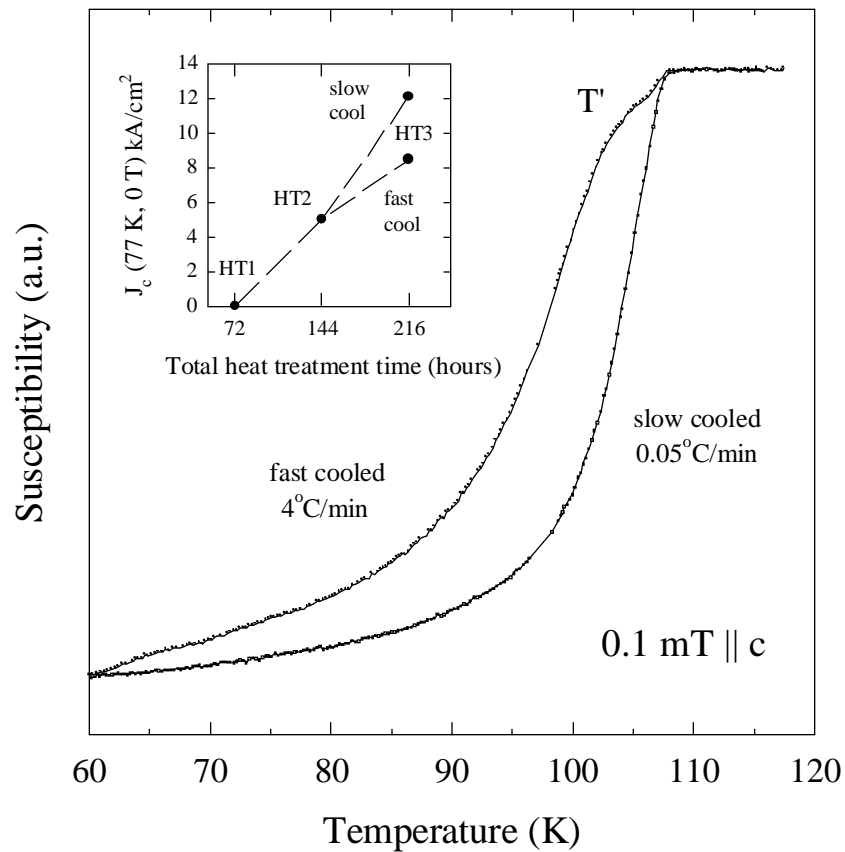


Figure 11-4. An example of the  $T_c$  and  $J_c$  improvements observed in samples cooled slowly after heat treatment. Cooling slowly sharpened the  $T_c$  transition and increased  $J_c$  by about 50%. Composite UWB41.

It can be concluded from these experiments that the  $J_c$  of a 2223 tape can be determined first by any of several connectivity-limiting factors, and in the end by the intragranular flux pinning. At the early stages of thermomechanical processing, a low volume fraction of the 2223 phase is the primary  $J_c$  limitation. As the phase purity is increased by further heat treatment, the porosity within the core limits the connectivity and  $J_c$ . This porosity can be reduced by mechanically deforming the sample between heat

treatments. However, deforming the sample when the 2223 phase purity is high, and is thus with little liquid-formation capacity, leaves residual microcracks throughout the tape. At this point the connectivity is limited by microcracking. Elimination of microcracks should increase  $J_c$ , but the connectivity can then be limited by small quantities of liquid phase that wet the 2223 grains, inhibiting supercurrent transport. Slow cooling can increase the connectivity by eliminating these liquid regions, crystallizing them into Pb-rich second phase particles. When this connectivity limit is removed,  $J_c$  becomes limited by the intragranular flux pinning (at least at 77 K). Improvements in the irreversibility field, which were used in this dissertation as a measure of flux pinning strength of the tape, is required to increase  $J_c$  at this point. Slow cooling is also effective at increasing the irreversibility field, probably by both reducing the anisotropy, and by introducing pinning defects into the crystal structure via decomposition of the 2223 phase.

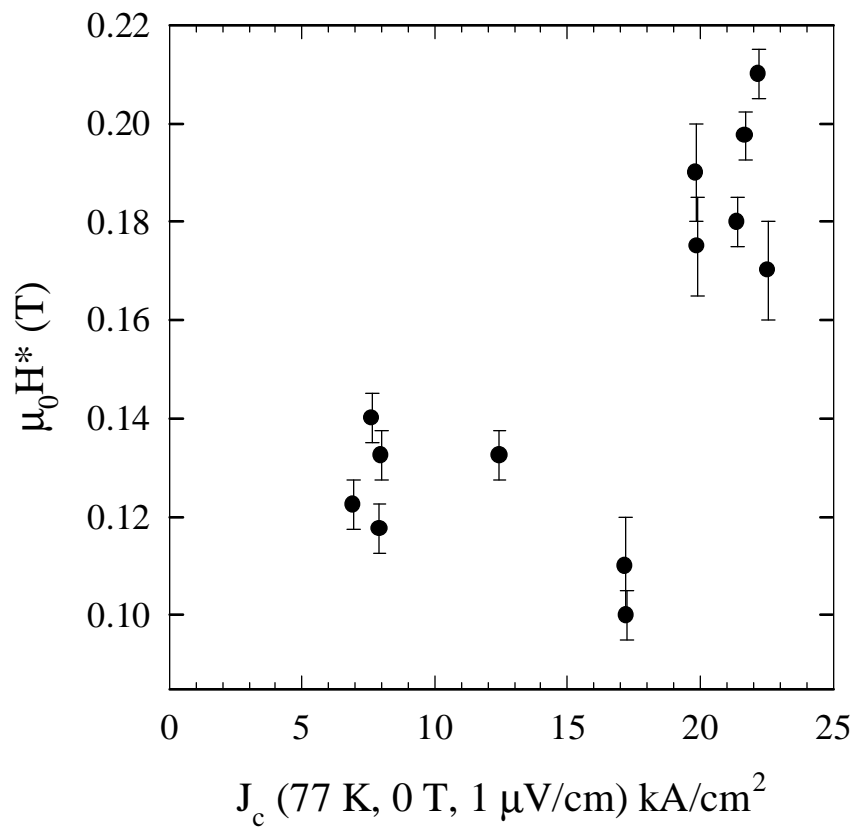


Figure 11-5.  $H^*$  as a function of  $J_c$  (77 K, 0 T) for samples of UWB71 cooled at different rates. Both  $J_c$  and  $H^*$  were increased by slow cooling.

## 12. References

- 1 J.G. Bednorz and K.A. Müller, *Z. Phys. B.* 64 (1986) 189.
- 2 M.K. Wu, J.R. Asburn, C.J. Torng, P.H. Hor, R.L. Meng, L.Gao, Z.J. Huang, Y.Q. Wang, and C.W. Chu, *Phys. Rev. Lett.* 58 (1987) 908.
- 3 D. Dimos, P. Chaudhari, and J. Mannhart, *Phys. Rev. B* 41 (1990) 4038.
- 4 M. Maeda, Y. Tanaka, M. Fukutomi, and T. Asano, *Jpn. J. Appl. Phys.* 27 (1988) L209.
- 5 A.C. Rose-Innes and E.H. Rhoderick, Introduction to Superconductivity, 2<sup>nd</sup> edition (Pergamon Press, Oxford, 1978).
- 6 Q. Li, M. Suenaga, T. Hikata, and K. Sato, *Phys. Rev. B* 46 (1992) 5957.
- 7 K. Osamura, S.S. Oh, and S. Ochiai, *Supercond. Sci. Technol.* 5 (1992) 1.
- 8 K. Osamura, M. Kamo, S.S. Oh, and S. Ochiai, *Supercond. Sci. Technol.* 5 (1994).
- 9 S. Patel, T. Haugan, F. Wong, S. Chen, S.S. Li, J. Ye, and D.T. Shaw, *Cryogenics* 35 (1995) 249.
- 10 D.C. Larbalestier, Proc. Of TcSUH 10<sup>th</sup> Anniversary Workshop, March 12, 1996, Houston, Texas.
- 11 G. Blatter, M.V. Feigel'man, V.B. Geshkenbein, A.I. Larkin, and V.M. Vinokur, *Rev. Mod. Phys.* 66 (1994) 1125.

- 12 M. Tinkham, *Physica C* 235-240 (1994) 3.
- 13 M. Karuna, J.A. Parrell, and D.C. Larbalestier, *IEEE Trans. Appl. Supercond.* 5 (1995) 1279.
- 14 B. Wolf, P. Paufler, M. Schubert, C. Rodig, and K. Fischer, *Supercond. Sci. Technol.* 9 (1996) 589.
- 15 M. Karuna, W. Zhang, E.E. Hellstrom, and D.C. Larbalestier, to appear in *Adv. Cryo. Engr.* (1996).
- 16 G.F. Dieter, *Mechanical Metallurgy* (McGraw-Hill, Inc., New York, 1986).
- 17 S. Thiagarajan and S.K. Varma, *Metall. Trans. A* 22A (1991) 258.
- 18 M. Satou, Y. Yamada, S. Murase, T. Kitamura, and Y. Kamisada, *Appl. Phys. Lett.* 64 (1994) 640.
- 19 G. Grasso, A. Jeremie, and R. Flükiger, *Supercond. Sci. Technol.* 8 (1995) 827.
- 20 J.M. Ponty, D.L. Slauson, and W.L. Starch, unpublished.
- 21 R.A. Outlaw, S.N. Sankaran, G.B. Hofland, and M.R. Davidson, *J. Mater. Res.* 3 (1988) 1378.
- 22 J.-H. Park, *Mater. Letters* 9 (1990) 313.
- 23 J. Sato, T. Sasaoka, and S. Kuma, in *Advances in Superconductivity VI*, edited by T. Fujita and Y. Shiohara, (Springer, Tokyo, 1994) p. 679.
- 24 K. Nomura, T. Sasaoka, K. Kato, S. Kuma, H. Kumakura, K. Togano, and N. Tomita, in *Advances in Superconductivity VI*, edited by T. Fujita and Y. Shiohara, (Springer, Tokyo, 1994).
- 25 Y. Yamada, M. Satou, and S. Murase, in *Advances in Superconductivity V*, edited by Y. Bando and H. Yamauchi, (Springer, Tokyo, 1993) p. 717.
- 26 Y. Yamada, M. Satou, T. Masegi, S. Nomura, S. Murase, T. Koizumi, and Y. Kamisada, in *Advances in Superconductivity VI*, edited by T. Fujita and Y. Shiohara, (Springer, Tokyo, 1994) p. 609.

- 27 J.-H. Ahn, K.-H. Ha, S.-Y. Lee, J.-W. Ko, H.-D. Kim, and H. Chung, *Jpn. J. Appl. Phys.* 33 (1994) L1298.
- 28 W. Goldacker, J. Kessler, B. Ullmann, E. Mossang, and M. Rikel, *IEEE Trans. Appl. Supercond* 5 (1995) 1834.
- 29 B.N. Hubert, R. Zhou, T.G. Holesinger, W.L. Hults, A. Lacerda, A.S. Murray, R.D. Ray II, C.M. Buford, L.G. Phillips, A. Kebede, and J.L. Smith, *J. Elect. Mater.* 24 (1995) 1869.
- 30 J.A. Parrell, S.E. Dorris, and D.C. Larbalestier, *Adv. Cryo. Engr.* 40 (1994) 197.
- 31 J.S. Luo, N. Merchant, E. Escorcía-Aparicio, V.A. Maroni, D.M. Gruen, B.S. Tani, G.N. Riley, Jr., and W.L. Carter, *IEEE Trans. Appl. Supercond.* 3 (1993) 972.
- 32 Y.S. Sung and E.E. Hellstrom, *J. Am. Ceram. Soc.* 78 (1995) 2003.
- 33 Y.E. High, Y. Feng, Y.S. Sung, E.E. Hellstrom, and D.C. Larbalestier, *Physica C* 220 (1994) 81.
- 34 J.S. Luo, N. Merchant, V.A. Maroni, S.E. Dorris, M.T. Lanagan, and B.S. Tani, *J. Am. Ceram. Soc.* 78 (1995) 2785.
- 35 S.A. Sunshine, T. Siegrist, L.F. Schneemeyer, D.W. Murphy, R.J. Cava, B. Batlogg, R.B. van Dover, R.M. Fleming, S.H. Glarum, S. Nakahara, R. Farrow, J.J. Krajewski, S.M. Zahurak, J.V. Waszczak, J.H. Marshall, P. Marsh, L.W. Rupp, Jr., and W.F. Peck, *Phys. Rev. B* 38 (1988) 893.
- 36 M. Takano, J. Takada, K. Oda, H. Kitaguchi, Y. Miura, Y. Ikeda, Y. Tomii, and H. Mazaki, *Jpn. J. Appl. Phys.* 27 (1988) L1041.
- 37 N. Kijima, H. Endo, J. Tsuchiya, A. Sumiyama, M. Mizuno, and Y. Oguri, *Jpn. J. Appl. Phys.* 27 (1988) L1852.
- 38 S. Koyama, U. Endo, and T. Kawai, *Jpn. J. Appl. Phys.* 27 (1988) L1861.
- 39 J. Tsuchiya, H. Endo, N. Kijima, A. Sumiyama, M. Mizuno, and Y. Oguri, *Jpn. J. Appl. Phys.* 28 (1989) L1918.

- 40 T. Uzumaki, K. Yamanaka, N. Kamehara, K. Niwa, *Jpn. J. Appl. Phys.* 28 (1989) L75.
- 41 Y. Ikeda, H. Ito, S. Shimomura, Z. Hiroi, M. Takano, Y. Bando, J. Takada, K. Oda, H. Kitaguchi, Y. Miura, Y. Takeda, and T. Takada, *Physica C* 190 (1991) 18.
- 42 S.S. Oh and K. Osamura, *Supercond. Sci. Technol.* 4 (1991) 239.
- 43 W. Wong-Ng, C.K. Chiang, S.W. Freiman, L.P. Cook, and M.D. Hill, *Am. Ceram. Soc. Bull.* 71 (1992) 1261.
- 44 Y.L. Chen and R. Stevens, *J. Am. Ceram. Soc.* 75 (1992) 1150.
- 45 Y. Yamada, B. Obst, and R. Flükiger, *Supercond. Sci. Technol.* 4 (1991) 165.
- 46 P.E.D. Morgan, J.D. Piché, and R.M. Housley, *Physica C* 191 (1992) 179.
- 47 H.K. Lee, K. Park, and D.H. Ha, *J. Appl. Phys.* 70 (1991) 2764.
- 48 G.M. Zorn, R. Hornung, H.E. Göbel, B. Seebacher, H.W. Neumüller, and G. Tomandl, *Supercond. Sci. Technol.* 8 (1995) 234.
- 49 S.S. Oh and K. Osamura, *Supercond. Sci. Technol.* 4 (1991) 239.
- 50 S.E. Dorris, B.C. Prorok, M.T. Lanagan, S. Sinha, and R.B. Poeppel, *Physica C* 212 (1993) 66.
- 51 S.E. Dorris, B.C. Prorok, M.T. Lanagan, N.B. Browning, M.R. Hagen, J.A. Parrell, Y. Feng, A. Umezawa, and D.C. Larbalestier, *Physica C* 223 (1994) 163.
- 52 A. Jeremie, K. Alami-Yadri, J-C Grivel, and R. Flükiger, *Supercond. Sci. Technol.* 6 (1993) 730.
- 53 J.L. MacManus-Driscoll, J.C. Bravman, R.J. Savoy, G. Gorman, and R.B. Beyers, *J. Am. Ceram. Soc.* 77 (1994) 2305.
- 54 J.-C. Grivel, A. Jeremie, B. Hensel, and R. Flükiger, *Supercond. Sci. Technol.* 6 (1993) 725.
- 55 L. Pierre, J. Schneck, D. Morin, J.C. Tolédano, J. Primot, C. Daguet, and H. Savary, *J. Appl. Phys.* 68 (1990) 2296.

- 56 J.-C. Grivel, A. Jeremie, B. Hensel, and R. Flükiger, Proceedings of ICMAS-93, Superconducting Materials, edited by J. Etourneau et al. (1994).
- 57 M. Xu, D.K. Finnemore, U. Balachandran, and P. Haldar, *Appl. Phys. Lett.* 66 (1995) 3359.
- 58 W.D. Kingery, H.K. Bowen, and D.R. Uhlmann, Introduction to Ceramics, Second Edition (John Wiley and Sons, New York, 1976).
- 59 M. Avrami, *J. Chem. Phys.* 7 (1939) 1103.
- 60 J.W. Anderson, J.A. Parrell, and D.C. Larbalestier, unpublished.
- 61 D.A. Porter and K.E. Easterling, Phase Transformations in Metals and Alloys (VNR International, London, 1989).
- 62 J.S. Luo, N. Merchant, V.A. Maroni, D.M. Gruen, B.S. Tani, W.L. Carter, and G.N. Riley, Jr., *Appl. Supercond.* 1 (1993) 101.
- 63 X.-H. Gao, J. Li, S.-F. Jiang, D. Gao, G.-D. Zheng, and S. Gao, *Physica C* 244 (1995) 321.
- 64 C.-H. Shan and S.H. Risbud, *Supercond. Sci. Technol.* 6 (1993) 736.
- 65 Q.Y. Hu, H.K. Liu, and S.X. Dou, *Physica C* 250 (1995) 7.
- 66 Y.D. Chiu, C.H. Kao, T.S. Lei, and M.K. Wu, *Physica C* 235-240 (1994) 485.
- 67 J.W. Christian, The Theory of Transformations in Metals and Alloys (Pergamon, London, 1987).
- 68 A. Blazek, Thermal Analysis (VNR International, London, 1973).
- 69 T. Hatano, K. Aota, S. Ikeda, K. Nakamura, and K. Ogawa, *Jpn. J. Appl. Phys.* 27 (1988) L2055.
- 70 P.E.D. Morgan, R.M. Housley, J.R. Porter, and J.J. Ratto, *Physica C* 176 (1991) 279.
- 71 J.-C. Grivel and R. Flükiger, *Supercond. Sci. Technol.* 9 (1996) 555.

- 72 P. Strobel, W. Korczak, J-L Hodeau, and J-L Tholence, *Physica C* 161 (1989) 167.
- 73 M.R. De Guire, N.P. Bansai, and C.J. Kim, *J. Am. Ceram. Soc.* 73 (1990) 1165.
- 74 Y. Massalker, A.N. Sembira, and J. Baram, *J. Mater. Res.* 8 (1993) 2445.
- 75 Y.L. Chen and R. Stevens, *J. Am. Ceram. Soc.* 75 (1992) 1160.
- 76 S. Ikeda, H. Ichinose, T. Kimura, T. Matsumoto, H. Maeda, Y. Ishida, and K. Ogawa, *Jpn. J. Appl. Phys.* 27 (1988) L999.
- 77 Y.S. Sung, Y. Feng, unpublished.
- 78 W. Bian, Y. Zhu, Y.L. Wang, and M. Suenaga, *Physica C* 248 (1995) 119.
- 79 Z.-X. Cai, Y. Zhu, and D.O. Welch, *Phys. Rev. B.* 52 (1995) 13035.
- 80 Y.-L. Wang, W. Bian, Y. Zhu, Z.X. Cai, D.O. Welch, R.L. Sabatini, M. Suenaga, and T.R. Thurston, *Appl. Phys. Lett.* 69 (1996) 580.
- 81 D.K. Finnemore, M. Xu, D. Kouzoudis, T. Bloomer, M.J. Kramer, S. McKernan, U. Balachandran, and P. Haldar, *Appl. Phys. Lett.* 68 (1996) 556.
- 82 N. Merchant, J.S. Luo, V.A. Maroni, G.N. Riley, Jr., and W.L. Carter, *Appl. Phys. Lett.* 65 (1994) 1039.
- 83 G. Grasso, A. Perin, and R. Flükiger, *Physica C* 250 (1995) 43.
- 84 J.W. Anderson, J.A. Parrell, P.V.P.S.S. Sastry, and D.C. Larbalestier, to appear in *IEEE Trans. Appl. Supercond.* 7 (1997).
- 85 A. Umezawa, Y. Feng, H.S. Edelman, Y.E. High, D.C. Larbalestier, Y.S. Sung, and S. Fleshler, *Physica C* 198 (1992) 261.
- 86 A. Umezawa, Y. Feng, H.S. Edelman, T.C. Willis, J.A. Parrell, D.C. Larbalestier, G.N. Riley, Jr., and W.L. Carter, *Physica C* 219 (1994) 378.
- 87 R.K. Wang, H.K. Liu, and S.X. Dou, *Supercond. Sci. Technol.* 8 (1995) 168.
- 88 O. Eibl, *Supercond. Sci. Technol.* 8 (1995) 833.

- 89 W. Gao and J.B. Vander Sande, *Physica C* 181 (1991) 105.
- 90 R.A. Outlaw, S.N. Sankaran, G.B. Hoflund, and M.R. Davidson, *J. Mater. Res.* 3 (1988) 1378.
- 91 J.-H. Park, *Mater. Lett.* 9 (1990) 313.
- 92 A. Oota, T. Horio, K. Ohba, and K. Iwasaki, *J. Appl. Phys.* 71 (1992) 5997.
- 93 Y.C. Guo, H.K. Liu, and S.X. Dou, *J. Mater. Res.* 8 (1993) 2187.
- 94 T. Matsushita, A. Suzuki, T. Kishida, M. Okuda, and H. Naito, *Supercond. Sci. Technol.* 7 (1994) 222.
- 95 H. Assmann, H. Krauth, H.-W. Neumüller, M. Wilhelm, G. Ries, G. Saemann-Ischenko, *Cryogenics* (1993).
- 96 Y.S. Sung and E.E. Hellstrom, *Physica C* 255 (1995) 266.
- 97 M.T. Malachevsky and D.A. Esparza, *Thermochimica Acta* 2424 (1995).
- 98 S.X. Dou, K.-H. Song, H.K. Liu, C.C. Sorrell, M.H. Apperley, and N. Savvides, *Appl. Phys. Lett.* 56 (1990) 493.
- 99 S.X. Dou, H.K. Liu, Y.C. Guo, R. Bhasale, Q.Y. Hu, E. Babic, and I. Kusevic, *Appl. Supercond.* 2 (1994) 191.
- 100 R.W. McCallum, K.W. Dennis, L. Margulies, and M.J. Kramer, Processing and Properties of Long Lengths of Superconductors, Proc. 1993 Fall TMS Meeting, Pittsburgh, PA, Oct. 17-21 (1993).
- 101 M. Lelethal, T.N. Blanton, C.L. Barnes, and H.J. Romanofsky, *Physica C* 193 (1992) 395.
- 102 J.S. Luo, N. Merchant, V.A. Maroni, G.N. Riley, Jr., and W.L. Carter, *Appl. Phys. Lett.* 63 (1993) 690.
- 103 Y. Feng, Y.E. High, D.C. Larbalestier, Y.S. Sung, and E.E. Hellstrom, *Appl. Phys. Lett.* 62 (1993) 1553.

- 104 Y. Fang, S. Danyluk, K. C. Goretta, Nan Chen, M. Runde, S. J. Rothman, J. L. Routbort, *Appl. Phys. Lett.* 60 (1992) 2291.
- 105 R.D. Parrella, Y.S. Sung, and E.E. Hellstrom, *IEEE Trans. Appl. Supercond.* 5 (1995) 1283.
- 106 R.H. Arendt, M.F. Garbaskas, E.L. Hall, K.W. Lay, and J.E. Tkaczyk, *Physica C* 194 (1992) 383.
- 107 L. Hua, Q.Z. Yao, M. Jiang, Y.Z. Wang, H. Tang, Z.R. Li, and G.W. Qiao, *J. Appl. Phys.* 78 (1995) 3274.
- 108 T.R. Thurston, U. Wildgruber, N. Jisrawi, P. Haldar, M. Suenaga, and Y.L. Wang, *J. Appl. Phys.* 79 (1996) 3122.
- 109 N.M. Hwang, G.W. Bahng, H.G. Moon, and J.C. Park, *Appl. Phys. Lett.* 54 (1989) 1588.
- 110 A. Maeda, K. Noda, K. Uchinokura, S. Tanaka, *Jpn. J. Appl. Phys.* 28 (1989) L576.
- 111 W. Zhu and P.S. Nicholson, *J. Appl. Phys.* 73 (1993) 8423.
- 112 R. Masini, L. Dimesso, A. Migliori, M.G. Francesconi, and G. Calestani, *Physica C* 223 (1994) 189.
- 113 J.C. Jao, L.J. Chang, H.E. Horng, and H.C. Yang, *Physica C* 162-164 (1989) 915.
- 114 U. Endo, S. Koyama, and T. Kawai, *Jpn. J. Appl. Phys.* 27 (1988) L1476.
- 115 L.M. Rubin, T.P Orlando, J.B. Vander Sande, G. Gorman, R. Savoy, R. Swope, and R. Beyers, *Appl. Phys. Lett.* 61 (1992) 1977.
- 116 M. Daümling, R. Maad, A. Jeremie, and R. Flükiger, to appear in *J. Mater. Res.* (1996).
- 117 J.S. Luo, N. Merchant, V.A. Maroni, D.M. Gruen, B.S. Tani, W.L. Carter, G.N. Riley, Jr., and K.H. Sandhage, *J. Appl. Phys.* 72 (1992) 2385.
- 118 M. Xu and D.K. Finnemore, *J. Appl. Phys.* 76 (1994) 1111.

- 119 J.A. Parrell, D.C. Larbalestier, and S.E. Dorris, *IEEE Trans. Appl. Supercond.* 5 (1995) 1275.
- 120 D.A. Korzekwa, J.F. Bingert, E.J. Podtberg, and P. Miles, *Appl. Supercond.* 2 (1994) 261.
- 121 M.F. Ashby and D.R.H. Jones, Engineering Materials 1 (Pergamon, Oxford, 1980).
- 122 K. Osamura, S.S. Oh, and S. Ochiai, *Supercond. Sci. Technol.* 3 (1990) 143.
- 123 R. Flükiger, T. Graf, M. Decroux, C. Groth, and Y. Yamada, *IEEE Trans. Magn.* 27 (1991) 1258.
- 124 A. Ono, *Jpn. J. Appl. Phys.* 27 (1988) L2276.
- 125 B.A. Glowacki and J. Jackiewicz, *J. Appl. Phys.* 75 (1994) 2992.
- 126 D.C. Larbalestier, X.Y. Cai, Y. Feng, H. Edelman, A. Umezawa, G.N. Riley, Jr, and W.L. Carter, *Physica C* 221 (1994) 299.
- 127 D.C. Larbalestier, Y. Feng, X.Y. Cai, H. Edleman, E.E. Hellstrom, Y.E. High, J.A. Parrell, Y.S. Sung, and A. Umezawa, in Proc. of the 7<sup>th</sup> International Workshop on Critical Currents in Superconductors, edited by H.W. Weber (World Scientific, Singapore, 1994) p. 82.
- 128 Q. Li, K. Broderson, H.A. Hjuler, and T. Freltoft, *Physica C* 217 (1993) 360.
- 129 D.W. Johnson Jr. and W.W. Rhodes, *J. Am. Ceram. Soc.* 72 (1989) 2346.
- 130 K.C. Goretta, M.T. Lanagan, D.Y. Kaufman, A.C. Biondo, C.-T. Wu, M.E. Loomans, M.R. Cheesman, R.B. Poeppel, and A.S. Nash, *Properties of Emerging P/M Materials* 8 (1992) 251.
- 131 L.N. Bulaevskii, L.L. Daeman, M.P. Maley, and J.Y. Coulter, *Phys. Rev. B* 48 (1993) 13798.
- 132 J. Tenbrink, M. Wilhelm, K. Heine, and H. Krauth, *IEEE Trans. Appl. Supercond.* 3 (1993) 1123.
- 133 J.A. Parrell, S.E. Dorris, and D.C. Larbalestier, *Physica C* 231 (1994) 137.

- 134 K. Shibutani, Q. Li, R.L. Sabatini, M. Suenaga, L. Motowidlo, and P. Haldar, *Appl. Phys. Lett.* 63 (1993) 3515.
- 135 B. Hensel, J.-C. Grivel, A. Jeremie, A. Perin, A. Pollini, and R. Flükiger, *Physica C* 205 (1993) 329.
- 136 W. Gao and J.B. Vander Sande, *Supercond. Sci. and Technol.* 5 (1992) 318.
- 137 G. Grasso, A. Perrin, and R. Flükiger, *Physica C* 250 (1995) 43.
- 138 P. Haldar, J.G. Hoehn, Jr., J.A. Rice, and L.R. Motowidlo, *Appl. Phys. Lett.* 60 (1992) 495.
- 139 P. Kovác, I. Husek, W. Pachla, T. Melisek, and V. Kilment, *Supercond. Sci. Technol.* 8 (1995) 341.
- 140 D.W.A. Willén, C. Richer, P.R. Critchlow, M. Goyette, R. Nadi, J.R. Cave, G. Quirion, and M. Aubin, *Supercond. Sci. Technol.* 8 (1995) 347.
- 141 G.N. Riley, Jr., D.R. Parker, C.J. Christopherson, P.K. Miles, J.J. Pickett, S.E. Hughson, J.D. Schreiber, A. Polyanskii, A. Pashitski, and D.C. Larbalestier, *Physica C* 235-240 (1994) 3407.
- 142 Q. Li, G.N. Riley, Jr., R.D. Parrella, S. Fleshler, M.W. Rupich, W.L. Carter, J.O. Willis, J.Y. Coulter, J.F. Bingert, V.K. Sikka, J.A. Parrell, and D.C. Larbalestier, submitted to *IEEE Trans. Appl. Supercond.* (1996).
- 143 I. Husek, P. Kovác, and W. Pachla, *Supercond. Sci. Technol.* 8 (1995) 617.
- 144 D.B. Ingerly, W.A. Ellingson, T.A.K. Pillai, and N. Vasanthamohan, *Supercond. Sci. Technol.* 8 (1995) 779.
- 145 F.H. Chen, H.S. Koo, and T.Y. Tseng, *Appl. Phys. Lett.* 58 (1991) 637.
- 146 M.G. Smith, D.S. Phillips, D.E. Peterson, and J.O. Willis, *Physica C* 224 (1994) 168.
- 147 M.T. Lanagan, D.S. Kupperman, G.A. Yaconi, S.H. Gilgore, and A. Saigal, *IEEE Trans. Appl. Supercond.* 5 (1995) 1475.

- 148 J.A. Parrell, Y. Feng, S.E. Dorris, and D.C. Larbalestier, *J. Mater. Res.* 11 (1996) 555.
- 149 M.P. James, B.A. Glowacki, J.E. Evetts, S.P. Ashworth, R. Garré, and S. Conti, *IEEE Trans. Appl. Supercond.* 5 (1995) 1838.
- 150 M. Lahtinen, J. Paasi, J. Sarkaniemi, Z. Han, and T. Freltoft, *Physica C* 244 (1995) 115.
- 151 L.A. Dorosinskii, M.I. Indebom, V.I. Nikitenko, Yu A. Ossip'yan, A.A. Polyanskii, and V.K. Vlasko-Vlasov, *Physica C* 203 (1992) 149.
- 152 V.K. Vlasko-Vlasov, M.V. Indebom, and A.A. Polyanskii, Springer Series in Materials Science Vol. 23, edited by V. Shekhtnam (Springer, Berlin, 1993) p. 111.
- 153 U. Welp, D.O. Gunter, G.W. Crabtree, J.S. Luo, V.A. Maroni, W.L. Carter, V.K. Vlasko-Vlasov, and V.I. Nikitenko, *Appl. Phys. Lett.* 66 (1995) 1270.
- 154 M. Turchinskaya, D.L. Kaiser, A.J. Shapiro, and J. Schwartz, *Physica C* 246 (1995) 375.
- 155 A.E. Pashitski, A. Polyanskii, A. Gurevich, J.A. Parrell, and D.C. Larbalestier, *Physica C* 246 (1995) 133.
- 156 A.E. Pashitski, A. Polyanskii, A. Gurevich, J.A. Parrell, and D.C. Larbalestier, *Appl. Phys. Lett.* 67 (1995) 2720.
- 157 Y.B. Huang, G.F. de la Fuente, M.T. Ruiz, A. Larrea, A. Badia, F. Lera, C. Rillo, and R. Navarro, *Cryogenics* 33 (1993) 117.
- 158 J. Joo, J.P. Singh, and R.B. Poeppel, *Supercond. Sci. Technol.* 6 (1993) 421.
- 159 S.X. Dou, H.K. Liu, Y.C. Guo, and D.L. Shi, *IEEE Trans. Appl. Supercond.* 3 (1993) 1135.
- 160 Y.C. Guo, H.K. Liu, and S.X. Dou, *Appl. Supercond.* 1 (1993) 25.
- 161 J.-C. Grivel and R. Flükiger, *Physica C* 235-240 (1994) 505.
- 162 Y. Kusano, T. Nanba, J. Takada, T. Egi, Y. Ikeda, and M. Takano, *Physica C* 219 (1994) 366.

- 163 J.A. Parrell and D.C. Larbalestier, unpublished.
- 164 M. Xie, L.W. Zhang, T.G. Chen, and J. Cai, *Physica C* 206 (1993) 251.
- 165 S.X. Dou, H.K. Liu, Y.L. Zhang, and W.H. Blain, *Supercond. Sci. Technol.* 4 (1991) 203.
- 166 C.L. Briant, E.L. Hall, K.W. Lay, and J.E. Tkaczyk, *J. Mater. Res.* 9 (1994) 2789.
- 167 J.A. Parrell, A.A. Polyanskii, A.E. Pashitski, and D.C. Larbalestier, *Supercond. Sci. Technol.* 9 (1996) 393.
- 168 J.S. Luo, N. Merchant, V.A. Maroni, M. Hash, and M. Rupich, to appear in Proc. Symp. High Temperature Superconductors, TMS Annual Meeting in Anaheim, CA Feb. 4-8, 1996.
- 169 B.J. Reardon and C.R. Hubbard, *Pow. Diff.* 7 (1992) 96.
- 170 K.W. Lay, Mat. Res. Soc. Symp. Proc. 275 (1992) 651.
- 171 E. Özdas and T. Firat, Physics and Materials Science of High Tc Superconductors II, NATO ASI series (1992) 381.
- 172 L.N. Bulaevskii, J.R. Clem, L.I. Glazman, and A.P. Malozemoff, *Phys. Rev. B* 45 (1992) 2545.
- 173 B. Hensel, G. Grasso, and R. Flükiger, *Phys. Rev. B* 51 (1995) 15456.
- 174 H. Mukai, K. Ohkura, N. Shibuta, T. Hikata, M. Ueyama, T. Kato, J. Fujikama, K. Muranaka, and K. Sato, in Advances in Superconductivity V, edited by Y. Bando and H. Yamauchi, (Springer, Tokyo, 1993).
- 175 S.S. Oh, T. Kubota, and K. Osamura, *Physica C* 171 (1990) 265.
- 176 Y.B. Huang, G.F. de la Fuente, A. Larrea, and R. Navarro, *Supercond. Sci. Technol.* 7 (1994) 759.
- 177 K. Yoshida, Y. Sano, and Y. Tomii, *Supercond. Sci. Technol.* 8 (1995) 329.

- 178 J.E. Tkaczyk, R.H. Arendt, M.F. Garbaskas, H.R. Hart, K.W. Lay, and F.E. Luborsky, *Phys. Rev. B* 45 (1992) 12506.
- 179 Y. Sun, F. Zhang, Z. Lu, J. Jiang, J. Du, and Y. Zhang, *Phys. Rev. B* 51 (1995) 519.
- 180 Q. Li, H.J. Wiesmann, M. Suenaga, L. Motowidlo, and P. Haldar, *Appl. Phys. Lett.* 66 (1995) 637.
- 181 Y. Mawatari, H. Yamasaki, S. Kosaka, and M. Umeda, *Cryogenics* 35 (1995) 161.
- 182 J. Paasi, P. Kottman, and M. Polak, *Physica C* 249 (1995) 350.
- 183 H.S. Edelman, Ph.D. thesis, University of Wisconsin-Madison (1995).
- 184 H.S. Edelman, J.A. Parrell, and D.C. Larbalestier, to appear in *J. Appl. Phys.* (1997).
- 185 P.J.M. Wöltgens, C. Dekker, R.H. Koch, B.W. Hussey, and A. Gupta, *Phys. Rev. B* 52 (1996) 4536.
- 186 J.A. Parrell, D.C. Larbalestier, G.N. Riley, Jr., Q. Li, R.D. Parrella, and M. Teplitsky, *Appl. Phys. Lett.* 69 (1996) 2915.
- 187 J.A. Parrell and D.C. Larbalestier, unpublished.
- 188 Y. Kotaka, T. Kimura, H. Ikuta, J. Shimoyama, K. Kitazawa, K. Yamafuji, K. Kishio, and D. Pooke, *Physica C* 235-240 (1994) 1529.
- 189 C. Allgeier and J.S. Schilling, *Physica C* 168 (1990) 499.
- 190 G. Triscone, J.-Y. Genoud, T. Graf, A. Junod, and J. Muller, *Physica C* 176 (1991) 247.
- 191 P. Krishnaraj, M. Lelovic, N.G. Eror, and U. Balachandran, *Physica C* 234 (1994) 318.
- 192 D.J. Brauer, D. Busch, R. Eujen, A. Gladun, and J. Hüdepohl, *Cryogenics* 32 (1992) 1052.
- 193 M. Tetenbaum and V.A. Maroni, *Physica C* 260 (1996) 71.

- 194 N. Hudáková, V. Plecháček, P. Dordor, K. Flachbart, K. Knizek, J. Kovác, and M. Reiffers, *Supercond. Sci. Technol.* 8 (1995) 324.
- 195 S. Kaesche, P. Majewski, and F. Aldinger, *J. Electronic. Mater.* 24 (1995) 1829.
- 196 P. Majewski, S. Elscher, and F. Aldinger, *Physica C* 249 (1995) 234.
- 197 H.-L. Su, P. Majewski, and F. Aldinger, *Physica C* 249 (1995) 241.
- 198 R.H. Arendt, M.F. Garbaskas, C.A. Meyer, F.J. Rotella, J.D. Jorgensen, and R.L. Hitterman, *Physica C* 194 (1992) 397.
- 199 H. Cömert, M. Altunbas, T.D. Dzhafarov, T. Küçükömeroglu, Y.G. Asadov, and H. Karal, *Supercond. Sci. Technol.* 7 (1994) 824.
- 200 CRC Handbook of Chemistry and Physics, (CRC Press, 1990).
- 201 K.C. Goretta, M. Jiang, D.S. Kupperman, M.T. Lanagan, J.P. Singh, N. Vasanthamohan, D.G. Hinks, J.F. Mitchell, and J.W. Richardson, Jr., submitted to *IEEE Trans. Appl. Supercond.* (1996).
- 202 Y.S. Sung and E.E. Hellstrom, *Physica C* 253 (1995) 79.
- 203 Y. Yan, W. Lo, J.E. Evetts, A.M. Campbell, and W.M. Stobbs, *Appl. Phys. Lett.* 67 (1995) 2554.
- 204 T.G. Holesinger et al., reported at 1995 MRS fall meeting, Boston, MA.
- 205 Y.H. Li, J.A. Kilner, M. Dhalle, A.D. Caplin, G. Grasso, and R. Flükiger, *Supercond. Sci. Technol.* 8 (1995) 764.
- 206 J.S. Luo, S.E. Dorris, A.K. Fisher, J.S. LeBoy, V.A. Maroni, Y. Feng, and D.C. Larbalestier, *Supercond. Sci. Technol.* 9 (1996) 412.